Onderzoek naar de blootstelling van wolfraam aan een intense H/He-flux en thermische belastingen voor kernfusie

Investigation of Tungsten Exposed to Fusion Relevant Intense H/He Particle Fluxes and Thermal Loads

Nathan Lemahieu

Promotors: Prof. J.-M. Noterdaeme, PhD, Prof. G. Van Oost, PhD, Prof. G. Tovar, PhD
Doctoral thesis submitted in order to obtain the academic degrees of
Doctor of Engineering Physics (Ghent University) and
Doktor der Naturwissenschaften (Dr. rer. nat.) (Universität Stuttgart)

Department of Applied Physics
Head of Department: Prof. C. Leys, PhD
Faculty of Engineering and Architecture

UNIVERSITEIT GENT

Institute of Interfacial Process Engineering and Plasma Technology
Head of Institute: Prof. G. Tovar, PhD
Faculty of Energy-, Process- and Bio-Engineering

Universität Stuttgart

Academic year 2015 - 2016

ISBN 978-90-8578-924-6
NUR 926, 971
Wettelijk depot: D/2016/10.500/56

This research was performed at:
Dit onderzoek werd uitgevoerd in:

Forschungszentrum Jülich
Institute for Energy and Climate Research
Microstructure and Properties of Materials
52425 Jülich, Germany

In collaboration with:
In samenwerking met:

Max Planck Institute for Plasma Physics
Department of Plasma Edge and Wall
Boltzmannstraße 2
85748 Garching, Germany

Ghent University
Faculty of Engineering and Architecture
Department of Applied Physics
Sint-Pietersnieuwstraat 41
9000 Ghent, Belgium

University of Stuttgart
Institute of Interfacial Process Engineering
and Plasma Technology
Pfaffenwaldring 31
70569 Stuttgart, Germany

FUSION-DC - International Doctoral
College in Fusion Science and Engineering
Erasmus Mundus Programme
Coordinated by Ghent University

Examination Board

Prof. Dr. ir. R. Van De Walle, Chairman of the Examination Board
Ghent University

Prof. Dr.-Ing. M. Resch, Co-Chairman of the Examination Board
University of Stuttgart

Prof. Dr. ir. K. Verbeken, Secretary of the Examination Board
Ghent University

Prof. Dr.-Ing. J. Starflinger
University of Stuttgart

Prof. Dr. U. Stroth
Technical University of Munich
Max Planck Institute for Plasma Physics

Dr. J. Linke
Forschungszentrum Jülich

Prof. Dr. Z. Zhou
University of Science and Technology Beijing

Dr. T. Hirai
ITER Organization

Prof. Dr. ir. J.-M. Noterdaeme, Promoter
Ghent University
Max Planck Institute for Plasma Physics

Prof. Dr. ir. G. Van Oost, Promoter
Ghent University

Prof. Dr. G. Tovar, Promoter
University of Stuttgart

Table of Contents

List of Figures

List of Tables

List of Symbols and Abbreviations

$\langle \sigma v \rangle$	Average reaction rate
τ_E	Energy confinement time
BSE	Backscattered Electron (image)
CCFE	Culham Centre for Fusion Energy
CFC	Carbon Fiber Composite
CNO-cycle	Carbon-Nitrogen-Oxygen cycle
DBTT	Ductile-Brittle Transition Temperature
DEMO	Future demonstration fusion power plant
DT-reaction	Fusion reaction of deuterium with tritium
EBSD	Electron BackScatter Diffraction (image)
EDM	Electric Discharge Machining
ELM	Edge Localized Mode
F_{HF}	Heat flux factor
FEM	Finite Element Method
FIB	Focussed Ion Beam
FZJ	Forschungszentrum Jülich
HHF	High Heat Flux
IPP	Max-Planck-Institut für Plasmaphysik
ITER	Experimental tokamak under construction in Saint-Paul-lez-Durance, France
JET	Joint European Torus, tokamak in Culham, UK
LCFS	Last Closed Flux Surface, also called the Separatrix
LC-SEM	Large Chamber Scanning Electron Microscope of RWTH Aachen
LID	Laser Induced Desorption
LM	Light Microscopy
MHD	Magnetohydrodynamics, the dynamics of magnetic and electrically conducting fluids
$n\tau_E T$	Triple product

PFC	Plasma Facing Component
PFM	Plasma Facing Material
PWI	Plasma-Wall Interaction
Q-factor	Fusion energy gain factor
R_a	Arithmetic mean roughness parameter
SE	Secondary Electron (image)
SEM	Scanning Electron Microscopy
SSHF	Steady State Heat Flux
TDS	Thermal Desorption Spectroscopy
TMX-U	Tandem Mirror Experiment, a decommissioned magnetic mirror in Livermore, USA
VDE	Vertical Displacement Event
W-7X	Wendelstein 7X, a stellarator in Greifswald, Germany
Z_{eff}	Effective atomic number

Abstract

Due to a combination of energy policy shifts and an increase in energy demand for the coming decades, several options are currently explored to obtain a reliable, long-term energy supply. One promising method is nuclear fusion. While fusion has several benefits, e.g. an abundance of fuel is available and although the tritium is radioactive, the resulting end product of the fusion reaction, i.e. helium, is not radioactive, further R&D is necessary before commercially viable electricity generation by fusion power plants is possible.

Among the topics that need further research is the field of plasma facing materials and components. In a fusion reactor, the generated power is deposited on the inner vessel wall and a special exhaust region, the divertor. These need to withstand a combination of transient heat loads, steady state heat loads, neutron irradiation, and a particle flux consisting of deuterium, tritium, helium, and impurities. As a result, several plasma-wall interaction processes will occur. Each of them has a different damage mechanism, e.g. crack formation, erosion, melting, or nanostructure formation on the surface.

Currently, tungsten is considered as the most promising candidate material for armour material in the divertor. In this work, two types of exposure conditions, i.e. ELM-like heat loads and a steady state particle flux, were applied on tungsten samples. Either the material was loaded to one of these exposure conditions or it was sequentially loaded with both.

The ELM-like tests were performed in the electron beam facility JUDITH 1. These experiments were done from room temperature to 1000 °C with 100 pulses having an absorbed power density from 190 $\mathrm{MW\,m^{-2}}$ and 1514 $\mathrm{MW\,m^{-2}}$. Additionally, the 1000 °C tests were also carried out with 1000 pulses.

The analysis of the ELM-induced damage on the tungsten samples shows that the proposed damage mechanism is in line with the results. Within the damage mechanism for low pulse numbers, there are two threshold values. For the power density, a damage threshold exists that must be exceeded before macroscopic damage, e.g. roughening, occurs. A second value, the cracking threshold, is identified for the base temperature. Only if the base temperature is below the cracking threshold, crack formation occurs. Fur-

ther material damage is seen for ELM-like loading at 1000 °C.

GLADIS, a neutral beam facility, was used to apply a steady state particle and heat exposure on the samples. Either a pure hydrogen beam or a mixed hydrogen/helium beam consisting of 94 % hydrogen and 6 % helium was used, both with the same beam profile. The peak particle flux of the beam was $3.7 \times 10^{21}\,\mathrm{m^{-2}\,s^{-1}}$ and the corresponding power density was $10.5\,\mathrm{MW\,m^{-2}}$. The range of surface temperatures obtained during the particle exposure span from 600 °C and 1500 °C and was achieved by different heights of the samples. Each sample had a total exposure time of 5400 s, resulting in a particle fluence of $2 \times 10^{25}\,\mathrm{m^{-2}}$.

The damage analysis of the particle exposed samples shows that the results are similar to experiments on other tungsten grades. For the hydrogen exposed samples the particle loading leads to the formation of distinctive erosion patterns. Also the samples exposed to the mixed hydrogen/helium beam had such erosion patterns when the surface temperature was 600 °C. If the surface temperature was higher, surface extrusions were formed on the sample. Further, the H/He-flux resulted in the creation of a porous sub-surface layer. The cavities in this layer are larger with increasing surface temperature.

Three types of sequential exposure test campaigns were performed to identify potential interactions between the damage mechanisms. Besides the ELM-like loading of a particle pre-exposed sample and the particle exposure of an ELM-like pre-exposed sample, one triple exposure campaign was also carried out. Therein, ELM-like loads were first applied on samples that were subsequently exposed to a particle flux, and to ELM-like loads once again.

The particle pre-exposed tungsten was shown to have a similar thermal shock behaviour as that of the pristine tungsten. For some loading conditions, pristine tungsten shows the occurrence of surface roughening, while no additional roughening is measured for the pre-exposed tungsten, which can be an effect from the particle-induced damage. In some cases, the formation of a crack network was impeded by the particle pre-exposure and another effect was observed in the porous sub-surface layer, where the H/He-induced cavities formed at 600 °C have increased in size after ELM-like loading at high temperatures. Modifications to the size and morphology of the surface extrusions were only observed as local melting after the highest power density. At last, it became clear that tungsten that was recrystallized during the pre-exposure had the worst performance from all the pre-exposed samples.

Only one interaction is identified for the samples that are pre-exposed with ELM-like loads and are exposed to a particle flux afterwards. Additional H/He-induced modifications, such as crack bridging, enhanced erosion, and the formation of sponge-like filling structures inside the crack occur in and near the ELM-induced cracks. However, the ELM-like pre-exposure did not alter the form and size of the H/He-induced surface extrusions. The

subsequent triple exposure experiments demonstrated that the surface extrusions are resilient against most ELM-induced damage. Only under the highest power density did a partial melting of the extrusions occur. In addition, the crack bridging that occurred after H/He-loading was completely removed by ELM-like heat loads.

High pulse number experiments were performed in which steady state and ELM-like heat loads were applied simultaneously in JUDITH 2 on tungsten that was pre-exposed to a H/He-flux. This demonstrated that after a long exposure time and high temperatures, the surface extrusions were removed. The dominant factor behind this removal procedure is the steady state heat flux and not the ELM-like transient heat loads. Despite the interactions between the H/He-exposure and the ELM-like loading that are identified, a comparison with previous experiments showed that after long pulse experiments, the H/He pre-exposure does not cause a deterioration of the thermal shock behaviour. Nevertheless, some of these interactions might cause a limitation of the acceptable loading conditions.

Samenvatting

– Summary in Dutch –

In de komende decennia zal de vraag naar energie stijgen, terwijl er tegelijkertijd een verschuiving in de energiepolitiek merkbaar is. Om op een duurzame manier de energiebevoorrading te garanderen, is het belangrijk om verscheidene opties te overwegen. Een beloftevol alternatief dat het gebruik van kernsplitsing en fossiele brandstoffen kan beperken of die technologieën kan vervangen, is kernfusie. Hierbij worden lichte atoomkernen samengevoegd tot een zwaardere atoomkern in een proces waar, voor sommige reacties, energie vrijkomt.

De fusiereactie die het meest in aanmerking komt is de DT-reactie, waar deuterium en tritium gefusioneerd worden tot helium. Bovendien komt er een neutron en 17,59 MeV aan energie vrij. Het is echter noodzakelijk dat de temperatuur zich tijdens deze fusiereactie bevindt tussen 10–15 keV. Dit komt ruwweg overeen met 150 miljoen °C, ofwel tien keer zo warm als de kern van de zon. Op deze temperatuur vormt de deuterium, tritium en helium samen met eventuele onzuiverheden een plasma.

Omdat geen enkel materiaal een direct contact met dit plasma kan weerstaan, wordt in een fusiereactor de plasma magnetisch opgesloten. Hierdoor vermindert de belasting op de verschillende componenten van de reactorwand. Desalniettemin blijft de keuze voor de aan plasma blootgestelde materialen die gebruikt kunnen worden, beperkt. Één van de onderzoeksvelden gerelateerd aan kernfusie waar verdere R&D cruciaal is voordat een commercieel rendabele fusie-energiecentrale kan gebouwd worden is het onderzoek in plasma blootgestelde materialen.

Momenteel is wolfraam de meest veelbelovende keuze voor plasma blootgesteld materiaal. Wolfraam is onder meer geselecteerd als eerste-wandmateriaal voor de divertor, een component waar het grootste gedeelte van de belastingen op geconcentreerd wordt, van ITER, een experimentele fusiereactor die in aanleg is nabij Saint-Paul-lez-Durance, Frankrijk. Als onderdeel van de plasma-wand-interactie zal wolfraam, zowel in ITER als in toekomstige fusie-energiecentrales, blootgesteld worden aan een combinatie van neutronenstraling, deeltjesflux en warmte. De hieruit voortvloeiende

schade omvat o.a. scheurvorming, erosie, smelten en de ontwikkeling van nanostructuren op het materiaaloppervlak.

De effecten van twee blootstellingstypes, de quasi-continue deeltjesbestraling en de kortstondige ELM-achtige thermische belastingen, op wolfraam zijn experimenteel bestudeerd. Behalve het bepalen van de materiaalschade die zij elk veroorzaken, is de invloed die de schade van het ene blootstellingstype heeft op de schade van het andere blootstellingstype onderzocht. Daarom zijn er naast de enkelvoudige blootstellingsexperimenten waarbij wolfraam ofwel enkel aan ELM-achtige belastingen ofwel enkel aan een deeltjesbestraling wordt blootgesteld, ook sequentiële experimenten uitgevoerd.

JUDITH 1, een elektronenstraalinstallatie in Forschungszentrum Jülich, werd gebruikt om de ELM-achtige thermische belastingexperimenten te doen. Die werden zowel uitgevoerd met de testspecimens op kamertemperatuur, als verhit tot een basistemperatuur van 400 °C en 1000 °C. Gedurende een experiment werd dezelfde kortstondige warmtepuls, met een 1 ms pulslengte, 100 maal herhaald. De geabsorbeerde vermogensdichtheid die gebruikt werd, was $190\,\mathrm{MW\,m^{-2}}$, $380\,\mathrm{MW\,m^{-2}}$ of $1514\,\mathrm{MW\,m^{-2}}$. Bovendien werden de experimenten op 1000 °C ook gedaan voor 1000 warmtepulsen.

De karakterisering van de ELM-geïnduceerde schade toont aan dat de experimentele resultaten in overeenstemming zijn zowel met ELM-achtige experimenten op andere wolfraam materiaaltypes als met het voorgestelde schademechanisme. Volgens dit mechanisme kan bij lage pulsnummers, het schadegedrag beschreven worden door twee drempelwaarden. De eerste drempelwaarde, de *schade-grens*, is verbonden met de geabsorbeerde vermogensdichtheid van de kortstondige thermische belasting. Enkel wanneer de ELM-achtige puls een grotere vermogensdichtheid heeft dan de *schade-grens*, zal schade zoals oppervlakteverruwing ontstaan. De tweede drempelwaarde, de *scheur-grens*, is dan weer verbonden aan de basistemperatuur van het testmateriaal en bepaalt het soort van schade dat ontstaat. Enkel wanneer de basistemperatuur onder de scheur-grens is, kan de materiaalschade zich manifesteren door scheurvorming, terwijl er daarboven sprake is van oppervlakteverruwing. Daarnaast is er vastgesteld dat er een verslechtering van het schadegedrag is bij hoge basistemperaturen, in dit geval de experimenten op 1000 °C.

GLADIS is een installatie voor bestralingen met neutrale deeltjes in het Max-Planck-Institut für Plasmaphysik die gebruikt werd voor de quasi-continue experimenten met een gecombineerde deeltjes-flux en warmtebelasting. Hiervoor zijn er twee deeltjesstralen, beide met hetzelfde Gaussische stralingsprofiel voor warmtedichtheid en flux. Enkel de atomistische samenstelling was anders, die bestond ofwel 100 % uit waterstof ofwel uit een combinatie van 94 % waterstof en 6 % helium. De deeltjesflux in het midden van de deeltjesstraal was $3{,}7 \times 10^{21}\,\mathrm{m^{-2}\,s^{-1}}$ met een bijhorende vermogensdichtheid van $10{,}5\,\mathrm{MW\,m^{-2}}$. Door het testmateriaal actief te koelen en gebruik te maken van testspecimens met verscheidene afmetingen, is het

mogelijk om een oppervlaktetemperatuur te bekomen van 600 °C, 1000 °C of 1500 °C. In totaal heeft elk specimen een blootstellingsduur van 5400 s gehad, wat resulteert voor het midden van de deeltjesstraal in een deeltjesfluentie van $2 \times 10^{25}\,\mathrm{m}^{-2}$.

Na de analyse van de experimentele resultaten blijkt dat de testspecimens na deeltjesbestraling modificaties vertonen op verscheidene aspecten. Het materiaal met H-bestraling vertoont, ongeacht de oppervlaktetemperatuur, een afgetekende verruwing van het oppervlak waarbij een duidelijk herkenbaar erosiepatroon aanwezig is. Zowel met elektronenmicroscopie als met laserprofilometrie is dit te observeren. Daarnaast vertoont elk testspecimen dat een oppervlaktetemperatuur had van 1500 °C tijdens de H-bestraling, rekristallisatie tot op ∼3,5 mm diep.

Wolfraam dat was blootgesteld aan de H/He-flux had ook een dergelijk erosiepatroon als de oppervlaktetemperatuur beperkt bleef tot 600 °C. Voor de hogere temperaturen, 1000 °C en 1500 °C, was de oppervlakte bedekt met nanostructuren. Een andere H/He-geïnduceerde modificatie is de creatie van een poreuze laag onder het materiaaloppervlak. Dit gebeurde bij elke oppervlaktetemperatuur, maar de bubbels in die laag zijn groter indien de temperatuur hoger is. Verder is er terug rekristallisatie te vinden bij de testspecimens die belast zijn met H/He bij een oppervlaktetemperatuur van 1500 °C.

Achter de karakterisering van de twee types enkelvoudige blootstellingsexperimenten, zijn er drie categorieën van sequentiële experimenten uitgevoerd om potentiële wisselwerkingen tussen de schademechanismes te identificeren. Hierbij wordt er ofwel een ELM-achtige belasting uitgevoerd op testspecimens die eerst bestraald waren met een deeltjesflux, ofwel wordt een deeltjesbestraling uitgevoerd op testspecimens die eerst een ELM-achtige belasting ondergaan hebben, ofwel een drievoudig belastingsexperiment. Daarbij wordt een testspecimen eerst ELM-achtig belast, daarna ondergaat het een deeltjesbestraling, waarna het opnieuw ELM-achtig belast wordt.

Na het uitvoeren van de experimenten waarbij wolfraam eerst werd belast met een deeltjesflux en daarna met ELM-achtige belastingen, zijn er voornamelijk vier conclusies te maken. Het materiaalgedrag bij de kortstondige thermische schokken is gelijkaardig voor gepolijst wolfraam en met deeltjes voorbelast wolfraam. Wanneer het materiaalgedrag bij de kortstondige thermische schokken in bepaalde gevallen gewijzigd is, is dit waar te nemen als een ontbreken van identificeerbare ELM-geïnduceerde schade, bijvoorbeeld in de ruwheid van het oppervlak. Voor sommige blootstellingscondities is ook de vorming van een scheurnetwerk belemmerd door de voorbelasting met een deeltjesflux. Verder is de enige merkbare verandering aan de oppervlaktestructuren na de ELM-achtige belastingen het lokaal voorkomen van smelten, al gebeurde dit enkel bij blootstellingscondities waar ook ook gepolijst wolfraam smeltlocaties had. Voor alle andere blootstellingscondities zijn er geen veranderingen aan de oppervlaktestructuren waar te nemen. Er is ook een verandering bij de H/He-geïnduceerde

bubbels onder het materiaaloppervlak die ontstaan zijn bij een oppervlaktetemperatuur van 600 °C, door een toename in hun omvang als ze bij hoge temperatuur ELM-achtig belast worden. Ten laatste is het ook duidelijk dat de wolfraam dat gerekristalliseerd is gedurende de voorbelasting de grootste ELM-geïnduceerde schade heeft van alle voorbelaste testspecimens.

Vanuit de experimenten waarbij wolfraam eerst ELM-achtig belast werd en daarna blootgesteld werd aan deeltjesstraling, zijn er twee duidelijke conclusies te maken. In geen enkel geval was het mogelijk om een verandering in de vorm of grootte van de H/He-geïnduceerde oppervlaktestructuren te vinden, veroorzaakt door een ELM-achtige voorbelasting. De enige wisselwerking die gevonden is tussen de H/He-flux en de ELM-achtige voorbelasting, is in en rond de ELM-geïnduceerde scheuren. Die is merkbaar door een verhoogde erosie rond de scheur, de vorming van sponsachtige vullingen in de scheur, en het bedekken van de scheur met de oppervlaktestructuren die scheur-overbruggingen genoemd worden.

De drievoudige belastingsexperimenten worden gebruikt om de voorgaande bevindingen te valideren. Het wordt daardoor onder meer duidelijk dat de oppervlaktestructuren een goede weerstand hebben tegen de meeste ELM-achtige belastingen. Enkel bij de belastingen met de hoogste vermogensdichtheid is er een gedeeltelijke smelting van de oppervlaktestructuren gebeurd. Verder kan worden besloten dat de scheur-overbruggingen verwijderd zijn door de finale ELM-achtige belastingen, op een manier die resulteert in stofvorming.

Als aanvulling op deze experimenten is er een extra testcampagne geweest die toegewijd is aan hoge pulsnummers. Hierbij werd een wolfraam module eerst belast met een H/He-flux in GLADIS, waarna die module met de elektronenstraal installatie JUDITH 2 in Forschungszentrum Jülich thermisch belast werd. Deze thermische belasting omvat het simultaan toepassen van kortstondige ELM-achtige belastingen en de quasi-continue thermische belasting. Met deze experimenten is het duidelijk dat na een lange belastingstijd of een hoge temperatuur de oppervlaktestructuren verdwijnen. Daarbij speelt niet de kortstondige ELM-achtige belastingen, maar de quasi-continue thermische belasting een dominante rol.

Een vergelijking van de hoge pulsnummer testcampagne met voorgaande experimenten toont duidelijk aan dat de H/He voorbelasting niet voor een achteruitgang van het schadegedrag zorgt. Integendeel, verschillende parameters tonen zowel een kwantitatieve als een kwalitatieve verbetering van het materaal gedrag bij sommige belastingcondities. Ondanks de verscheidene interacties tussen de deeltjesbestraling en de thermische belastingen die geïdentificeerd zijn, wijzen de experimenten op een stabiele of verbeterd materiaalgedrag. Desalniettemin, sommige van die interacties kunnen nog altijd leiden tot een beperking van de aanvaardbare belastingcondities.

Kurzfassung

– Summary in German –

In den kommenden Jahrzehnten wird die Nachfrage nach Energie zunehmen, während es zur gleichen Zeit eine Verschiebung der Energiepolitik gibt. Um die Energieversorgung nachhaltig zu gewährleisten, ist es unerlässlich alternative Energiequellen zu den bereits Bestehenden zu erforschen und auszubauen. Eine vielversprechende Alternative, um die Nutzung der fossilen Brennstoffe und der Kernspaltung einzuschränken oder um diese Technologien zu ersetzen, könnte die Kernfusion sein. Im Gegensatz zur Kernspaltung wird bei der Kernfusion durch das Verschmelzen von zwei leichten Kernen Energie freigesetzt.

Die wichtigste Fusionsreaktion ist die DT-Reaktion, bei welcher Deuterium und Tritium zu Helium verschmelzen. Die Reaktion ergibt zusätzlich sich ein Neutron und 17,59 MeV Energie. Es ist jedoch notwendig, dass die Temperatur bei der Fusionsreaktion zwischen 10–15 keV liegt, dies entspricht etwa 150 Millionen °C oder zehnmal so heiß wie der Sonnenkern, damit sich ein vollständig ionisiertes Gas bildet, ein sogenanntes Plasma, und somit die Coulombabstoßung überwunden werden kann.

Da kein Material einem direkten Kontakt mit diesem Plasma widerstehen kann, wird in einem Kernfusionsreaktor das Plasma magnetisch eingeschlossen. Dies verringert die Belastung auf die verschiedenen Komponenten der Reaktorwand. Trotzdem ist die Auswahl der Plasma-Wand-Materialien, die verwendet werden können, begrenzt. Ein Forschungsschwerpunkt in der Kernfusion und ein entscheidender Faktor bei der Entwicklung eines kommerziellen Fusionskraftwerkes, ist die Forschung an dem Plasma zugewandten Materialien.

Im größten experimentellen Fusionsreaktor, ITER, welcher sich derzeit unter Konstruktion in der Nähe von Saint-Paul-lez-Durance, Frankreich befindet, werden unterschiedliche Werkstoffe zum Einsatz kommen, welche den Belastungen standhalten müssen. Für den Bereich des Divertors, der mit den höchsten Belastungen beaufschlagt werden wird, wurde Wolfram ausgewählt. Die Belastungen für die Plasma-Wand-Materialien sind hierbei eine Kombination von Neutronenstrahlung, Teilchenflüssen und hohen

Wärmeflüssen. Zu den daraus resultierenden Schäden gehören zum Beispiel Rissbildung, Erosion, Schmelzen und die Bildung von Nanostrukturen auf der Materialoberfläche.

Die Effekte von zwei Belastungsarten statische Teilchenstrahlung und transiente, ELM-ähnliche, Wärmelasten, auf Wolfram wurden im Rahmen dieser Doktorarbeit untersucht. Nicht nur der Schaden, den jede Belastungsart am Material verursacht, wurde untersucht, sondern auch der Einfluss, den die Schädigung der einen Belastungsart auf die Schädigung der anderen Belastungsart hat. Deshalb wurden, zusätzlich zu den Einzelbelastungsexperimenten, bei denen entweder nur ELM-ähnliche, transiente, thermische Belastungen oder nur stationäre Teilchenstrahlung genutzt wurde sequentielle Experimente durchgeführt.

JUDITH 1, eine Elektronenstrahlanlage am Forschungszentrum Jülich, wurde verwendet um die ELM-ähnlichen Belastungen zu realisieren. Die Proben wurden bei Raumtemperatur, 400 °C und 1000 °C mit jeweils 100 identischen Pulsen mit einer Pulslänge von 1 ms belastet. Die verwendeten absorbierten Leistungsdichten waren $190\,\mathrm{MW\,m^{-2}}$, $380\,\mathrm{MW\,m^{-2}}$ und $1514\,\mathrm{MW\,m^{-2}}$. Außerdem wurden die Experimente bei 1000 °C auch für 1000 Pulse durchgeführt.

Die Charakterisierung der ELM-induzierten Schädigung zeigt, dass die experimentellen Ergebnisse sowohl dem Thermoschockverhalten von anderen Wolframsorten als auch dem erwarteten Schädigungsverhalten entsprechen. Bei niedrigen Pulszahlen kann das Schädigungsverhalten anhand von zwei Grenzwerten beschrieben werden. Der erste Grenzwert, der *Schädigungsgrenzwert*, ist abhängig von der absorbierten Leistungsdichte der kurzfristigen thermischen Belastung. Das heißt, nur ELM-ähnliche transiente Belastungen, die eine höhere Leistungsdichte hat als der Schädigungsgrenzwert aufweisen, führen zu Schädigungen der Probe, wie zum Beispiel Oberflächenaufrauung. Der zweite Grenzwert, der *Rissgrenzwert*, ist abhängig von der Basistemperatur der Probe und gibt somit die Temperatur an, oberhalb derer das Material duktil genug ist, um die erzeugte Spannung im Material rein durch plastische Verformung zu kompensieren. Liegt die Basistemperatur unterhalb des Rissgrenzwertes können Risse entstehen. Experimente mit einer Basistemperatur von 1000 °C führten zu einer Verschlechterung des Schädigungsverhaltens, welche sich in frühzeitiger Materialermüdung, ein Effekt der hohen Temperatur, äußerte.

GLADIS, eine Testanlage für Bestrahlungen mit neutralen Teilchen am Max-Planck-Institut für Plasmaphysik, wurde für die Experimente mit stationärem Teilchen- und Wärmefluss verwendet. Es wurden Experimente mit unterschiedlicher atomistische Zusammensetzung durchgeführt. Zum einen mit einem reinen Wasserstoffstrahl und zum anderen mit einer Kombination aus 9494 % Wasserstoff und 6 % Helium. Der Teilchenfluss in der Strahlmitte betrug $3{,}7 \times 10^{21}\,\mathrm{m^{-2}\,s^{-1}}$ und die absorbierte Leistungsdichte $10{,}5\,\mathrm{MW\,m^{-2}}$. Da die Wolframproben in ihrer Größe variierten und eine aktive Kühlung verwendet wurde, konnten unterschiedliche Oberflächentem-

peraturen, 600 °C, 1000 °C und 1500 °C, erreicht werden, wobei die Gesamtbelastungszeit immer 5400 s betrug. Die Teilchenfluenz in der Strahlmitte ist demnach $2 \times 10^{25}\,\mathrm{m}^{-2}$.

Die experimentellen Ergebnisse zeigen, dass die Proben nach der Teilchenbestrahlung verschiedene Modifikationen aufweisen. Wolframproben, die mit reinem Wasserstoff belastet wurden, weisen auf eine deutliche Oberflächenaufrauung mit einem stark ausgeprägten Erosionsmuster, unabhängig von der Oberflächentemperatur. Dies wurde mit Hilfe von Elektronenmikroskopie und Laserprofilometrie nachgewiesen. Außerdem zeigt jede Testprobe, die während der H-Bestrahlung eine Oberflächentemperatur von 1500 °C hatte, eine Rekristallisation bis zu einer tiefe von 3,5 mm.

Wolfram, das dem H/He-Fluss ausgesetzt war, hat ebenfalls ein solches Erosionsmuster, wenn die Oberflächentemperatur auf 600 °C begrenzt ist. Bei höheren Temperaturen, 1000 °C und 1500 °C, ist die Oberfläche mit Nanostrukturen bedeckt. Des Weiteren führte die H/He Belastung zur Ausbildung einer porösen Schicht unterhalb der Probenoberfläche und die Blasen in dieser Schicht sind größer mit steigender Oberflächentemperatur.

Nach der Charakterisierung der Einzelbelastungsexperimente wurden drei Kategorien von sequentiellen Experimenten durchgeführt, um mögliche Wechselwirkungen zwischen den Schädigungsmechanismen zu identifizieren. In der ersten Kategorie wurden transiente thermische Belastungen auf Proben die vorher eine Teilchenbelastung gehabt haben. In Kategorie zwei wurden Proben, welche bereits mit transienten thermischen Ereignissen vorgeschädigt wurden, einer Teilchenbelastung ausgesetzt. Für die dritte Kategorie, oder die Drittbelastungsexperimente, wurde eine Probe zuerst transient thermisch belastet, danach mit einem Teilchenfluss belastet und zuletzt wieder transient thermisch belastet.

Die Durchführung der Experimente, in denen Wolfram zuerst mit einem Partikelfluss und danach mit einem ELM-ähnlichen Ereignis belastet wurde, brachte hauptsächlich vier Feststellungen hervor. Das Thermoschockverhalten von mit Partikeln vorbelasteten Wolfram ist ähnlich zu dem Thermoschockverhalten von poliertem Wolfram. Bei Proben, die ein verändertes Verhalten aufweisen, wurde zumeist das Fehlen von erwartetem Schaden (auf polierten Proben) beobachtet. Beispiele hierfür sind Aufrauungen, die möglicherweise durch von Partikeln induzierten Schaden überlagert wurden, oder eine Verhinderung von Rissbildung durch die H/He-induzierten Modifikationen. Die zweite Feststellung ist, dass die einzige merkliche Veränderung der Oberflächenstrukturen nach der transienten thermischen Belastung das lokale Erscheinen von Aufschmelzungen ist, aber nur unter den wenigen Belastungsbedingungen, die bei poliertem Wolfram ebenfalls zum Aufschmelzen geführt haben. Für alle anderen Belastungsbedingungen wurden keine Änderungen der Oberflächenstrukturen festgestellt. Die dritte Hauptfeststellung ist, dass die H/He-induzierten Blasen unterhalb der Materialoberfläche an Größe zunahmen, wenn sie bei höherer Temperatur (1500 °C) ELM-ähnlich belastet wurden. Die Letzte Feststellung ist, dass

die schwersten Schäden bei rekristallisiertem Wolfram zu finden waren.

Aus den Versuchen, in denen Wolfram erstens einer ELM-ähnlichen Belastung und danach einer Teilchenstrahlung ausgesetzt wurde, können zwei bedeutungsvolle Schlussfolgerungen gezogen werden. Erstens wurde keine Änderung, weder in der Form noch der Größe, an denen durch die Vorbelastung entstandenen Oberflächenstrukturen festgestellt. Die einzige Auswirkung der H/He Belastung auf die bereits vorhandene Schädigung, konnte nur innerhalb der ELM-induzierten Risse oder um diese herum festgestellt werden. Die Auswirkungen der H/He Belastung zeigten sich wie folgt, es kam zu einer erhöhten Erosion um den Riss herum, zur Bildung von porösen Füllungen im Riss bis hin zur Abdeckung des Risses beziehungsweise *Rissüberbrückung* durch diese Strukturen.

Die Dreifachbelastungsexperimente wurden verwendet, um die bisherigen Ergebnisse zu validieren. Unter anderem ergab sich daraus, dass die Oberflächenstrukturen eine gute Beständigkeit gegenüber den ELM-ähnlichen Belastungen aufweisen. Nur bei der Belastung mit den höchsten Leistungsdichten wurde ein partielles Schmelzen der Oberflächenstrukturen festgestellt. Weiterhin zeigte sich daraus folgern, dass die Rissüberbrückungen durch eine nachfolgende Belastung mit transienten Ereignissen ausgelöscht wurden und in Staub umgewandelt wurden.

Um diese Versuche zu ergänzen, gab es eine zusätzliche Testkampagne mit hohen Pulszahlen. Für diese Experimente wurde ein Modul von Wolfram zuerst mit einem H/He-Fluss in GLADIS belastet, anschließend wurde das Modul thermisch belastet mit der Elektronenstrahlanlage JUDITH 2 am Forschungszentrum Jülich. Diese thermische Belastung war eine Kombination von gleichzeitiger stationärer und transienter thermischer Belastung. Bei diesen Experimenten konnte herausgefunden werden, dass die Oberflächenstrukturen nach einer langen Expositionszeit oder einer hohen Temperatur verschwinden. Hierbei stellte nicht die transiente, ELM-ähnliche, Belastung sondern die stationäre Wärmebelastung die Hauptursache dar.

Der Vergleich der Hochpulstestkampagne mit vorangegangene Experimenten zeigte deutlich, dass die H/He Vorbelastung keine Verschlechterung des Schädigungsverhaltens bewirkt. Im Gegensatz dazu zeigen einige Parameter sogar eine qualitative sowie quantitative Verbesserung des Schädigungsverhaltens unter bestimmten Belastungsbedingungen. Trotz der festgestellten Wechselwirkungen zwischen Partikel- und Wärmebelastung demonstrierten die durchgeführten Experimente ein stabiles beziehungsweise teilweise verbessertes Schädigungsverhalten. Dennoch können einige dieser Wechselwirkungen zu einer Limitierung der höchsten akzeptablen Belastungsbedingungen führen.

Chapter 1

Introduction

1.1 Background to Magnetic Confined Fusion

Nuclear fusion is a physical reaction in which multiple nuclei combine to form a heavier nucleus. In nature, such fusion processes occur in stars where you can find the CNO-cycle and the proton-proton chain reaction, which produces the energy [1, 2]. However these reactions are not suitable for use in a fusion power plant. In order to develop commercially viable fusion power plants, a reaction needs to be identified that delivers sufficient energy under acceptable conditions.

The amount of energy that is either released or absorbed in a nuclear reaction, can be determined through the difference of the atomic mass of all constituents before and after the reaction. This change of mass is related through the mass-energy equivalence with the amount of energy changed during the reaction. For light elements, such as helium or hydrogen isotopes, the binding energy per nucleon increases with the atomic mass number, making a fusion reaction exothermic. However, for heavier elements, the binding energy decreases with higher atomic mass number. In this case, instead of nuclear fusion, a fission reaction would release energy [1].

Nuclei have a positive electrical charge, therefore according to Coulomb's law there is a repulsive force between the two nuclei. For a fusion reaction to occur, the kinetic energy of the nuclei needs to overcome the potential energy. When the nuclei are close enough to each other, in the range of a few femtometres, the strong interaction provides an attractive force which is higher than the repulsive Coulomb force. Therefore, as depicted in figure 1.1, in classical physics fusion will only occur if the energy is higher than the Coulomb barrier. According to the laws of quantum mechanics, even if the energy is lower, there is still a possibility to overcome the Coulomb barrier. This phenomenon is called quantum tunnelling.

The probability of two particles colliding, taking into account overcoming the coulomb barrier with classical physics and quantum tunnelling, is

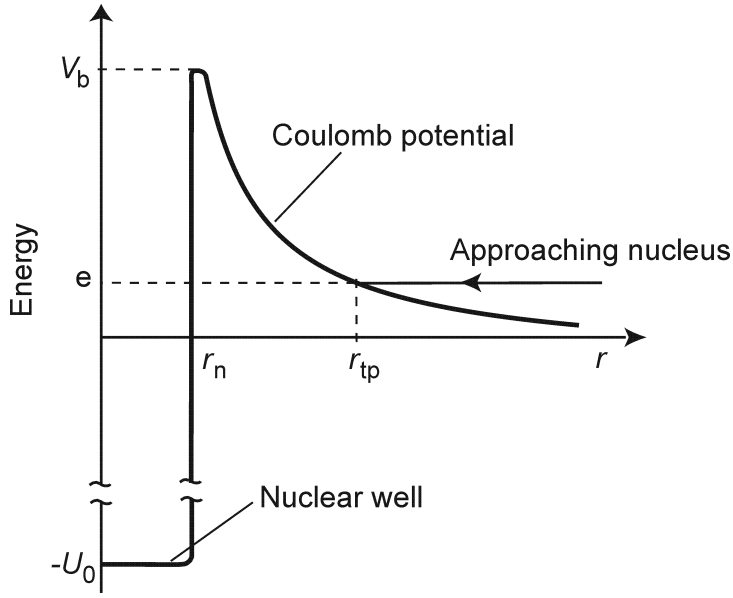

Figure 1.1: The potential energy for two charged nuclei that approach each other with a center-of-mass energy ϵ, illustrating the Coulomb barrier, the nuclear well, and the classical turning point [1].

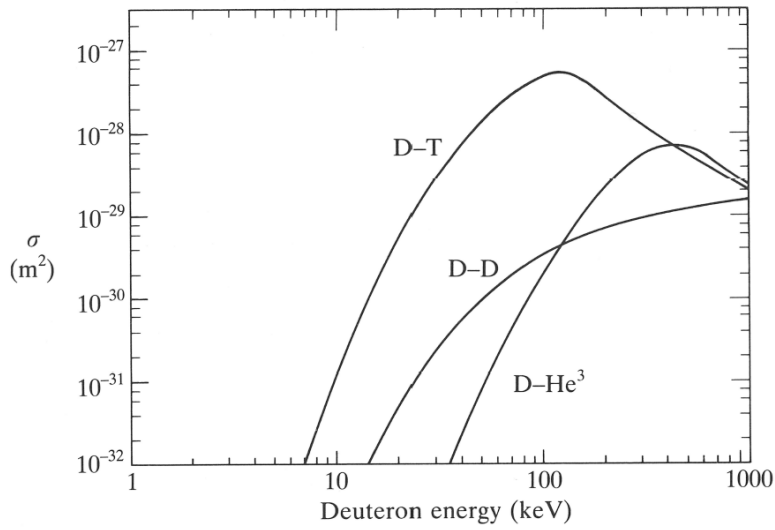

Figure 1.2: The cross sections of the reactions most relevant for controlled thermonuclear fusion [3].

given by the energy dependent cross section. Figure 1.2 shows the cross sections for some fusion reactions. Assuming that the energy distribution is a Maxwellian, the average reaction rate $\langle \sigma v \rangle$, as shown in figure 1.3, can be calculated. Both the cross section and the reaction rate is the highest for the DT-reaction, given in Eq. (1.1). Also the peak value of reaction rate for the DT-reaction occurs at the lowest temperature of all possible reactions [1, 3].

$$\mathrm{D} + \mathrm{T} \longrightarrow {}^4\mathrm{He} + \mathrm{n} + 17.59\,\mathrm{MeV} \tag{1.1}$$

These characteristics make the DT-reaction one of the most promising processes for nuclear fusion reactors. Therefore most experimental work is focussed on this reaction and the currently planned devices are going to make use of it. The specific energy gain for the DT-reaction can be calculated through the mass deficit. The reactants, deuterium and tritium, have an atomic mass of 2.014 101 u and 3.016 049 u respectively. The atomic mass of the products, ^{4}He, also called the *ash* of a fusion 'burn', and a neutron, are 4.002 603 u and 1.008 664 u respectively [4]. Since the products have a mass which is 0.018 883 u lower, the equivalent energy of 17.59 MeV is released.

A fusion reactor operating with deuterium and tritium will need to keep the temperature around 10 keV to 15 keV. This roughly corresponds with temperatures of 150 million°C, or ten times higher than the temperature at the core of the sun. At these temperatures, no material would be solid, liquid, or gaseous. Instead, the atoms will ionize and a plasma is formed. Since a plasma consists of moving charged particles, i.e. electrons and ions, electromagnetic fields can interact with the plasma through the Lorentz force $\mathbf{F}$, Eq. (1.2), where q is the charge of the moving particle, $\mathbf{v}$ is the velocity of the moving particle, $\mathbf{E}$ is the electric field, and $\mathbf{B}$ the magnetic field.

$$\mathbf{F} = q\,(\mathbf{E} + \mathbf{v} \times \mathbf{B}) \tag{1.2}$$

The fusion reaction takes place inside the plasma where energy is released at the plasma core. Subsequently, the energy is lost to the reactor vessel, which is unavoidable because the 14 MeV neutrons will not be contained to the plasma. It is the escaped energy that can be used to generate electricity. On the other hand, this energy loss cools down the plasma despite and reduces thereby the average reaction rate. Hence, all other forms of heat should stay inside the plasma. Therefore, besides the temperature of the plasma, which affects the average reaction rate, the energy confinement τ_E is also important. This quantity represents the time it takes for the plasma to lose $1/e$ of its energy. When τ_E is not high enough, the energy of the plasma will dissipate too fast.

Another physical quantity, the particle density n, also plays an essential role. If the particle density n is too low, fewer nuclei will collide and the amount of fusion reactions will be reduced. The Lawson criterion is a minimal value for $\mathrm{n}\tau_E$ that needs to be exceeded at a certain temperature [5].

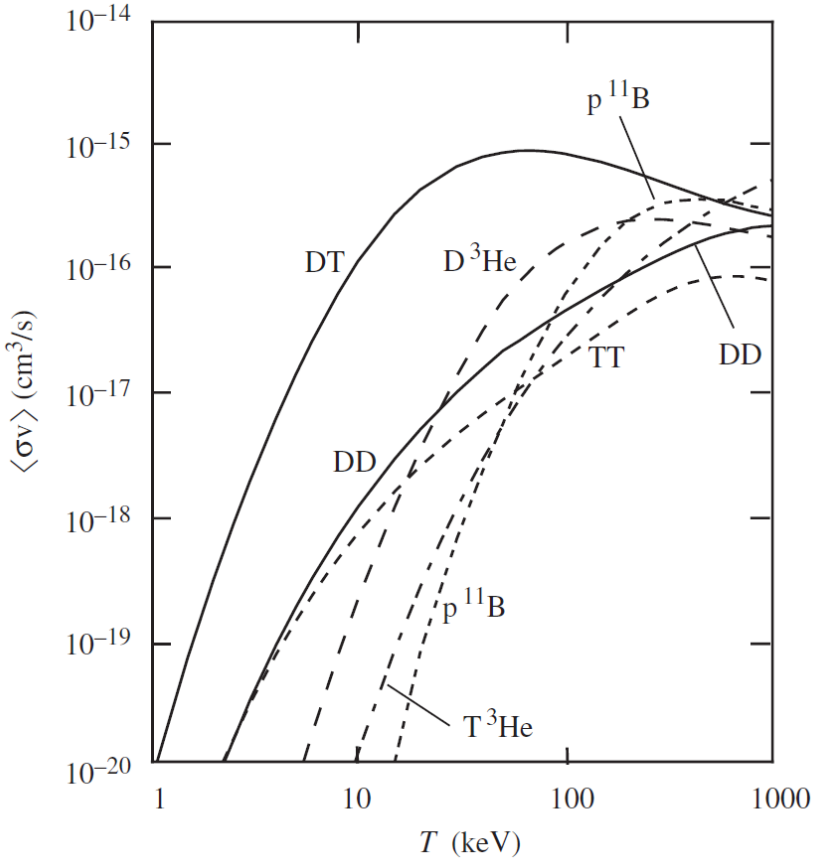

Figure 1.3: The average reaction rate of possible fusion reactions, assuming a Maxwellian distribution of the plasma temperature [1].

This requirement is shown in Eq. (1.3) for the DT-reaction [1]. The three parameters n, T, and τ_E can also be combined into $n\tau_E T$, the triple product. This important figure of merit needs to be higher than $3 \times 10^{24}\,\mathrm{eV\,s\,m^{-3}}$ for the DT-reaction [6].

$$n\tau_E \geq 2 \times 10^{20}\,\mathrm{s\,m^{-3}} \text{ with } T \simeq 20\,\mathrm{keV} \tag{1.3}$$

For a commercial fusion power plant, the triple product is a necessary but not sufficient requirement. It is possible that the required heating power is higher than the power generated by the fusion reaction, due to the substantial amount of external heating that the plasma needs to obtain these conditions. While the neutrons leave the plasma, the helium ash, containing 20 % of the released energy, is confined inside the plasma and can transfer its energy to maintain the plasma energy and reduce the required amount of heating power. To take the heating power into account, a fusion energy gain factor Q is defined in Eq. (1.4) as the ratio between the released fusion power P_{fus} and the heating power P_{ext}.

$$Q = \frac{P_{fus}}{P_{ext}} \tag{1.4}$$

When additional losses are also taken into account, it becomes essential that the Q-value, which is a function of the triple product, is high enough. The current goal for experimental devices is reaching Q = 10, while commercial power plants should exceed this [7]. Only when this can be obtained in a stable mode where the reactor lifetime provides an acceptable return on investment can nuclear fusion power plants be commercially used.

1.2 Fusion Devices

Since the beginning of fusion research, multiple types of fusion devices with different concepts for electromagnetic fields have been explored. A few examples are the zeta-pinch, the magnetic mirror (e.g. the TMX-U shown in figure 1.4), and the θ-pinch. While they have been useful in research, these experiments had difficulties to reach the temperatures, densities, and confinement times necessary for fusion [6, 8].

Currently, two concepts, both originating from the 50s, are mainly being pursued for magnetic confined fusion and have the potential to be used in power plants. The most advanced is the tokamak, a Russian invention of Igor Tamm and Andrei Sakharov [9]. An alternative is the stellarator, proposed by Lyman Spitzer for the American fusion research program [6].

In a stellarator, a set of external current coils generate the electromagnetic field necessary to confine a closed plasma. This requires a rotational transform of the magnetic field lines. Spitzer's concept, shown in figure 1.5, bends a torus into the shape of the number eight to achieve this.

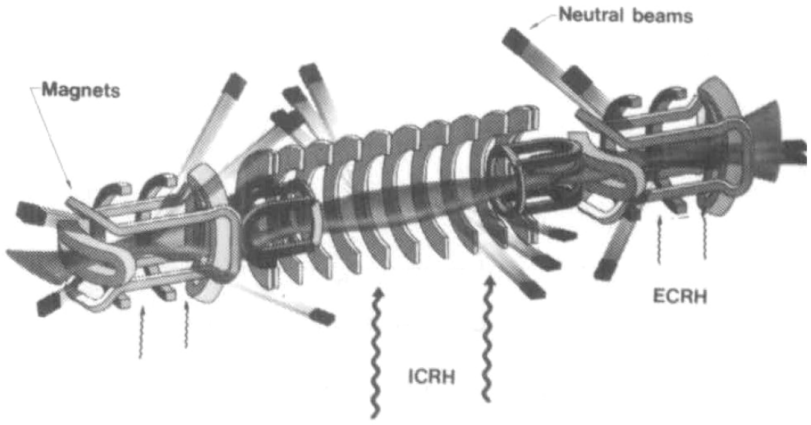

Figure 1.4: Drawing of the magnet mirror TMX-U at Lawrence Livermore National Laboratory, showing the magnet configuration and the location of the heating systems [8].

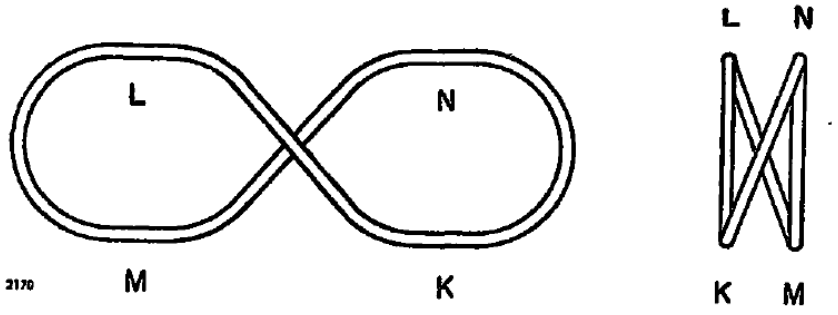

Figure 1.5: The geometry of Spitzer's 'figure-eight stellarator' [10].

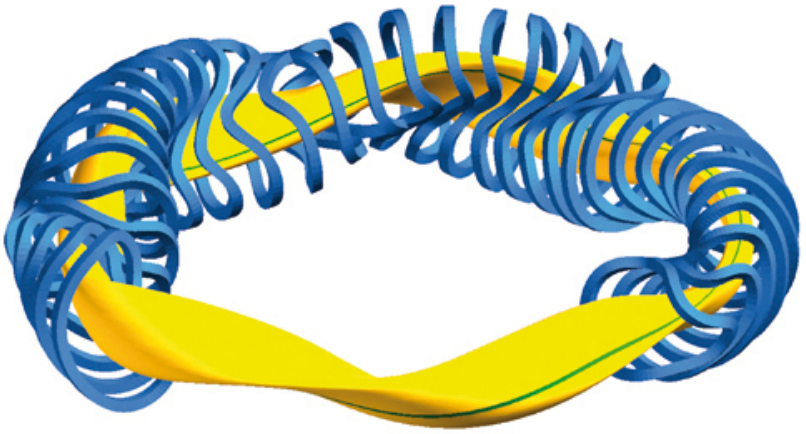

Figure 1.6: A schematic of the modular magnetic coil system in Wendelstein 7-X, a stellarator in Max-Planck-Institut für Plasmaphysik - Greifswald, with the plasma contour visualized [11].

Later on the toroidal shape is used. The rotational transform is then obtained by one or more helical coils located around the vacuum vessel. These helical coils can be combined with toroidal and/or poloidal current coils. In such a way, different set-ups can be constructed that vary in the number of coils that are used, how many times each coil is wrapped around the plasma, and the direction of the current in a coil. Alternatively, the helical coils can be replaced by a modular non-planar coil-system that generates the same complicated 3-dimensional magnetic field configuration. This is done with Wendelstein 7-X, shown in figure 1.6, a stellarator located at the Max-Planck-Institut für Plasmaphysik in Greifswald, Germany [11].

Because the magnetic fields in stellarators are solely generated by external coils, there is no electrical current necessary in the plasma. This ensures that a stellarator can be operational as long as there is current flowing through the coils. Especially with the use of superconducting coils, this makes the stellarator a steady-state device. This is an ideal characteristic for future commercial fusion power plants [12], because the electricity production would not have to be stopped on a regular basis.

Computational methods used to design non-planar coils, can calculate complicated magnetic field configurations that optimize different parameters. For example, such optimization makes it possible to achieve quasi-symmetry. Alternatively, the particle and energy confinement can be improved, or the neo-classical effects can be minimized. Although there are many potential benefits with the stellarator concept, the development is not

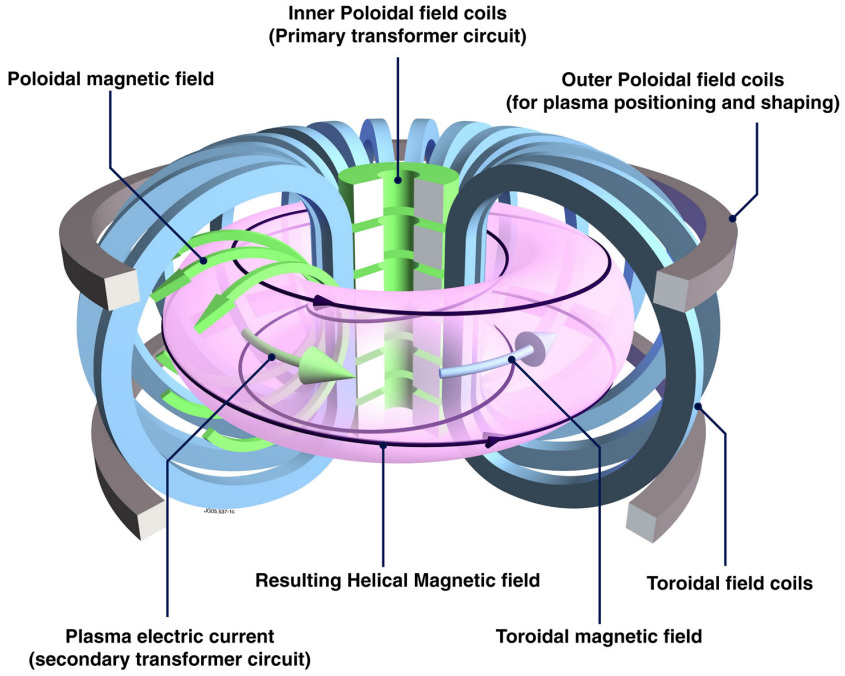

Figure 1.7: A schematic overview of the coil system in JET at Culham Centre for Fusion Energy, as a typical example of the tokamak principle [13].

yet as advanced as is the case for the tokamak design [12].

The tokamak is for the moment the most developed and promising device. Instead of solely using external coils to generate the magnetic field, a current inside the plasma generates a component of the magnetic field. Therefore, as shown in figure 1.7, three types of coils are used in a tokamak [13].

Around the torus-shaped plasma the toroidal field coils, which are on figure 1.7 depicted in blue, are placed. The resulting magnetic field from these coils is not homogeneous. At the inner edge of the torus, or high field side, the magnetic flux density is higher than at the outer edge, the low field side. To achieve the required magnetic confinement, this effect needs to be sufficiently countered by making the magnetic fields helical.

Therefore, in the middle of the torus stands the inner poloidal field coils, or central solenoid, depicted in green on figure 1.7. By ramping up the voltage in these coils, a current is induced in the plasma. Hence, this coil system functions as a transformer where the inner poloidal field coils form the primary winding and the plasma forms the secondary winding of the transformer. The plasma current creates a poloidal magnetic field, which is substantially smaller than the toroidal magnetic field and related with

each other through Eq. (1.5), where B_θ is the poloidal magnetic field, B_T the toroidal magnetic field, q the safety factor, and $\frac{a}{R}$ the inverse aspect ratio [14].

$$B_\theta = \frac{1}{q}\frac{a}{R}B_\mathrm{T} \tag{1.5}$$

The toroidal and the poloidal magnetic field form together the required helical magnetic field with a rotational transform. To have a poloidal component of the magnetic field, the plasma current is essential in tokamaks. Because the plasma current is (partially) induced by a constant direct current through the central solenoid, a tokamak runs in a pulsed operation. The maximal length of each pulse depends on the maximal charge of the capacitors connected to the central solenoid and the possibility to induce a current in other ways.

The third coil system, depicted in grey on figure 1.7, is formed by the vertical field coils also known as the outer poloidal field coils. They are essential to position the plasma correctly and adjust the plasma shape. Without these coils, the plasma would not be stable.

Currently, the largest tokamak in operation is the Joint European Torus (JET) at Culham Centre for Fusion Energy (CCFE). To demonstrate the technological feasibility of fusion power plants, a drastic increase in scale is necessary. Therefore ITER, shown in figure 1.8, is being built in Saint-Paul-lez-Durance, France. Originally, the name ITER stood for International Thermonuclear Experimental Reactor, but this abbreviation has been deprecated. Instead, the ITER Organization now refers to the Latin word 'iter', which means 'the way'. The different responsibilities and costs for the construction and operation of this tokamak are divided between 7 partners. The ITER members are China, the European Union (including Switzerland), India, Japan, Korea, Russia, and the USA. This consortium represents more than 50 % of the world population and 80 % of the Gross World Product.

ITER is essential to tackling the remaining challenges and to reach significant milestones in the path to realise fusion energy [21]. It is designed to reach a Q-value of 10, for pulses of at least 400 s, to generate 500 MW of fusion power. A comparison between the design specifications of JET and ITER, as shown in table 1.1, clearly demonstrates the required increases in radius, plasma volume, current, etc. for both devices.

While ITER should prove that nuclear fusion is a viable concept for future power plants, it remains an experimental reactor. This results in a higher amount of flexibility in operational scenarios and more diagnostics for ITER than would be necessary for future fusion power plants. Simultaneously, for fusion power plants there is a need to increase efficiency, pulse length, material resistance against radiation, and component lifetime, while the loading conditions will be heavier. This already indicates that ITER and future power plants will have different design specifications.

Hence, between ITER and the development of commercial fusion power

Table 1.1: The design specifications of JET (in divertor configuration) [15–17] and ITER [17–19].

Design parameter	JET	ITER
Major radius [m]	2.85	6.2
Minor radius [m]	0.95	2.0
Plasma current [MA]	≤ 6	15
Plasma volume [m^3]	~ 90	837
Plasma surface [m^2]	~ 150	678
First Wall surface [m^2]	~ 200	~ 680
Divertor surface [m^2]	~ 30	~ 80
Magnetic field at axis [T]	3.6	5.3
Pulse duration [s]	20 to 60	≥ 400
Fusion power [MW]	~ 16	500
Gain factor Q	~ 1	≥ 10

plants, one additional intermediate stage is necessary. This would be a demonstration power plant, named DEMO. Figure 1.9 shows a schematic overview of a pre-conceptual design of such a DEMO-reactor that will be a prototype of an economically profitable fusion plant. DEMO will be designed and operated under one tested and controllable scenario.

Unlike for ITER, there is presently no broad international cooperative effort to build one unique DEMO. Several countries are already busy investigating technologies and determining the required parameters and goals. However, there are not yet any design specifications for DEMO, only conceptual studies [22–24].

1.3 Plasma-Wall Interaction

For ITER as well as for future fusion reactors, e.g. DEMO, there are still several areas where further research is needed. One of these topics is the Plasma-Wall Interaction (PWI). This term describes a group of processes at the plasma edge and the vessel wall that describes an essential part of the physics in fusion devices. At one side, PWI is largely responsible for the exposure conditions on the armour material, i.e. the material closest to the plasma, and the corresponding choice of armour material. On the other hand, it provides the necessary particle and heat exhaust from the plasma.

First of all, the wall is exposed to a high particle flux from the plasma. The *fuel*, i.e. deuterium and tritium, and the *ashes*, i.e. helium, of the fusion reaction form one part of this flux. Another particle source comes from the plasma impurities, e.g. material eroded from diagnostic components or wall armour. Although neutrons are also particles, neutron irradiation is

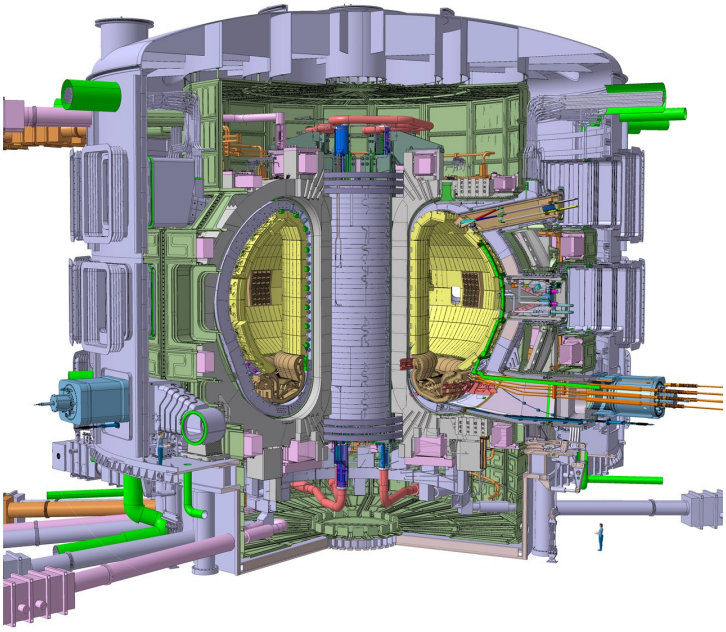

Figure 1.8: A schematic overview of ITER showing a cut-out of the reactor. A person is depicted in the right, bottom corner to indicate the scale [20].

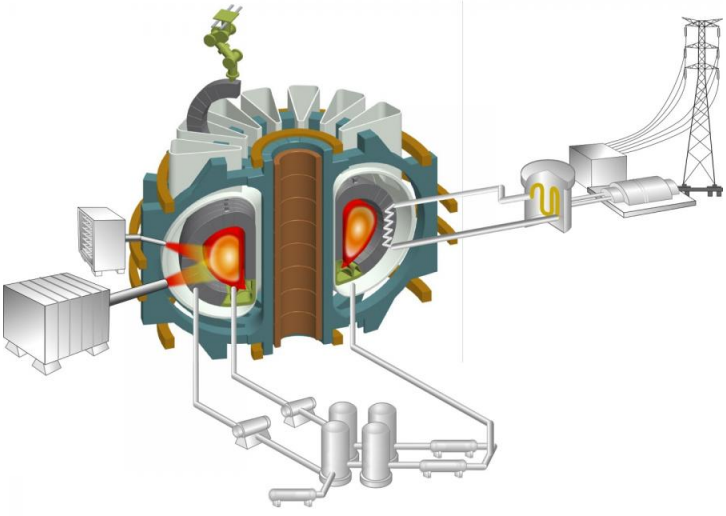

Figure 1.9: A schematic overview of K-DEMO, a pre-conceptual design for a DEMO reactor by National Fusion Research Institute, South Korea [25].

considered separately from the flux of the plasma particles. Secondly, the material is also exposed to high heat fluxes. Part of these thermal loads are caused by the incoming particles that transfer their energy to the wall components and the neutrons that have a volumetric heat loading. Another part comes from electromagnetic radiation of the plasma core or the plasma edge, e.g. Bremsstrahlung or ionization of impurities.

Understanding and controlling the PWI ensures that a fusion device can be operated without damaging the wall and increases the performance. Taking PWI into account is therefore essential in the choice for plasma facing materials (PFMs) and the design of plasma facing components (PFCs).

1.3.1 Particle Irradiation of the Inner Wall

The PFMs shield the underlying materials, during which they will be subjected to several processes which are schematic depicted in figure 1.10. These processes can be divided into three main categories: erosion, deposition, and implantation.

Multiple erosion mechanisms that have an effect on PFMs can be identified. The most straight-forward one, **physical sputtering**, occurs when an incoming particle penetrates the material. The energy and momentum transfer that occurs during the resulting collisions can knock one or more atoms out of the lattice of the PFM. Such a process can only happen if the projectile atom's energy is higher than the surface binding energy of the target atoms. While physical sputtering will not be completely stopped in a fusion reactor, it can be significantly reduced by the choice of PFM. The sputtering yield is not only strongly depending on energy and angle of coincidence, but also on the atom species from both the projectile and the PFM [26].

For **chemical sputtering** the projectile atoms undergo collisional interactions. Thereafter, a chemical reaction between a projectile atom and the PFM results in a product that is weakly bound to the surface. A thermally driven desorption process will then cause the release of the product from the surface. The function of the projectile is solely to start the chemical reaction and not to directly cause the erosion. Erosion yield is a temperature dependent property which varies strongly among materials. This mechanism only occurs for some combinations of target and projectile material.

Carbon is very susceptible to chemical sputtering when it is exposed to energetic hydrogen ions, which penetrate the surface and collide with the bulk atoms. After this phase, which has similarities with physical sputtering, the ions are slowed down and become thermal. From that point, a chemical reaction can occur which produces a hydrocarbon. This will diffuse to the surface where it desorbs after some time. Since the projectile atom damages the bulk and in this way creates additional defects which can act as hydrocarbon reaction sites, this is a very effective form of erosion [27].

With **chemical erosion**, a third mechanism, the projectile atoms are

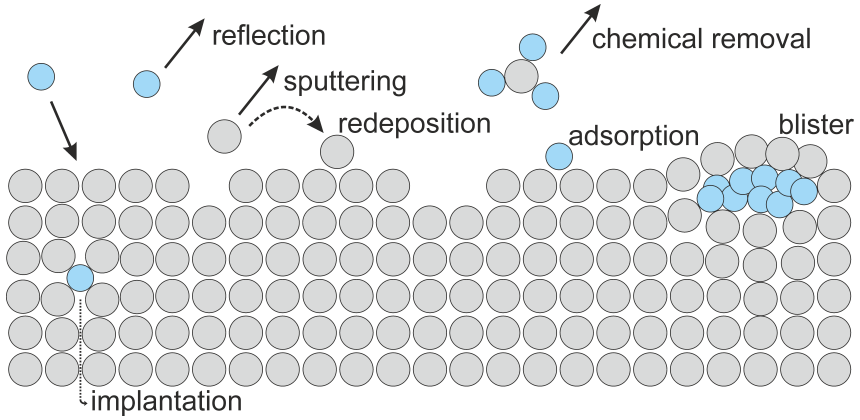

Figure 1.10: A schematic representation of several important PWI processes that might occur when the bulk material is subjected to an incoming particle flux.

thermal and only undergo a chemical reaction with the surface atoms. The resulting product is more weakly bonded with the surface, increasing the desorption rate. Similar to chemical sputtering, this does not happen for each combination of target and projectile atoms.

For example, when carbon is exposed to thermal hydrogen ions, chemical erosion occurs through the hydrogenation of an sp^2-configured carbon atom into an sp^3 complex. These hydrocarbon complexes desorb at temperatures above 100 °C. For surface temperatures above 300 °C, an intermediate sp^x state can recombine with adsorbed atoms. In this way, the net-erosion rate is strongly decreased at these higher temperatures [26].

Another significant erosion process of PWI is the **flaking** or evaporation of material due to **blisters**. After a high fluence of light atoms, e.g. helium or hydrogen, the particles accumulate at voids just below the surface and create blisters [28, 29]. This would only happen at low enough surface temperatures, since at higher temperatures the atoms would have enough energy to be released from the trap and diffuse through the material. Heat transport is reduced at such a blister, which can lead to local overheating and evaporation of the blister cap. Furthermore, a thin layer of material could flake away when the stresses are too high [27].

Under the right circumstances, the PFC could also suffer from **deposition**, as visualized in figure 1.10. In its most simplistic form, an ion collides with the PFM and sticks to the surface instead of backscattering or penetrating the material. This happens based on a *sticking factor*, which depends on energy, angle of incidence, and the involved atoms. However, normally the surface is not smooth, making it possible for backscattered atoms to interact with the surface several times. Thereby the deposition

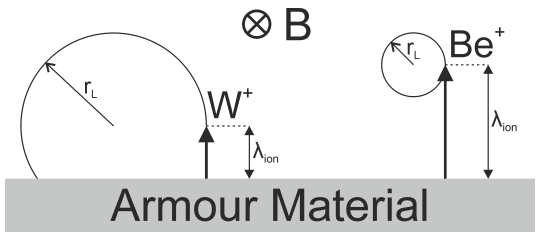

Figure 1.11: Prompt deposition occurs when the ionization length λ_{ion} of an atom that is sputtered from the armour material in the presence of a magnetic field B, is shorter than the Larmor radius r_L of the respective ion.

probability may be increased as the roughness of the surface locally changes the angle of incidence.

Furthermore, due to **chemical** reactions there is a deposition of hydrocarbon layers or mixed materials layers, e.g. beryllium and tungsten. Another possibility is **prompt deposition**, shown in figure 1.11, where a sputtered particle is immediately redeposited. This happens if the distance the sputtered atom covers before being ionised is smaller than the Larmor radius with which the ion rotates in the presence of a magnetic field. Prompt deposition is mainly observed for tungsten and not for other materials, e.g. berylium, because tungsten has a relative short ionization length and long Larmor radius.

Thermal particles can also bind with surface atoms through **adsorption**. In the case of chemisorption, chemical bonds are formed with a binding energy of several electronvolts. Alternatively, physisorption can occur when van der Waals forces are used for a weak binding, with a binding energy below 0.5 eV.

Besides the diverse erosion and deposition processes mentioned above, **implantation** should also be taken into account. This can become problematic, for example if tritium is implanted. For safety reasons, the amount of tritium inside the reactor is limited. The tritium retention depends upon material characteristics such as permeation, solubility, diffusivity and trapping of the tritium in the PFM.

Other atoms, besides tritium, can also get implanted in the material and change material properties. They may affect the ductility, strength and recrystallization behaviour. Furthermore, they can be trapped and start to accumulate. This can result in the formation of cavities and gas bubbles. When this happens in a narrow near-surface-region, blisters and pinholes can appear on the surface.

Another process that can occur then, is the creation of surface extrusions [30]. These surface extrusions take the form of nano-sized fibres, *fuzz*, or coral-like structures and are essential elements in the degradation of the wall armour and have been observed for several metals, eg. tungsten,

molybdenum. On tungsten are these surface extrusions formed under a wide range of exposure conditions, such as a surface temperature of 1000 K to 2400 K, energies of 20 eV to 35 keV, and fluences of $1.3 \times 10^{24}\,\mathrm{m}^{-2}$ and higher [31, 32].

1.3.2 Heat Loading of the Inner Wall

Within a fusion reactor, two types of thermal loads occur. The first is called the steady state heat flux (SSHF) and is inherent to plasma operation. It consists of a relatively constant heat flux that under certain conditions is temporarily increased, i.e. *slow transients*. In superposition to the SSHF, there are several types of transient heat loads on a time scale below a second. The resulting deposited power densities are summarized in figure 1.12.

The origin and parameters of these high heat fluxes (HHF) vary for each fusion device, based on design and operational scenarios. As a consequence, the energy deposition on in-vessel walls can result in different challenges for every reactor. For clarity, this section does not only give a description about the occurring phenomena, but also contains relevant values and parameters. These are, unless explicitly mentioned otherwise, the expected values for ITER. Design and reactor operation choices will give other values for DEMO and fusion power plants. However some of the heat flux phenomena that the PFMs in ITER have to withstand, e.g. edge localized modes, can also occur in next generation fusion reactors.

The **SSHF** during normal plasma operation is substantially different for each component. In ITER, as is discussed in subsection 1.4.3, there will be two types of first wall panels, i.e. the 'normal ITER first wall panels' and the 'enhanced ITER first wall panels'. It is expected that the 'normal ITER first wall panels' will be loaded with $\sim 0.5\,\mathrm{MW\,m}^{-2}$ during operation. Nevertheless, the ITER design requires these panels to have the ability to handle steady state power densities up to $2\,\mathrm{MW\,m}^{-2}$. The required power capability is higher for the 'enhanced ITER first wall panels', which will have to be able to withstand $5\,\mathrm{MW\,m}^{-2}$. For the divertor, another type of PFC which is discussed in subsection 1.4.3, these loads are even higher. During normal operation the divertor will have to endure a SSHF up to $10\,\mathrm{MW\,m}^{-2}$, which could be increased up to maximal $20\,\mathrm{MW\,m}^{-2}$ when slow transients occur [36].

Just as the SSHF is inherent to plasma operation, some transient heat fluxes are currently considered unavoidable as well. To obtain the necessary plasma parameters, a high confinement regime is used during operation. This regime, the H-mode, is characterized by an edge barrier in the pedestal region. The barrier reduces the transport of particles and energy out of the plasma, thereby improving the confinement [37]. As an effect of the improved confinement and reduced transport, a steep pressure gradient is created, as shown in figure 1.13.

This gradient grows until it becomes unstable at which point the edge

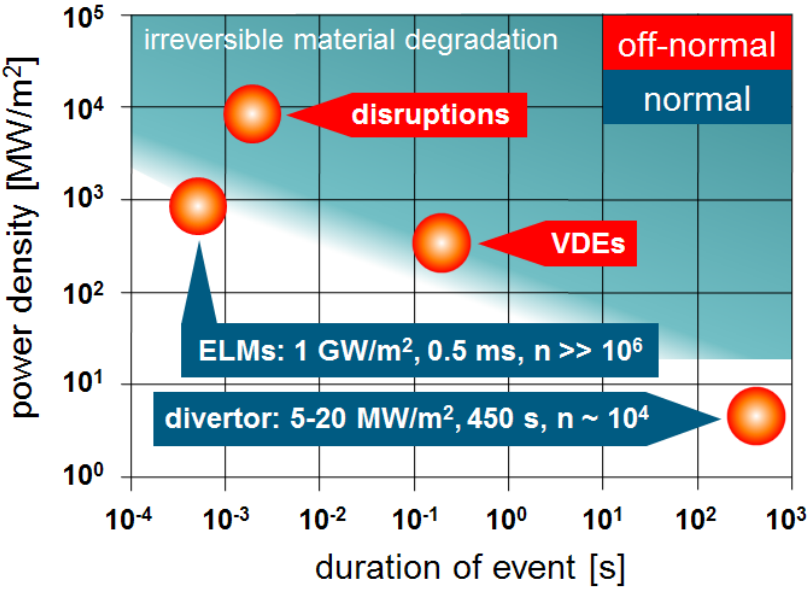

Figure 1.12: Overview of the expected power density and duration for different events that will occur in the ITER divertor [33–35].

transport barrier relaxes resulting in the release of particles and energy. These recurrent instabilities are called **edge localized modes (ELMs)** and can occur at frequencies up to kHz. After each ELM, the pressure will restabilize and then build up again until a new ELM occurs. While the partial loss of confinement decreases the plasma energy, the overall plasma performance is still better than during other regimes of plasma operation. Furthermore, the repeated partial loss of confinement prevents the accumulation of impurities [38].

An analogue phenomenon to ELMs can be found in nature. The ELM-filaments resemble solar flares as shown in figure 1.14. Although both phenomena have morphological similarities and have both phases where they are driven by magnetohydrodynamics, they are governed by different regimes of magnetized plasma physics [39, 40].

Magnetohydrodynamics or MHD, which is fluid dynamics for magnetic and/or electrical conductive fluids, can be used to describe plasmas. It has been found that different MHD instabilities can be responsible for ELMs. Three different ELM-types have been identified, each of them triggered by different instabilities and having their own characteristics [42].

After the H-mode has started, there is an initial 'ELM-free' period. Thereafter, **Giant ELMs** or **Type I ELMs** occur until the plasma is no longer externally heated. The natural repetition rate of these ELMs is

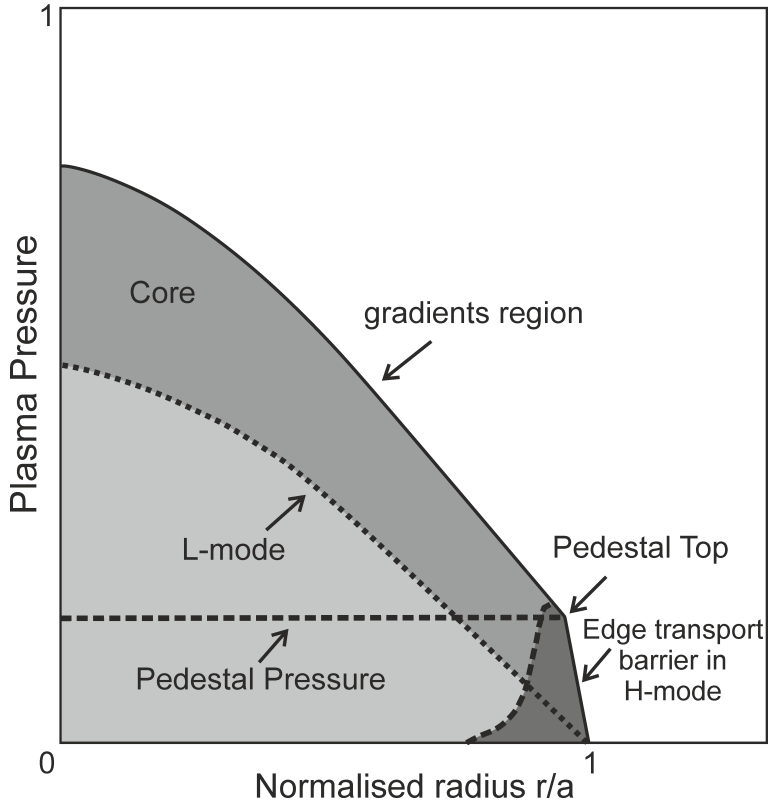

Figure 1.13: A comparison of the radial pressure profile structure for the L-mode and the H-mode with the characteristic features of the H-mode, the edge transport barrier, and the plasma pedestal, identified. [37]

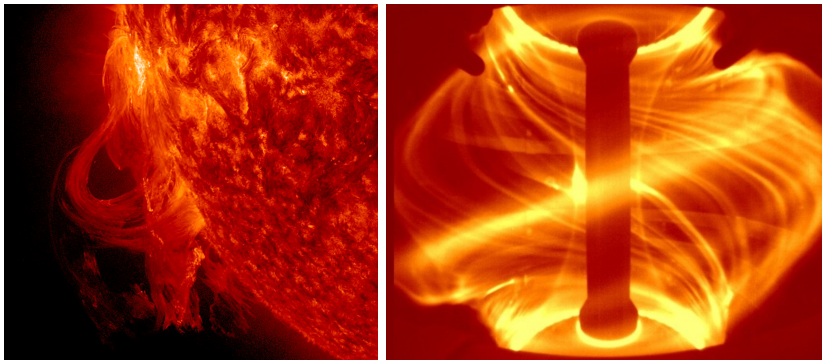

Figure 1.14: On the left picture is a solar flare shown [41], which is very similar to ELMs. The right picture shows such ELMs occurring on the MAST device, located at CCFE [20].

situated around 1 Hz to 2 Hz. It increases together with the particle flux into the plasma edge and the heating power. During such an ELM, which has a duration of $\sim 500\,\mu s$, the energy loss can be estimated based on the assumption of an $\sim 5\,\%$ to $10\,\%$ loss of the energy stored in the pedestal region. Alternatively, the assumption can be used that there is a correlation between ELM energy loss and *pedestal collisionality*. For ITER, these two methods correspond with an energy loss of 5 MJ and 22 MJ respectively. Taking into account a contact area of $\sim 10\,m^2$, the power deposited on the PFMs can easily go above $1\,GW\,m^{-2}$ [35, 38, 43, 44].

The elongation and triangularity of the plasma can be changed through the magnetic field configuration. ELMs with a strongly reduced power density deposited on the PFMs can be observed in some devices for discharges with a high degree of plasma shaping. Known as **Grassy ELMs**, or **Type II ELMs**, these have frequencies in the kHz-range and a large pressure gradient that is similar to Type I ELMs. A transition from Type I to Type II ELMs or a mixed Type I-II ELMy-regime can occur. Due to the size of these ELMs, they are not considered to be a problem for the armour materials [38, 42].

Type III ELMs typically have a smaller amplitude than giant ELMs and a higher frequency. These Type III ELMs are preceded by magnetic precursors. In contrast to Type I ELMs, the repetition rate, ~ 0.1 kHz to 1 kHz, decreases with higher heating power. As a result, Type III ELMs only appear with low heating power, and therefore near the H-mode boundary [38].

Due to the required energy confinement, the reference regime for ITER will be the Type I ELMy H-mode. However, the energy deposited on PFCs by these giant ELMs can be unacceptably high and can result in a reduced lifetime of the components, which necessarily leads to strategies to mitigate

the power loads. Fortunately, the particle and energy losses corresponding to a single ELM is reduced when the repetition rate increases [35, 44].

Several mitigation techniques are based upon artificially increasing the ELM-frequency. One such strategy is fuel pellet pacing, where the injection of frozen deuterium pellets triggers an ELM. Alternatively, resonant magnetic perturbation fields are used. These are small fluctuating magnetic fields which partially suppress ELMs and increase their frequency by increasing the edge turbulence [44].

While ELMs need to be mitigated, they do not necessarily have to be completely avoided. This is different than for other types of transient events, discussed below, which are considered to be *off-normal* and should be prevented or suppressed below critical threshold values. After each of these off-normal transients, the remaining lifetime of the PFCs is strongly reduced.

One of these events is the **Plasma Disruption**. This is the sudden decay of the plasma current due to spatial confinement instabilities. Without the plasma current in the tokamak, the magnetic field configuration is altered and confinement is lost. As a consequence, the plasma discharge is terminated and all energy is deposited on the walls. This event is often preceded by a *precursor phase* where the magnetic field is modified.

The moment the internal magnetic surfaces are destroyed a *thermal quench* will start. During this phase, the plasma energy will escape to the walls. Following this, during the *current quench*, the plasma current will break down and the confinement will be lost.

A plasma disruption will lead to large amounts of energy being deposited in a small near-surface layer. During 0.1 ms to 5 ms, a power density of $1\,\mathrm{GW\,m^{-2}}$ to $10\,\mathrm{GW\,m^{-2}}$ is expected to be deposited on the armour material for the thermal quench in ITER. This will lead to serious damage, e.g. melting, which will either reduce the components lifetime or destroy the component. Additionally, the current quench will deposit radiative thermal loads on the PFC, although their size is considered to be limited in comparison with the normal energy deposition, i.e. ELMs and SSHF [45]. Furthermore, due to the high power density during the thermal quench, a shielding vapour cloud is produced in front of the PFM, reducing the absorbed power density. Although the PFCs are only able to endure a limited number of disruptions, it is assumed that $\sim 10\,\%$ of all full performance discharges in ITER will result in a plasma disruption [46].

A strongly elongated plasma needs to be actively stabilized in the vertical direction. When the vertical control of the plasma is lost, the plasma can touch the wall components. Such a collision is called a **Vertical Displacement Event (VDE)**. During the vertical movement, the plasma current slowly shrinks. When this current drops below a threshold value a thermal quench will be initiated. This is similar to a plasma disruption and is also followed by a current quench.

A VDE will deposit an energy $60\,\mathrm{MJ\,m^{-2}}$ in 100 ms to 300 ms on the

PFC. Despite the fact that the heat flux for VDEs is lower than for disruptions, a VDE has the potential to damage the component more severely. This is related to two differences between plasma disruptions and VDEs. One distinction between the two transient events is the duration, which is much longer for VDEs. Another distinction is the shielding vapour cloud, which is not produced during a VDE, in contrast to what happens during a plasma disruption. Furthermore, the VDE could also damage the cooling channels and structural materials below the PFM-layer on a component [47].

1.4 Plasma Facing Materials & Components

Other topics where further research is needed are the choice of plasma facing material (PFMs) and the design of plasma facing components (PFCs). They directly face the hot plasma and shield the rest of the device. This is crucial, since the severe environment of fusion plasmas can cause significant damage.

First of all, the 14 MeV neutrons generated in the fusion reaction are not retained by the magnetic field and will irradiate the in-vessel components of the reactor. The PFCs will endure the highest damage from the neutrons, since they are located the closest to the plasma. Furthermore, with the PFCs located the closest to the neutron source, they will endure the highest neutron fluence due to the *inverse square law*. Neutrons can cause transmutation of nuclei, changing of thermal and mechanical properties, material activation, formation of voids, and heating of the material.

PFMs are not only irradiated by neutrons, they also have to endure the PWI, as discussed in section 1.3. In order to withstand both the particle fluxes and the energy deposition for a long enough time, there are several properties that are desirable in PFMs, which limit the available choices. Therefore, compromises have to be made and all design choices about PFCs and PFMs are the result of weighing the pros and cons. This means that decisions which are optimal for one device, e.g. W-7X, might not be appropriate for another device, e.g. DEMO.

1.4.1 Selection Criteria

In order to build PFCs that have an acceptably long lifetime and put only a reasonable amount of limitations on the reactor operations, the material requirements are strict. The list of the various material properties for the PFM that are desired is therefore rather long. Table 1.2 summarises the most important material properties for a PFM. Unfortunately, no material exists that provides all of these properties so compromises have to be made during the selection of PFMs.

One advantageous property is a **low Z-number**, or atomic number, to minimize the plasma cooling through Bremsstrahlung losses. The energy irradiated away by Bremsstrahlung increases with Z_{eff}, the effective atomic

Table 1.2: Overview of the most important material requirements that are desired for PFMs [17, 48, 49].

Desired requirement	Benefit
Low Z-number (atomic number)	Limit Bremsstrahlung
Low erosion	Increase PFC lifetime Limit plasma contamination
Low tritium retention	Adhere to safety limit
High melting temperature	Increase PFC lifetime Limit plasma contamination
High thermal conductivity	Reduce operating temperature
Thermal shock resistance	Increase PFC lifetime Limit plasma contamination
Low activation	Reduce radioactive waste
Resistance against neutron damage	Prevent property degradation
High recrystallization temperature	Prevent property degradation
Low Ductile-Brittle Transition Temperature (DBTT)	Improve thermal shock behaviour Facilitate production
Low temperature dependency of material properties	Prevent temperature limitation

number [6]. Since particles with a high atomic number increase the Z_{eff} more, they have a lower acceptable concentration. Therefore, materials with a less stringent limit for impurity accumulation in the plasma core are preferred.

A more straight-forward way to reduce the plasma contamination, is reducing the influx of impurities. Therefore, the PFM should have a **low erosion** rate. In addition, a PFC which has a high amount of erosion can no longer function properly and will be replaced. When materials with a low erosion rate are used, the lifetime of the component will be extended.

During operation, tritium will be implanted into the PFM, resulting in a tritium inventory which is a matter of concern. Tritium is a relatively short-lived isotope with a half-life of 12.32 year. For safety reasons, fusion reactors will have to restrict the total tritium content. This means that PFMs need to have a **low tritium retention**. In the case for ITER, the French Nuclear Safety Authority (Autorité de Sûreté Nucléaire, ASN) enforces a tritium limitation. As a result, ITER has a 700 g in-vessel tritium safety limit [50].

The SSHF on the PFC already causes a high operating temperature. When transient heat fluxes occur, the temperature can (locally) strongly increase. Thus, a **high melting temperature** is an important material property. A re-solidified surface layer will have degraded properties, which can result in detrimental effects on the thermal shock behaviour and component lifetime. Furthermore, a locally molten surface results to enhanced erosion. This also has a negative effect on the lifetime of the PFC and will result in an increased plasma contamination.

The heat transport from the PFM to the cooling channel should be sufficiently high in order to reduce the size of the temperature spikes during transient heat fluxes and to enable operation with high SSHF. A **high thermal conductivity** is therefore essential, since it is one of the main factors to increase the heat transfer.

Since ELMs are not completely avoidable and off-normal events like VDEs and disruptions can still occur, the PFM should have a good **thermal shock resistance**. If a PFM can withstand more severe transient thermal fluxes without any consequent damage, the lifetime of the PFC on which the PFM is used will be higher. Furthermore, the amount of required ELM mitigation would be slightly reduced. Since thermal shocks can lead to enhanced erosion, a better resistance to thermal shock damage would reduce the plasma contamination.

Due to the neutron-flux, a fraction of the atoms in PFMs will be activated. For safety and operational reasons it is important to use a material that has a **low activation**. After activation, the material will be radioactive and will have to be handled remotely. Only after a cool-down period can the material be disposed of or recycled. Furthermore, transmuted material has different properties, e.g. thermal conductivity, than the original material.

Beside activation, neutron irradiation can result in other damage. Crystal defects, e.g. the creation of an interstitial atom and a vacancy, are generated. Often the lifetime of these defects is limited, but it can still have an effect on the material. For example, a crystal defect can act as a trap for hydrogen isotopes and thus increase the tritium retention. Therefore, it is not always common to express neutron irradiation with the energy profile of the neutrons, the exposure time, and the flux. Instead, neutron induced damage is often expressed in displacements per atom (dpa), giving the average number that each atom has left its crystal position and moved to another location. It is vital that the material is **resistant against neutron damage** to reduce the degradation of material properties. For some materials high neutron irradiation might result in alterations of the dimensions, e.g. material shrinkage and swelling.

Various materials that are considered for PFM are polycrystalline. The microstructure, i.e. the size and shape of the crystallites (or grains), influences multiple characteristics. As a consequence, it is not opportune if the selected material grade, which has a specific microstructure, loses that microstructure during operation. This means that a **high recrystallization temperature** is desired in order to prevent the loss of microstructure and the accompanying property degradation.

For the manufacturing of components, it is beneficial to work with ductile materials. In addition, the thermal shock behaviour for brittle materials is disadvantageous. As such, materials with a **low Ductile-Brittle Transition Temperature (DBTT)**, which exhibit ductile behaviour at a low temperature, are preferable.

Most material properties are temperature dependent. Due to the strict material requirements, it is not desirable that in the temperature range during operation a property would significantly change. Various factors, e.g. the chosen plasma-regime or the successfulness of mitigation techniques, will also change (locally) the heat flux and operating temperatures. This does not make it possible to know an exact operating temperature, only a broad range of values. A **low temperature dependency** of the material properties, i.e. the material properties do not change strongly in the required temperature range, is therefore important as it prevents a restriction of the window of values that the operating temperature is allowed to have. This window has for most PFMs, in particular for tungsten, a lower limit at the DBTT and an upper limit at the recrystallization temperature.

1.4.2 Plasma Facing Materials (PFMs)

The increase of scale and performance between the first experimental lab-devices, the current devices, and future fusion power plants affects the choice of PFMs. The requirements, e.g. operational temperature, heat load capabilities, or irradiation resistance, have changed with each design. Therefore, some of the materials that were used in the past are no longer adequate.

Table 1.3: An overview of the main characteristics for beryllium, CFC (carbon fiber composites), and tungsten. Due to the anisotropic behaviour of CFC are its characteristics only given for the pitch-direction [51–53].

Property	Beryllium	CFC	Tungsten
Z-number	4	6	74
Crystal structure	hexagonal	-	body-centered cubic
Density [$\mathrm{g\,cm^{-3}}$]	1.85	~ 2.0	19.35
Melting point [K]	1560	-	3695
Sublimation point [K]	-	3915	-
Thermal conductivity [$\mathrm{W\,m^{-1}\,K^{-1}}$]	201	≤ 500	173
Thermal expansion [$10^{-6}\,\mathrm{K^{-1}}$]	11.3	≤ 0.4	4.5
Young's modulus [GPa]	287	~ 110	411
Tolerable concentration in the plasma [%]	15	12	0.0001

The list of materials that are used as PFM in one or more components in previous devices includes aluminium, beryllium, boron carbide, carbon, gold, molybdenum, stainless steel, titanium, and tungsten [17]. The materials which were originally planned for use as PFMs in ITER, i.e. beryllium, carbon, and tungsten, are discussed here. A summary of their properties can be found in table 1.3. However, after a decision of the ITER Organization, the choice of PFM has changed and carbon will not be used in ITER. For future devices it is also possible that alternatives to the materials that are discussed in this subsection, are used, e.g. liquid PFMs.

A metal that has already been used successfully in fusion devices, e.g. JET, is **beryllium**, whose material properties are summarized in table 1.3 while the most important advantages and disadvantages are mentioned in table 1.4. Since it has a low atomic number (Z=4), the issue of plasma contamination is for beryllium less severe. The maximum allowed concentration is then also determined by fuel dilution instead of contamination. This means that the concentration of beryllium in the plasma has become so high that if two atoms collide, the chances they would be a deuterium and a tritium atom are reduced. Further benefits of beryllium are its behaviour as an *oxygen getter*, which improves the vacuum in the reactor, and its low tritium retention [54].

There are other material properties that allow beryllium to function very well as a PFM. It has a good thermal conductivity, low thermal expansion coefficient, and high specific heat, all of which results in a high heat transport without the creation of high thermal stresses. Furthermore, this element has a low activation under neutron irradiation, it can moderate and

Table 1.4: An overview of the benefits and drawbacks when using beryllium as a PFM in a fusion reactor.

Benefits	Drawbacks
Low Z-number	Low melting point
Good oxygen getter	High erosion
Low activation	Toxicity
Low thermal expansion coefficient	Property degradation under neutron irradiation
Good thermal conductivity	
Low tritium retention	

reflect neutrons, and it is a neutron multiplier material. Nevertheless, there are essential drawbacks when using this element.

The first of these is that the melting temperature of beryllium, 1560 K, is low while the vapour pressure is high. For reactors such as ITER or future power plants the heat loads deposited on PFMs can be high enough to melt beryllium. This affects the microstructure, the surface morphology, and the erosion. Additionally, liquid beryllium will, due to its vapour pressure, evaporate fast, increasing the melt layer loss. As a consequence, the surface temperature of beryllium needs to be kept low enough during transient loading and SSHF. Because it is such a light element, the physical sputtering yield is also very high. Furthermore, due to high oxidation, thick BeO-layers with characteristics that not yet have been fully determined, can be formed [17].

While beryllium is not radioactive and is not easily activated, it does show property degradation after irradiation. Example of neutron damage in beryllium is increased brittleness and transmutation that results in tritium and helium production. Furthermore, safety is the primary concern when working with beryllium.

Inhalation of beryllium is the most problematic occurrence. Over time, prolonged inhalation of beryllium can result in the chronic lung disease *berylliosis*. In certain cases, a single exposure to beryllium dust might also lead to *acute beryllium disease*. This either disappears after a few weeks/months, or it develops into berylliosis. There is no cure available for both acute beryllium disease and berylliosis, although the symptoms can be treated. Therefore, the major focus when working with beryllium is protecting the respiratory system and avoiding beryllium dust [55].

Ingestion and dermatological effects are, in most cases, minor. For humans there have been no reports of health issues after digesting it. Contact with the skin, if the skin is intact and there is no enhanced beryllium sensitivity, would at most result in local irritation, but for damaged skin or skin that has been cut rashes, ulcers, granulomas, etc. can develop. Besides

Table 1.5: An overview of the benefits and drawbacks when using CFC as a PFM in a fusion reactor.

Benefits	Drawbacks
Low Z-number	High erosion rate
No melting	High tritium retention
Large experience	Needs cleaning of machine
Excellent thermal conductivity	Property degradation
Good thermal shock resistance	under neutron irradiation

injured skin, also the eyes might react badly after beryllium contact.

Carbon Fiber Composites (CFC), whose material properties are summarized in table 1.3 and the most important benefits and shortcomings are mentioned in table 1.5, also has a history of use as PFM. There exists a large experience with operating devices containing carbon. Besides as CFC, carbon has also been used in the form of graphite. CFCs, which were part of the initial ITER design, consists of a carbon matrix that is reinforced by a number of carbon fibres, which provide additional strength and can lead to higher thermal conductivity. The fibre-direction will affect the properties, so CFC is pre-eminently an anisotropic material.

Unlike other materials, carbon does not melt, however at high temperature, 3915 K, carbon starts to sublimate. If components are misaligned and there is local overheating, rather than the formation of melt layers or droplets, part of the carbon will evaporate until the components are perfectly shaped. Furthermore, the high sublimation temperature means that a local or temporal rise in temperature due to transient heat fluxes, can be handled without major material damage.

Similar to beryllium, the low Z-number (Z=6) of carbon ensures an excellent plasma compatibility. Fuel dilution would be a bigger problem than plasma contamination. The low radiative losses for carbon are quite essential, for there is a substantial amount of both physical and chemical erosion, which could strongly reduce the lifetime of components in the environment of future fusion reactors.

Another positive characteristic of CFCs is their thermal conductivity. If the carbon fibres are positioned in the direction of the heat transport, the thermal conductivity can become very high. Due to their rather low thermal expansion, combined with the lack of melting and a high sublimation point, CFCs have a good thermal shock resistance. Furthermore, crack propagation is hindered due to the reinforcement of the carbon matrix with the fibres, giving CFCs better resistance against thermal fatigue degradation [56].

Unfortunately, there are huge drawbacks when using carbon in fusion reactors. To start, the tritium retention is very high, which requires either

Table 1.6: An overview of the benefits and drawbacks when using tungsten as a PFM in a fusion reactor.

Benefits	Drawbacks
Low erosion	High Z-number
High melting point	High DBTT
Low tritium retention	Activation
Good thermal conductivity	Recrystallization
Good thermal shock resistance	

relaxing the limit of tritium inventory or a regular cleaning of the device. Such a procedure should not only remove the tritium which is located in co-deposited surface layers, but also the tritium stored in the PFC. In addition, CFC components suffer from the loss of their thermal conductivity, which can be seen at high temperature and after neutron irradiation. Other mechanical and physical properties of CFC will also degrade under neutron irradiation [53]. CFC is a very good PFM for experimental devices that do not use tritium and do not generate a large amount of neutrons and many tokamaks have also used carbon in one or more of their PFCs. However, the tritium retention and the neutron-induced degradation make it difficult to use CFC in tritium-fuelled reactors.

This difficulty led to the initial, but currently outdated, plan for ITER, where CFC would solely be used in the first operational phase. During that period, when the first plasmas will be generated, no tritium will yet be used. In this phase, the ITER-staff can learn how to operate the device and see if unexpected issues arise. Because there would be no tritium in the plasma, the neutron irradiation would also be very limited. For the following phases of operation in this initial and outdated plan for ITER, which involve the use of tritium, CFC would be replaced by another PFM. However, in order to save time and reduce costs, it has been decided to modify this initial plan. The current design of ITER no longer uses any carbon at all and tungsten will instead be used from the beginning [33, 57].

The most promising candidate for PFM, **tungsten**, is found within the refractory metals. A summary of its material properties and the most important benefits and disadvantages for using tungsten are given in table 1.3 and table 1.6, respectively. In contrast to carbon and beryllium, tungsten is a high Z-material (Z=74), therefore, the amount of plasma contamination has to be strongly limited. Fortunately, tungsten has a very low erosion yield due to the high difference in mass between tungsten and the other possible projectile atoms from the fuel, ashes, or other plasma impurities. Also, there is a high physical sputtering threshold and tungsten is not prone to chemical sputtering.

Many of the thermal and mechanical properties of tungsten are also

advantageous for fusion applications. Tungsten has the highest melting point of any metal at 3695 K. It also has a high thermal conductivity, which does not deteriorate after neutron irradiation at high temperatures, a low coefficient of thermal expansion, and a low vapour pressure. Furthermore, tungsten is characterized by high hardness values, high mechanical strength, and a high Young's modulus.

The tritium retention of tungsten is low, due to a low solubility for hydrogen isotopes and co-deposition layers of tungsten and tritium are not expected to occur. The hydrogen, including tritium, that is trapped within tungsten, can also be released easily by increasing the temperature. Due to these properties, the limit on tritium inventory can be adhered to much more easily for tungsten than for other materials.

Tungsten however has a few important shortcomings. Unless it is shaped in a very thin foil or wire, tungsten shows brittle behaviour at room temperature. Tungsten used in PFCs, will only begin to behave ductile at higher temperatures. This DBTT depends on microstructure, impurities, fabrication method, sample history, and the size and shape of the specific material and can vary for tungsten between 100 °C to 600 °C. This brittle behaviour at lower temperatures complicates the machinability and production of tungsten components. In addition, the thermal shock behaviour is better for ductile than for brittle materials. Accordingly, the DBTT sets a lower limit for the operational temperature of the PFCs.

The recrystallization temperature of tungsten is relatively low. Depending on the material grade, tungsten can already be fully recrystallized after a heat treatment at 1000 °C to 1200 °C for one hour. Since the microstructure of the selected tungsten grade is vital to the material performance, the recrystallization temperature acts as an upper limit of the operating temperature.

The activation of tungsten under neutron irradiation is high. Rhenium and osmium are the main transmutation products of tungsten. But the impurities which are present in industrial tungsten products, form an additional source of activation, which can deteriorate the properties of tungsten in the long term. As a result, the radioactive waste from tungsten components is not negligible. Furthermore, tungsten is subjected to property degradation after neutron irradiation.

1.4.3 Plasma Facing Components (PFCs)

The PFMs will be joined with structural materials and cooling tubes to form the PFCs. In early devices, the wall of the vacuum vessel was the only material that had direct contact with the plasma. When the generated plasmas reached higher energies, a dedicated first wall was necessary to protect the vacuum vessel. To improve confinement and lifetime, it became clear that it would be useful to have a sacrificial structure.

Such a structure would take up a larger part of the energy and/or particle

flux, thereby protecting the first wall or the vacuum vessel. Two types have been developed. Originally there was a *limiter*, or a protruding component that forces the plasma to stay away from the wall. Later-on, in larger tokamak devices the magnetic field was used to modify the plasma shape so particles, including the helium ash and ionized impurities, could be diverted to a dedicated component, the *divertor*, where they are pumped out. For ITER, DEMO, and future fusion power plants, a divertor and first wall are necessary. Under the current knowledge, it would not be possible to achieve the required confinement, density, and purity with a limiter.

The **First Wall** or *blanket* is the PFC that directly covers the main chamber of the vacuum vessel and has the largest surface of all the PFCs. The magnetic configuration, i.e. with magnetic field lines parallel to the first wall panels, deflects most, but not all of the particles, so they would not collide with the first wall panels, but are directed towards the divertor. However, the radiation and neutron flux are not influenced by the magnetic fields, so the first wall needs to withstand these exposures. Because the components behind the blanket, e.g. superconducting magnets, are sensitive to neutrons and can not withstand high heat loads, the first wall panels need to provide thermal and neutron shielding.

For larger reactors, this thermal shielding can only be achieved with an active cooling system. In fusion power plants, the cooling fluid would be sent through a heat exchanger and the thermal energy can be converted into electric energy. The high-energy neutrons need to be stopped in the blanket and their energy will be converted in heat to contribute to the production of electric energy.

There is an additional function that the blanket needs to fulfil. It is an essential requirement for the DT-reaction, Eq. (1.1), that both reactants, i.e. deuterium and tritium, be present in the plasma. There are no serious obstacles to secure the necessary deuterium supply. This is not the case for tritium, whose natural abundance on earth is $\sim 10^{-18}$ [58] but can be produced from lithium-6, Eq. (1.6), in an exothermic reaction and from lithium-7, Eq. (1.7), in an endothermic reaction.

$$^{6}\mathrm{Li} + \mathrm{n} \longrightarrow {}^{4}\mathrm{He} + \mathrm{T} + 4.8\,\mathrm{MeV} \tag{1.6}$$

$$^{7}\mathrm{Li} + \mathrm{n} + 2.5\,\mathrm{MeV} \longrightarrow {}^{4}\mathrm{He} + \mathrm{T} + \mathrm{n} \tag{1.7}$$

Therefore, the first wall of fusion power plants will contain breeder modules to thermalize the neutrons and produce tritium. They will provide the majority of tritium that is consumed by the reactor. This breeding technology will be tested and validated for the first time in ITER, so DEMO and other reactors will be able to produce their own tritium supply.

The ITER blanket, which is depicted as the yellow components in the ITER overview shown in figure 1.8, will use beryllium as PFM due to the relatively low heat fluxes. The beryllium tiles will be joined to a heat sink made from CuCrZr (copper-chrome-zirconium), which is cooled with

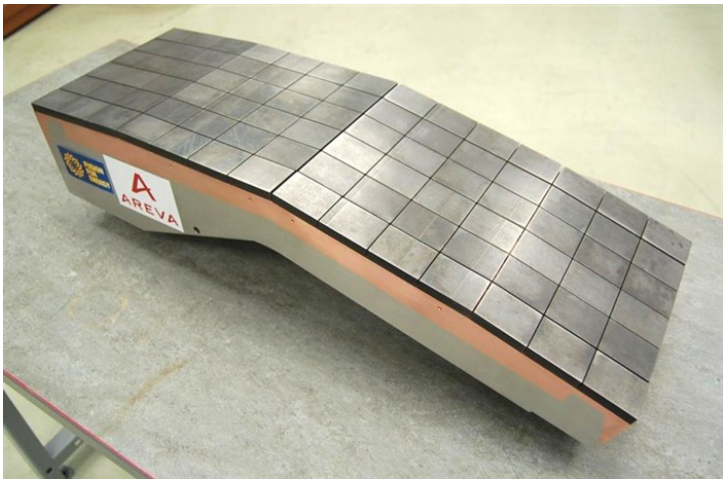

Figure 1.15: A semi-prototype of the ITER first wall blanket, containing beryllium to face the plasma, CuCrZr as heat sink and stainless steel as structural material [59].

pressurized water. A stainless steel support structure is used to preserve the integrity of the module and to connect it to the vacuum vessel.

There will be 440 blanket modules installed in ITER. Figure 1.15 shows a semi-protoype of such module, which is build at a scale of $^1/_6$ from the designed component [59]. Since not every position of the first wall will be exposed to the same heat flux, two different types of modules are planned. There will be 234 *normal* first wall panels, which should be able to withstand a heat flux of up to $2\,\mathrm{MW\,m^{-2}}$. For the 216 other modules, the *enhanced* first wall panels, the design allows a heat flux of up to $5\,\mathrm{MW\,m^{-2}}$. These special modules have an improved heat transport due to the use of a hypervapotron, instead of a standard cooling tube [36].

In order to spare the first wall, the majority of the particle fluxes and heat fluxes are redirected to the **divertor**. This is done by modifying the magnetic field topology so that the last closed flux surface (LCFS), also called the *Separatrix*, intersects and strikes the divertor. The intersection, depicted in figure 1.16, is called the X-point. This modification has no detrimental effect on the confinement, but it alters the way particles behave after they escape from the plasma core. As a consequence, the confinement can actually be improved.

A charged particle will move on a magnetic flux surface. When this flux surface is no longer closed, the particle can leave the plasma core. Since the magnetic field lines lead to the divertor region, the particle will follow them and strike on the divertor target plates. A *private plasma* is formed in the divertor. This private plasma, which is located in the private flux

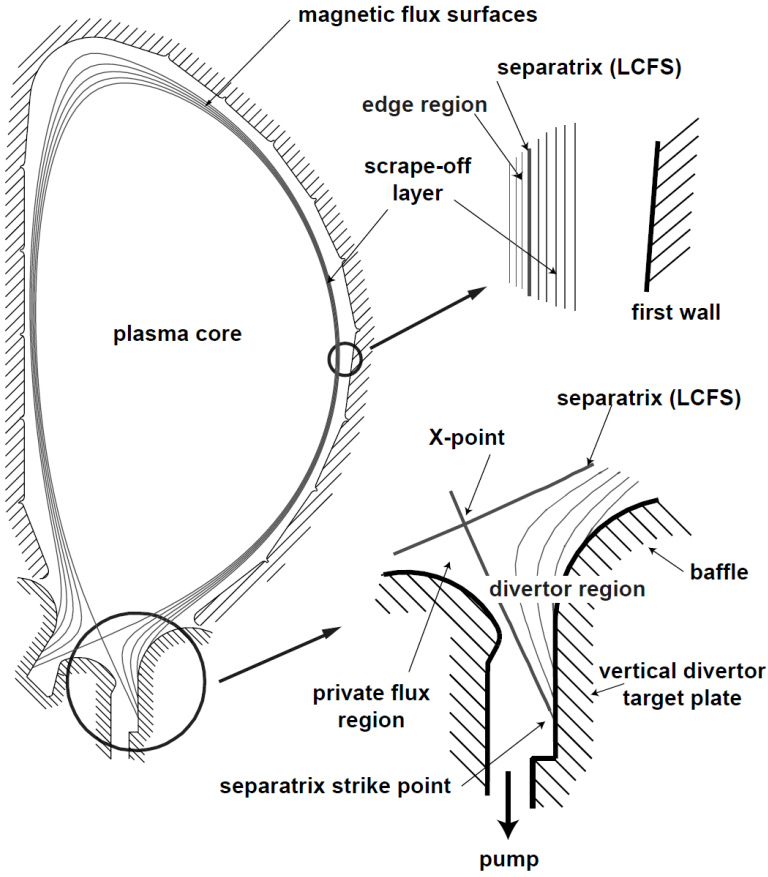

Figure 1.16: An overview of the divertor, showing the underlying principles and illustrating the X-point, the separatrix or LCFS, the strike points, and the private flux region [17].

region, is characterized by a high density and a low temperature. This is in contrast to the plasma core, which is a plasma with a low density and a high temperature.

There are many advantages to such a system, even if it concentrates the majority of the particle irradiation and a part of the energy deposition on a limited surface. There are no longer components in direct contact with the plasma core, as was the case for the limiter. As a result, the amount of impurities that penetrate the plasma is strongly reduced. Furthermore, the particles in the divertor region can easily be pumped away, since they do not form a hot and reactive plasma, and as such the divertor functions as an exhaust-system of the tokamak.

The pumping will maintain the vacuum conditions, remove the impurities and helium ash, and makes it possible to recycle the fuel. This is necessary because the vacuum should not deteriorate and the impurities should not accumulate. Also, the helium produced by the DT-reaction, Eq. (1.1), needs to be removed, otherwise, the fuel dilution in the plasma core could become so high that the reaction will slow down or even stop. Naturally, besides the impurities and the ash, also the fuel will be pumped out. Because only a small fraction of the tritium will undergo a fusion reaction, less than 1 % for ITER, not recycling the fuel would result in immense requirements for tritium breeding. Therefore, the tritium that is pumped out during operation will be recycled to be re-used as fuel [60, 61].

The ITER divertor consists of 54 cassettes of which a set of three are illustrated in figure 1.17. Each cassette extends over $6°40'$. The support structure, or cassette body, is made from stainless steel and has cooling tubes embedded. Three distinct parts are mounted on the cassette body, the inner vertical target, the dome, and the outer vertical target.

These three parts have a steel support structure of their own and connect the water tubes of the cooling system from the cassette body to the heat sink, which is made from CuCrZr. Segments of tungsten monoblocks, as shown in figure 1.18, are used to form the plasma facing layer. The initial ITER design also contained CFC as a PFM for parts of the divertor, but that has been changed and only tungsten will be used as the PFM of the divertor [36, 57].

1.5 Scope of the Work

Fusion reactors rely on basic physical principles, but building them requires more scientific and technological knowledge and progress than was originally thought decades ago. Much of this progress has already been achieved and tokamaks like JET have shown that fusion power is within our grasp. Nevertheless, for a successful construction and operation of ITER or future fusion reactors and power plants there are still challenges that need to be tackled. These can be found in multiple domains, such as plasma physics,

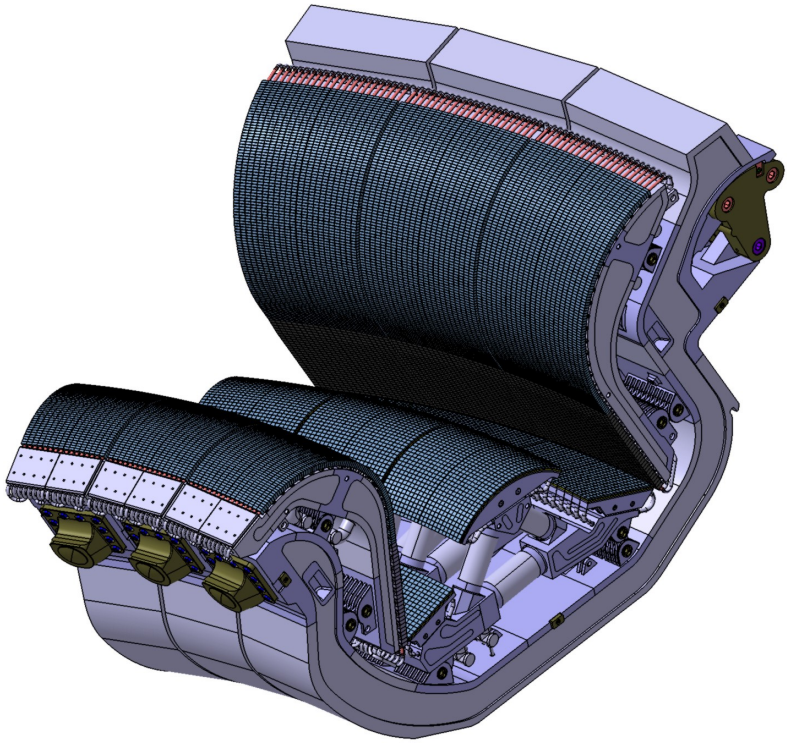

Figure 1.17: A schematic of three ITER divertor cassettes, manufactured from a stainless steel support structure, a heat sink in CuCrZr, and a top layer of tungsten as the PFM [20].

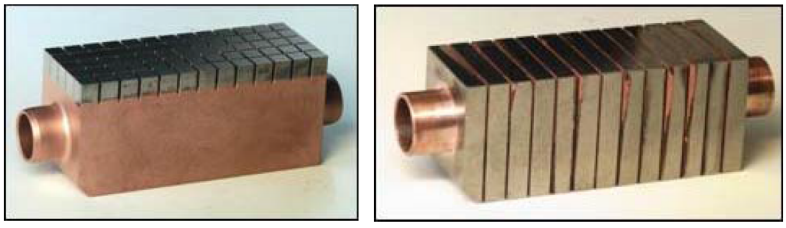

Figure 1.18: An example of two mock-up designs with tungsten as PFM, with either a flat tile (macrobrush) concept (left) where the PFM is joined on top of the heat sink, or the monoblock concept (right), where the heat sink and the cooling tube are integrated in the PFM [62].

superconducting technology, computational modelling, etc.

One of the remaining challenges is related to the design and choice of material for PFCs. The ITER design has been determined based on the current knowledge, although some questions still remain. Under some loading conditions, the amount and type of damage that has to be expected is well known, but this is not completely clear for every possible loading condition, nor for combinations of exposure conditions. Furthermore, if a new and currently unforeseen scenario will be tested during ITER operation, this also might have consequences for the PFCs. At a certain point, designs for DEMO or a fusion power plant will become more concrete. There will be substantial differences in the loading conditions for ITER and the next generation of fusion reactors. Some of them are beneficial for the PFMs, e.g. a stable steady state operational scenario, while others are very detrimental, e.g. higher neutron flux.

These examples show that a profound knowledge of the plasma facing materials and their reactions to the loading conditions is essential. This requires a fundamental understanding of the connection between physical properties and the performance under different exposure conditions. More specifically, this also requires an understanding of the interaction between the heat loads, the particle fluxes, and the neutron irradiation. Only then is it possible to determine if certain operating scenarios need to be avoided, the extent to which mitigation, e.g. from ELMs, is necessary, and the exact damage that will occur.

Any material located in a fusion reactor will be exposed to a combination of a SSHF and transient heat loads, both of which come from electromagnetic radiation, particle fluxes, and neutron irradiation. In addition, there are additional effects from the neutron and particle fluxes besides the heat loading. There will constantly be a combination of these loading conditions present and the damage resulting from one exposure might influence the damage behaviour from another.

All work was done with a single material, tungsten, which is one of the few materials that has been retained as a PFM. It will be used in ITER and there is a profound chance that DEMO and other future fusion reactors will select it as well. The focus here was on a single double forged tungsten grade with elongated grains, procured from the Austrian company Plansee, from charge #0090519648. Additionally, one experimental campaign was also performed with a tungsten monoblock mock-up, W-MMU-12-16, also produced by Plansee.

Of the different exposure conditions, two were selected and combined for an extensive analysis. The first loading conditions are the pure thermal ELM-like transient loads that are part of the normal operation. Their energy deposition is simulated by the electron-beam facility JUDITH 1 in Forschungszentrum Jülich, Germany. In addition, the second set of loading conditions are the steady-state particle fluxes of hydrogen isotopes and helium, which contain a corresponding SSHF. These can be applied on test

samples in the neutral beam facility GLADIS in the Max-Planck-Institut für Plasmaphysik, Germany. For one experimental campaign, the electron-beam facility JUDITH 2 in Forschungszentrum Jülich, Germany, is used for a simultaneous exposure of SSHF and ELM-like transient heat loads.

These exposure conditions are selected for several reasons. First of all, it is possible that the damage behaviour of both ELMs and steady state hydrogen/helium fluxes might influence each other. For example, ELMs can result in material cracking, with cracks running parallel to the surface. These will act as a heat barrier which reduces the heat transport and could result, locally, in increased surface temperatures. Because the damage mechanism of particle fluxes is strongly dependent upon the surface temperature, ELMs might affect the damage coming from the particle flux. It is important, not only for ITER, but also for future devices, to identify if this potential scenario also occurs and to what extent.

Moreover, both exposure conditions and their damage mechanisms have been extensively examined on their own in Forschungszentrum Jülich and the Max-Planck-Institut für Plasmaphysik. Without the knowledge gathered by this previous research, it would not be feasible to examine or understand the potential synergistic effects of combined loading. This also means that the necessary know-how and devices are available to tackle questions regarding these loading conditions.

In contrast to the environment of fusion reactors, this work will combine the particle flux and the transient heat loads consecutively instead of simultaneously. This is necessary due to the set-up of the experimental facilities, but also has a benefit of its own. Hereby the influence of ELM-like loads on the damage resulting from particle irradiation and the effect of the particle flux on the ELM-damage mechanism, can be studied separately.

Chapter 2

Experimental Methods

2.1 Sample Preparation and Analysis

2.1.1 Tungsten Fabrication

Tungsten is currently the preferred candidate for PFM, although there are drawbacks to using this material, as discussed in 1.4.2. These drawbacks are noticeable during component manufacturing and tokamak operation. Furthermore, there is a wide range of tungsten grades, which differ in chemical composition, microstructure, and fabrication method. Understanding the differences between the grades and selecting the most appropriate material grade is therefore crucial.

Through chemical processes, tungsten powder is extracted from ores which contain tungsten compounds. Casting tungsten ingots that could be processed further, is not a feasible method, especially not on a industrial scale. The high melting temperature of tungsten is primarily responsible for this, as it requires temperatures that are too high for most moulds. Instead, different powder metallurgy methods are used to first densify the powder, or green body, and subsequently transform it into a solid. These methods, e.g. hot pressing, cold isostatic pressing, hot isostatic pressing, and sintering, can be used to make a final or a semi-finished material. In order to obtain the desired microstructure and material geometry, the production process is often concluded with steps such as forging, rolling, swaging, hammering, annealing, cutting, and grinding.

An alternative manufacturing route is the deposition of a tungsten layer on a substrate of up to a few millimetres in thickness. Several of these techniques, e.g. Vacuum Plasma Spraying (VPS) or Chemical Vapor Deposition (CVD), are available to deposit tungsten on the required industrial scale. However, the thermomechanical properties of these tungsten coatings are degraded with respect to bulk tungsten materials, among others due to a high porosity or bad attachment between the substrate and the deposi-

tion layer. This makes deposition methods not suitable for each situation, however a potential use for these techniques could be the repair of damaged surface layers of bulk tungsten as opposed to producing the armour on PFCs [63].

All production methods start with a tungsten powder, whose properties influence the bulk material. There are variations in purity, the size distribution of the powder particles, and the grain sizes of the crystallites in each powder particle. Alloying materials can also be added to the tungsten powder to adjust the material properties and improve them for specific applications, for example, tungsten containing rhenium has a remarkably lower DBTT than pure tungsten. Moreover, it is easier to weld and produce these rhenium-alloyed material grades [64]. An alternative alloying element is yttrium, which inhibits grain growth and strengthens the grain boundaries. A similar effect can be achieved by using lanthanum instead of yttrium. The addition of these elements, or their oxides, results in a dispersion-strengthened alloy which increases the recrystallization temperature [64, 65].

The microstructure of tungsten is determined by the properties of the tungsten powder, the metallurgy techniques used during fabrication, and the finishing steps. Several material properties are influenced by the microstructure of the material. One way this can happen is by the different grain sizes in a sample. Another way is by the shape and orientation of the grains. Grains can be preferentially elongated in one direction or be more isotropic. In cases where the grain shape is anisotropic, the material properties are anisotropic as well. Therefore, the direction in which the samples are cut, will influence the performance of the material.

2.1.2 Test Specimens

A single tungsten grade was used for this research. This material, manufactured by the Austrian *Plansee SE*, was double forged tungsten. Several of these double forged tungsten disks, shown in figure 2.1, are available in Forschungszentrum Jülich. They were all produced in the same batch, charge #0090519648.

Each disk was manufactured in a five-step procedure. Through cold isostatic pressing, the tungsten powder was first compressed into a dense cylindrical compact. Thereafter, the material was sintered at a temperature between 2000 °C and 2500 °C. The first forging process was then performed in the radial direction, until a 1.7 deformation ratio was reached. The intermediate product was a tungsten rod with a radius of ~ 40 mm, that was cut at a length of ~ 140 mm. Thereafter the material was forged along the axial direction until a 1.75 deformation ratio was obtained. The resulting tungsten disk had a radius of ~ 70 mm and a height of ~ 45 mm. As a final step, the material received a stress-relieving heat treatment at 1000 °C. Due to the tungsten powder used and the contamination during manufacturing,

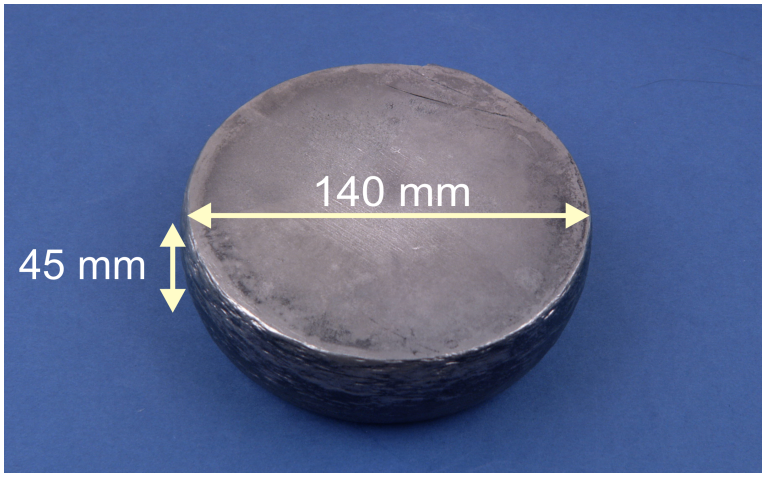

Figure 2.1: An example of a double forged tungsten disk produced by *Plansee SE*.

the finished disks have according the manufacturer a purity of 99.97 wt% tungsten.

Every test specimen was cut from the same disk through electric discharge machining (EDM). In this way, if there is any variation between two disks, e.g. impurity content, this would not be reflected in the test samples. To minimize the influence of variation of the microstructure within the disk, the specimens do not originate from the outer edge of the tungsten disk. The disk from which the test specimens were cut has previously undergone extensive characterisation [66, 67]. Both from this data and from additional analyses performed on the test specimens, it is known that the double forged tungsten is anisotropic. The average aspect ratio from the grains is 0.44 and the average circularity is 0.51. Due to deformation in the two forging steps, the grains have a 'pancake'-like shape, with the elongation of each grain parallel to the top surface of the disk.

Depending on the way that a sample was cut, two main orientations of the grain shape could be obtained, as is schematically depicted in figure 2.2. Such orientation of the grain shape is called the 'grain orientation' and is not related with the crystal orientation of the grain. When the elongation of the pancake-like grains is oriented parallel to the loaded top surface of the test specimen, the grain orientation is called *longitudinal*. Alternatively, the grain orientation is called *transversal* in the case that the elongation of the grains is oriented perpendicular to the loaded top surface of the test specimens.

During this research, the focus was put on a single grain orientation. Therefore, test specimens with a longitudinal grain orientation were cut from the double forged tungsten disk in three different sizes. Each sample

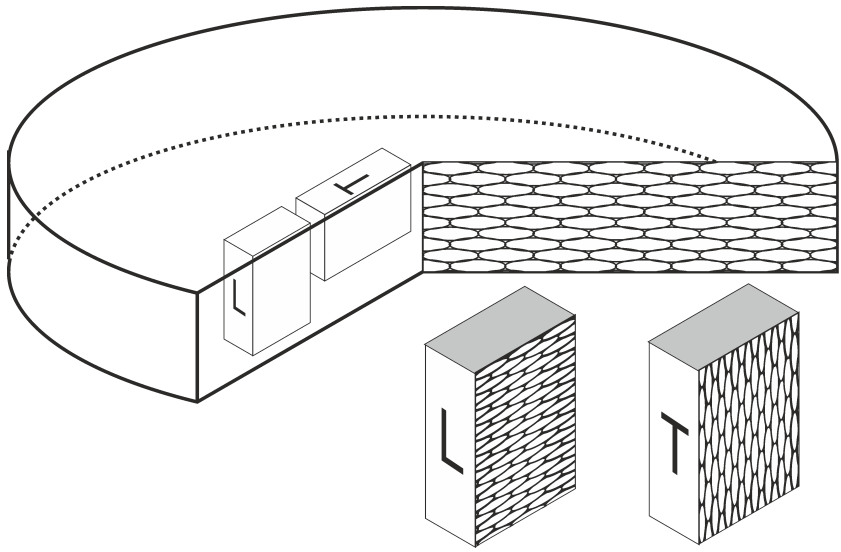

Figure 2.2: A schematic overview of the tungsten disk which shows (not to scale) the microstructure of the tungsten disk and the orientation of the samples while cutting. As a result of this cutting scheme, samples have a longitudinal (L) or transversal (T) grain orientation, depending on the orientation of the grains with respect to the top surface of the sample, indicated in grey.

had a rectangular surface of 5 mm × 10 mm, but varied in height between 5 mm, 10 mm, and 15 mm.

2.1.3 Sample Preparation

After cutting, the samples had to be prepared by removing surface damage, such as the thermally induced defects from the EDM. This sample preparation consisted of wet grinding with abrasive SiC paper rotating on a SAPHIR polisher and grinder device from *ATM GmbH*. On each surface of the test specimens, this was done step-by-step with increasingly finer abrasive paper, going up to P800 for the top surface. The sides of the samples were then marked with an *Arkograf* electric arc engraver pen, to enable sample identification.

In addition, the top surface that would be exposed during the experiments, was polished to a mirror-like finish in order to have a well-defined reference state. Diamond paste, with a maximum particle size of 6 µm was distributed on a hard polishing disk, which was mounted on a polishing device, such as the mentioned SAPHIR. As a lubricant, a water-based polishing liquid was used. This process was repeated with a 3 µm diamond paste, until all grooves from the previous polishing step had disappeared.

Thereafter, the top surface was further polished with a soft polishing cloth made from cotton, instead of a hard polishing disk. This was first done with 3 µm paste, until the scratches from the previous polishing step were removed. After that, this step was repeated with 1 µm diamond paste. At last, a *fine polishing* step was made to remove the last visible scratches. For this step, the diamond paste was substituted by an alkaline polishing suspension and no additional lubricant was used.

2.1.4 Analysis Methods

To properly characterize all samples, after preparation and post-mortem, several complementary analysis methods were used. The surface morphology was characterized with laser profilometry. In Forschungszentrum Jülich two profilometers were used that measured the distance between the sensor and the surface by the reflection of a confocal laser beam.

The first profilometer was delivered by *UBM Messtechnik GmbH* and has a maximum lateral resolution of 2000 points/mm. With an accuracy of 0.01 µm, the height difference from a reference point can be measured up to ± 500 µm. During one scan, a surface of up to 5 cm by 5 cm can be scanned. The software *UBSoft1.9* is used to control the device and to analyze the scanned surfaces, mainly by calculating the arithmetic mean roughness R_a, according the ISO4287/1 standard. This roughness parameter has also been used in previous experiments at Forschungszentrum Jülich, which makes it possible to quantitatively compare results. The R_a is the average over the absolute values of the difference in height between each measurement point

of the surface, i.e. z_i, and the average height of the surface, i.e. $\bar{z}$, as shown by equation (2.1).

$$R_a = \frac{1}{n} \sum_{i=1}^{n} |z_i - \bar{z}| \tag{2.1}$$

A profilometer from *OPM Messtechnik GmbH* was used in a later phase because of its increased scanning speed. All the other specifications, such as resolution and accuracy, were identical. The software package *Inspector* is used to operate this profilometer and to calculate the roughness parameter R_a, in the same way as was previously done by *UBSoft1.9*.

Polished samples have typically a R_a of 0.05–0.12 µm [68]. Besides a variation between two polished samples, a comparison of different equally sized areas on a single sample shows that the maximal difference in R_a is in the range of 0.03–0.06 µm. Therefore, a threshold value is used in the comparison between several samples to determine if a noteworthy roughness increase has taken place. Only R_a differences of at least 0.09 µm are considered a meaningful difference.

Light microscopy (LM) was used to capture overview pictures of the damaged surfaces. In addition, LM can be used to characterize metallographic cross sections and visualize the microstructure, porosities, crack depth, and crack propagation. These cross sections were made by cutting the samples near the area of interest for the cross section with a diamond-covered blade saw. The required part of the test specimen was then embedded in a cold resin.

Thereafter, the same polishing method was used as during the sample preparation, described in subsection 2.1.3. The amount of material that was ground away during this step has to be sufficiently large to remove any damage induced by the cutting and to arrive at the location of interest. LM images were made after polishing and etching of the cross sections with a water based HNO_3/HF solution, containing 25 vol% HNO_3 and 5 vol% HF. Due to the etching, transgranular and intergranular crack propagating can be visualized.

Besides LM, other microscopy techniques were consequently used. Scanning Electron Microscopy (SEM) images was used in two different modes, where either the secondary electrons (SE) or the backscattered electrons (BSE) were detected. While the SE images are especially suited for visualising the topographical characteristics of the surface, BSE images reflect the contrast provided by the atomic number and thereby take into account the chemical composition. Electron backscatter diffraction (EBSD) was used to obtain the crystal orientation and microstructure. In addition, Focussed Ion Beam (FIB) was used in combination with SEM and Transmission Electron Microscopy (TEM) to create high-magnification images of the near-surface layer.

2.2 Neutral Beam Facility GLADIS

As discussed in section 1.3, PFMs will be exposed to a combination of heat and particle loads. The Max-Planck-Institut für Plasmaphysik - Garching constructed a neutral beam high heat flux facility, which provides a homogeneous heating of the test material. In this *GLADIS*-facility or Garching large divertor sample test facility, both smaller samples and complete mock-ups can be tested with a steady state heat and particle flux.

GLADIS, shown in figure 2.3, is composed of two individually controllable neutral beam injection (NI) systems installed on a water-cooled test chamber. Each NI system was part of the radial neutral beam injection used at the Wendelstein 7-AS stellarator [69], but were modified to enable long pulse operation of up to 45 s. These gas discharge ion sources use a radiofrequency induced plasma rather than electrodes. The water-cooled RF copper coil is wound around an alumina ceramic cylinder. An actively cooled Faraday shield is installed, which reduces the thermal stresses in the ceramic cylinder [70, 71].

Water cooled triode grids, which were part of the long pulse injection system from the former ASDEX tokamak [72], are used to extract the particles.

For each NI system, this gives an expected current of between 5 A and 22 A, while the acceleration voltage can be set from 20 kV to 55 kV. Because both neutral beams can be used simultaneously, GLADIS can perform HHF experiments with a maximal power of the combined beams of up to 2.2 MW [71]. Due to the relatively high gas pressure, up to 5×10^{-2} Pa, in the tube connection to the NI system with the test chamber, after acceleration most ions are again neutralized. Although this is not measured during the experiments, less than 1 % of the particles should still be ionized [73]. No additional neutralisers or ion removal systems are installed.

Depending on the acceleration voltage selected, the operational charac-

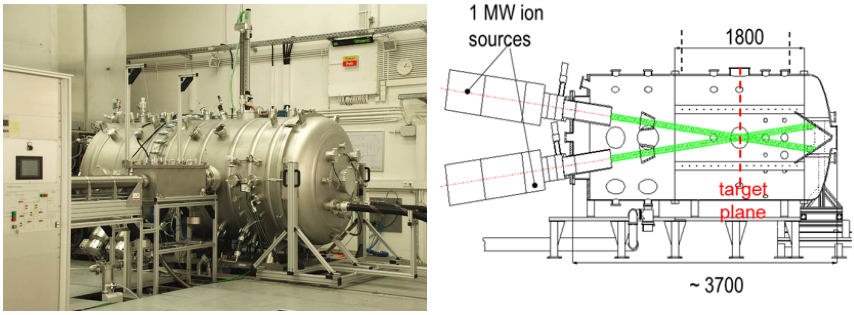

Figure 2.3: A photograph of GLADIS installed at IPP Garching (left) and a schematic overview of the neutral beam facility (right).

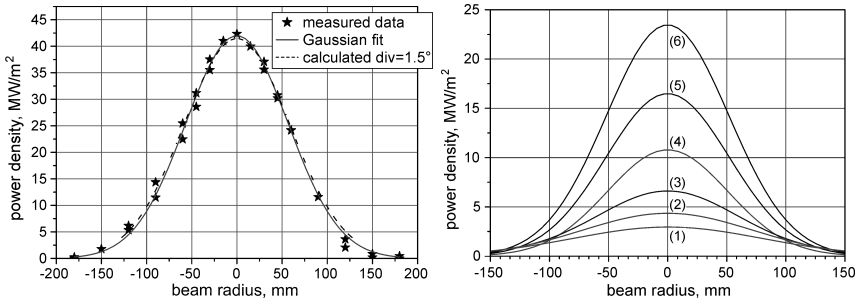

Figure 2.4: The power density distribution of an 876 kW beam is measured by an inertially cooled calorimeter and fitted to a Gaussian function (left). Such fits are done for a range of beam powers (130 kW, 155 kW, 182 kW, 252 kW, 353 kW, and 560 kW for power distributions 1 through 6, right) [71].

teristics of the beam will vary. This requires a measurement of the power density distribution of the beam, which is fitted to a Gaussian function, as shown in figure 2.4. An inertially cooled calorimeter is used in combination with several thermocouples to measure the temperature rise and deduce the beam profile [71].

For fusion relevant experiments in GLADIS, pure hydrogen gas, pure helium gas or a hydrogen/helium gas mixture is used [32, 74]. Deuterium and tritium are not used due to safety regulations, despite being the fuel of the fusion reaction. In the case of experiments conducted with a mixed hydrogen/helium beam, the ratio of hydrogen to helium atoms inside the seeding gas differs from the ratio inside the beam. Hence, the beam composition needs to be verified, which is done by comparing the extraction currents of several operational scenarios [32, 75].

It must be taken into account that the ion source will produce mainly protons, i.e. H^+, from the hydrogen gas, but two molecular ions, H_2^+ and H_3^+, are also formed. This results in an energy distribution where only a part of the hydrogen in the neutral beam is at full energy, while the rest is either at half or one-third of the full energy per atom. The exact distribution depends on the current and the extraction voltage. This is not the case for the helium gas, as only He^+ is formed.

The vacuum vessel is made from two cylindrical sections. All the equipment that is required for operation, e.g. pumping ports, diagnostic ports, or beam scraper, is installed in the first section. The second section is the target chamber, which contains windows for visual inspection, a sample support system, and a sample exchange port. It has ample space for exposures on 2 m long mock-ups. The facility is closed by a mobile end-door, which also functions as a beam dump. The vacuum vessel is connected to six turbo-molecular pump systems, which together deliver a volumetric flow rate of $12\,m^3\,s^{-1}$. During a neutral beam exposure, the maximum hydro-

gen pressure is 0.1 Pa in the target chamber. GLADIS is equipped with active cooling for components and test specimens, which is performed with a maximal water pressure of 2.5 MPa. A flow rate up to 8500 $cm^3 s^{-1}$ can be achieved within this system.

Several diagnostics are installed in GLADIS to measure the thermal response of the test object. The temperature distributions can be measured through a combination of the 40 thermocouples, the infra-red camera system, and the installed pyrometers. *InfraTec*'s infra-red camera system, the *VarioCAM HD* is used to give the real-time temperature distribution of the whole component. Point measurements of the temporal temperature distribution can be obtained through two infra-red pyrometers in a temperature range of 300–3500 °C.

Calorimetry is used to quantify the total or the local absorbed power density. This is done by using flow meters and platinum-based resistance temperature detectors. In addition a movable calorimeter is placed within the test chamber. During a single test campaign, this can be positioned in the beam path to measure the beam profile, as is shown in figure 2.4. Other diagnostics installed in GLADIS include strain gauges and a mass spectrometer. Furthermore, a digital camera is used for the visual inspection of the test object [70].

2.3 Electron Beam Facilities

2.3.1 JUDITH 1

In order to have an exposure on the armour materials that is limited to the relevant heat loads, an electron beam facility can be used. The Hot Materials Laboratory of Forschungszentrum Jülich, has the Jülich divertor test facility in hot cells, *JUDITH 1*, that is used as a HHF facility. Because this device is located in a hot cell, it is capable of handling activated material, e.g. after neutron irradiation, and toxic material, such as beryllium.

JUDITH 1, shown in figure 2.5, is made from a modified electron beam gun, which is installed at the top of a stainless steel vacuum chamber. The 60 kW electron gun uses the free electrons emitted by a tungsten filament, which are then accelerated by an electrostatic field. An acceleration voltage of up to 150 kV can be used. However, at the highest acceleration voltages, the electron beam power is not stable. For that reason, the acceleration voltage is limited to 120 kV, resulting in a maximal power of 48 kW. Under these conditions, 95 % of the absorbed electron beam power will be deposited within a 7 µm deep tungsten layer.

Magnetic coils focus the beam, resulting in a full width at half maximum (FWHM) diameter of 1 mm. To have a homogeneously exposed area on the tested material, the beam scans a part of the surface in a triangular mode, as shown in figure 2.6. This means the beam deflection system sweeps

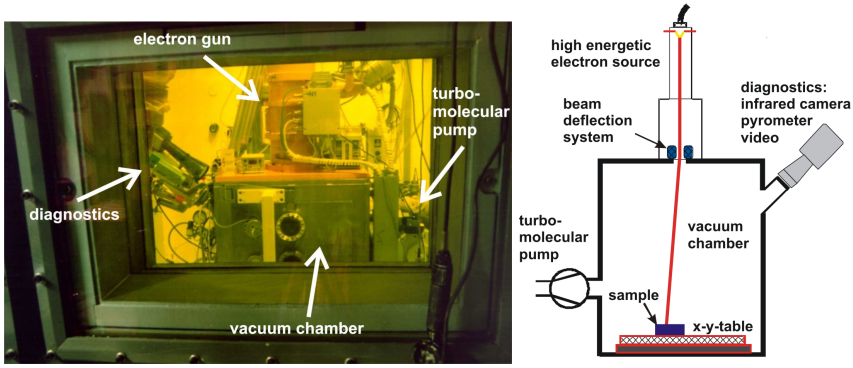

Figure 2.5: A photograph of JUDITH 1 installed in a hot cell at Forschungszentrum Jülich (left) and a schematic view of the electron beam facility (right).

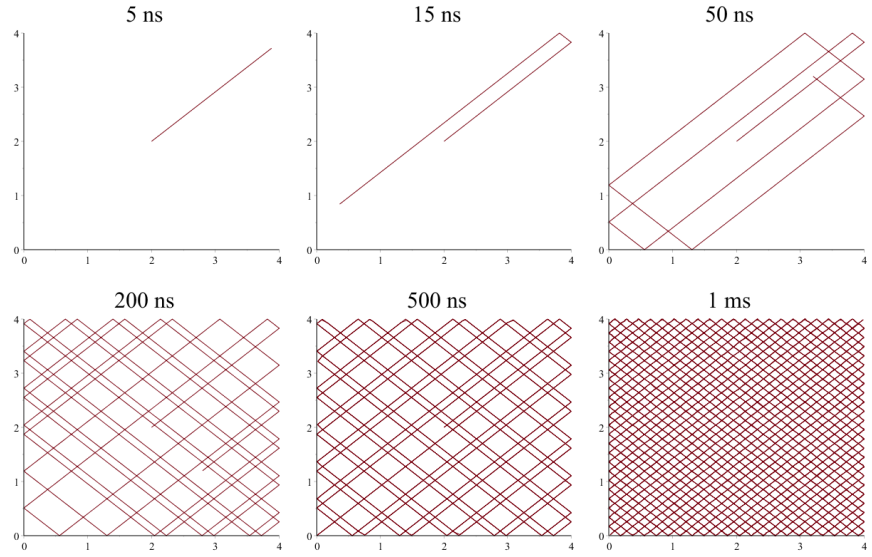

Figure 2.6: The electron beam in JUDITH 1 scans the loaded area in a triangular mode. The beam path is visualized for a 4 mm × 4 mm loaded area with a frequency for the x- and y-direction of 47 kHz and 43 kHz, respectively after 5 ns, 15 ns, 50 ns, 200 ns, 500 ns, and 1000 ns.

the beam spot both in the x- and in y-direction in a triangular wave with frequencies up to 100 kHz. During experiments the sweep frequency for the x- and y-direction was 47 kHz and 43 kHz, respectively, resulting in a uniformly loaded area. The loaded area is furthermore determined by the maximal beam deflection on the target, which is ± 50 mm.

Before operation of JUDITH 1, a vacuum of 10^{-3} Pa and 10^{-2} Pa is obtained with a turbo-molecular vacuum pump system in the beam generating system and the test chamber, respectively. The flow rate of the vacuum pump is $2.2\,\mathrm{m^3\,s^{-1}}$. If necessary, e.g. when testing neutron irradiated beryllium, the pump system can operate in conjunction with a tritium trap in order to adhere to the radiation limits.

Furthermore, a slide valve can separate the vacuum chamber from the electron beam unit, in order to exchange test specimens without ventilating the whole facility. The chamber itself has a height of 0.9 m, a width of 0.8 m, and a length of 0.6 m, while the stainless steel walls are 25 mm thick. The samples can be placed in the facility, either manually or with remote handling equipment, through a 66 cm × 66 cm door.

Inside the vacuum chamber the test objects can be connected with the cooling circuit's water. This connection is made with flexible pressure hoses and delivers water at room temperature. Both before entering and after leaving the actively cooled component, the temperature, flow rate, and pressure are measured. There is a linear relation between the water pressure and flow rate with a maximal water pressure of 4 MPa and a related flow rate of $1000\,\mathrm{cm^3\,s^{-1}}$.

The samples, test components, or sample holders are put on an electronic xy-table, which can be operated from the control panel of JDUITH 1. In this way, several samples can be placed inside JUDITH 1 and tested one after another without breaking the vacuum. The height of the xy-table can be adapted, which is necessary to ensure that the sample surface is located in the focal plane of the electron beam. However, this is only possible manually and therefore precludes doing experiments on several samples without opening the vacuum chamber, unless the height is identical for each sample.

A heating system can be installed on the sample table. For reaching temperatures up to 400 °C, a set-up can be used that consists of a sample holder in combination with a tubular heating cartridge. All other experiments at elevated base temperatures, up to 1200 °C, are done with the HTR1003 heater from *tectra GmbH*, shown in figure 2.7. This high temperature pyrolytic boron nitride/pyrolytic graphite (pBN/PG) heater allows for a heating rate up to $100\,\mathrm{K\,s^{-1}}$. In order to prevent the xy-table from being overheated, the heater is located within a heat shielding kit, consisting of two tantalum boxes which are separated from each other through ceramic spacers. In addition, the heat shielding kit is placed on top of a ceramic insulator. Several different graphite sample holders are available based on the geometry of the test specimens. The sample holder serves the dual purpose of preventing the motion of test specimens during experiments

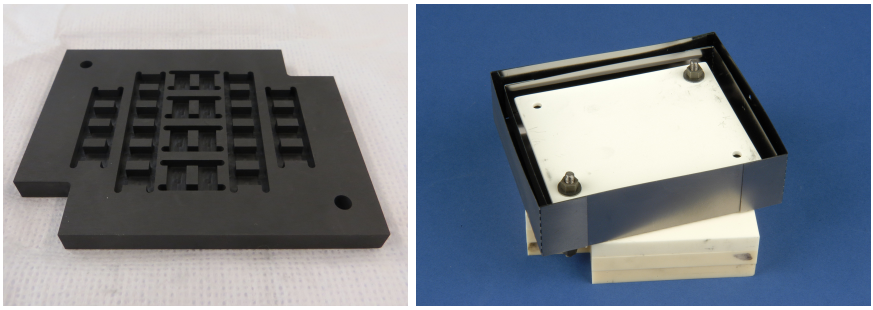

Figure 2.7: JUDITH 1 heating system containing a graphite sample holder (left) and the high temperature heater HTR1003 placed in a heat shielding kit on top of a ceramic insulator (right).

and shielding the heater from the electron beam.

Several diagnostic devices are available in JUDITH 1 to monitor the experiments. The absorbed current can be measured in experiments without active cooling and where no heating system is used. This is possible because the sample holder is grounded and attached through a resistor to a digital oscilloscope. Visual inspection is done with a video and a digital camera. The infra-red camera system, with a cooled detector, can be used for sample temperatures as high as 2000 °C. Calorimetry of the water from the active cooling is done by a chromel/alumel thermocouple.

The temperature of the samples can be detected through four different pyrometers. A single wavelength infra-red pyrometer is used in the temperature range of 200–1000 °C. Two different double-wavelength infra-red pyrometers are used to measure higher temperatures, in the range of 550–1600 °C and 1000–3500 °C. These double-wavelength pyrometers are less sensitive to the temperature depending emissivity of the surface, than the single wavelength pyrometer. Each of these three infra-red pyrometers performs point measurements. In contrast, the fourth pyrometer has a lower lateral resolution and measures the optical emissivity of a surface. This fast pyrometer works in the range 500–2500 °C with a minimum time resolution of 10 µs.

2.3.2 JUDITH 2

A second electron beam facility located in Forschungszentrum Jülich is JUDITH 2. The machine name refers to the older facility JUDITH 1, which stood for Jülich divertor test facility in hot cells. This device is licensed to handle beryllium and is situated in a controlled area, but is not placed inside a hot cell. For that reason, it is not used for testing neutron irradiated or radioactive material.

The design of JUDITH 2, shown in figure 2.8, was intended for con-

ducting high cycle, steady state and transient exposures on relatively large components, e.g. for qualification of a mock-up. For this reason a spacious vacuum chamber was required. This cylindrical main chamber, with a diameter and a length of 0.8 m and 1.8 m, respectively, is closed on the front side by a door that forms a single component with the specimen carrier system. The electron beam gun is located above the main vacuum chamber and is connected with the main chamber through an intermediate vacuum chamber. JUDITH 2 is equipped with a set of diagnostics focussed on temperature measurements and a separate water-based active cooling system for the test components.

The acceleration voltage of the electron beam gun can be set within the range of 40 kV to 60 kV. As a consequence, the electron penetration depth is lower for JUDITH 2 than for JUDITH 1. In this case, 95 % of the electron beam power for tungsten is deposited in a $\sim 5\,\mu m$ deep layer. The electron beam gun has a maximum power of 200 kW. The current of the device is limited to 3.3 A.

In JUDITH 2, the electron beam passes three magnetic lenses. The first two lenses focus the beam, while the third, deflecting, lens guides the beam in the desired direction. Through a control program, it is possible to create a beam path by stipulating for each time-step the beam location on the test object, which corresponds with a change in the parameters of the magnetic lenses. A dwell time of the electron beam spot of between 5 µs and 1 s can

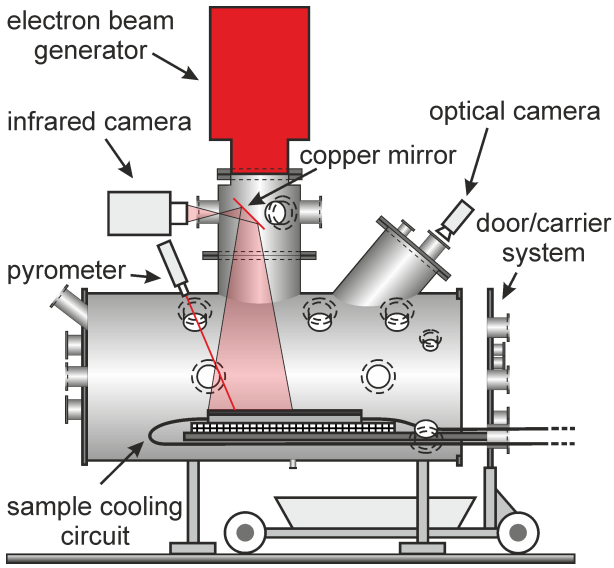

Figure 2.8: A schematic view of the electron beam facility JUDITH 2, located at Forschungszentrum Jülich [68].

be used. The beam profile of JUDITH 2 depends on parameters such as pressure, acceleration voltage, and the settings of the magnetic lenses. This characteristic is used to obtain different heat fluxes and/or sizes of the beam spot depending on the experimental requirements.

Before operation, JUDITH 2 with its three chambers, i.e. the main chamber where the sample lies, the intermediate vacuum chamber, and the upper chamber which contains the electron beam gun, need to be vacuum pumped. This results in pressures of 10^{-2} Pa to 10^{-3} Pa for the main chamber, 10^{-3} Pa to 10^{-4} Pa for the intermediate chamber, and 10^{-4} Pa for the upper chamber. Each vacuum chamber has its own turbomolecular pump system for evacuating. Furthermore, a valve can close the connection between the intermediate chamber and the main chamber in order to preserve the vacuum during sample exchange.

Both the main vacuum chamber and the electron beam gun have their own independent cooling systems. In addition, the samples or mock-ups can be cooled through a third, water-based, cooling circuit. The inlet temperature of this system can be set between room temperature and 100 °C. A flow rate up to $\sim 3300\,\mathrm{cm^3\,s^{-1}}$ is achievable, and the maximal water pressure is 3 MPa.

Similar to JUDITH 1, chromel-alumel thermocouples are used to monitor the water temperature. Moreover, the temperature can be measured through the infra-red camera and pyrometers which are installed on the diagnostic ports. The infra-red camera, from *FLIR Systems*, is used in combination with a copper mirror to protect the camera and operates over a temperature range that can be increased up to 2000 °C. Higher temperatures can only be measured through the fast single-colour pyrometer, measuring from 350 °C to 3500 °C with a time resolution of up to 10 µs, or the high temperature two-colour pyrometer, covering a range of 1000 °C to 3300 °C. Two other two-colour pyrometers have a range of 300 °C to 900 °C and 600 °C to 1600 °C. In addition, JUDITH 2 is equipped with an optical camera.

2.4 Nd:YAG LID Set-up

The hydrogen and helium retention in tungsten can be altered by damage originating from thermal shock experiments, which can result in a modified behaviour of the test material during hydrogen and helium irradiation. At the same time, the behaviour during thermal shock experiments of tungsten which is implanted with hydrogen and helium might be influenced by the hydrogen and helium retention. If thermal desorption spectroscopy (TDS) is used to determine the retention, the whole sample is heated. Because the sample size varies and the hydrogen and helium content has a gradient within a sample, the results obtained by TDS are not directly comparable with each other.

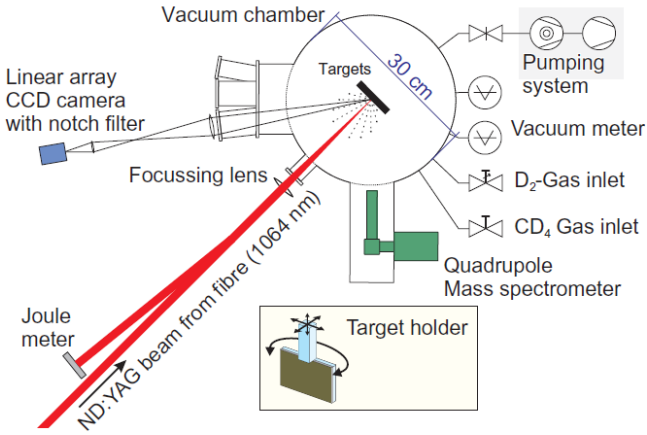

Figure 2.9: A schematic view of the Nd:YAG LID facility, located at Forschungszentrum Jülich [76].

A method which can be used instead of TDS is Laser Induced Desorption (LID) [76], where a laser beam locally heats a small area on the sample surface with a single pulse. The laser parameters are chosen so that the required elements, i.e. hydrogen and helium, are desorbed without the occurrence of melting and/or sublimation of the sample surface [77]. Forschungszentrum Jülich has a laboratory Nd:YAG LID set-up with a mass spectrometer that is able to perform both LID measurements [76] as HHF experiments [65,78].

The facility, shown in figure 2.9, is equipped with a pulsed Nd:YAG laser from *LASAG Industrial-LASER*, which has a wavelength of 1064 nm. The pulses have a duration of 0.1 ms to 20 ms, an average power of 200 W, and is limited to an energy of 60 J per pulse. Transmission between the Nd:YAG laser and the vacuum chamber is done through an optical fibre with a core diameter of 400 µm and a length of 35 m.

The cylindrical vacuum chamber, with a radius of 0.15 m, has a total volume of 0.085 m^3. Inside, a sample holder is mounted with an adjustable incidence angle that can be moved in the xyz-direction. The required vacuum pressure of 10^{-5} Pa is obtained by a turbopump system. Subsequently, the increase of the partial pressure during measurements is determined after closing a gate valve, before the laser shot.

A quadrupole mass spectrometer is used to measure the amount and type of desorbed species. It is installed in an equatorial plane with a 45° tilt to the laser beam. Before each measurement, the mass spectrometer is calibrated and the sensitivity for a specific gas species is determined. This is done by filling the vacuum chamber with a single species, e.g. helium, until a pressure of 10^{-3} Pa is reached. Subsequently, a measurement is performed and then the process is repeated for another gas species.

2.5 Thermal Simulations

During the experiments, both in GLADIS and in the JUDITH-facilities, the temperature is partially monitored through single-colour pyrometers and an infra-red camera. These methods rely on the emissivity of the sample surface, which can be altered during an exposure. In order to validate the measured results and to plan the experiments, thermal simulations are performed using finite element method (FEM) [79].

FEM is a numerical technique to solve partial differential equations. A geometrical model of the test material is produced and divided into several elements through a mesh discretization, as shown in figure 2.10. Through a convergent iterative process, approximations for the equations and imposed boundary conditions are sought at the nodes of the mesh.

ANSYS Workbench 14.0, a software package from the company *ANSYS, Inc.*, was used to perform the FEM calculations. The transient thermal analysis module, which uses the *Mechanical APDL* solver of ANSYS, is selected in combination with the material properties from the ITER PFC Materials Database [80]. The heat removal from the sample through radiation or convection is neglected, so that only the heat conduction towards the sample holder or cooling structure is taken into account. This approach is justified since heat conduction is the dominant mechanism for heat transfer.

For example, during a GLADIS exposure the estimated maximum steady state temperature is 1500 °C. According the Stefan-Boltzmann law, the heat transfer due to radiation cooling for tungsten at that temperature is $168\,\mathrm{kW\,m^{-2}}$ if a total emissivity of 0.3 is used, which is an overestimation [81]. An underestimation of the heat conduction is obtained by assuming a temperature of 150 °C at the bottom of the tungsten specimen, resulting in a heat transfer of $15.6\,\mathrm{MW\,m^{-2}}$ according to Fourier's law.

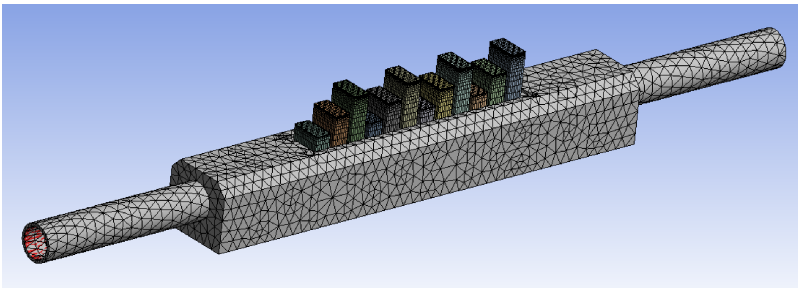

Figure 2.10: A model within ANSYS Workbench of a cooling structure with different sized samples. The mesh used for this model, which contains 34 031 elements and 108 608 nodes, is shown, indicating the different mesh size and discretization methods used in generating the mesh for the cooling structure and the samples.

A fixed heat transfer coefficient h is used to approximate the heat transfer between the cooling structure and the cooling water. This coefficient is obtained through Eq. (2.2), which contains λ, the thermal conductivity of the cooling liquid, D_H, the hydraulic diameter of the cooling tube, and the Nusselt number (Nu), which is the ratio between total heat transfer and the heat conduction [82].

$$h = \lambda \frac{\mathrm{Nu}}{D_H} \tag{2.2}$$

In order to calculate the Nusselt number, the Reynolds number (Re) and the Prandtl number (Pr) for heat transport need to be known. The Reynolds number is the ratio between the inertial and the viscous forces [82]. It is determined by the dimension and roughness of the cooling pipe, the temperature dependent density and dynamic viscosity of the fluid, and the flow rate [83]. The Prandtl number is the ratio between the momentum diffusion and the heat diffusion [82]. It is only dependent on the properties and the temperature of the fluid [83].

In certain cases an explicit function exists to determine the Nusselt number. For liquid that has a turbulent flow within a pipe and is heated, the Dittus-Boelter equation, as introduced by McAdams [83,84], which is shown in Eq. (2.3), can be used. For the active cooling performed in GLADIS, this results in a heat transfer coefficient of $0.044\,\mathrm{W\,mm^{-2}\,K^{-1}}$.

$$\mathrm{Nu} = 0.023\,\mathrm{Re}^{0.8}\,\mathrm{Pr}^{0.4} \tag{2.3}$$

A range of exposure conditions and sample designs have been simulated with different FEM parameters. By decreasing the time step and the maximal mesh size, the calculation time increased and the results became more accurate. A set of standardized simulation parameters were chosen in order to achieve an acceptable accuracy within a reasonable calculation time. This was reached for a mesh with 34 031 elements and 108 608 nodes, shown in figure 2.10, with a maximal mesh size for the tungsten samples of 0.75 mm. Under these conditions, the simulations for a steady state simulation are performed with a minimal and maximal time step of 10^{-3} s and 0.1 s, respectively, and could be completed within 1 h. Simulations of the transient loading, were conducted with a minimal and maximal time step of 10^{-7} s and 10^{-5} s, respectively. Because the results show both the achieved temperatures and their respective time evolutions, operational parameters such as the minimal inter-pulse time could be deduced. In figure 2.11 an example is given for a 30 s GLADIS exposure with a $10.5\,\mathrm{MW\,m^{-2}}$ power density at the beam centre.

For transient heat loads, as an alternative to a complete thermal simulation of the samples, the temperature rise on the surface can also be approximated analytically using the one dimensional heat equation. Hereby the assumption is made that the heat loads represent a homogeneous loading

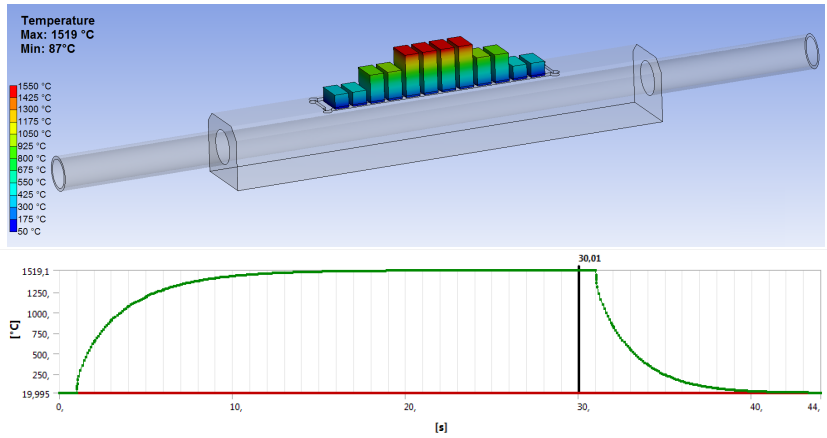

Figure 2.11: An ANSYS temperature simulation of a 30 s-long GLADIS pulse, which has a maximal power density of 10.5 MW m^{-2}. The results show a graphical representation of the temperature for the exposed samples in a steady-state regime after 29 s seconds of GLADIS exposure (top) and the time evolution of the minimum and maximum temperatures of the entire tested mock-up, including the cooling structure (bottom).

of a semi-infinite surface, taking solely the heat conduction into account. The analytical solution, Eq. (2.4) depends on the absorbed power density P and the pulse length Δt, as well as the material's density ρ, specific heat capacity c_p, and thermal conductivity λ [85].

$$\Delta T = 2P\sqrt{\frac{\Delta t}{\pi \rho c_p \lambda}} \tag{2.4}$$

This equation is used as a 'rule of thumb' for the local rise in surface temperature during the transient heat load experiments in the JUDITH-facilities. It does not provide an adequate estimation in the case of steady state heat loads or long quasi-stationary heat pulses.

2.6 Summary

Because the microstructure and chemical content of tungsten has an influence on its material properties and damage behaviour, the focus is on a single tungsten grade. The material, double forged tungsten from the company Plansee, is anisotropic and was cut into samples with a longitudinal grain orientation. After grinding and polishing, a mirror-like surface was obtained that served as a pristine and undamaged reference state. Pre-characterization and post-mortem analysis was performed with LM, laser

profilometry, SEM, FIB, TEM and metallographic cross sections. Furthermore, an Nd:YAG laser facility was used to measure the hydrogen and helium retention through LID.

The particle exposure and thermal load experiments were performed in three HHF facilities. GLADIS, a neutral beam facility in the Max-Planck-Institut für Plasmaphysik, performed a simultaneous particle loading and SSHF on actively cooled mock-ups. The other two facilities are located in Forschungszentrum Jülich and are electron beam facilities used for ELM-like exposures. In JUDITH 1 only ELM-like exposures were applied, making it necessary to use a heating system instead of an SSHF to obtain increased temperatures. JUDITH 2 can simultaneously combine SSHF and ELM-like transient heat loading, and usually uses actively cooled mock-ups.

Because the temperature affects the damage behaviour of tungsten, the experimental temperature must adhere to the required loading conditions. Therefore, a thermal simulation is performed beforehand with FEM in preparation of the experiments. These thermal simulations were used after the experiments to validate the measured surface temperatures. For the thermal shock experiments, an approximation of the one dimensional heat equation can also be used to estimate the temperature rise during a transient thermal load.

Chapter 3

Single Exposure Experiments

3.1 Steady State Particle and Heat Fluxes

The as-received, polished, double forged tungsten samples, which are described in subsection 2.1.2, underwent steady state particle and heat flux exposure. These experiments were performed in the GLADIS-facility, described in section 2.2. In this section, the results are described for samples that only underwent an exposure in GLADIS. Because these results are used in the discussion of the sequential exposure experiments, described in chapter 4, to determine if the steady state damage and/or damage mechanism alters if exposure conditions are combined, these experiments and samples are also referred to as the 'GLADIS reference'.

For GLADIS experiments, it is required due to the steady state heat flux of $\sim$10 MW m^{-2} that the samples are actively cooled, thus they are are brazed upon a CuCrZr structure that has a $\varnothing$ 10 mm internal cooling channel. A silver based brazing alloy from Umicore is used that has a melting temperature of 780 °C and is composed of 28 wt% copper, 2 wt% germanium, and 0.3 wt% cobalt [86]. The brazing temperature of 820 °C is held for a duration of 10 minutes. Figure 3.1 shows the temperature of a CuCrZr mock-up during the whole brazing process.

The experiments in GLADIS were done with both a pure H flux and a mixed H/He-flux. While the gas input for the mixed H/He experiments contained 90 % hydrogen and 10 % helium, this ratio does not resemble the beam composition. Due to a different efficiency in ionisation, the beam contains 94 % hydrogen and 6 % helium, which is in line with the hydrogen/helium ratio for ITER. In both cases the same beam profile was used.

The beam profile is obtained through an extraction current of 9.5 A and an extraction voltage of 29–31 kV. While each helium atom in the beam has

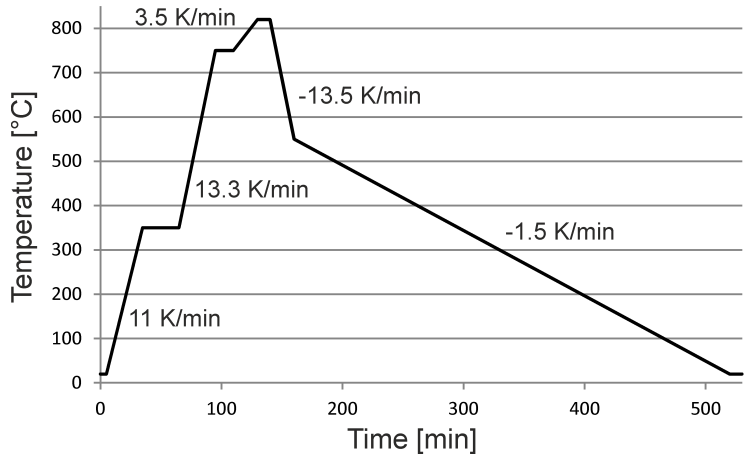

Figure 3.1: The temperature and average heating up or cooling down rate of the CuCrZr mock-ups during the brazing procedure to attach the tungsten samples to the cooling structure.

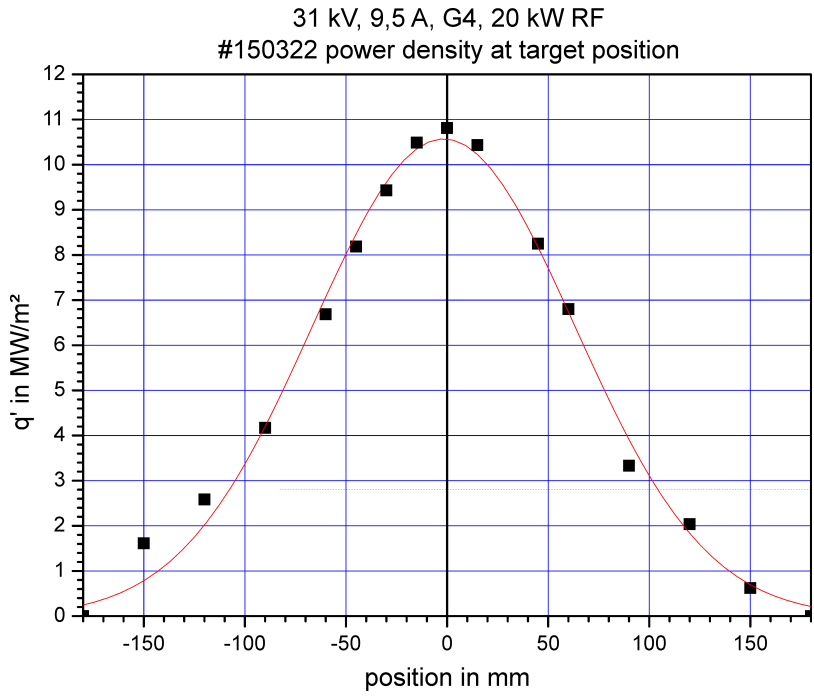

Figure 3.2: The heat flux distribution of a GLADIS beam as used for the GLADIS reference tests, measured by a movable calorimeter and fitted to Gaussian function.

Table 3.1: Overview of the different exposure conditions in the GLADIS facility for the single exposure experiments. The values depend on the position of the samples on the cooling structure and the fluence is the total fluence for H and He combined.

Label	Height [mm]	T_{Surf} [°C]	Beam	Heat Flux [MW m^{-2}]	Fluence [m^{-2}]
S-H	5	600	pure H	9.4	1.8×10^{25}
S-H/He	5	600	H/He	9.4	1.8×10^{25}
M-H	10	1000	pure H	10.2	1.9×10^{25}
M-H/He	10	1000	H/He	10.2	1.9×10^{25}
L-H	15	1500	pure H	10.5	2.0×10^{25}
L-H/He	15	1500	H/He	10.5	2.0×10^{25}

full energy, this is not the case for the hydrogen, as mentioned in section 2.2. For these experiments, only 22 % of the hydrogen has full energy, 43 % at half energy and 35 % at one-third energy [87]. This results in a penetration depth of 60 nm for the helium atoms and 40–120 nm for the hydrogen atoms [30].

The peak particle flux of the beam is 3.7×10^{21} m^{-2} s^{-1}. As shown in figure 3.2, this corresponds to an absorbed power density of 10.5 MW m^{-2} at the beam maximum. The samples were exposed to 180 pulses, each with a duration of 30 s. After these 5400 s of exposure time, a maximum fluence of 2×10^{25} m^{-2} was reached.

Based on the beam profile, the sample height, and the location of the samples on the cooling structure, different surface temperatures can be reached. For the samples with a height of 5 mm, the surface temperature reached 600 °C. These samples are labelled *S-samples*. A surface temperature of 1000 °C is obtained for the so-called *M-samples*, which are 10 mm high. The *L-samples*, or the samples with a height of 15 mm, reached temperatures up to 1500 °C. FEM simulations, as discussed in 2.5, verified that these temperatures are reached, even if there are small deviations in the sample height or in the sample location with respect to the beam centre.

Based on these parameters, the GLADIS experiments had six different exposure conditions. For each of the three surface temperatures, two types of exposures were done. One with the pure H-flux and one with the mixed H/He-flux. In table 3.1, an overview is given for each reference, while the relation between the heat flux and the total particle fluence is given in table 3.2. Furthermore, the appendix contains also an overview of the loading conditions of the applied GLADIS exposures in tables A.1 and A.2.

At these loading conditions the erosion is higher than what is expected from the physical sputtering yield. Calculations show that a tungsten layer

Table 3.2: The relation between heat flux and total particle fluence for the experiments performed in GLADIS.

Total Fluence	Heat Flux		
	$9.4\,\mathrm{MW\,m^{-2}}$	$10.2\,\mathrm{MW\,m^{-2}}$	$10.5\,\mathrm{MW\,m^{-2}}$
$1.8 \times 10^{25}\,\mathrm{m^{-2}}$	S-sample		
$1.9 \times 10^{25}\,\mathrm{m^{-2}}$		M-sample	
$2.0 \times 10^{25}\,\mathrm{m^{-2}}$			L-sample

of 1.0–1.2 µm should be eroded by physical sputtering during the hydrogen/helium exposure. However, as reported in the literature, the total erosion under these specific loading conditions is roughly double the expected value, but a mechanism that can completely account for this increase is not yet identified [74, 88].

3.1.1 Exposure with a pure hydrogen beam

The reference samples S-H, M-H, and L-H were characterized after their exposure in GLADIS to a pure hydrogen particle beam. Each tungsten sample that was exposed to pure hydrogen showed a clear erosion pattern and changes in the surface morphology that varied for each grain and is depending on the crystal orientation. The uneven surface of the S-H and the M-H samples looks similar in SEM-pictures, as shown in figure 3.3 and figure 3.4. Heights differences are detected at the grain boundaries up to 0.5 µm for S-H and 1 µm for M-H, but neither of the two samples were blistered. There is also no evidence of micro- or nano-sized pores on the surface.

On the surface of the L-sample, shown in figure 3.5, no blisters were found either. However, the surface has several holes or craters with a width up to 4 µm, which potentially were blisters from which the blister cap was removed. Also height differences of 2 µm are observed at the grain boundaries. EBSD, shown in figure 3.6, and SEM show that the L-H surface became recrystallized. The deviation between the S-, M-, and L-samples with regard to the heat flux, the particle flux, and the fluence is limited to 10 %, while the surface temperature differs between each sample-type. Hence, the differences that are seen between the surfaces of the S-H, M-H, and L-H samples are attributed to the surface temperature.

These findings are partially in agreement with previous research performed in GLADIS with other tungsten grades at loading conditions with surface temperatures up to ∼2100 °C and fluence up to $3.3 \times 10^{25}\,\mathrm{m^{-2}}$ [32]. Blisters were also not found on the tungsten surface in these experiments. However, the pores that were described in literature are smaller than what was observed with the reference samples.

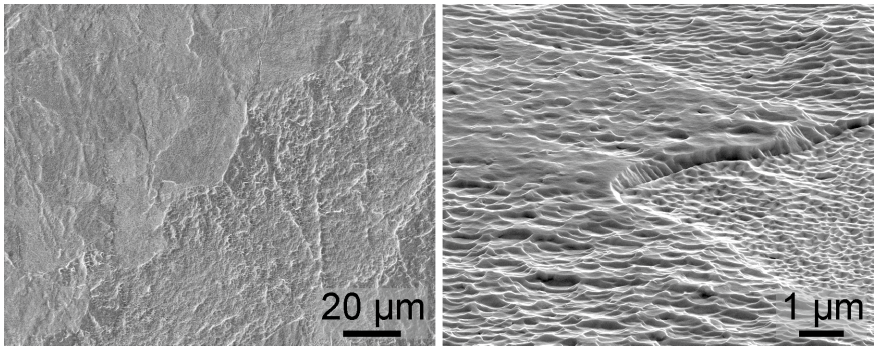

Figure 3.3: Two surface locations for the S-H sample (600 °C), taken perpendicular (left) or at a 70° angle (right).

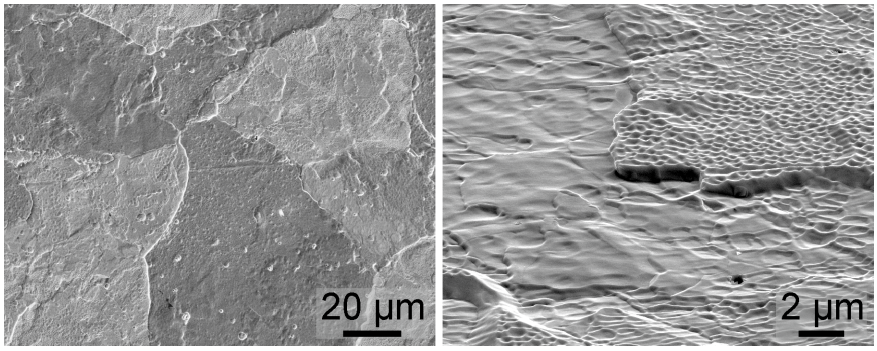

Figure 3.4: Two surface locations for the M-H sample (1000 °C), taken perpendicular (left) or at a 70° angle (right).

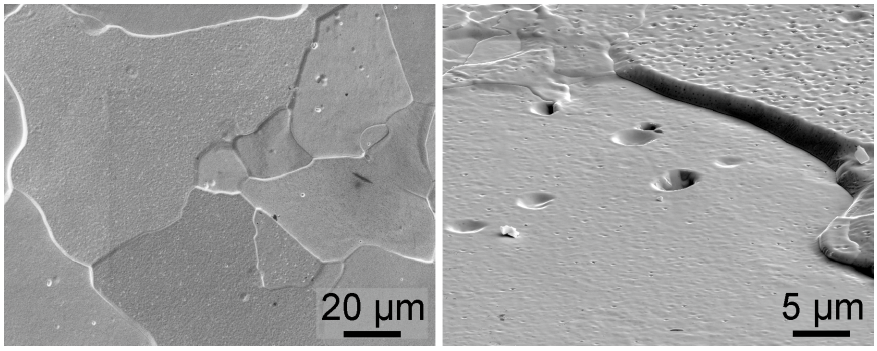

Figure 3.5: Two surface locations for the L-H sample (1500 °C), taken perpendicular (left) or at a 70° angle (right).

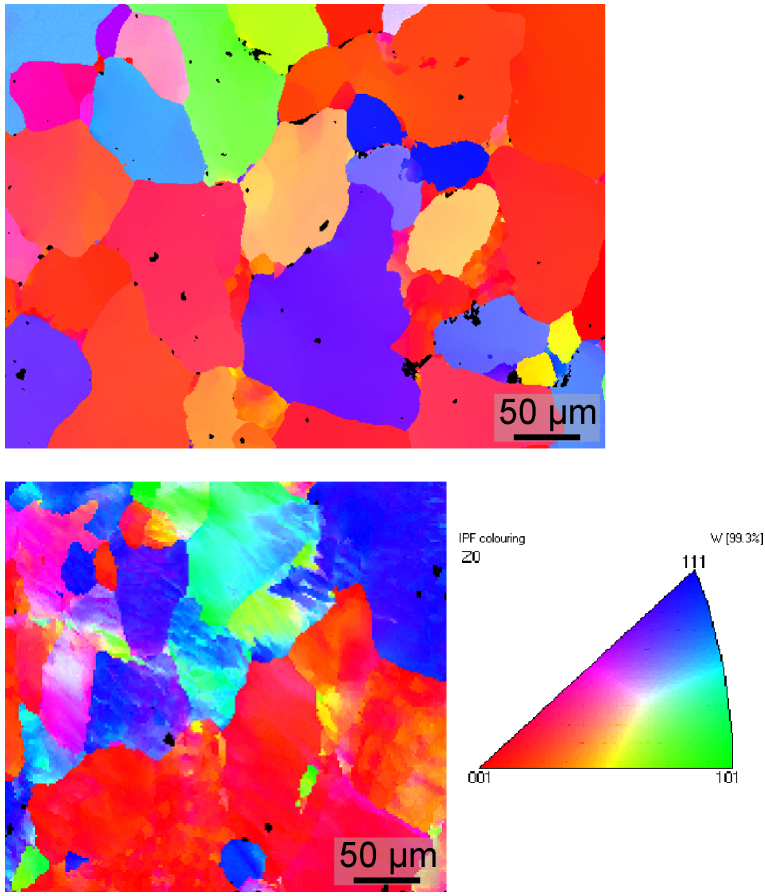

Figure 3.6: EBSD pictures of the surface from a M-H (bottom) and a L-H (top) sample, showing that L-H has undergone recrystallization.

Table 3.3: The arithmetic mean roughness R_a of unexposed, polished samples and samples exposed in GLADIS to a H-flux. The R_a is calculated with a 50 points/mm laser profilometry scan.

Sample	R_a [µm]
polished	0.08
S-H	0.39
M-H	0.34
L-H	0.33

Through laser profilometry, described in subsection 2.1.4, the roughness parameter R_a was determined. Previous scans on tungsten damaged through ELM-like exposure conditions, were performed with a resolution of 50 points/mm. In order to enable the comparison of data, the same resolution was chosen. The results are given in table 3.3 and do not indicate a relevant difference between the roughness of S-H, M-H, and L-H.

FIB cross sections, shown in figure 3.7, and metallographic cross sections were made from these samples. Visual inspection and optical microscopy show for the metallographic cross sections of the L-H sample that in a layer up to ∼3.5 mm deep, grain growth and recrystallization had occurred. A FEM simulation showed that the steady state temperature at this depth is ∼1125 °C. S-H and M-H did not show any changes of the microstructure. These findings about recrystallization confirm the observation from the SEM and EBSD analysis. Furthermore, in FIB sections of M-H and L-H are a few bubbles or porosities observed and S-H has cleavages and/or the creation of longer porosities at the grain boundaries.

For each type of reference sample, an LID measurement was performed with the set-up described in section 2.4, to determine the hydrogen content. A circular area of 3.1 mm^2 was heated by a 28.5 J Nd:YAG laser. The beam was switched on for 3 ms. FEM simulations show that the temperature increases up to 2950 °C on the test surface. Temperatures above 1000 °C would be found to a depth of 250–300 µm.

A measurement was done both on the sample surface and on the side of the sample. For comparison, measurements on the polished surface were also done with two unexposed polished sample of which one underwent a heat treatment identical to the brazing temperature profile. These comparison measurements were also performed in duplicate. However, in the case of the reference measurements on the polished and brazed samples, LID was always done on the polished surface and not on the sample side.

Results from the LID measurements are shown in table 3.4. However, several discrepancies are detected for measurement #2. The hydrogen content of the unexposed, polished sample in measurement #2 is decreased by a factor of 30 in comparison with measurement #1 and the brazed sam-

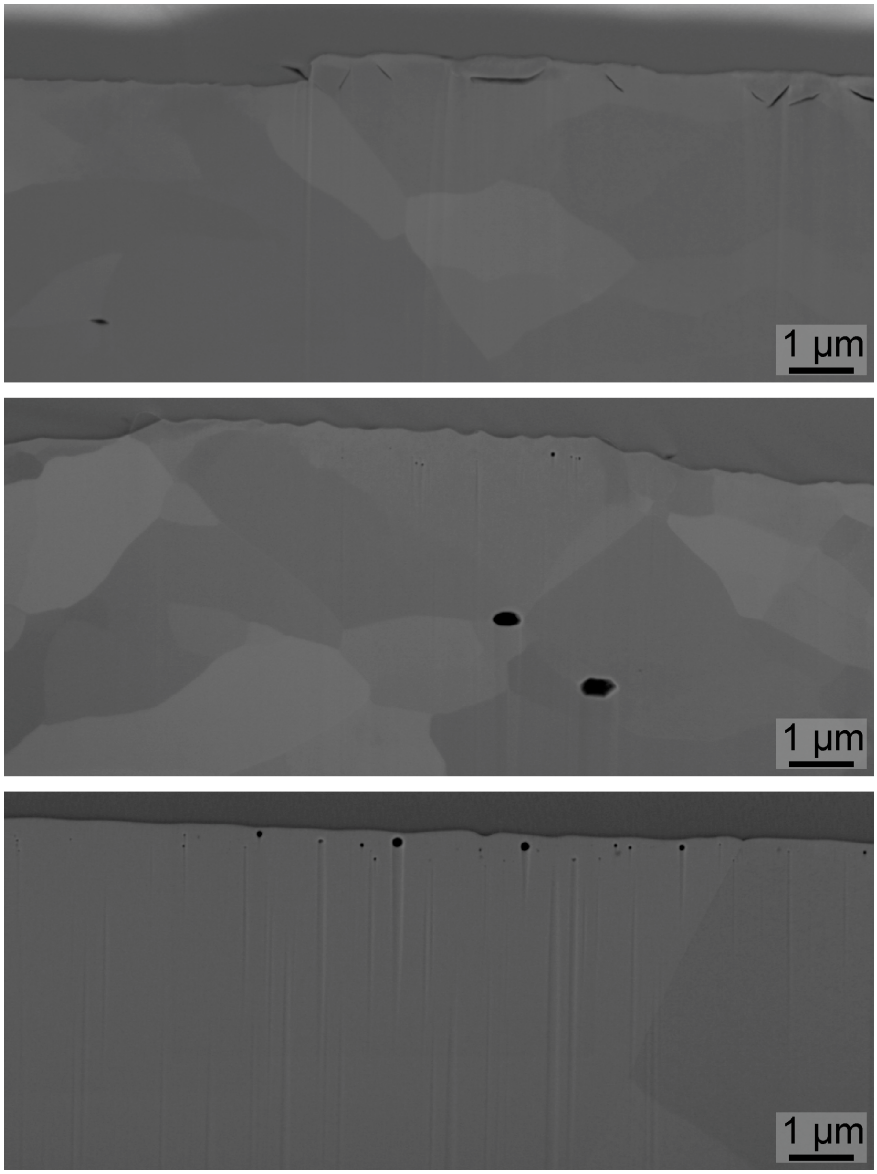

Figure 3.7: Cross sections made through FIB from samples only exposed in GLADIS with a H-flux, with a surface temperature of 600 °C (S-H, top), 1000 °C (M-H, middle), and 1500 °C (L-H, bottom). The samples were covered by a protection layer from platinum before FIB, which is still visible at the top of each image.

Table 3.4: Hydrogen retention in tungsten measured with LID on the sample surface, with the exception of Measurement #2 for M-H and L-H, which were done on the sample side. The asterisk indicates that also helium is detected.

Sample	Pre-exposure	Hydrogen content [m^{-2}]	
	to H [m^{-2}]	Measurement #1	Measurement #2
polished	0	2.34×10^{20}	8.07×10^{18}
brazed	0	2.53×10^{20}	5.68×10^{18}
S-H	1.8×10^{25}	2.13×10^{20}	no data
M-H	1.9×10^{25}	7.04×10^{19}	$*6.92 \times 10^{19}*$
L-H	2.0×10^{25}	9.34×10^{19}	8.87×10^{16}

ple shows a decrease by a factor of 45 in hydrogen content between measurement #1 and measurement #2. Neither samples were exposed to any hydrogen flux, but were reference samples that were not used for another purpose. There is no explanation for these samples to have a fluctuating hydrogen content. In addition, another discrepancy is detected for sample M-H. Despite that M-H was not exposed to any helium, the spectrometer measured a helium content of $5.85 \times 10^{19}\,m^{-2}$. After controlling the measurement data and set-up, the only remaining explanations for this behaviour is either human error, e.g. operating of the LID Nd:YAG set-up with wrong machine parameters, or an unidentified malfunctioning of the set-up. Hence, all data that was obtained in measurement #2 is discarded and not taken into account for any analysis.

The data of Measurement #1 shows only a minimal difference in hydrogen content between the polished reference sample and the reference sample that received the same heat treatment as the one applied during brazing. Because crystal defects influence the retention properties, the measurements indicate that the amount and/or type of the crystal defects that occur in the as-received tungsten are not altered by the brazing. Because both the brazing temperature and the brazing time are below the temperature and duration, respectively, for the stress relief heat treatment, it is indeed plausible to assume that the brazing is not responsible for a change in the type and/or amount of crystal defects.

S-H, M-H, and L-H have a hydrogen retention with the same order of magnitude as the two reference samples. Despite the hydrogen-flux, there is no increase with respect to the two reference samples. The most probable explanation for this is that it took several seconds before the surface temperature was again at room temperature after the exposure, as shown in figure 2.11, and a part of the implanted hydrogen has in this period diffused. This could also be the reason that M-H and L-H, which have the two

highest surface temperatures during GLADIS exposure, have a retention that is lower by a factor 2 to 3.

3.1.2 Exposure with a mixed hydrogen/helium beam

The reference samples S-H/He, M-H/He, and L-H/He underwent the same characterization. Figure 3.8 shows such reference samples while they are still brazed upon the cooling structure. For these samples, the GLADIS particle flux consisted of 94 % hydrogen and 6 % helium. The addition of helium to the beam had a direct influence on the surface morphology. The M-H/He and L-H/He samples, especially, more closely resemble the pure helium exposed samples [32] than the pure hydrogen exposed samples from subsection 3.1.1. The same surface modifications can also be seen in other tungsten grades exposed to H/He-fluxes in GLADIS [89].

S-H/He, shown in figure 3.9, has a very characteristic surface morphology, which results in a change of optical reflectivity, which can be observed by the surface that is matte and light grey after the H/He-exposure. Height differences can be observed, either through several 'terraces' which are formed by stepwise increases, or through a series of ridges. In addition, several holes are visible on the surface with a diameter up to the micrometre-range. Throughout the surface of the S-H/He sample several variations in morphology are seen, which are allocated to the crystal orientation of the underlying grains.

Such grain depending surface morphology is more apparent with the M-H/He samples, which had a surface temperature of 1000 °C. Surface extrusions have grown on the surface, but this did not occur homogeneously and depends from grain to grain. In figure 3.10 areas with higher and shorter extrusions can be identified. While the height differs from grain to grain, most extrusions from the M-H/He sample have a height below 1 µm, although a few extrusions are detected which measure up to ∼3 µm.

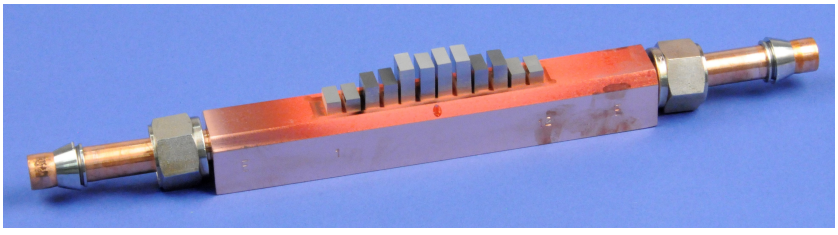

Figure 3.8: A picture after H/He exposure in GLADIS of the CuCrZr cooling structure with S, M, and L-samples brazed upon. The picture contains from each sample geometry three reference samples and one pre-exposed sample. The pre-exposed samples can be found (starting left) at locations 8, 10, and 12.

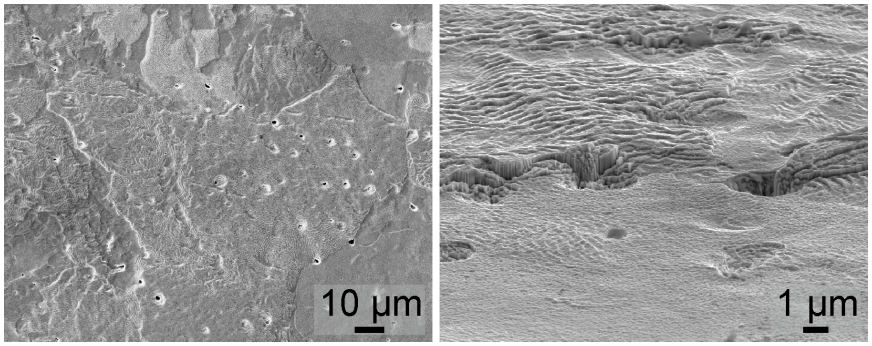

Figure 3.9: Two surface locations for the S-H/He sample (600 °C), taken perpendicular (left) or at a 70° angle (right).

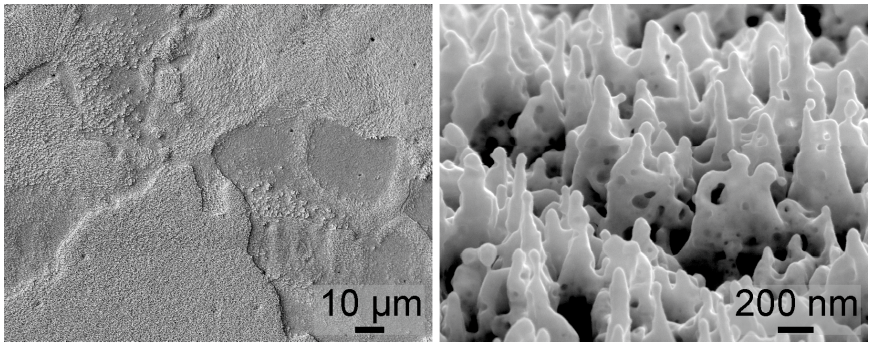

Figure 3.10: Two surface locations for the M-H/He sample (1000 °C), taken perpendicular (left) or at a 70° angle (right).

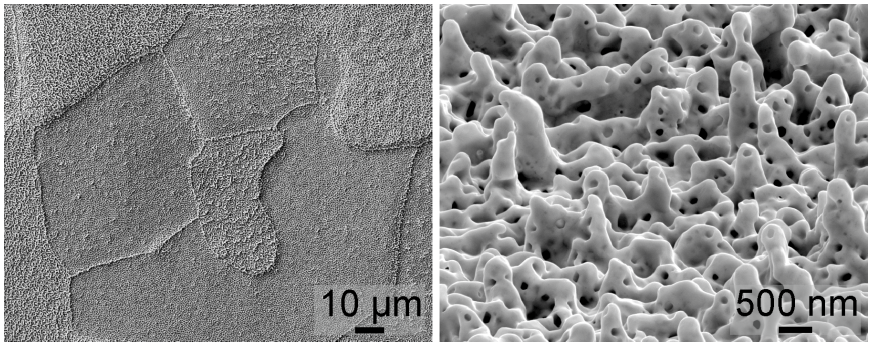

Figure 3.11: Two surface locations for the L-H/He sample (1500 °C), taken perpendicular (left) or at a 70° angle (right).

The difference in shape and height of the extrusions are, due to an abrupt change, very clear in SEM pictures at some grain boundaries. However, during a visual inspection, the surface looks completely homogeneous. While the S-H/He samples has a matte surface, the M-H/He samples have a clear change in colour to dark grey/black. Such surface blackening is also reported in literature for exposures with pure helium and at lower energies [90, 91].

The L-H/He samples which had a surface temperature of 1500 °C during exposure, shown in figure 3.11, also have surface extrusions, with a height similar to the height of the M-H/He extrusions, and a shape that again differs from grain to grain. These extrusions can be distinguished in two different ways from the 1000 °C-extrusions that occur for M-H/He. First, there are several pinholes with a diameter below 200 nm on the surface of such L-H/He type extrusions. Secondly, the grain boundaries are not only visible through a sharp change in extrusion size and/or morphology, but in the case of L-H/He, can also be indicated by a *wall*, or line, of extrusions that are higher than the surrounding ones and have grown on the grain boundary as seen in the lower magnification SEM picture in figure 3.11.

During visual inspection the sample surface is homogeneous, as it is the case for the other samples, despite the visibility of the different grains on SEM-pictures. Also for L-H/He, the reflectivity is changed due to the surface modifications and expressed by the grey colour of the exposed surface.

Similar to the samples exposed to the pure H-flux, only the L-samples that had H/He-exposure show grain growth and recrystallization. This is seen both on SEM and EBSD pictures. The reasons to attribute the surface temperature as the only parameter for the difference between S-H/He, M-H/He, and L-H/He are the same as for the pure hydrogen exposed samples.

The surface roughness parameter R_a for these samples is calculated from a 50 points/mm laser profilometry scan. Because the SEM-pictures show that the damage from particle exposure is substantially different than the ELM-induced damage, a higher scanning resolution was used in addition. This higher accuracy scan was done at 250 points/mm and is used to identify further changes in the surface morphology that stays undetected at 50 points/mm. Naturally, also with this accuracy it is still not possible to detect the extrusions visible in figures 3.10 and 3.11, because the distance between two neighbouring measuring points is higher than the distance between two neighbouring extrusions. As figure 3.12 shows, even if the resolution is increased to 1000 points/mm, the surface extrusions induced by the H/He-beam stay undetected. The laser profilometry is not used nor intended to characterize the surface extrusions, but only the roughness of the underlying surface morphology, which is determined by deformation and a grain orientation dependent erosion [92].

Table 3.5 gives the R_a, which is calculated from both the 50 and the 250 points/mm profilometry scans. For each sample, including the polished reference, the variation in R_a between the two scans is minimal. This is not only lower than the 0.09 µm threshold defined in subsection 2.1.4, it is also

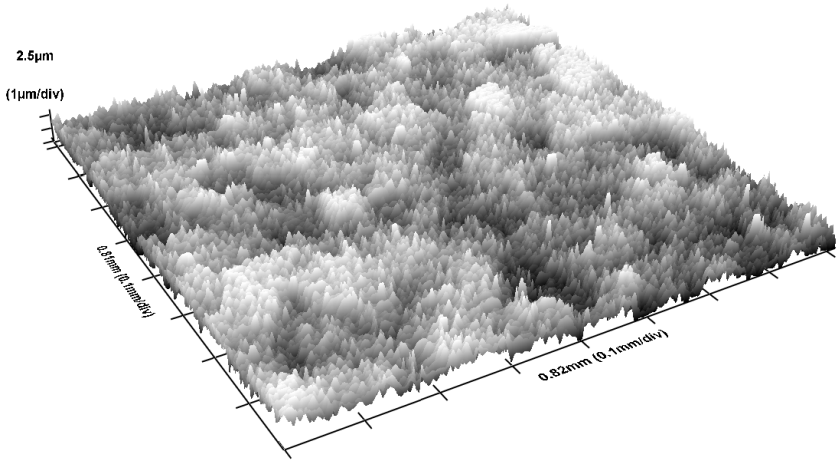

Figure 3.12: An isometric view of the laser profilometry scan performed with a resolution of 1000 points/mm on an L-H/He sample, which had a surface temperature of 1500 °C.

Table 3.5: The arithmetic mean roughness R_a of unexposed, polished samples and samples exposed in GLADIS to a mixed H/He-flux. The R_a is calculated with either a 50 points/mm or a 250 points/mm laser profilometry scan.

Sample	R_a [µm]	
	50 points/mm	250 points/mm
polished	0.08	0.09
S-H/He	0.52	0.54
M-H/He	0.35	0.37
L-H/He	0.35	0.41

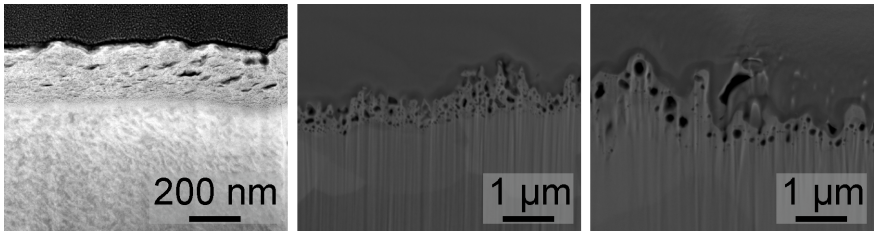

Figure 3.13: FIB and TEM analysis of the near-surface layer for S-H/He (TEM, left), M-H/He (FIB, middle), and L-H/He (FIB, right). The samples were covered by a protection layer from platinum before FIB, which is still visible at the top of each image.

in the same range of variations that are obtained when scanning the same sample several times. Additionally, the roughness of M-H/He and L-H/He is similar, and only S-H/He shows more roughening.

Metallographic and FIB cross sections were made as well as TEM analyses for selected samples. These confirm that grain growth and recrystallization occurred for L-H/He and not for S-H/He or M-H/He, i.e. only for specimens with surface temperatures of 1500 °C. A similar recrystallization depth of 3.5 mm is observed on the L-H/He sample as for L-H. While the sub-surface layer for the hydrogen exposed sample obtained only a few bubbles, porosities, or cleavages, the situation is different for the samples which were exposed to a beam containing helium. This is shown in figure 3.13 for the S-H/He, M-H/He, and L-H/He samples.

LID measurements on S-H/He, M-H/He, and L-H/He were performed with the same procedure as described in subsection 3.1.1 for the hydrogen exposed samples. Table 3.6 gives the resulting hydrogen and helium content. Besides the detection of helium in the H/He-exposed samples, the same observations as for the pure hydrogen exposed samples are made. Also for S-H/He, M-H/He, and L-H/He the hydrogen content is in the same order of magnitude as for the reference samples and no increase of hydrogen is detected. Accordingly, the helium in the H/He-flux does not result in a substantial change in retained hydrogen.

A first effect of helium is observed in the FIB sections through the creation of sub-surface cavities or voids. These pictures indicate fewer cavities, although they are larger in size, for the higher surface temperatures. This can be explained through the Greenwood mechanical equilibrium condition [93, 94] given in Eq. (3.1).

$$P_{\mathrm{LP}} \geq \frac{2\gamma + bG}{r_b} \tag{3.1}$$

As long as the pressure inside a cavity is above the threshold pressure P_{LP}, the cavity size will increase. The parameters for this equilibrium are

Table 3.6: Hydrogen and helium retention in tungsten measured with LID on the sample surface. The data for the polished and brazed reference samples are identical to table 3.4.

Sample	Pre-exposure [m^{-2}]		Measurement #1 [m^{-2}]	
	to H	to He	H content	He content
polished	0	0	2.34×10^{20}	0
brazed	0	0	2.53×10^{20}	0
S-H/He	1.7×10^{25}	1.1×10^{24}	2.18×10^{20}	5.79×10^{21}
M-H/He	1.8×10^{25}	1.1×10^{24}	7.63×10^{19}	7.91×10^{21}
L-H/He	1.9×10^{25}	1.2×10^{24}	1.06×10^{20}	3.30×10^{21}

the surface tension of the cavity interface γ, the radius of the cavity r_b, the Burgers vector of the dislocation loop b, and the shear modulus of tungsten G. Since the shear modulus for tungsten decreases with increasing temperature, the pressure necessary to grow bubbles will be lower at higher temperatures.

Furthermore, the layer affected by the hydrogen/helium beam is deeper than the implantation depth of both the hydrogen atoms and the helium atoms, which is up to 120 nm under these loading conditions. S-H/He shows modifications deeper than 200 nm. Tungsten with a surface temperature starting from 1000 °C is reported to have cavity formation as deep as 500 nm under the same H/He-exposure in GLADIS [74].

A second effect of helium bombardment is the appearance of surface structures, which can be seen in the SEM pictures in figures 3.10 and 3.11. Depending on their shape and size, they are described in the literature as 'nano-tendrils', 'fuzz', and 'fibreform structures'. These extrusions are formed under a broad range of exposure conditions. As reported in the literature, surface temperatures from 1000 K to 2000 K and ion energies above ∼20 eV are required for the formation process [31]. While the energy of the impinging particles in the GLADIS-performed experiments is with 9.7 keV to 31 keV substantially higher than several 10 eV, similar helium-induced surface extrusions as after experiments in GLADIS can be found after experiments with several 10 eV although the size of the extrusions differ [95].

Several mechanisms have already been proposed to explain the formation process, which are among others the growth of surface extrusions by adsorbed tungsten atoms knocked-out by the helium exposure [96], a combination of loop punching and rupture of helium bubbles [97], and a viscoelastic growth model [98]. However, there is currently no agreement on the driving mechanism behind the formation of these surface extrusions. In the discussion of the performed multiple exposure experiments, two of these

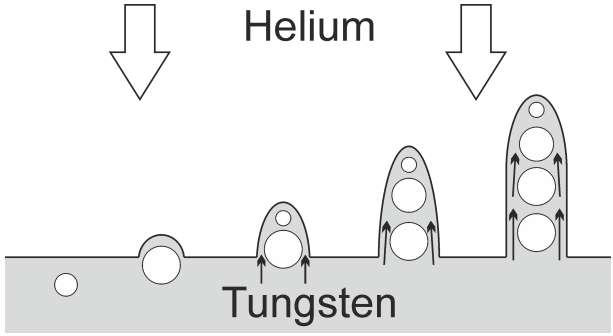

Figure 3.14: Schematic view of surface extrusion growth according to the viscoelastic model, which starts with the formation of helium bubbles in a near-surface layer. The bubble will move to the surface and a new bubble can grow in the thin tungsten layer between the surface and the original bubble, thereby creating additional stress and a viscoelastic flow of tungsten [98].

mechanisms are used. Therefore, they are shortly summarized here.

According to the hypothesis of extrusion growth by adsorbed atoms, the sample surface is covered by adsorbed tungsten atoms that are knocked-out by the impinging helium flux. Most of these atoms will recombine with the vacancies generated, however a fraction of them will diffuse on the surface and attach on the edges of pinholes, protrusions, or a point where the curvature reaches a local maximum, e.g. the top of a bubble. Since the amount of traps for adsorbed atoms is the highest on surface extrusions, the incorporation of knocked-out adsorbed atoms would be concentrated to these extrusions, leading to their growth [96].

Another theory is based on the viscoelastic properties of tungsten. Because the material stress near the helium bubbles is asymmetric due to the vicinity of the surface, a force is exerted on these bubbles. If the temperature is sufficiently high, the low viscosity will enable a movement of the helium bubbles towards the tungsten surface. When such a bubble approaches the surface, a newly-formed bubble can start to grow in the thin layer of tungsten between the old bubble and the surface. As a result, additional stress is created which initiates a viscoelastic flow of tungsten from the bulk to the newly-formed surface extrusion. This process, shown in figure 3.14, continues until equilibrium is reached [98].

3.2 Transient Thermal Loads

The double forged tungsten samples, which are described in subsection 2.1.2, were exposed to ELM-like transient heat loads. Similar to the experiments

described in section 3.1, these samples were in the as-received state and polished before the heat load tests. JUDITH 1, the facility which is presented in subsection 2.3.1, was used to perform these ELM-simulations. Because the results presented in this section are limited solely to ELM-like heat loads, they are used as a basis for comparison. Hence, these samples and experiments are also referred to as the 'ELM reference'.

Each experiment in JUDITH 1 was performed with an acceleration voltage of 120 kV, resulting in a 7 µm electron penetration depth, and a pulse duration of 1 ms. The electron beam current was chosen to obtain the required heat flux. With a scanned area of 4 mm × 4 mm, the selected currents of 46 mA, 92 mA, and 367 mA result in absorbed power densities of 190 MW m^{-2}, 380 MW m^{-2}, and 1514 MW m^{-2} respectively, due to an electron reflection coefficient of 0.45 for tungsten. To compare the effects of transient thermal loads in experiments with different pulse durations, it is possible to use the heat flux factor F_{HF} [85] as an alternative to the absorbed power density. F_{HF}, defined by Eq. (3.2), is proportional to the temperature rise during the heat pulse as shown in Eq. (2.4). This heat flux factor is used without mentioning its unit, which is MW s$^{0.5}$ m^{-2}.

$$F_{HF} = P_{abs}\sqrt{\Delta t} \tag{3.2}$$

In addition to experiments at room temperature (RT), where the sample was not heated, base temperatures of 400 °C and 1000 °C were also used. These ELM-like exposure conditions were all performed with 100 pulses. In addition, experiments with a base temperature of 1000 °C were done with 1000 pulses. Each exposure condition is labelled in a systematic way. The label is composed out of three parts, which refer to the cycle number, the base temperature, and the heat flux factor. The amount of cycles is represented with a single capital letter, i.e. H for 100 pulses or T for 1000 pulses, which is directly followed by the base temperature, i.e. RT, 400, or 1000. Thereafter is given the heat flux factor, i.e. 6, 12, or 48, which is separated from the temperature by a dash.

An overview of these loading conditions is given in table 3.7, together with the estimated temperature rise during the pulse calculated with Eq. (2.4), where the required parameters for tungsten at RT are taken from the ITER materials database [80]. The accuracy of this estimation is lower for the heat pulses with the highest F_{HF}. Furthermore, the appendix contains also an overview of the loading conditions of the applied JUDITH 1 exposures in tables A.3 and A.4.

If the sample behaviour follows the damage mechanism described in the literature [99], there are two distinctive possible cases, depending on the base temperature. The first case occurs when the base temperature is above the DBTT and tungsten is ductile during the whole exposure. When the F_{HF} is below a certain level, the so-called damage threshold, no surface damage is observed. On the other hand, when the F_{HF} is above the melting threshold,

Table 3.7: Overview of the different exposure conditions in the JUDITH 1 facility for the ELM-like thermal shock experiments. Each pulse has a duration of 1 ms.

Label	Pulses	Base Temperature [°C]	F_{HF}	Power Density [MW m^{-2}]	ΔT [K]
HRT-6	100	RT	6	190	325
HRT-12	100	RT	12	380	651
HRT-48	100	RT	48	1514	2595
H400-6	100	400	6	190	325
H400-12	100	400	12	380	651
H400-48	100	400	48	1514	2595
H1000-6	100	1000	6	190	325
H1000-12	100	1000	12	380	651
H1000-48	100	1000	48	1514	2595
T1000-6	1000	1000	6	190	325
T1000-12	1000	1000	12	380	651
T1000-48	1000	1000	48	1514	2595

the surface temperature exceeds the melting point of tungsten and a melt layer is formed.

If the F_{HF} is situated between these thresholds, the temperature rise creates thermal stress in a thin layer near the surface, which leads to plastic deformation. Such plastic deformation occurs both during the surface heating by the pulse by compressive stress and during the cool-down period between the pulses by tensile stress. This results in a clear surface roughening with a severity that depends on the specific material grade and the F_{HF} used. The roughening is the beginning of a fatigue process which with increasing pulse number continues in the emergence of small unconnected cracks and finally results in the formation of a crack network [100].

The second case is for the samples that are exposed while the base temperature is below the DBTT. If the F_{HF} is sufficiently high, a melting threshold can also be observed for these lower base temperatures. For a sufficiently low F_{HF}, below the so-called damage threshold, no damage is observed either. It is shown that for most material grades, the damage threshold for base temperatures below the DBTT is similar or equal to the damage threshold that is observed for base temperatures above the DBTT.

If the F_{HF} is between the damage threshold and the melting threshold, the temperature rise of the heat pulse is sufficiently high to have a ductile sub-surface layer of tungsten. The thermal stresses mentioned earlier will still occur and will, again, result in plastic deformation. However, during the cool down period, if the time between two pulses is sufficiently long, the

temperature will drop below the DBTT and the tensile stresses inside the material will lead to crack formation. It is possible for even one pulse, or only a few pulses, to result in the formation of these cracks. It is shown in the literature that cracking, according to the damage process described here, happens within the first 100 pulses [101].

3.2.1 ELM-like exposure with 100 transient heat loads

After the ELM-like loading conditions in JUDITH 1, the samples are characterized with the methods described in subsection 2.1.4. The transient heat load damage can not only be observed through LM and SEM, but for most loading conditions the difference between the loaded area and the rest of the sample surface can also be seen in a visual inspection. For the samples which are tested at a base temperature of room temperature (RT) or 400 °C, the effects of ELM-like heat loads are similar to previous tests, that are performed either with the same double forged tungsten or with other tungsten grades [67, 99].

Tungsten which is exposed to ELM-like loads with F_{HF} 6 at these two base temperatures does not exhibit observable surface damage. This is not the case for the other loading conditions at RT or 400 °C. For experiments at HRT-12 and HRT-48, the surface is covered with several cracks that are connected to each other, as shown in figure 3.15. Only for the highest power density, HRT-48, were small droplets or other indications of local melting present on the surface. These are located at crack edges, where several factors can result in a local increase of the surface temperature above the melting point of tungsten. Due to the crack, there is a reduced heat transport capability between the surface and the bulk, especially when the crack does not propagate perpendicular to the surface. Furthermore,

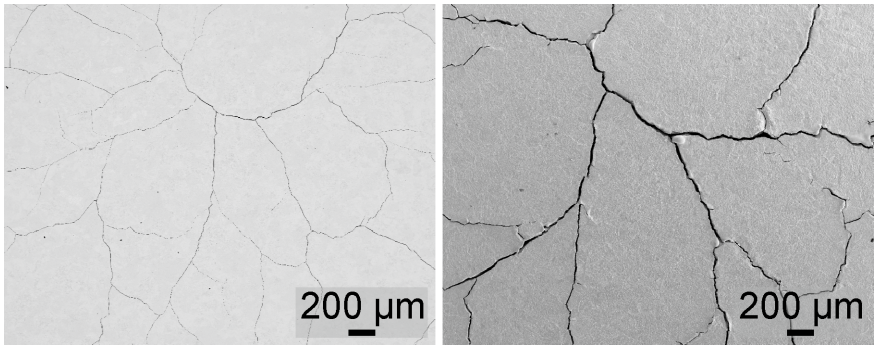

Figure 3.15: Tungsten after exposure in JUDITH 1 at HRT-12 (left) and HRT-48 (right), which shows the occurrence of a crack network for both samples and small tungsten droplets for the HRT-48 sample.

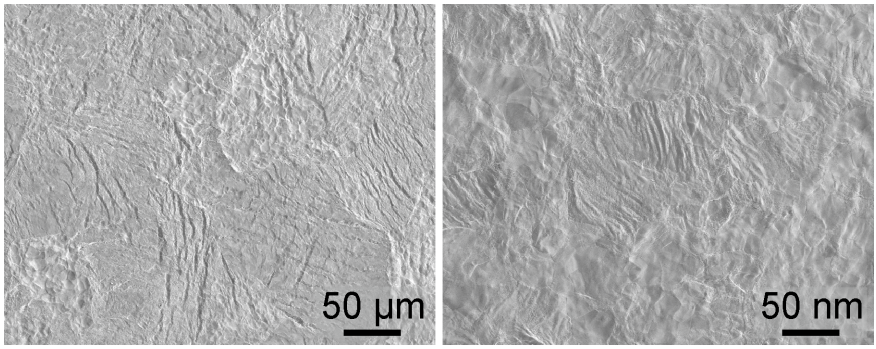

Figure 3.16: Tungsten after exposure in JUDITH 1 to H400-12 (left) and H400-48 (right), which indicate deformations of the surface, without the occurrence of cracking or melting.

the effective electron absorption in the crack is higher because electrons that enter the crack can reflect several times on the crack walls before being either absorbed or leaving the crack. At last, during the heat pulse will the crack (partially) close, which result on some locations into friction between the crack edges.

These crack networks are further analysed through the determination of the average *crack distance* and the average *crack width*. For that purpose an equidistant grid is placed on SEM-pictures with different magnifications in the software program *analySIS pro*. On each grid line, at the intersection of the line with a crack, the width of the crack or the distance to the next intersection with a crack on this grid line is measured. The uncertainty that is given, together with this data, corresponds to the standard deviation. For the sample exposed to HRT-12, this leads to an average crack distance of $433.0 \pm 28.2\,\mu m$ and an average crack width of $3.3 \pm 1.3\,\mu m$. The other cracked sample, loaded at HRT-48, has an average crack distance of $620.0 \pm 44.8\,\mu m$ and an average crack width of $20.9 \pm 6.8\,\mu m$.

The ELM-reference samples with 400 °C base temperature and exposed at F_{HF} 12 and F_{HF} 48 do not show any cracking. Instead, there are indications of surface deformation, as shown in figure 3.16. Since the surface has no cracks, there is no reason for the temperature rise during the H400-48 test to substantially exceed the estimation of 2595 K, given in table 3.7. Therefore no indication of melting is expected, which is in accordance with the images obtained through SEM.

After the ELM-reference experiments at 1000 °C, the tests with the lowest power density, i.e. H1000-6, did not result in surface damage, as is the case for the other base temperatures. However, after exposure to H1000-12, the surface has not only deformation, as expected, but also small, thin cracks in a few locations, as shown in figure 3.17. These cracks are not

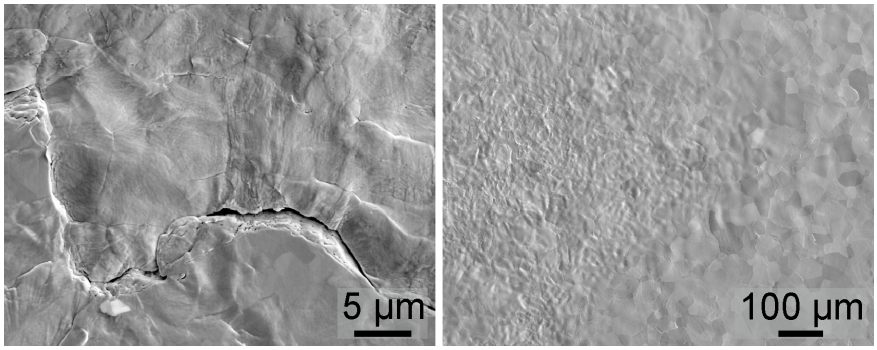

Figure 3.17: Tungsten after exposure in JUDITH 1 to H1000-12 (left), which shows a thin crack, and H1000-48 (right), where both a rough region due to deformation, and a smoother region due to melting, can be distinguished.

connected with each other and are unlike the crack network that can be observed for the samples tested at RT. They are the first cracks that appear as part of a high temperature fatigue cracking and will develop further with increasing pulse numbers. In addition, several thin lines are observed on the surface, for which it can not be determined if they are also these thin cracks or only height differences on the sample surface along a grain boundary.

The sample exposed to H1000-48 did not have any of these thin cracks. In the loaded area, two regions could be distinguished, one that is clearly deformed and another that is smooth, as figure 3.17 shows. Based on two indications, it is assumed that the smooth part of the region is due to a small melt layer on the surface. The first indication is given by the temperature rise during the heat pulse. The result of these loading conditions is an increase of the surface temperature to near the melting point of tungsten at 3420 °C, as indicated by table 3.7. Second, it is known that due to the machine parameters, the diagonals of the loaded area are exposed to a heat load which is slightly higher than it is for the rest of the loaded area. It is near these diagonals that the smoother regions of the sample surface are found.

The roughness parameter R_a is used to confirm some of the observations from the microscopy images. For each sample a profilometry scan was performed with the standard accuracy of 50 points/mm and a higher accuracy of 250 points/mm. The R_a from the samples exposed to 100 transient thermal loads is given in table 3.8. Only a minimal difference in the R_a can be seen when comparing the data from the two profilometry scans. Each difference stays below the threshold, $\Delta R_a \geq 0.09\,\mu m$, that needs to be reached before being considered a relevant increase. Therefore, a scan with the standard accuracy of 50 points/mm is considered to be sufficient, even as is shown in subsection 3.1.2 some surface phenomena are not detected

Table 3.8: The arithmetic mean roughness R_a of the unexposed, polished sample and the samples exposed in JUDITH 1 to 100 ELM-like transient heat loads. The R_a is calculated with a 50 points/mm and a 250 points/mm laser profilometry scan.

Sample	R_a [µm]	
	50 points/mm	250 points/mm
Polished	0.08	0.09
HRT-6	0.10	0.10
HRT-12	0.20	0.20
HRT-48	1.12	1.14
H400-6	0.12	0.12
H400-12	0.47	0.47
H400-48	1.16	1.15
H1000-6	0.12	0.12
H1000-12	0.56	0.55
H1000-48	0.82	0.81

with this accuracy.

After F_{HF} 6 transients, there is, independent of the base temperature, no surface damage according to the R_a value. This lack of observed damage is in accordance with the observations of the SEM-pictures and with the proposed damage mechanism from the literature [99]. Similarly, for ELM-like thermal loads with F_{HF} 12, the absorbed power density is higher than the damage threshold and this is reflected in the R_a value. While each sample is clearly roughened after transients with F_{HF} 12, the increase of the R_a is affected by the base temperature. If the sample was brittle and cracked, as happened for the RT-sample, the increase of the R_a is smaller, while it is higher if the ductility of the sample prevented the formation of a crack network. The R_a is higher for the test at 1000 °C than for the tests at 400 °C, which is caused by a higher plasticity of tungsten with increasing temperature.

ELMs with F_{HF} 48 at all three base temperatures resulted in further roughening. The sample exposed to HRT-48 shows that the roughening also occurs after a crack network has been formed. Furthermore, the R_a of the samples at RT or at 400 °C differ only slightly from each other at this power density, while after F_{HF} 12 exposure there was a substantial difference between the R_a of the sample at RT and at 400 °C. While the sample exposed at H1000-48 also exhibits a relevant R_a-increase, the increase is much lower than for the other samples. However, this sample is the only one with 100 ELM-like heat loads which had a partially molten surface, as shown in figure 3.17. The smoother regions on the surface with a melt layer

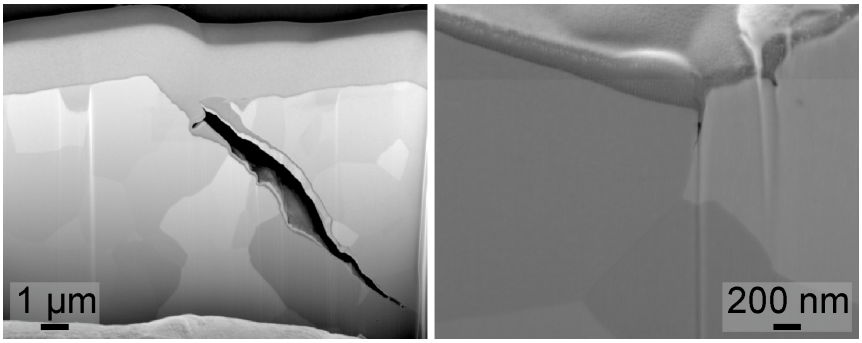

Figure 3.18: FIB analysis of tungsten exposed to H1000-12 on two surface locations. The sample was covered by a protection layer from platinum before FIB, which is still visible at the top of each image. The shallow damage in a sub-surface layer constitutes the beginning of the crack formation process.

are considered to be the reason that this sample, of all samples that were exposed to F_{HF} 48 ELMs, has the lowest R_a.

Because the behaviour of the samples exposed with H1000-12, i.e. the appearance of a few thin and isolated cracks, was not observed earlier for these pulse numbers, further analysis is done. FIB-sections, as shown in figure 3.18, were performed on several locations of the sample. These images indicate that these cracks constitute the beginning of the crack formation process and are still relatively shallow, in comparison with the crack depths found for samples with crack networks. For example, crack initiations of around ∼300 nm are detected in addition to the ones that extend up to 6–9 µm deep. To clearly distinguish between the deep cracks, as can be found in crack networks, and the shallow damage from the beginning of the crack formation process, only the first are considered cracks, while the latter are referred to as *crack initiations*.

After etching, metallographic cross sections for this sample showed a few locations with similar crack initiations in the range of 10 µm. No damage, especially the existence of deeper cracks, is otherwise detected. It must be taken into account that this scale is the lowest for which these metallographic cross sections can be prepared. Higher magnifications would only lead to the observation of artefacts introduced in the cross section during preparation. Due to the potential introduction of these artefacts, e.g. grain loss, an analysis of the surface is not done with the pictures of the cross sections.

For the other reference samples, except for the sample that was loaded with H1000-48 and had a partially molten surface, metallographic cross sections are made to investigate the sub-surface layer. In accordance with the SEM-pictures of the sample surfaces, cracks are only observed for the

Figure 3.19: LM pictures of an etched cross section of tungsten that exhibited a crack network on the surface, i.e. HRT-12 (top) and HRT-48 (bottom).

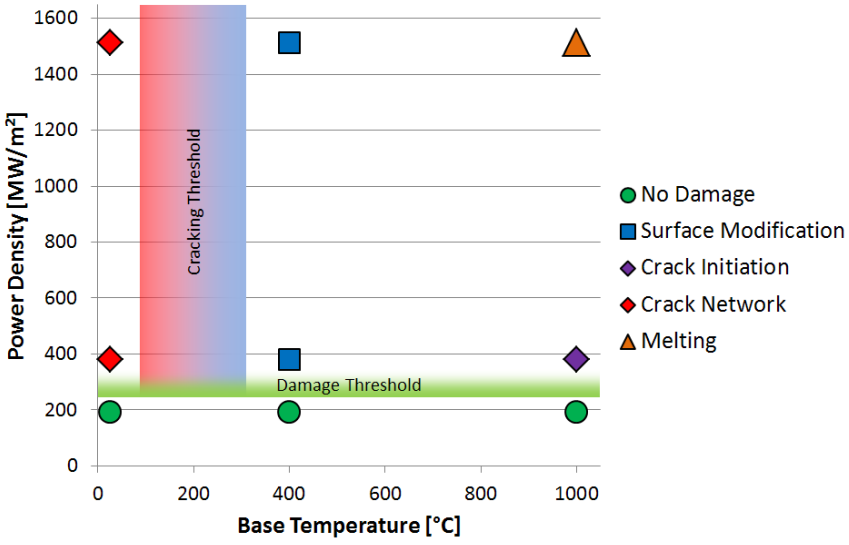

Figure 3.20: A damage mapping graph for the ELM-reference samples exposed to 100 transient heat loads. It shows the two threshold values for this double forged tungsten material grade, i.e. the 'Damage Threshold', located between F_{HF} 6 and F_{HF} 12, and the 'Cracking Threshold' for brittle cracking located between RT and 400 °C.

RT exposures above the damage threshold, which corresponds with loading conditions HRT-12 and HRT-48. Cracks are indeed exclusively found on the cross sections of F_{HF} 12 at RT and F_{HF} 48 at RT, as shown in figure 3.19. The depth of the detected cracks is between 105–192 µm with a mean crack depth of 142 µm for F_{HF} 12 exposure at RT. The observed crack depths for the samples exposed to F_{HF} 48 at RT lies within 70–457 µm, with a mean crack depth of 301 µm. For all of the other samples, i.e. in the SEM-pictures or the analysis of the laser profilometry, either no damage was found or only roughening was detected. No sub-surface damage is discovered in the cross sections.

For each sample, the analysis of the damage can be combined and used to categorize the sample into one of five categories. These are *No Damage*, *Surface Modifications*, *Crack Initiations*, *Crack Network*, and *Melting*. If there are only a few local indications of melting or a few tungsten droplets that are detected in addition to the existence of a clear crack network, the sample is also categorized under the *Crack Network* category. A schematic representation of the samples with their respective damage category can be done in a damage mapping graph, as shown in figure 3.20.

3.2.2 ELM-like exposure with 1000 pulses

As is shown in table 3.7, the experiments with 1000 transient heat loads were only done at a base temperature of 1000 °C, but they were performed with all heat flux factors, i.e. F_{HF} 6, F_{HF} 12, and F_{HF} 48. On one spot of a T1000-6 exposed sample, an indication of deformation is observed. This occurred, despite the fact that this heat flux does not result in any damage for lower pulse numbers. It seems that for these loading conditions, the material is locally no longer similar to a pristine sample. Previous research with the same tungsten grade, albeit with active cooling, showed a change of the damage threshold at higher pulse numbers, such as 10^4 or 10^5 pulses [100], which makes it plausible that this deformation is observed near the pulse number where the damage threshold is located at F_{HF} 6.

The reference sample with F_{HF} 12 had a strongly deformed surface with an abundance of cracks, shown in figure 3.21. On first sight it looks like a multitude of unconnected smaller cracks, but these cracks could be linked with each other through finer cracks. Melt droplets are not detected for these loading conditions. A similar surface was reported for actively cooled JUDITH 2 experiments when 10^5 ELM-like heat loads with a duration of 0.5 ms and F_{HF} 12 were used, while an SSHF of 10 MW m^{-2} kept the surface temperature above 700 °C [102]. The only difference is the occurrence of small tungsten droplets on the surface for the sample tested in JUDITH 2. The reference sample that was exposed to T1000-48, also shown in figure 3.21, has a loaded area with both a roughened and a smoothed region as happened with the sample exposed to H1000-48. This smoothed region is in this case again considered to be a melt layer. No evidence of cracking is

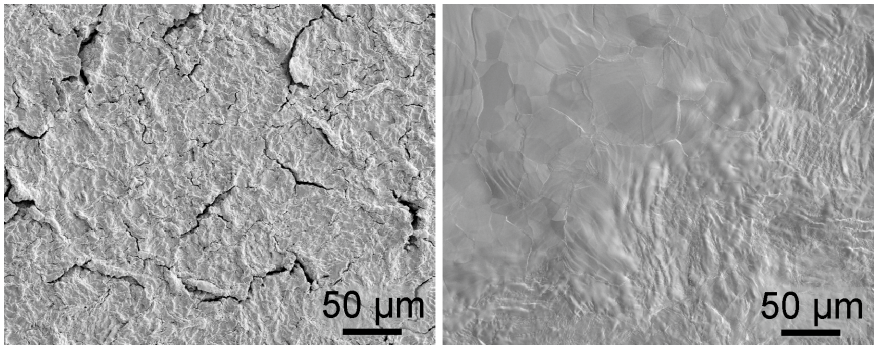

Figure 3.21: SEM pictures of tungsten after exposure to T1000-12 (left), which shows a strongly deformed surface with cracking, and T1000-48 (right), where both a rough region due to deformation and a smoother region due to melting can be distinguished.

detected for this T1000-48 sample.

For the samples exposed to 1000 transient thermal loads, laser profilometry scans were also performed. The R_a is given in table 3.9. On the T1000-48 sample, as the only sample, a difference in the R_a from the 50 points/mm data and the R_a from the 250 points/mm data is measured, that is high enough to be considered a relevant difference. With the standard accuracy laser profilometry, the calculated R_a of this T1000-48 sample is 1.52 µm, while the 250 points/mm scan resulted in a lower R_a, which amounted to 1.35 µm. This sample has the highest roughness of all ELM-reference samples, including the samples exposed to 100 transient heat loads. Such difference in R_a occurred only for one loading condition, which was also one of the most severe exposure conditions that was used in the experiments. Because the 50 points/mm profilometry scan leads either to comparable results with the higher accuracy scan, or in a single case to a difference that could be at worst an overestimation of the damage and not an underestimation, it is acceptable to use the 50 points/mm profilometry scan.

In the SEM-pictures of the sample exposed to T1000-6, a single indication of surface deformation was found. The profilometry scan, as shown in figure 3.22, also suggests the existence of surface modifications. It has a relief that does not coincide with the surface of a pristine sample. Despite the observation from the profilometry, a deformation of the surface after loading with T1000-6 is not clearly reflected in the R_a-value, which only differs by 0.05 µm from a polished surface.

The roughness for the sample exposed to T1000-12 has, as could be expected from the SEM-pictures, increased with respect to the pristine case and the T1000-6 case. A comparison between exposure to H1000-12 (R_a of 0.56 µm) and T1000-12 (R_a of 1.02 µm), demonstrates that an increase

Table 3.9: The arithmetic mean roughness R_a of unexposed, polished samples and samples exposed in JUDITH 1 to 1000 ELM-like transient heat loads. The R_a is calculated with either a 50 points/mm or a 250 points/mm laser profilometry scan.

Sample	R_a [µm]	
	50 points/mm	250 points/mm
Polished	0.08	0.09
T1000-6	0.13	0.13
T1000-12	1.02	1.05
T1000-48	1.52	1.35

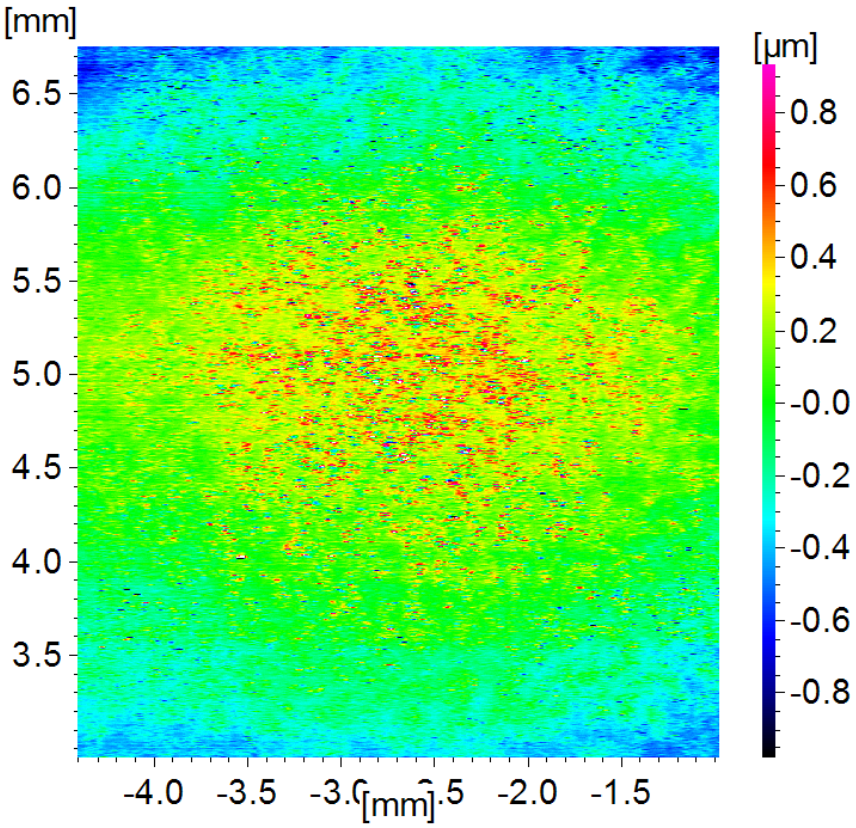

Figure 3.22: Laser profilometry scan, performed with a resolution of 250 points/mm, of a tungsten sample exposed to T1000-6, showing that the sample surface is not completely flat and has some minor deformation.

of the pulse number leads to further roughening. According to the data reported in the literature, this trend of further roughening continues for pulse numbers up to at least 10^6 [68].

While the melt layer, which is observed after an H1000-48 exposure, smooths the sample surface and prevents the roughening from reaching similar levels to those at other base temperatures that had no melt layer, this is no longer the case after an T1000-48 exposure. The high pulse number resulted in the repeated melting of a re-solidified melt layer. Although, the surface appears to be relatively smooth in SEM-pictures, the roughness in this case is higher than for any other ELM-reference sample, including the samples exposed to 100 pulses.

FIB was also performed for the 1000-pulse experiments. On the SEM-pictures it could already be seen that the crack initiations, which are observed after 100 pulses of F_{HF} 12 at 1000 °C, seemed to be connected with each other if the pulse number is increased to 1000. Therefore, the aim of the FIB is to determine if this might indeed be the case and whether the crack depth has simultaneously encountered a substantial growth.

As shown in figure 3.23, neither of these two potential effects have actually occurred to a noteworthy extent. Instead, a pronounced deformation and surface roughening is clearly detectable. The possibility that the crack initiations are connected can not be excluded based on the FIB images, although the FIB suggests that the damage is limited to unconnected crack initiations and strong deformation.

An analysis of the crack depth, which is in the range of 1.8–16.6 µm, does not suggest a clear and substantial depth increase. Because the strongly-deformed surface complicates the determination of the reference level from where the depth is measured, the data is obtained based on a 'worst-case scenario' basis, where in case the correct reference level is not clear, the level that leads to the highest crack depth is taken. This could result in an overestimation of the crack depth.

Metallographic cross sections were made from the samples to detect sub-surface damage. This was not found in the samples exposed to T1000-6 and T1000-12. Only the surface modifications also seen on the SEM and FIB images were observed, together with artefacts from the cross section preparation. For the T1000-48 exposure, a change in microstructure is found, due to the thin surface melting that occurred at the ELM-loaded region. Additionally, despite the lack of cracks seen on the surface, several sub-surface cracks are found that propagate parallel to the surface, as shown in figure 3.24. This only occurred below the surface that neighbours the ELM-loaded region.

Categorizing the 1000-pulse experiments is less straightforward than for the experiments described in subsection 3.2.1, since some analysis methods gave contradictory indications. The F_{HF} 6 sample, despite the lack of a noteworthy increase in the R_a, is categorized under *Surface Modifications* due to the laser profilometry scan and the indications on the SEM-pictures.

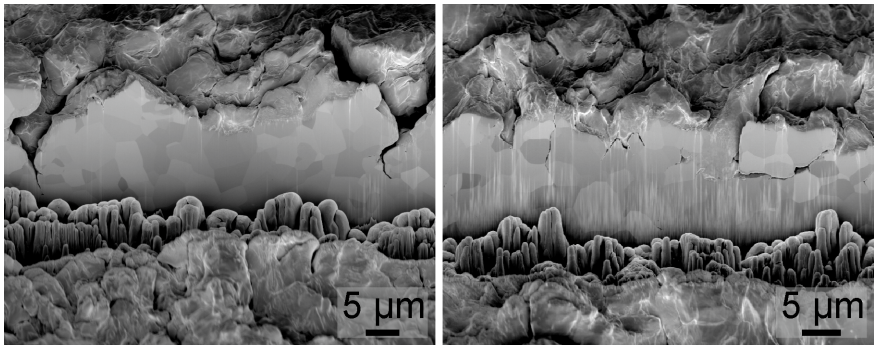

Figure 3.23: FIB analysis on two surface locations of tungsten exposed to T1000-12.

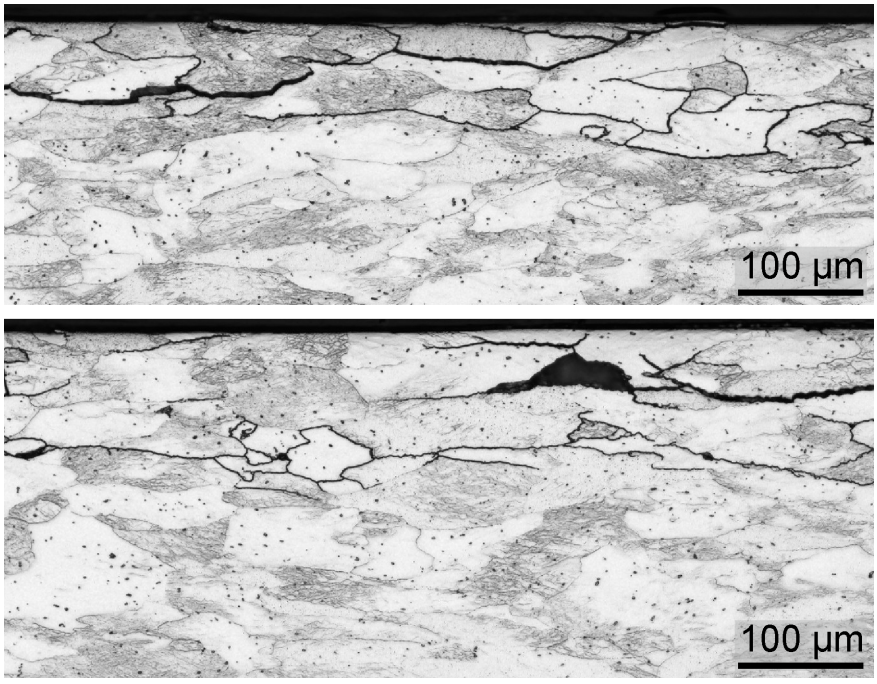

Figure 3.24: LM pictures of an etched cross section from tungsten exposed to T1000-48, on two different surface locations located next to the ELM-loaded region.

For the sample exposed at F_{HF} 12, the cracking observed in the metallographic cross sections determined that the appropriate damage category is *Crack Network*, although the FIB suggested that the damage is less severe. The situation for the F_{HF} 48 sample is clearer and it belongs to the category *Melting*.

3.3 Summary

Double forged tungsten was exposed to either a particle beam in GLADIS or ELM-like heat loads in JUDITH 1. The particle exposure was performed with a pure hydrogen beam and a mixed hydrogen/helium beam, containing 6% helium, at a surface temperature of 600 °C, 1000 °C, and 1500 °C. The ELM-like experiments applied either 100 heat loads of 190 MW m^{-2}, 380 MW m^{-2}, and 1514 MW m^{-2} on samples at RT, 400 °C, and 1000 °C, or 1000 heat loads with the same power densities at 1000 °C.

After the hydrogen loading, an erosion pattern appeared on the sample surface and the roughness increased. Porosities, bubbles, and cleavages have formed in a thin sub-surface layer at all three surface temperatures. Furthermore, the sample exposed at 1500 °C was recrystallized up to ∼3.5 mm deep.

The hydrogen/helium-exposed samples also show erosion, a changed surface morphology, and an increased roughness, and after an exposure with a surface temperature of at least 1000 °C surface extrusions have also grown on the sample. The shape and size of the surface extrusions is not uniform over the whole surface but differs based on the underlying grain. Below the surface, the H/He-exposure resulted in a porous near-surface layer of which the cavities have a volume that grows with increasing surface temperature. In addition, the exposure at 1500 °C again resulted in recrystallization.

The ELM-like heat loads with 100 pulses followed the thermal shock behaviour that is described in the literature. Below the damage threshold, at 190 MW m^{-2}, no damage is observed. In the other cases, a plastic deformation of the surface is observed, which is accompanied by a crack network if the base temperature is under the cracking threshold, i.e. the RT experiments. However at high base temperatures, the deformation was so severe that crack initiations are observed and the temperature that is reached during a heat pulse at the highest power density is sufficiently high for the loaded area to undergo melting.

An increase of the pulse number to 1000 pulses caused surface damage at all tested power densities. The ELM-like loading with 190 MW m^{-2} led to minor surface modifications, while this loading condition did not result in any damage when it is performed for 100 pulses. For the two other power densities, while the same type of damage is observed after 100 pulses and after 1000 pulses, the damage is more severe after the 1000 pulses.

Chapter 4

Sequential Exposure Experiments

4.1 ELM-Like Loading of Particle Exposed W

The surface morphology of the tungsten armour in fusion devices will be influenced by a steady state heat flux and particle exposure. In addition, there are micro-structural changes below the surface, e.g. recrystallization, the formation of cavities, etc. Identifying how the damage induced by steady state heat and particle fluxes influences the thermal shock behaviour is done by the sequential testing in GLADIS and JUDITH 1. First the particle-exposure tests in GLADIS are performed, which results in the damage described in section 3.1. Thereafter, transient ELM-like heat load tests are conducted in JUDITH 1 on these samples.

4.1.1 ELMs on W exposed to a pure H beam

Four ELM-like loading conditions are chosen to be applied on S-, M-, and L-samples exposed to a pure H-flux which had a surface temperature of 600 °C, 1000 °C, and 1500 °C, respectively. In order to be able to assess if the hydrogen exposure has an influence on the thermal shock behaviour, the chosen exposure conditions are situated just above and below the damage and cracking thresholds for this tungsten grade. The corresponding JUDITH 1 loading conditions, with respect to the threshold values established in subsection 3.2.1, are HRT-6, HRT-12, H400-6, and H400-12. As a result, a total of twelve different combined loading conditions, summarized in table 4.1, were used as part of this test campaign.

The six different loading conditions with F_{HF} 6, i.e. HRT-6 and H400-6 after S-H, M-H, and L-H, were analysed through visual inspection, LM and SEM. In none of these six cases, was it possible to detect the 4 mm × 4 mm

Table 4.1: Overview of the loading conditions for ELM-like heat loads loads applied to tungsten which was pre-exposed to a pure H-flux.

First Exposure	Label	Second Exposure	Label
H-flux at 600 °C	S-H	$100 \times F_{HF}$ 6 at RT	HRT-6
H-flux at 600 °C	S-H	$100 \times F_{HF}$ 12 at RT	HRT-12
H-flux at 600 °C	S-H	$100 \times F_{HF}$ 6 at 400 °C	H400-6
H-flux at 600 °C	S-H	$100 \times F_{HF}$ 12 at 400 °C	H400-12
H-flux at 1000 °C	M-H	$100 \times F_{HF}$ 6 at RT	HRT-6
H-flux at 1000 °C	M-H	$100 \times F_{HF}$ 12 at RT	HRT-12
H-flux at 1000 °C	M-H	$100 \times F_{HF}$ 6 at 400 °C	H400-6
H-flux at 1000 °C	M-H	$100 \times F_{HF}$ 12 at 400 °C	H400-12
H-flux at 1500 °C	L-H	$100 \times F_{HF}$ 6 at RT	HRT-6
H-flux at 1500 °C	L-H	$100 \times F_{HF}$ 12 at RT	HRT-12
H-flux at 1500 °C	L-H	$100 \times F_{HF}$ 6 at 400 °C	H400-6
H-flux at 1500 °C	L-H	$100 \times F_{HF}$ 12 at 400 °C	H400-12

area exposed in JUDITH 1 on the sample surface, independent of the analysis method used. The resulting surface morphologies, shown in figure 4.1, are similar to the ones found for the 'GLADIS reference'-samples shown in figures 3.3, 3.4, and 3.5. The observed small differences between the samples with the same GLADIS-exposure are already present after the experiments in GLADIS and are not caused by the ELM-like heat loads. They originate either from differences in particle flux and surface temperature or from small variations in the sample itself. This indicates that the damage threshold is not decreased below F_{HF} 6.

The samples exposed to HRT-12 after the GLADIS pre-exposure show no variation in surface morphology compared to the GLADIS reference. Furthermore, they have a crack network covering the ELM-exposed area, shown for L-H pre-exposure in figure 4.2, as was the case for the HRT-12 ELM-reference sample. After analysis of the cracks, it is found that there is an average crack distance of 586.0 ± 35.5 µm, 438.0 ± 25.4 µm, and 309.0 ± 19.3 µm and an average crack width of 1.9 ± 0.9 µm, 2.7 ± 0.9 µm, and 2.5 ± 1.1 µm for a HRT-12 exposure after S-H, M-H, and L-H pre-exposure, respectively. Due to the large standard deviation, the statistics are not good enough to determine a clear variation compared to the data from the HRT-12 ELM-reference sample. The ELM-induced damage is limited to the loaded area, there is no propagation of the cracks outside the exposed area.

For the samples which were exposed to H400-12, the ELM-like loading caused a slight change in surface reflectivity in the loaded area. Nevertheless, on the SEM-pictures there was no damage observed for the samples

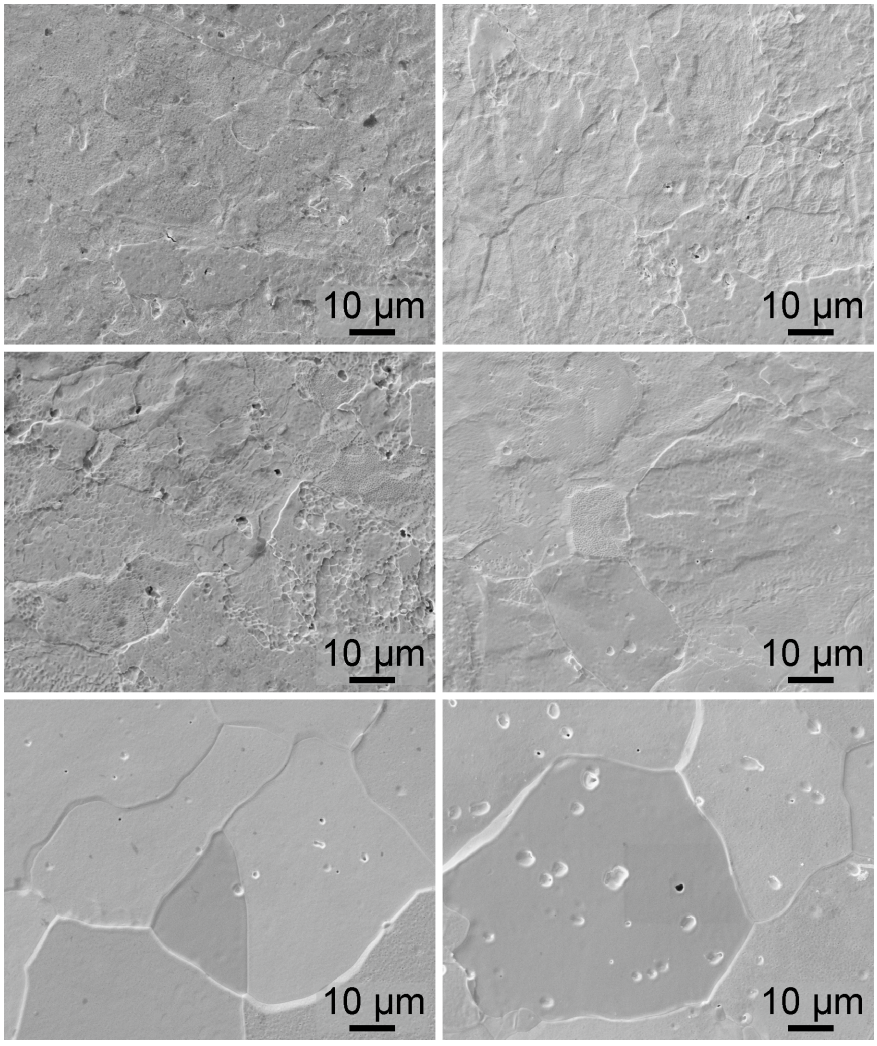

Figure 4.1: SEM pictures of tungsten which is first pre-exposed in GLADIS to S-H (top), M-H (middle), or L-H (bottom) and thereafter exposed in JUDITH 1 to HRT-6 (left) or H400-6 (right).

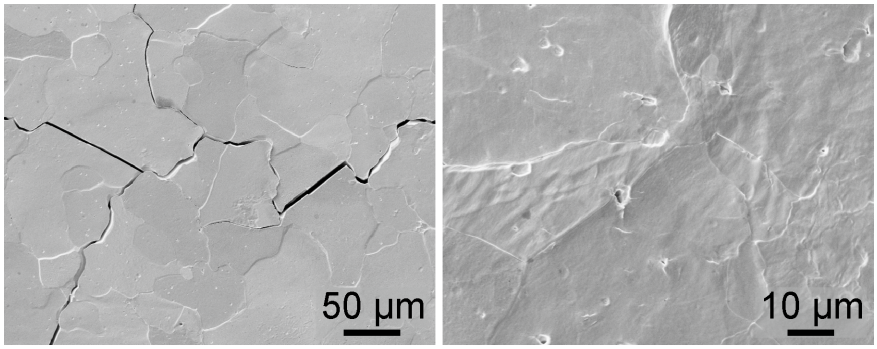

Figure 4.2: SEM pictures of tungsten which is first pre-exposed in GLADIS to L-H and thereafter exposed in JUDITH 1 to HRT-12 (left) or H400-12 (right).

pre-exposed to S-H and M-H. Only for the sample pre-exposed to L-H, shown in figure 4.2, there are indications of further damage in the form of surface roughening.

These observations are verified with the data from laser profilometry scans, shown in figure 4.3. Since the GLADIS pre-exposure resulted in samples without a flat, pristine surface to be used in the thermal shock experiments, an interpretation of the data is not as straight forward, as it was the case for the 'ELM reference' samples discussed in subsection 3.2.1.

For the S-H pre-exposed samples the maximal difference in R_a that is found between a sample with only hydrogen exposure and a sample that had both hydrogen pre-exposure and ELM-like exposure is 0.05 µm. Since this is lower than the stipulated threshold value of 0.09 µm, these differences are considered to be not distinct enough. Therefore there is in the R_a no indication of ELM-induced damage, also not after F_{HF} 12 exposure. This is also the case for the M-H pre-exposed samples, where the maximum R_a difference is 0.04 µm. Despite the expectation of additional roughening after loading with H400-12, it is observed that the H400-12 sample without pre-exposure has a higher roughness than the H400-12 samples with S-H and M-H pre-exposure. Under these two loading conditions, the hydrogen pre-exposure seems to have mitigated the ELM-induced roughening.

The samples pre-exposed to L-H react differently to ELM-like heat loading. Upon exposure to F_{HF} 6 the R_a seems to decrease although this decrease was only for the HRT-6 loading bigger than the stipulated threshold. An explanation for this relaxation of the R_a was not found yet. Upon exposure with HRT-12, the difference in R_a is again too small to take into account. However, the expected roughening after H400-12 exposure is clearly observed with an R_a increase of 0.30 µm. This is in contrast with the S-H and M-H samples with H400-12 exposure and is explained by the recrystal-

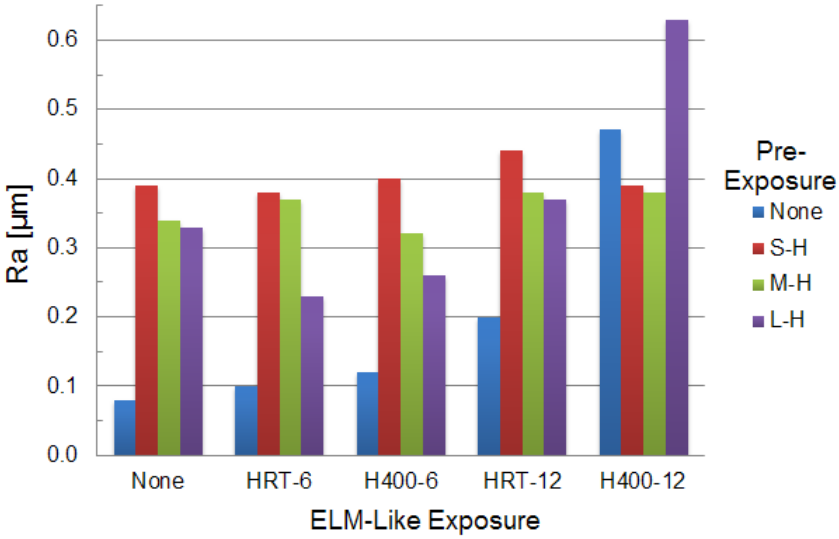

Figure 4.3: The roughness value R_a, derived from a 50 points/mm laser profilometry scan, after the experiments with ELM-like thermal shocks in JUDITH 1 on tungsten that has been pre-exposed to a pure hydrogen beam in GLADIS. In addition, the respective 'GLADIS references' and 'ELM references' are also given for comparison.

lization of the L-H sample.

From each sample also a metallographic cross section was made, from which pictures were taken after polishing and after etching. In the etched cross section pictures it can be seen that all the samples with L-H pre-exposure have, like their respective 'GLADIS reference'-sample, a layer of recrystallization and grain growth up to ∼3.5 mm deep. What could furthermore be noticed, is a large amount of grain-loss that occurred during preparation, solely for the HRT-12 loaded sample with L-H pre-exposure. This points to a weakening of the cohesion between single grains, which is a combined effect from the recrystallization and the thermal shocks. Because this did not occur for the S-H and M-H pre-exposed samples, it is concluded that if the hydrogen implantation has an effect on the grain cohesion it only plays a role in combination with the recrystallization and the thermal shocks.

ELM-induced damage was detected in the cross sections for each sample with HRT-12 loading, as shown in figure 4.4, but not in any other case. The depth of the detected cracks is in the range of 36–222 µm with a mean crack depth of 138 µm for the HRT-12 with S-H pre-exposure. For the M-H pre-exposed sample the depth is between 63–193 µm with a mean of 130 µm, while the acquired data for the L-H pre-exposure is located between 18–382 µm with a mean of 253 µm. Only for the L-H pre-exposure this crack depth range and mean crack depth is substantially larger than it was the case for the HRT-12 'ELM reference' sample. This is caused by recrystallization and weakened grain boundaries.

As shown in figure 4.5, a damage mapping after ELM-like thermal loads is compiled for the samples that are pre-exposed with hydrogen. To enable a comparison of the thermal shock behaviour despite the particle-induced predamaging, one damage category is altered. Instead of *Surface Modifications*, this category now covers all *Additional Surface Damage* that is not part of any of the four other categories that has been introduced in subsection 3.2.1. Taking into account all the acquired data, there is no indication that the S-H and M-H pre-exposed samples have a deteriorated thermal shock behaviour. For each ELM-like loading condition there was the same or less damage identified for the S-H and M-H pre-exposed samples as for the respective 'ELM reference' sample.

The recrystallized L-H pre-exposed sample showed an increase in crack depth after HRT-12, just like it has been reported in literature for the same recrystallized double forged tungsten material [66, 67] and other recrystallized tungsten grades [103]. When the thermal shock behaviour of this sample is compared to the thermal shock behaviour of recrystallized tungsten there is no deterioration noticeable. For example, recrystallized tungsten has an R_a of 2.22 µm after 100 ELM-like heat loads of 380 MW m^{-2} (if an electron absorption coefficient of 0.55 is assumed, this corresponds to 320 MW m^{-2} if an electron absorption coefficient of 0.46 is assumed) at RT [103]. This is 6 times larger than the R_a of the HRT-12 loaded L-H

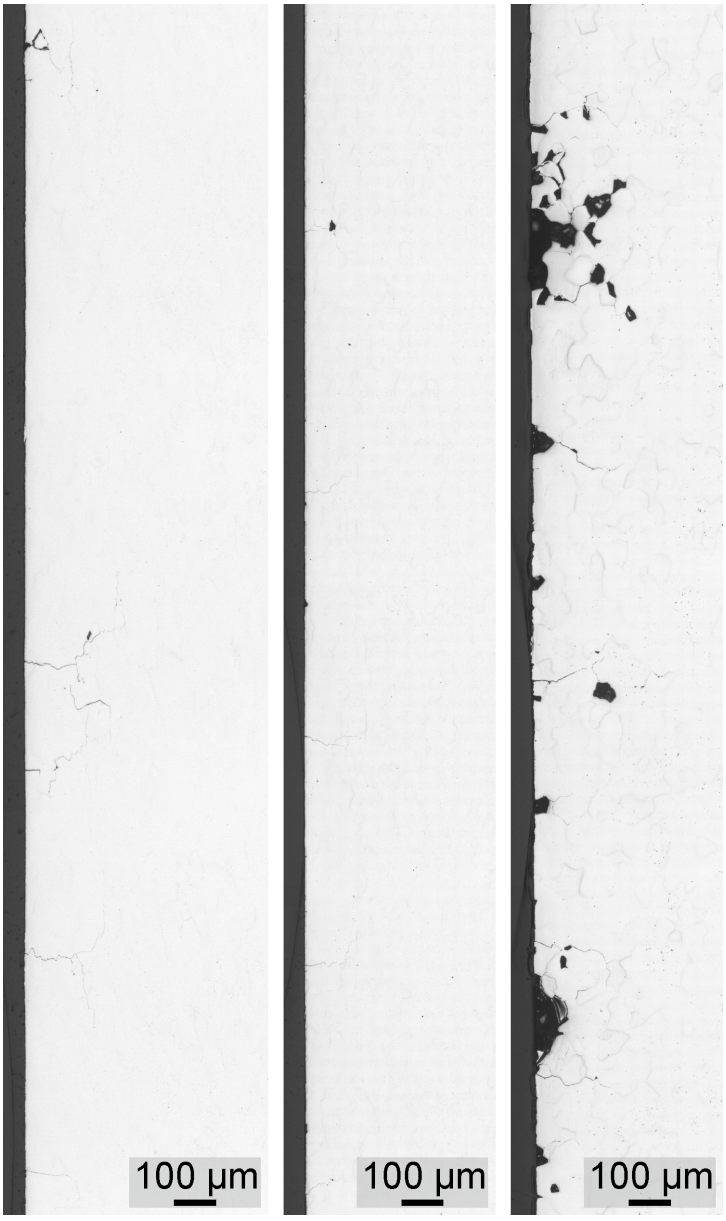

Figure 4.4: LM pictures of a polished cross section of the cracked samples, which were exposed in JUDITH 1 to HRT-12 after a pre-exposure in GLADIS with S-H (left), M-H (middle), and L-H (right). For the L-H pre-exposed sample a substantial amount of grain loss, that occurred during sample preparation, is visible.

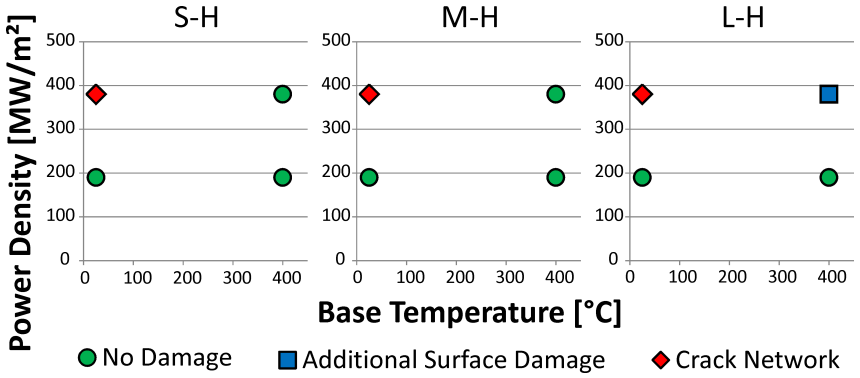

Figure 4.5: The damage mapping after ELM-like thermal loads for the samples that were pre-exposed with a pure hydrogen-beam in GLADIS.

sample, i.e. 0.37 µm as shown in figure 4.3, which can be explained by three potential causes. Firstly, not the same tungsten grade is used and there are differences between these two tungsten materials, e.g. impurity content. Secondly, the L-H sample is not completely recrystallized in contrast to the recrystallized tungsten that has the high roughening. At last, the hydrogen implantation and the consequential modifications for the L-H sample could have limited the increase in roughening. Most likely a combination of these three causes together is responsible for the difference between the R_a for the L-H sample and the higher R_a for the reported recrystallized tungsten.

While the hydrogen pre-exposure does not cause a deteriorated thermal shock behaviour with respect to the 'ELM reference', a difference can be seen between the hydrogen exposure at a surface temperature of 1000 °C or lower, i.e. S-H and M-H, and the hydrogen exposure at a surface temperature of 1500 °C, i.e. L-H. For the two samples with the lower temperatures during hydrogen exposure, the expected roughening after H400-12 transients does not occur, while the expected roughening does occur for the L-H sample. No other changes in the thermal shock behaviour, e.g. crack propagation outside the loaded area, are observed. This could be an indication that the hydrogen-induced effects, i.e. alteration of surface morphology and hydrogen implantation, could conceal or reduce additional roughening during ELM-like loading and that this is no longer completely valid when the material is recrystallized.

4.1.2 ELMs on W exposed to a mixed H/He beam

The same four ELM-like exposures that were used in subsection 4.1.1, i.e. HRT-6, HRT-12, H400-6, and H400-12, are applied in the JUDITH 1 facility to samples with S-H/He, M-H/He, and L-H/He pre-exposure in GLADIS. As summarized in table 4.2, this results in twelve different combined loading

Table 4.2: Overview of the loading conditions for ELM-like heat loads loads applied to tungsten which was pre-exposed to a mixed H/He-flux.

First Exposure	Label	Second Exposure	Label
H/He-flux at 600 °C	S-H/He	$100 \times F_{HF}$ 6 at RT	HRT-6
H/He-flux at 600 °C	S-H/He	$100 \times F_{HF}$ 12 at RT	HRT-12
H/He-flux at 600 °C	S-H/He	$100 \times F_{HF}$ 6 at 400 °C	H400-6
H/He-flux at 600 °C	S-H/He	$100 \times F_{HF}$ 12 at 400 °C	H400-12
H/He-flux at 1000 °C	M-H/He	$100 \times F_{HF}$ 6 at RT	HRT-6
H/He-flux at 1000 °C	M-H/He	$100 \times F_{HF}$ 12 at RT	HRT-12
H/He-flux at 1000 °C	M-H/He	$100 \times F_{HF}$ 6 at 400 °C	H400-6
H/He-flux at 1000 °C	M-H/He	$100 \times F_{HF}$ 12 at 400 °C	H400-12
H/He-flux at 1500 °C	L-H/He	$100 \times F_{HF}$ 6 at RT	HRT-6
H/He-flux at 1500 °C	L-H/He	$100 \times F_{HF}$ 12 at RT	HRT-12
H/He-flux at 1500 °C	L-H/He	$100 \times F_{HF}$ 6 at 400 °C	H400-6
H/He-flux at 1500 °C	L-H/He	$100 \times F_{HF}$ 12 at 400 °C	H400-12

conditions. These experiments are conducted to investigate if the presence of helium during particle exposure and the consequential modification in surface morphology, which is described in subsection 3.1.2, would modify the thermal shock behaviour differently than it is the case for a pure hydrogen exposure.

An initial damage analysis was performed on the samples through visual inspection, LM and SEM. No damage or modification of the surface morphology, including the size and shape of the H/He-induced surface extrusions, could be detected with either of these methods for the H/He pre-exposed samples which were loaded with HRT-6 or H400-6. For the samples loaded with F_{HF} 12 transients, shown in figures 4.6, 4.7, and 4.8, the loaded area could, due to a small change in the reflectivity, be identified in a visual inspection, which points to a modification of the surface morphology. This is identical to the observations for all other samples with the same loading conditions, i.e. HRT-12 and H400-12, but which had either no pre-exposure or a hydrogen pre-exposure.

After the HRT-12 transients, a crack network has formed on the loaded area for the S-H/He and the L-H/He pre-exposed samples, as was the case for the 'ELM reference' and the hydrogen exposed samples. These have an average crack distance of $441.0 \pm 22.4\,\mu m$ and $442.0 \pm 24.5\,\mu m$ and an average crack width of $2.8 \pm 0.8\,\mu m$ and $3.1 \pm 1.7\,\mu m$ for S-H/He and L-H/He respectively, which is in line with the data given in subsection 3.2.1 for the 'ELM reference'.

However, no cracking nor any other kind of damage, was observed after HRT-12 transients on the sample with M-H/He pre-exposure, shown

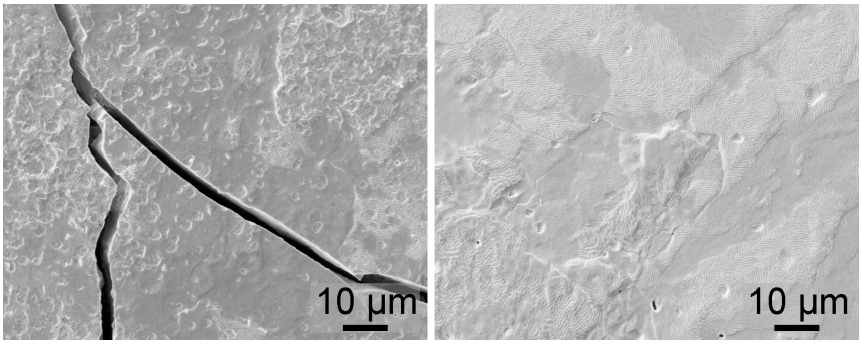

Figure 4.6: SEM pictures, of tungsten which is first pre-exposed in GLADIS to S-H/He and thereafter exposed in JUDITH 1 to HRT-12 (left) or H400-12 (right).

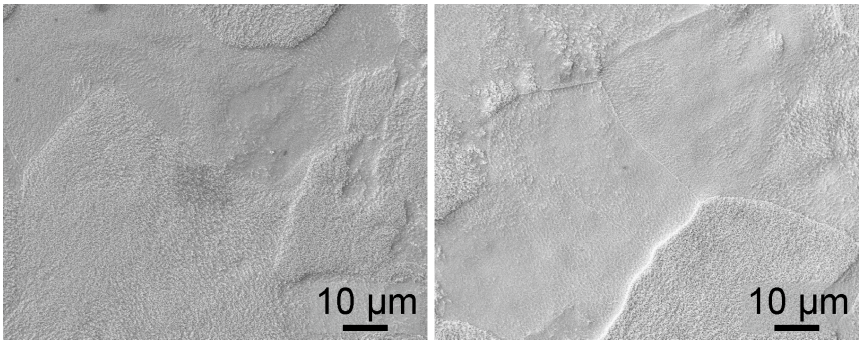

Figure 4.7: SEM pictures of tungsten which is first pre-exposed in GLADIS to M-H/He and thereafter exposed in JUDITH 1 to HRT-12 (left) or H400-12 (right).

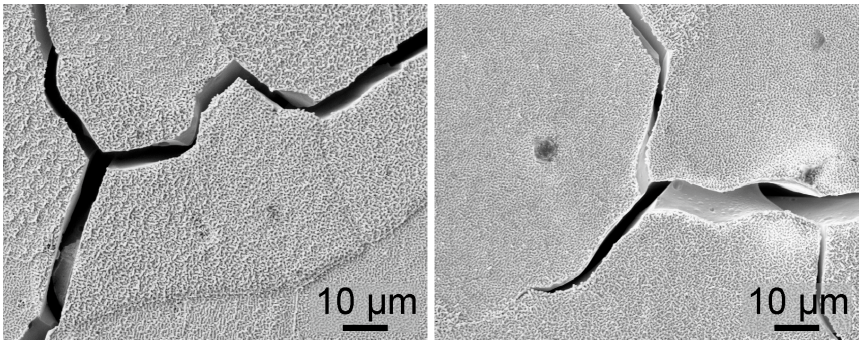

Figure 4.8: SEM pictures of tungsten which is first pre-exposed in GLADIS to L-H/He and thereafter exposed in JUDITH 1 to HRT-12 (left) or H400-12 (right).

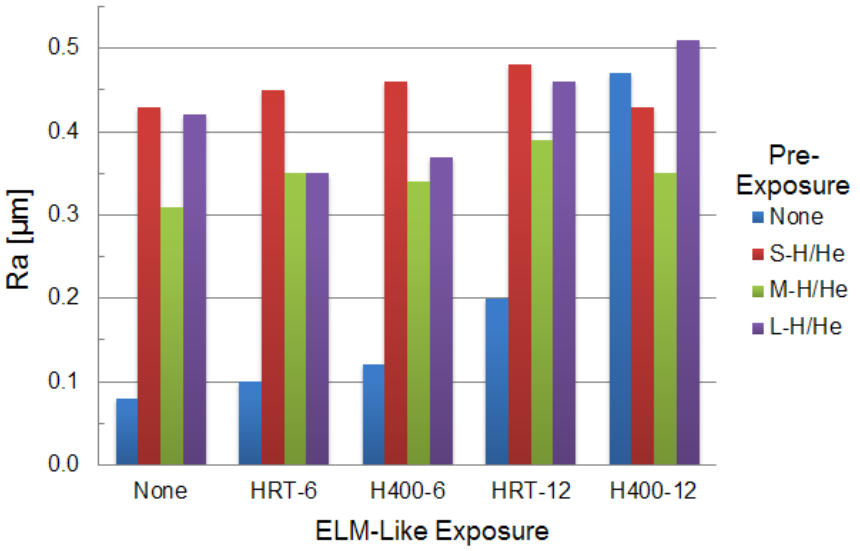

Figure 4.9: The R_a-value, derived from a 50 points/mm laser profilometry scan, after the experiments with ELM-like thermal shocks in JUDITH 1 on tungsten that has been pre-exposed to a mixed hydrogen/helium beam in GLADIS. In addition, the respective 'GLADIS references' and 'ELM references' are also given for comparison.

in figure 4.7. This fact represents a remarkable change in the material's thermal shock behaviour. Solely on the basis of SEM-pictures, LM, and visual inspection is it not possible to determine neither the reason behind this change nor if this change represents an improvement of the material performance. As described below, after additional analysis with FIB, this topic is revisited.

With a higher base temperature during the ELM-like heat loads, i.e. 400 °C, the 'ELM reference' exposed to F_{HF} 12 exhibited a roughening of the surface. This, or any other change in surface morphology, was not detected for the samples pre-exposed to S-H/He and M-H/He, shown in figures 4.6 and 4.7, respectively. However, the L-H/He pre-exposed sample loaded with H400-12 has indications of surface roughening and, in addition, the formation of two singular small cracks, which are not connected to each other. One of these cracks is featured in figure 4.8. This does not fall under the category of a *Crack Network*, because of their limited length and the fact that they are not connected with other cracks. Nor does it constitute what is characterized as *Crack Initiations*, due to the shape and width of these two singular cracks.

Laser profilometry, and the R_a parameter derived from this data, are

compared with the initial analysis results. The maximum difference in R_a that is found between the pre-exposed samples with ELM-like loading and the pre-exposed sample without ELM-like loading is 0.05 µm and 0.08 µm for S-H/He and M-H/He, respectively, which is lower than the stipulated threshold value that needs to be achieved. In both cases this maximal difference is found with the cracked sample, i.e. HRT-12 exposure. Furthermore, the H400-12 reference sample has an R_a of 0.47 µm, which is 0.12 µm higher than the R_a of 0.35 µm for the M-H/He sample with H400-12 exposure. This difference is above the threshold value and shows that the total roughening after H400-12 is higher for pristine tungsten than for M-H/He tungsten. For samples with S-H/He or M-H/He pre-exposure there is no indication of ELM-induced damage detected in the R_a-values.

The samples with L-H/He pre-exposure, which have encountered recrystallization during the pre-exposure in GLADIS, have a relevant R_a difference for one combination of loading conditions, i.e. H400-12. Under these transient heat loads is a roughness increase also expected as the 'ELM reference' samples in subsection 3.2.1 showed. However, the increase for the L-H/He pre-exposed sample, i.e. 0.09 µm, has just met the threshold value and is notably smaller than the roughness increase for the H400-12 reference sample, i.e. 0.39 µm.

In the R_a-values of the H/He pre-exposed samples is no degradation of the thermal shock behaviour due to particle pre-exposure detected. Under one combination of loading conditions, i.e. L-H/He with H400-12, an R_a increase is detected, but that also occurred for that H400-12 with the 'ELM reference' sample. In all other cases the variation of the R_a is within the normal fluctuation, even if the 'ELM reference' sample had a change in roughness. Therefore, it is concluded with respect to the roughness that the H/He pre-exposure have either no effect on the thermal shock behaviour, which is most likely, or it might partially mitigate or conceal the thermal shock damage, as is indicated by the total roughening for the H400-12 reference that is higher than the total roughening for H400-12 on a M-H/He pre-exposed sample.

FIB-sections were performed on the HRT-12 exposed samples to determine if the ELM-like loads altered the H/He-induced damage located in a near-surface layer, particularly around the cracks. Such an analysis is very localised and is not per se representative for the whole surface. In order to take this into account, several FIB-sections were made in specifically chosen regions on the surface. The sections on the S-H/He pre-exposed sample which was loaded with HRT-12, as shown in figure 4.10, show the existence of a ∼200 nm deep modified layer. This was also observed in the TEM-image for the S-H/He reference sample in figure 3.13. The ELM-induced crack formation did not result in any observable changes.

The FIB-sections for the other combination of loading conditions where a crack network was formed, i.e. HRT-12 transients after pre-exposure with L-H/He, resulted in the same observations. There is no difference in the sub-

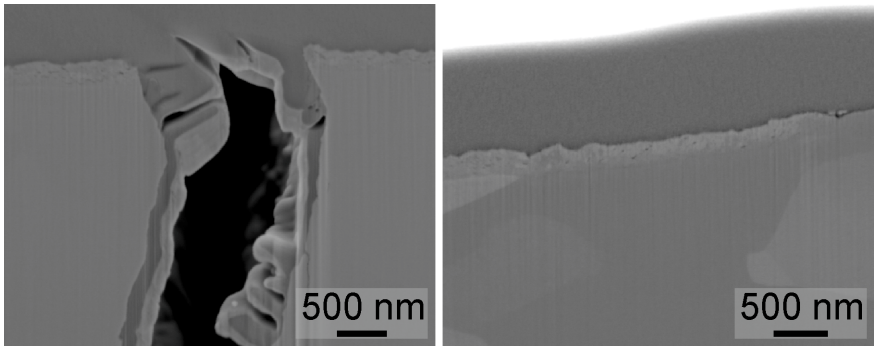

Figure 4.10: FIB performed on S-H/He pre-exposed tungsten which is loaded with HRT-12 in JUDITH 1. The two FIB-sections are taken ∼200 µm apart from each other. The sample was covered by a protection layer from platinum before FIB, which is still visible at the top of each image.

surface layer between the L-H/He reference sample and the L-H/He sample with ELM-exposure, independent of the location on the sample surface, i.e. near a crack or between two cracks. The M-H/He sample loaded with HRT-12 transients, which did not crack, had as well no ELM-induced modifications of the H/He-effects detected in the near-surface layer, as shown in figure 4.11.

Metallographic cross sections were subsequently made from each sample. The earlier mentioned recrystallization and grain growth, can again be seen for the cross sections of each L-H/He pre-exposed sample. An example of this is shown in figure 4.12. Furthermore, the substantial amount of grain loss that was observed on L-H samples, is not seen at all on any cross section. This shows that the H/He-induced modifications, particularly the formation of sub-surface cavities and the He implantation, did not lead to a substantial loss of cohesion between the grains during the recrystallization, which is observed for hydrogen exposure in subsection 4.1.1. The helium implantation can have resulted in a pinning of crystal defects, which would reduce the decrease in cohesion during recrystallization. An extensive TEM investigation is required to confirm if this is indeed the main mechanism.

The only ELM-damage that is observed on the cross sections, are the cracks that were formed after HRT-12 transients for the S-H/He and L-H/He pre-exposed samples, as seen in figure 4.13. However, only a few cracks were observed, which influences the reliability of the measured crack depth data. These measurements result for the S-H/He sample in a crack depth between 110–164 µm with a mean of 138 µm, while for the L-H/He sample this is located between 241–365 µm with a mean of 292 µm. These crack depths are for S-H/He and L-H/He similar to values for S-H and L-H, respectively. Consequently, the S-H/He pre-exposed sample has a similar

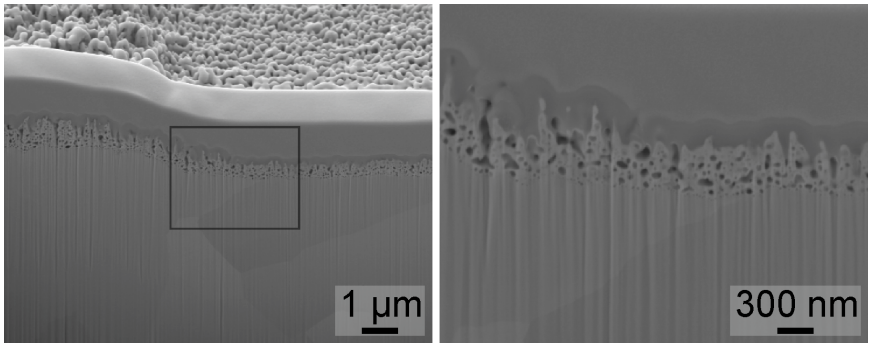

Figure 4.11: FIB performed on a M-H/He pre-exposed sample which is loaded with HRT-12 in JUDITH 1. The two pictures are taken from the same FIB-section, but differ in magnification. The sample was covered by a protection layer from platinum before FIB, which is still visible at the top of each image.

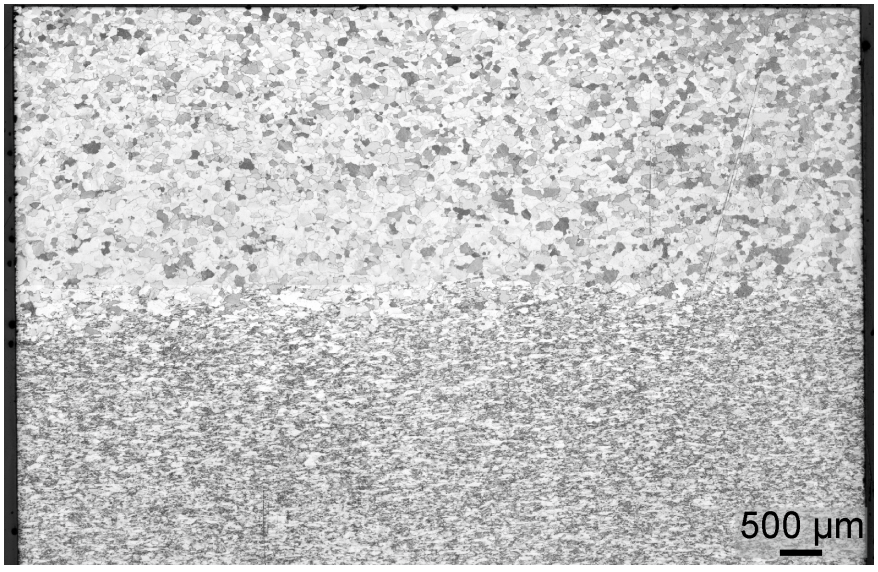

Figure 4.12: LM pictures of an etched cross section of a sample loaded in JUDITH 1 to H400-12 after pre-exposure in GLADIS with L-H/He. The area of recrystallization and grain growth, 3.5 mm to 4 mm deep, is distinguishable from the bulk material.

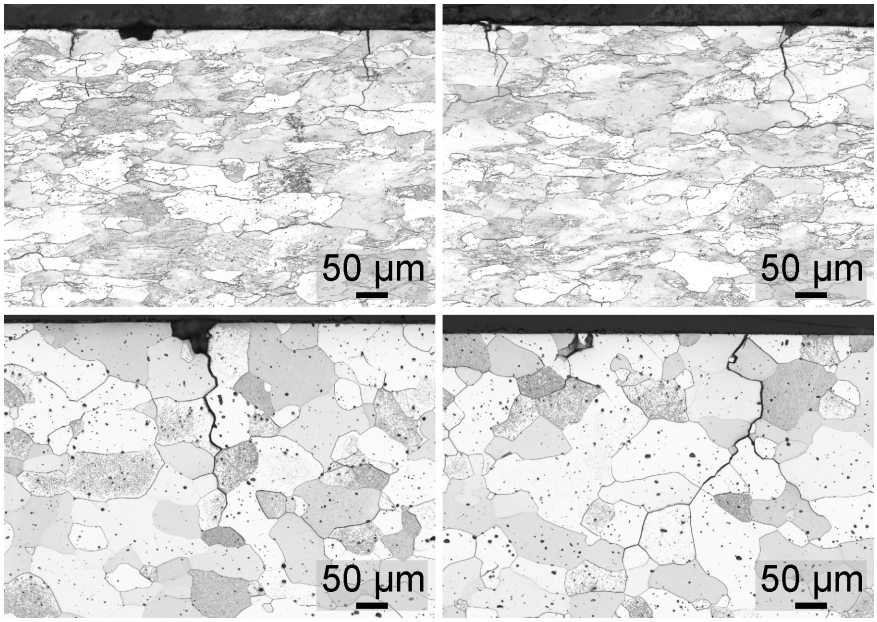

Figure 4.13: LM pictures of an etched cross section of the cracked samples, which were exposed in JUDITH 1 to HRT-12 after a pre-exposure in GLADIS with S-H/He (top), and L-H/He (bottom), both on two different locations.

crack depth as the reference HRT-12 sample, but the L-H/He pre-exposed sample has deeper cracks than the reference. The H/He pre-exposure only has an effect for the sample which is recrystallized, which would be an effect from the recrystallization and not the H/He pre-exposure itself.

Taking into account the information acquired from the different analysis methods, a damage mapping after ELM-like transients is made for the hydrogen/helium pre-exposed samples, as shown in figure 4.14. Due to the damage induced by the H/He particle flux in GLADIS before the heat load experiments were performed in JUDITH 1, the category *Additional Surface Damage*, described in subsection 4.1.1, is used instead of the category *Surface Modifications*. Moreover, independent of the damage category that was assigned to a specific combination of transient heat loads and mixed hydrogen/helium pre-exposure, the H/He induced cavities and surface extrusions were not altered.

For each sample, independent of the H/He pre-exposure and the base temperature during the ELM-like heat loading, there was no damage detected after F_{HF} 6 transients. The formation of a crack network, which occurs for the 'ELM reference' samples after HRT-12, can also be found for the mixed hydrogen/helium pre-exposed samples at HRT-12. However, this

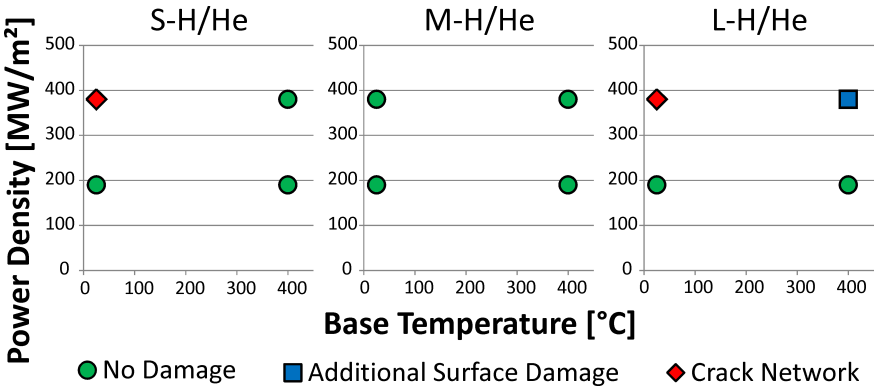

Figure 4.14: The damage mapping after ELM-like thermal loads for the samples that were pre-exposed with a mixed hydrogen/helium-beam in GLADIS.

only happens for the S-H/He and L-H/He pre-exposed samples, since the M-H/He sample stays undamaged. Furthermore, while there is additional surface modification expected after H400-12, this only occurred for the L-H/He pre-exposed sample. For none of the H/He pre-exposed samples is any deterioration observed in the thermal shock behaviour, while for some loading conditions even an apparent improvement is noticeable with respect to the 'ELM reference' damage mapping shown in figure 3.20.

One of these differences is the lack of ELM-induced damage found for H400-12 on the hydrogen/helium exposed samples that were not recrystallized, i.e. S-H/He and M-H/He. This indicates, similar as for the S-H and M-H pre-exposed samples in subsection 4.1.1, that the particle pre-exposure could conceal or partially decrease the ELM-induced damage and at least does not have a deteriorated thermal shock behaviour. Due to the lack of crack formation, it is excluded that the particle exposure made the sample surface brittle at 400 °C. Since this behaviour is also found for the pure hydrogen-exposed samples, the assumption is made that this effect would be caused by a common factor in these samples, namely the implantation of hydrogen inside the sample in a layer up to 120 nm deep. Although this does not result in increased hydrogen retention, as shown in table 3.4 and 3.6, this can nevertheless alter the sample and its material properties.

The other noticeable change in the damage mapping can be seen for M-H/He pre-exposed samples. Under each ELM-like thermal loading condition, including HRT-12 where the formation of a crack network is expected, these samples stay undamaged. The difference with M-H sample, which did not had this improvement, is the presence of helium during the particle exposure. A comparison between S-H and S-H/He, or L-H and L-H/He, did not show in neither case an improvement or change in thermal shock

behaviour. Therefore, the retention of helium in the tungsten sample is not sufficient to explain this change. Because experiments with different tungsten grades have shown that 100 pulses are sufficient for brittle crack formation [101], the lack of cracking after HRT-12 for the M-H sample is most likely not a statistical effect.

An hypothesis is that the other clear observable effect of the H/He particle flux, i.e. the sub-surface bubbles and/or the H/He-induced surface structures, is responsible for this change. The dominant mechanism might be that the material has a thin porous cavity-rich layer which can facilitate the thermal expansion and contraction without an accumulation of stress and prevent in this way the formation of cracks. Throughout the investigation, no increase of the depth of the H/He-induced layer is observed, so the depth of the sub-surface layer, up to a few 100 nm, stays small in comparison with the JUDITH 1 electron penetration depth of 7 µm. The H/He-modified sub-surface layer will alter the thermal conductivity, but the extent to which this occurs and the effects it has are not known yet. Hence, the heat penetration depth of the transient thermal loads is considered to have no effect, but the temperature of the surface and in the porous layer during transient thermal loads might play a role. In addition, an increase of the effective surface, as has been suggested in literature as a reason for the increased cracking resistance of fuzzy surfaces [104], also occurs for these samples. When it is taken into account that the recrystallization, which manifests itself at the L-H/He sample, weakens the material and increases the ductility, the observed damage at L-H/He can still be considered consistent with these hypothesises.

4.1.3 ELMs at high temperature on pre-exposed W

To further investigate the influence of particle pre-exposure on the thermal shock behaviour, a dedicated experimental campaign was set-up with the focus on the high surface temperatures that can occur in future fusion devices. For that purpose, the transient loading conditions H1000-6 and H1000-12, as described in subsection 3.2.1, are combined with the six different particle pre-exposure conditions, i.e. S-H, M-H, L-H, S-H/He, M-H/He, and L-H/He. In total, as summarized in table 4.3, this leads to 12 different combinations of loading conditions. The focus of these experiments is located on the crack initiations observed with the 'ELM reference' samples and the detection of any deterioration of this damage type.

Due to a technical failure of the electron beam deflection system in JUDITH 1 during the H1000-6 transient heat load tests, the heat flux was deposited on a 4 mm long line instead of a 4 mm × 4 mm area for the L-H and the L-H/He pre-exposed samples. As a consequence, the absorbed power density was much higher and the samples were melted. Hence, there is no data available for H1000-6 exposure on samples preloaded with L-H and L-H/He.

Table 4.3: Overview of the loading conditions for ELM-like loads applied to tungsten which was pre-exposed to a either a pure H-flux or a mixed H/He-flux.

First Exposure	Label	Second Exposure	Label
H-flux at 600 °C	S-H	$100 \times F_{HF}$ 6 at 1000 °C	H1000-6
H-flux at 600 °C	S-H	$100 \times F_{HF}$ 12 at 1000 °C	H1000-12
H-flux at 1000 °C	M-H	$100 \times F_{HF}$ 6 at 1000 °C	H1000-6
H-flux at 1000 °C	M-H	$100 \times F_{HF}$ 12 at 1000 °C	H1000-12
H-flux at 1500 °C	L-H	$100 \times F_{HF}$ 12 at 1000 °C	H1000-12
H/He-flux at 600 °C	S-H/He	$100 \times F_{HF}$ 6 at 1000 °C	H1000-6
H/He-flux at 600 °C	S-H/He	$100 \times F_{HF}$ 12 at 1000 °C	H1000-12
H/He-flux at 1000 °C	M-H/He	$100 \times F_{HF}$ 6 at 1000 °C	H1000-6
H/He-flux at 1000 °C	M-H/He	$100 \times F_{HF}$ 12 at 1000 °C	H1000-12
H/He-flux at 1500 °C	L-H/He	$100 \times F_{HF}$ 12 at 1000 °C	H1000-12

A visual inspection, LM, and SEM-pictures are used for the other samples, to have a first comparison for each combination of loading conditions. This did not show any differences between the samples exposed to the moderate thermal shocks of H1000-6 and their respective 'GLADIS reference' with either method. While on the other-hand, the intense exposure to H1000-12 leads to surface modifications that can be observed with these methods, as shown in figure 4.15. These entails either a noticeable roughening, the formation of crack initiations, or a combination of both. Only in the case of the L-H pre-exposure the damage showed only surface roughening, what can be a direct effect of the recrystallization of the L-H sample, that did result in an increased plasticity. Additionally a single broader crack is detected on the L-H/He sample, but it is not clear why this sample has also crack initiations, while it is also recrystallized like the L-H specimen.

The observed crack initiations, which occurred after H1000-12 transients for all pre-exposed samples except L-H, are similar to the crack initiations observed for the respective 'ELM reference' samples, as is shown by an analysis of the crack width. For the 'ELM reference', the average width of the crack initiations is 0.2 µm with a standard deviation of 0.3 µm. The highest average width for the crack initiations, 0.5 µm with a standard deviation of 0.4 µm, is found for the sample with M-H/He pre-exposure. In contrast, the average crack width for a HRT-12 crack network is 3.3 ± 1.3 µm. Hence, it is determined that the crack initiations observed for the particle pre-exposed samples are the same damage type as the crack initiations observed at the 'ELM reference'.

The R_a, as shown in figure 4.16, was determined through laser profilometry. These results show for each sample that H1000-6 transients do not result in damage, since the maximal observed increase in R_a between a

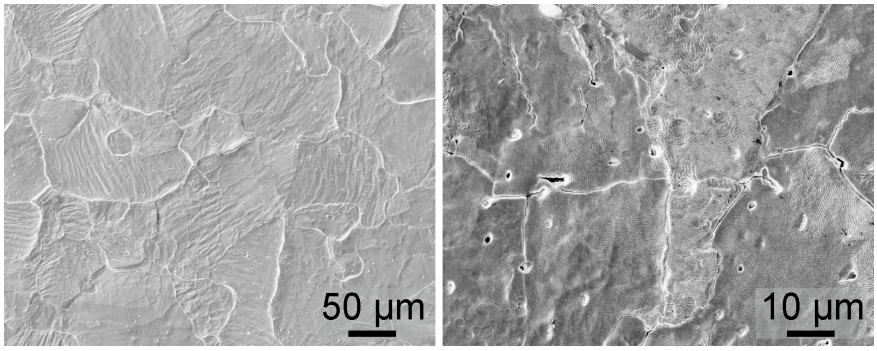

Figure 4.15: SEM pictures of tungsten which is first pre-exposed in GLADIS and thereafter exposed in JUDITH 1 to H1000-12. The resulting surface damage is either an observable deformation as shown for the L-H pre-exposure (left), or the occurrence of crack initiations as shown for the S-H/He pre-exposure (right).

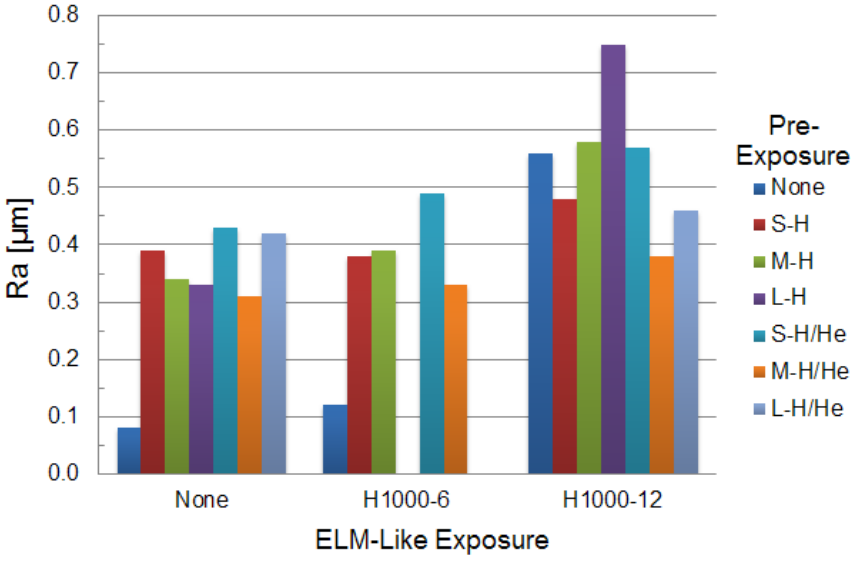

Figure 4.16: The roughness value R_a, derived from a 50 points/mm laser profilometry scan, after the experiments with ELM-like thermal shocks at a base temperature of 1000 °C in JUDITH 1 on tungsten that has been pre-exposed to a particle beam in GLADIS. In addition, the respective 'GLADIS references' and 'ELM references' are also given for comparison.

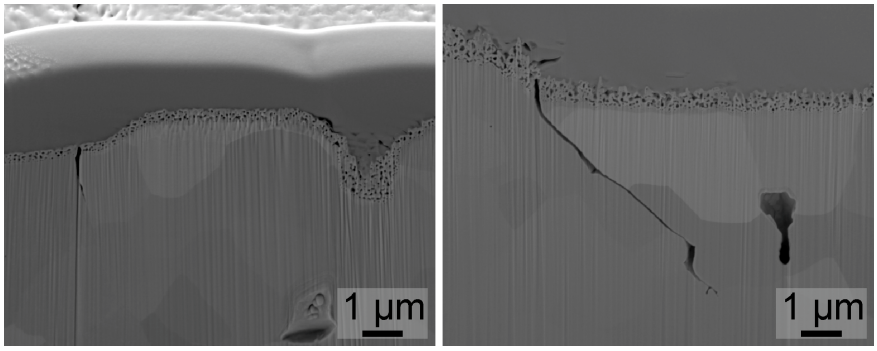

Figure 4.17: Cross sections made through FIB from samples exposed to H1000-12 after a mixed hydrogen/helium pre-exposure in GLADIS with S-H/He (left) or M-H/He (right). The samples were covered by a platinum protection layer before FIB, which is still visible at the top of each image.

sample and its respective 'GLADIS reference' is merely 0.06 µm.

After H1000-12 transients, the pre-exposed samples have an increase in R_a that is higher than the threshold value for S-H, M-H, L-H, and S-H/He. Only for the L-H sample, which is recrystallized and therefore can have an increased ductility [103], this increase in R_a is in the same order of magnitude as the increase that occurred for the 'ELM reference' H1000-12 sample. This L-H sample differ from the other samples with H1000-12 exposure, because it did not encounter the formation of crack initiations. As observed in subsection 4.1.1 with H400-12, the highest increase in roughness appears for the L-H sample, where it follows the damage behaviour of the 'ELM reference'. The other three roughened samples, i.e. S-H, M-H, and S-H/He, show after H1000-12 an increase that is above the threshold value, but that increase is not as high as the roughness increase for the 'ELM reference'. The total roughness for S-H, M-H, and S-H/He is with respect to the threshold value similar to the total roughness of the H1000-12 reference.

In case of the remaining two samples with H1000-12 exposure, i.e. M-H/He and L-H/He, the difference in R_a after H1000-12 is 0.07 µm and 0.04 µm, respectively, so no ELM-induced roughening is observed. Furthermore, the difference in total roughness of the H1000-12 reference sample, i.e. 0.56 µm, and the total roughness of the M-H/He pre-exposed and the L-H/He pre-exposed samples, i.e. 0.38 µm and 0.46 µm, respectively, is higher than the stipulated treshold value to be considered distinct enough. A lack of observed ELM-induced damage in the roughening occurs only for the two samples which were covered with surface extrusions.

As an additional analysis method, FIB-sections were performed on the H/He pre-exposed samples that are loaded with H1000-12 transients, as shown in figure 4.17 for the S-H/He and M-H/He pre-exposure. From the

FIB-sections, it is due to the H/He-induced modifications on and below the surface, not evident to determine the exact depth of the crack initiation. This was not present on the 'ELM reference' sample. In order to be consistent, the deepest possible depth is taken, although this would result in an overestimation in some cases. The depth measurements of the crack initiations from all the H/He pre-exposed samples are located between around ∼980 nm and around ∼5.45 µm. These values lie within the range of crack initiation depth that is found for the respective 'ELM reference' sample mentioned in subsection 3.2.1, but these crack initiations are deeper than the depth of the H/He-induced cavities.

After the FIB-analysis it is observed that the cavities present in the sub-surface layer of the S-H/He sample exposed to H1000-12 have undergone a considerable growth in size. This can be noticed when a comparison is made between the high magnification TEM-picture of the S-H/He reference sample in figure 3.13 and the sample exposed to H1000-12 after S-H/He pre-exposure in figure 4.17. From these pictures the maximal width is determined from the observable cavities and/or cleavages in a manually performed process.

In order to achieve the most accurate data, a different magnification was used in the analysis of both samples. Nevertheless, sufficiently sharp pictures at the required magnifications were not available, which makes it possible that some cavities are not detected, or two cavities are taken together and considered to be a single, larger, cavity. The analysis resulted for the S-H/He reference in a maximum width between 4.7–85.5 nm with a mean maximum cavity width of 23.9 nm. For the S-H/He pre-exposed sample loaded with H1000-12 transients, the maximum width was located between 19.4–148.5 nm with a mean maximum cavity width of 61.9 nm. The sub-surface layer in which these cavities are located has for both cases the same depth-range.

It has to be noticed that the cavities and cleavages for the S-H/He reference are clearly elongated, while this is not the case for the sample loaded with H1000-12 transients. Therefore, the volume-increase in the cavities is larger than the increase of the maximal cavity width would suggest. A clear example of the cavity growth can be seen in figure 4.18. In this figure two SE pictures of the FIB section for both samples, are shown with the same magnification. While the S-H/He sample loaded with H1000-12 transients has clear cavities, the S-H/He reference only has a visible porous sub-surface layer where no individual cavity can distinctly be detected.

This bubble growth is only observed for the S-H/He sample after the H1000-12 transients. Neither for other particle pre-exposures, nor for other transient heat loads for which FIB is performed this can be noticed. For example, figure 4.10 shows that HRT-12 transients on an S-H/He sample generates a porous sub-surface layer that is in accordance with the S-H/He reference sample. The explanation for this behaviour is given in Eq. (3.1), the Greenwood mechanical equilibrium condition. Apparently there is even

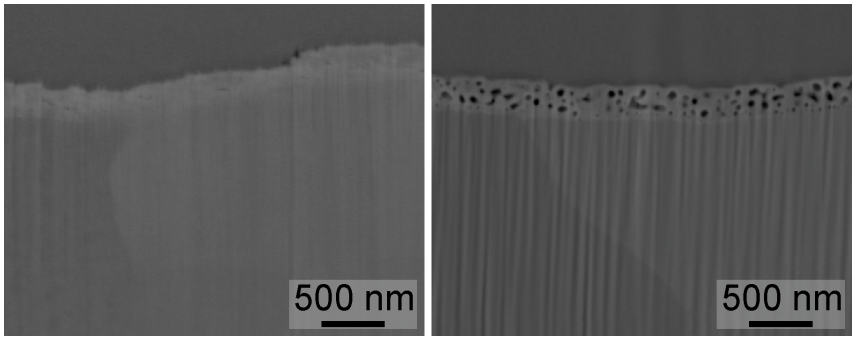

Figure 4.18: FIB cross sections from tungsten either only exposed to S-H/He (left) or first exposed to S-H/He and subsequently exposed to H1000-12 transients (right), showing a different size of the cavities inside the sub-surface layer between both samples, while the depth of the sub-surface layer is the same. The samples were covered by a platinum protection layer before FIB, which is still visible at the top of each image.

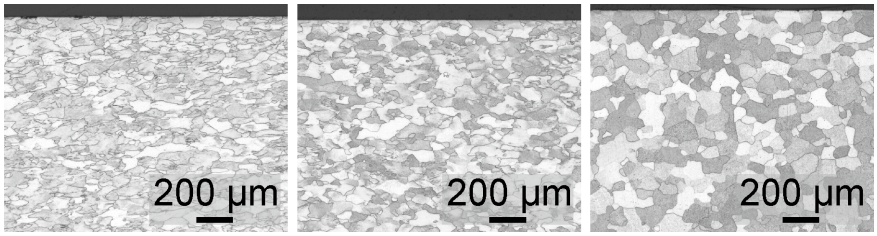

Figure 4.19: LM pictures of a polished cross section of the samples, which were exposed in JUDITH 1 to H1000-12 after a pre-exposure in GLADIS with S-H (left), M-H (middle), and L-H (right).

without a particle flux directed towards the material during the transient loading, still a pressure inside the cavity. Due to the increased temperature, and the resulting reduced shear modulus, the minimal pressure that is required for bubble growth will be decreased. Therefore, the main factor will either be the base temperature of 1000 °C that is obtained for the transient heat load testing or the combination of the temperature rise during a transient with the high 1000 °C base temperature. Taking into account the limited pulse duration of the transients, the base temperature is assumed to be the dominant factor.

The surface temperature of the S-H/He loaded sample is merely 600 °C during the particle exposure. Consequently, the pressure inside such a bubble that is required before growth can occur is higher during the particle exposure in GLADIS than during the transient heat loading in JUDITH 1. Furthermore, the lack of an alteration in the cavities for the M-H/He and

the L-H/He samples strengthens the conclusion that the temperature is the main contributing factor, because these samples have a surface temperature of respectively 1000 °C and 1500 °C during the H/He exposure. Hence the required pressure for growth will not be lower during the transient experiments than it was during the particle exposure.

The metallographic cross sections, made for each sample and shown in figure 4.19 for H1000-12 loading after pure hydrogen pre-exposure, do not result in the detection of any additional damage. None of the crack initiations can even be seen on the cross sections, which strengthen the observation made from the FIB-sections that these crack initiations are the same damage type as was seen on their respective 'ELM reference' sample, i.e. H1000-12 loading. Also there is no occurrence of substantial grain loss in these samples. The recrystallization for the L-H/H and the L-H/He pre-exposed samples could clearly be seen and is in line with the previous observations.

Through combining the data from the different analysis methods, each set of loading conditions is assigned a damage category. Each pre-exposed sample that was exposed to H1000-6 transients is categorized as *No Damage*. The category *Additional Surface Damage* is only assigned to the H1000-12 loaded sample with L-H pre-exposure. All the other samples, i.e. transient H1000-12 loading on a sample pre-exposed with S-H, M-H, S-H/He, M-H/He, or L-H/He, belong to the category *Crack Initiations*.

This clarifies that also after ELM-like transient heat loads at higher temperatures, there is no decrease of the damage threshold due to the particle pre-exposure. Both for pure hydrogen as for the mixed hydrogen/helium exposure this statement is valid. The only deviation in damage category could be noticed for the L-H pre-exposed sample loaded with H1000-12, whose damage is limited to surface roughening. A decrease of the yield strength and ultimate tensile strength and an increase of plasticity after recrystallization [103] is deemed to be responsible for the absence of crack initiation. Stress relief in the sub-surface layer could in this case only be achieved through plastic deformation, since crack initiations are not formed. Hence, this sample has, as the only one, a R_a that is substantially higher than it is the case for the reference sample, which is not necessarily a manifestation of damage deterioration. While there is no indication of synergistic effects between the ELM-like exposure at high temperature and the particle pre-exposure, that leads to an clear improvement of the thermal shock behaviour, there is also no degradation of the material performance [87].

In addition, the roughness of the M-H/He and L-H/He samples with H1000-12 exposure, which is similar to the roughness of respectively the M-H/He and L-H/He reference samples, is in both cases below the roughness of the H1000-12 exposure. Hence, the possibility that H/He pre-exposure might conceal or partially reduce the ELM-induced damage, as mentioned in subsection 4.1.2, is here again indicated.

4.1.4 1000 ELM-like loads on H/He pre-exposed W

The ELM-like loading conditions with 1000 pulses, i.e. T1000-6, T1000-12, and T1000-48, as described in subsection 3.2.2, are applied on pre-exposed samples. Only tungsten with a mixed H/He pre-exposure was used during these experiments, i.e. S-H/He, M-H/He, and L-H/He. This results, as summarized in table 4.4, in nine different loading conditions.

A first analysis is performed through visual inspection, LM, and SEM to investigate the effect of the pre-exposure on the thermal shock behaviour. For the S-H/He pre-exposed samples, there is no damage or surface modification observable after the T1000-6 transient loading. On the sample with T1000-12 exposure, a combination of strong deformation and either crack initiations or deeper cracks can be detected, as shown in figure 4.20. This looks identical to the ELM-induced damage on a pristine sample, as shown in figure 3.21. Remnants of the erosion pattern, originating from the S-H/He pre-exposure, are still found on the surface.

Tungsten that after an S-H/He pre-exposure is loaded with T1000-48 ELM-like loads, shown in figure 4.21, no longer has any features of the erosion pattern that remain. As occurred to the reference sample without pre-exposure shown in figure 3.17, the loaded area of the pre-exposed sample is divided in a rougher and a smoother area. Additionally, the surface around the loaded area has deformed and has (shallow) cracks, which resulted for some cracks in a melting of the crack edge.

No damage is observed on tungsten with M-H/He pre-exposure after it is loaded to T1000-6. For M-H/He pre-exposed tungsten that is loaded with T1000-12 and T1000-48 transients, as shown in figure 4.22, ELM-induced damage is found. This damage takes the form of surface cracking and/or crack initiation in combination with a strong deformation for the T1000-12

Table 4.4: Overview of the loading conditions where 1000 ELM-like loads at a base temperature of 1000 °C are applied to tungsten which was pre-exposed to a mixed H/He-flux.

First Exposure	Label	Second Exposure	Label
H/He-flux at 600 °C	S-H/He	$1000 \times F_{HF}$ 6 at 1000 °C	T1000-6
H/He-flux at 600 °C	S-H/He	$1000 \times F_{HF}$ 12 at 1000 °C	T1000-12
H/He-flux at 600 °C	S-H/He	$1000 \times F_{HF}$ 48 at 1000 °C	T1000-48
H/He-flux at 1000 °C	M-H/He	$1000 \times F_{HF}$ 6 at 1000 °C	T1000-6
H/He-flux at 1000 °C	M-H/He	$1000 \times F_{HF}$ 12 at 1000 °C	T1000-12
H/He-flux at 1000 °C	M-H/He	$1000 \times F_{HF}$ 48 at 1000 °C	T1000-48
H/He-flux at 1500 °C	L-H/He	$1000 \times F_{HF}$ 6 at 1000 °C	T1000-6
H/He-flux at 1500 °C	L-H/He	$1000 \times F_{HF}$ 12 at 1000 °C	T1000-12
H/He-flux at 1500 °C	L-H/He	$1000 \times F_{HF}$ 48 at 1000 °C	T1000-48

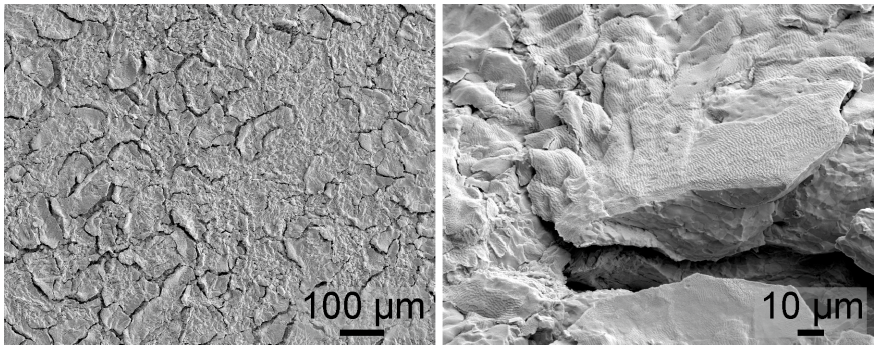

Figure 4.20: SEM images of tungsten which is first pre-exposed with S-H/He and subsequently loaded with T1000-12, indicating a strong deformation of the surface in combination with the occurrence of cracking.

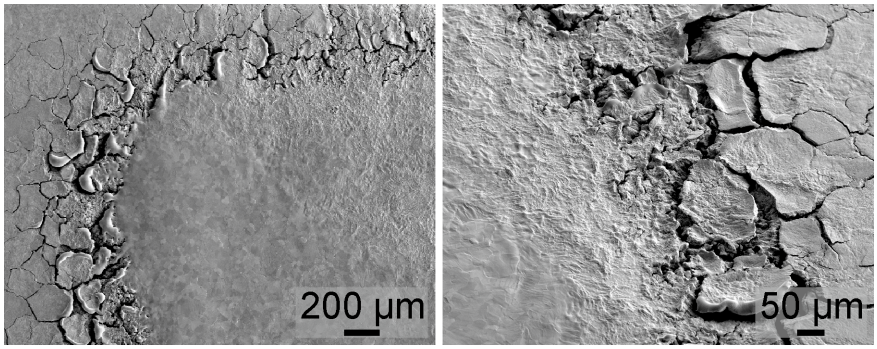

Figure 4.21: SEM images of tungsten which is first pre-exposed with S-H/He and subsequently loaded with T1000-48, where the surface around the loaded area is cracked, while the loaded area is divided in a rough and a smooth region.

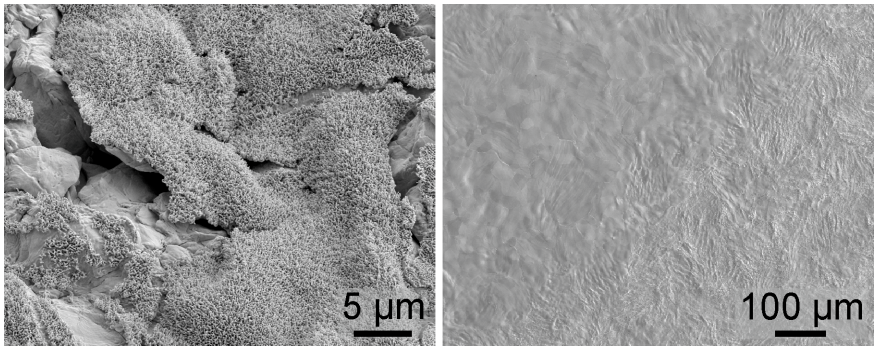

Figure 4.22: SEM images of tungsten which is first pre-exposed with M-H/He and subsequently loaded with T1000-12 (left) and T1000-48 (right).

exposure. However, the surface extrusions are on several locations within the ELM-loaded region not modified. In the case of T1000-48 exposure again a smooth region, due to local melting, and a rougher deformed region can be identified. The surface extrusions have completely disappeared in the ELM-loaded area and on the surface near the ELM-loaded area minor crack formation is found.

Although the vacuum conditions in JUDITH 1 should have prevented the oxidation of tungsten, an oxidation layer is observed during a visual inspection on the samples with L-H/He pre-exposure after the transient loading. This oxidation layer was present on the whole surface of the T1000-6 and T1000-12 loaded samples, but for the T1000-48 sample it only was present on parts of the surface that were not ELM-like loaded. Energy-dispersive X-ray spectroscopy (EDX) confirmed the presence of oxygen on the sample. Since the oxidation of tungsten can occur both at 1000 °C and below 1000 °C [105], it can not be concluded if the partial pressure of oxygen was too high during the experiments or if the vacuum was broken too soon after the experiment finished and the samples were still cooling down.

As shown in figure 4.23, the oxidation for the T1000-6 exposed sample is clearly visible on high magnification SEM. Instead of the H/He-induced surface extrusions, the surface is covered with tungsten oxide crystallites. The lower magnification images show that the whole loaded area is cracked, which did not occur for T1000-6 loading on pristine tungsten, S-H/He pre-exposed tungsten, and M-H/He pre-exposed tungsten. Because it is not known at which moment the oxidation took place, there are two possible causes for this ELM-induced damage at T1000-6. Most likely has the oxide layer, which is more prone to crack formation than bulk tungsten, cracked due to the transient heat loads and these small initial cracks could subsequently propagate and result in the observed crack network. Alternatively, the H/He pre-exposure might have resulted in decrease of the crack resis-

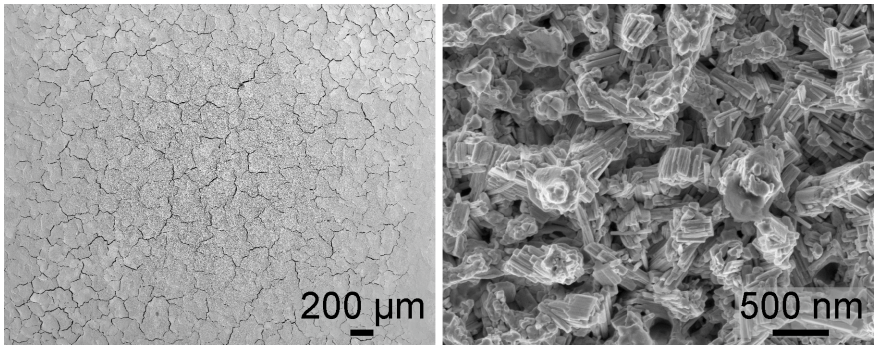

Figure 4.23: SEM images of tungsten which is first pre-exposed with L-H/He and subsequently loaded with T1000-6, showing the cracked surface and the formation of tungsten oxide on the surface extrusions.

tance, although this is not observed for any other sample so far. While neither cause can be ruled out, it is in all likelihood the oxidation that is responsible for this ELM-induced damage.

The sample with T1000-12 exposure has, as shown in figure 4.24, a combination of strong deformation and surface cracking, as is the case for the pristine tungsten, the S-H/He pre-exposed tungsten and the M-H/He pre-exposed tungsten with the same ELM-like loading. Although some SEM images suggest that the typical surface extrusions are still present on some locations, an analysis with higher modifications showed each time that this H/He-induced structures are all oxidized. Besides the oxidation, the observed damage after T1000-12 for this sample is identical to the damage that occurred for the S-H/He and M-H/He pre-exposed samples after T1000-12.

While the T1000-48 loaded sample with L-H/He pre-exposure also has oxidization, this does not occur in the ELM-loaded area. As is the case for the other T1000-48 loaded samples, the ELM-loaded area is characterized by a rough and a smooth region and lacks surface extrusions. The surface around the ELM-loaded area is cracked, similar to what is seen in figure 4.21, and shows melting around the crack edges. It can not be determined if the ELM-loaded area did not oxidise at all, or if the oxidation was removed during the tests.

The reason for the oxidation of the L-H/He pre-exposed tungsten, which occurred either during or after the ELM-like experiments in JUDITH 1, is not known. In subsequent and previous experimental campaigns of pre-exposed tungsten with similar loading conditions, this did not occur. After another test campaign with pristine tungsten, shown in figure 4.25, an oxide layer is found that not only covers the ELM-loaded regions and the sample surfaces, but also parts of the sample sides. This rules out that the pre-exposure is responsible for the oxidation, although it might be the

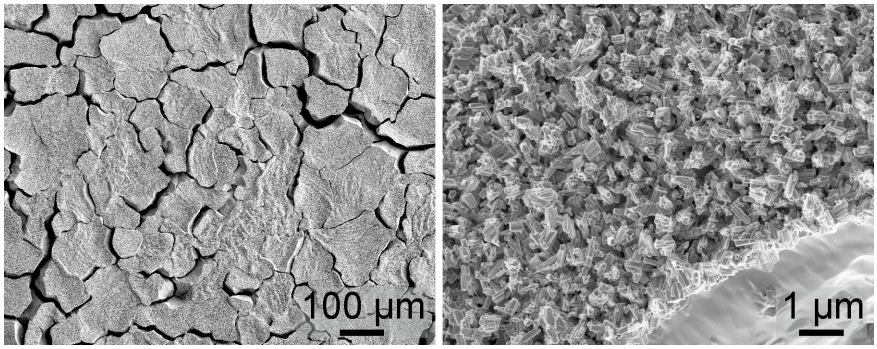

Figure 4.24: SEM images of tungsten which is first pre-exposed with L-H/He and subsequently loaded with T1000-12, indicating a strong deformation of the surface in combination with the occurrence of cracking and an oxidization of the surface extrusions.

case that the oxidization-process is facilitated by the surface extrusions due to an increase of the effective surface. However, as long as it is unclear when the oxidation occurred, i.e. during the transient heat loading or after the transient heat loading, it is not possible to determine either if the suggested facilitation of the oxidization has occurred, nor if the oxidization is responsible for any observed changes in the thermal shock behaviour.

The R_a of the samples, calculated based on a 50 points/mm laser profilometry scan, is shown in figure 4.26. Here also no damage is observed after T1000-6 transients for the reference sample, the S-H/He pre-exposed tungsten and the M-H/He pre-exposed tungsten. For oxidized tungsten, i.e. pre-exposed with L-H/He, that cracked after T1000-6 transients, the surface roughening clearly increased to the same order of magnitude compared to samples with similar cracking, e.g. pristine tungsten loaded with T1000-12.

The increase of roughening after T1000-12 exposure for the S-H/He and L-H/He is higher than for the pristine tungsten. Because the size of the sub-surface cavities for S-H/He pre-exposed tungsten increases after ELM-like loading at 1000 °C, as shown in subsection 4.1.3, the growth of sub-surface cavities can be responsible for additional roughening under T1000-12 loading. The L-H/He pre-exposed sample, i.e. the oxidized tungsten, has a remarkably high roughness after T1000-12 transients with an R_a of 3.13 µm. After T1000-48 exposure, all the pre-exposed tungsten had a lower roughness than the pristine tungsten. It needs to be noted that the roughness is measured in the ELM-loaded area. Therefore, the cracking that occurred on the surface near the ELM-loaded area is not taken into account to calculate the R_a.

From the samples which cracked or had a melt layer, metallographic cross sections are made. In case of T1000-6 exposure, this only occurred for the L-H/He pre-exposed tungsten. As shown in figure 4.27, the cracks do

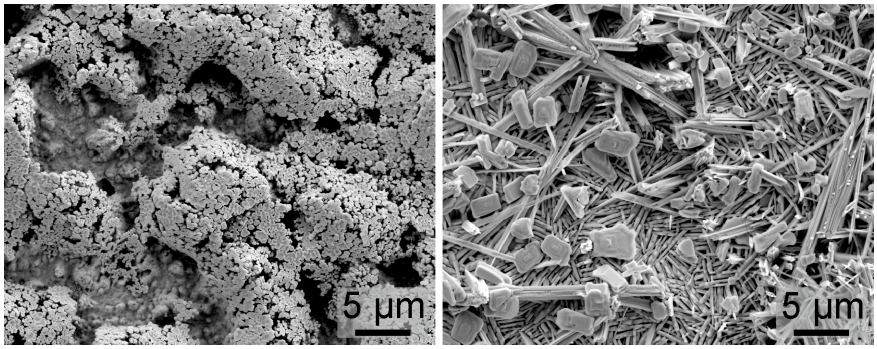

Figure 4.25: SEM figures of tungsten oxide formation on pristine, polished tungsten during or after JUDITH 1 experiments with H1000-12 transient loading either on the ELM-loaded area (left) or on a location of the surface not loaded (right).

not propagate in the bulk and the damage is confined to a layer of less than 100 µm. Grain loss in the ELM-loaded area, originating from the sample preparation, is observed on the cross section. This can be explained by a weakening of the grain boundary, a partial detachment of the grains from each other through small cracks, or a combination of the two.

Cross sections are made for all three pre-exposed tungsten samples that are loaded with T1000-12 transients, since they are all cracked. On the cross sections of the S-H/He and M-H/He pre-exposed tungsten, shown in figure 4.28, small cracking on the surface and a few minor cracks propagating parallel to the surface are observed. This could lead to local overheating, increased erosion and the release of tungsten dust. Additionally, what appears to be very small grains that have formed at the surface can be observed on some locations. The L-H/He pre-exposed tungsten after T1000-12 loading has similar cross sections as after T1000-6 loading, making the observations for T1000-6 loading also valid for T1000-12 loading.

In the case of T1000-48 ELM-like transients, the cross sections for each of the three pre-exposures, shown in figure 4.29, are similar. The part of the surface that was loaded with ELM-like transients has a modified microstructure in a layer up to ∼500 µm deep. No other damage on the cross sections can be identified in this ELM-loaded region. As expected from the SEM, cracks are observed on the surface near the ELM-loaded region.

One change in damage category is found between the 'ELM reference' samples with 1000 pulses and the exposures on pre-exposed tungsten, i.e. T1000-6 loading. For T1000-6 loading on the S-H and M-H/He pre-exposed tungsten, the damage category is *No Damage*, while for the L-H/He pre-exposed tungsten, the sample is categorized as *Crack Network*. This is

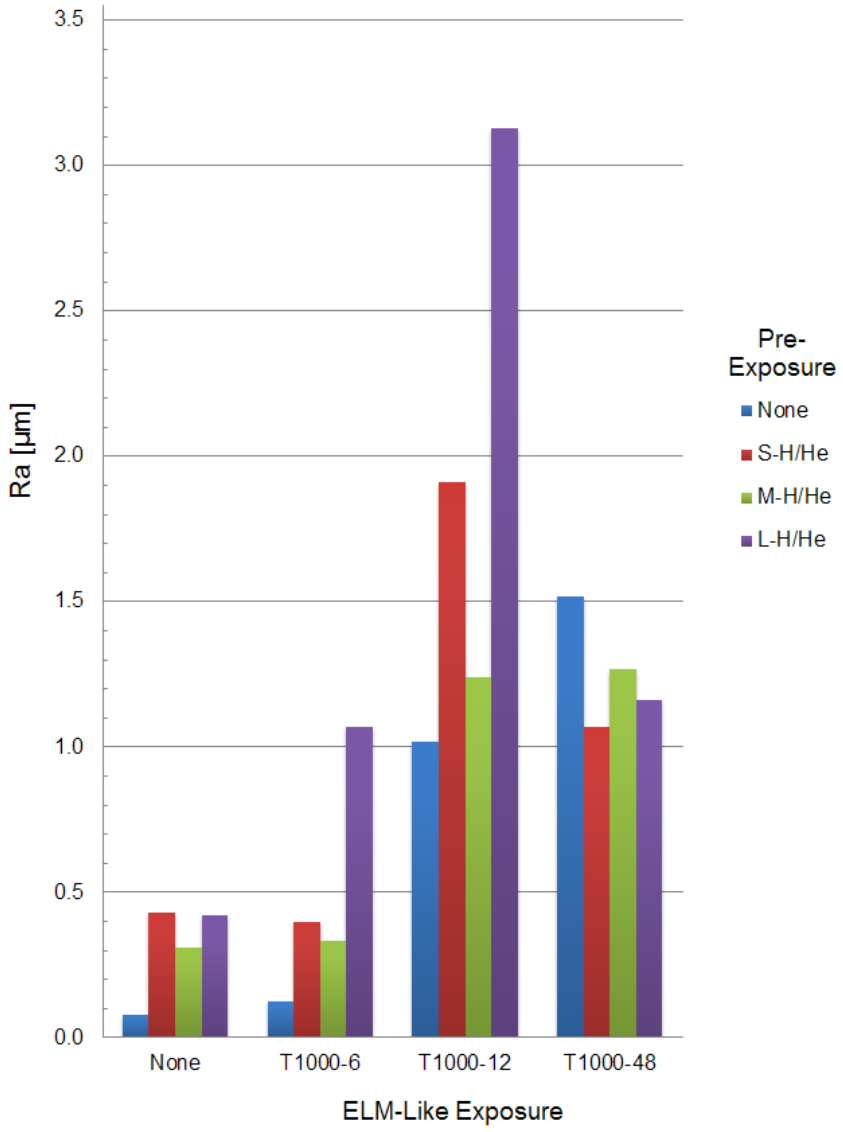

Figure 4.26: The R_a-value, derived from a 50 points/mm laser profilometry scan, after the experiments with 1000 ELM-like thermal shocks in JUDITH 1 on tungsten that has been pre-exposed to a mixed H/He beam in GLADIS. In addition, the respective 'GLADIS references' and 'ELM references' are also given for comparison.

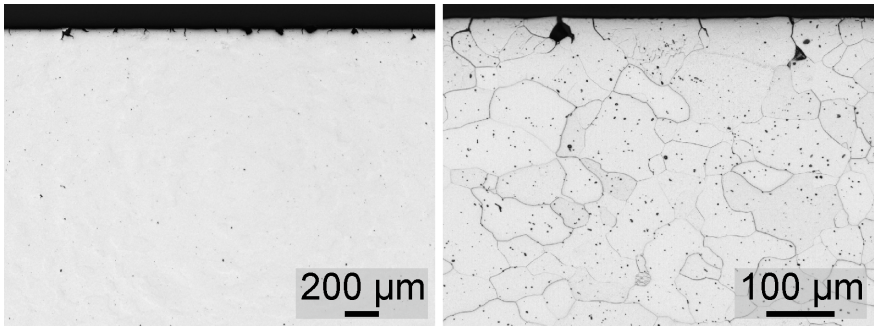

Figure 4.27: LM pictures of the cross section of L-H/He pre-exposed tungsten, which was exposed in JUDITH 1 to T1000-6. A polished overview of the loaded area (left) and an etched detailed view (right) are featured.

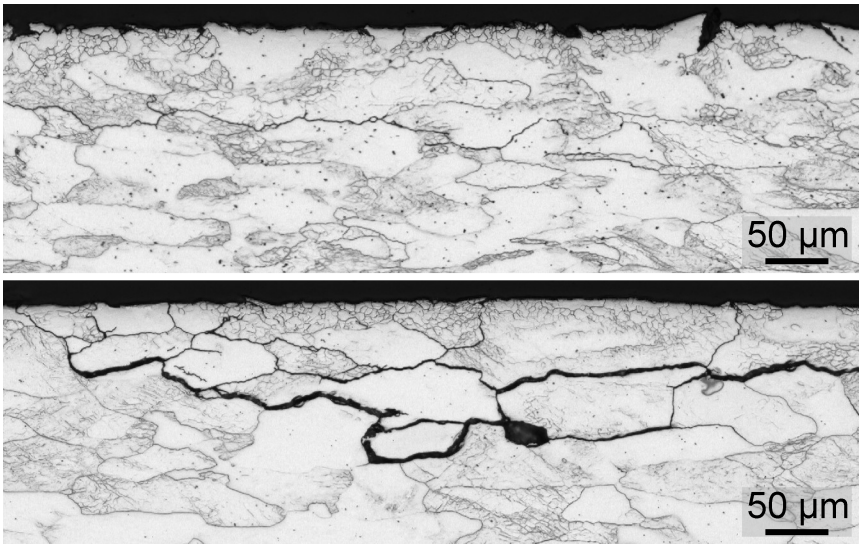

Figure 4.28: LM pictures of a detailed view from the etched cross section of S-H/He (left) and M-H/He (right) pre-exposed tungsten, which was loaded in JUDITH 1 to T1000-12.

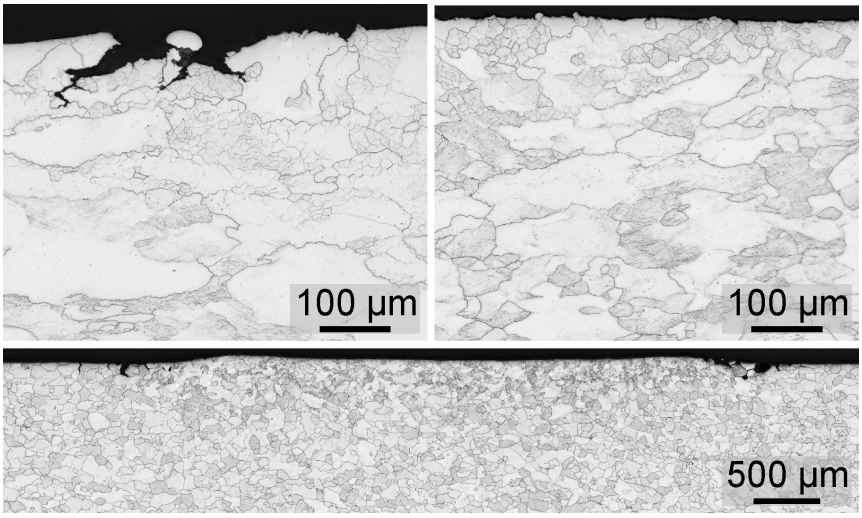

Figure 4.29: LM pictures from the etched cross sections of H/He pre-exposed tungsten, which was loaded in JUDITH 1 to T1000-48. The pictures contain a detailed view from the surface neighbouring the ELM-loaded area for S-H/He pre-exposed tungsten (left, top), a detailed view from the ELM-loaded area for M-H/He pre-exposed tungsten (right, top), and an overview for L-H/He pre-exposed tungsten (bottom).

for all three cases in contrast to the 'ELM reference' sample with T1000-6 loading, which belongs to the *Surface Modifications* category. However, it needs to be noted that the cracking of the L-H/He pre-exposed sample is probably related to the oxidation. The other samples have the same damage category as the reference samples, i.e. *Crack Network* for T1000-12 loading and *Melting* for T1000-48 loading.

Additionally, it is observed that the roughening for pre-exposed tungsten is higher than for pristine tungsten when the ELM-like loading caused the surface to heavily deform and initiate several smaller cracks. This indicates that if the pulse number is increased, the pre-exposure can have a negative effect on the thermal shock behaviour. For the T1000-48 loading this is also the case, since the 'ELM reference' sample only has sub-surface cracks in the area near the ELM-loaded region, while the pre-exposed samples showed also a strong deformation and crack initiations on the surface. These findings show that, especially for higher pulse numbers, a deterioration of the thermal shock behaviour has to be considered.

4.2 H/He-Irradiation of ELM-Like Loaded W

ELM-like loading conditions can damage tungsten on a macroscopic scale, as shown in subsection 3.2.1. In addition, TEM analysis shows that even the stress fields generated by low transient heat loads, i.e. ELM-like loads below the damage threshold, introduce crystal defects in tungsten, e.g. dislocations near grain boundaries, line dislocations, and clusters [106]. Hence, there are several differences between pristine and ELM-damaged tungsten samples, which potentially might lead to an alteration of the H/He-induced damage. This is investigated by first performing transient heat load experiments in JUDITH 1 on polished tungsten samples. Thereafter, the material is loaded with a mixed hydrogen/helium particle flux in GLADIS. A summary of the loading conditions is given in table 4.5.

As pre-exposure, four different transient ELM-like heat load tests were conducted three times on pristine samples, once for each sample geometry, i.e. S-, M-, and L-samples. The ELM-like loads correspond with the loading conditions above the damage threshold with as base temperature either room temperature or 400 °C. For the pre-exposures at RT, i.e. HRT-12 and HRT-48, the loaded area was covered with a crack network, while the pre-exposures at 400 °C resulted in surface roughening. The damage is completely in agreement with the observations for their respective 'ELM reference' sample, including the traces of local melting that are found after HRT-48 transients.

After the pre-exposure, the samples were irradiated with a mixed hydrogen/helium flux that corresponds to the 'GLADIS reference' S-H/He, M-H/He, and L-H/He. However, one sample got damaged during transport and could not be analyzed. This is the sample pre-exposed to HRT-48 and

loaded under L-H/He conditions.

The first analysis step is a visual inspection. Without optical equipment, it is only possible to observe the 4 mm × 4 mm area loaded during the pre-exposure in JUDITH 1 for the M-H/He exposed sample with HRT-48 pre-exposure and for the S-H/He exposed samples that were pre-exposed with HRT-48, H400-12, and H400-48. For the other samples, the pre-exposure area is only detectable with microscopy.

The S-H/He loaded samples with ELM-like pre-exposure has, as it is the case for the S-H/He reference sample, a matt surface. On the SEM pictures, as shown in figure 4.30, there is a distinct erosion pattern visible. They are similar for each of the four samples with ELM-like pre-exposure. Furthermore, they show a strong resemblance with the surface morphology of the reference sample, shown in figure 3.9. None of the pre-exposures resulted in a change of the H/He-induced surface morphology.

The same observations are made for the samples loaded with M-H/He and L-H/He after an ELM-like pre-exposure. Due to the particle exposure the surface colour is either black or grey for the M-H/He and L-H/He samples respectively. The SEM-pictures, shown in figure 4.31 for the M-H/He sample and in figure 4.32 for the L-H/He sample, have in both cases the same surface extrusions as their respective reference samples, shown in figure 3.10 and 3.11. Once more no modification of the H/He-induced surface morphology was observed.

These observations are all made on the basis of SEM pictures with several magnifications and angles. The main purpose of these pictures is to investigate if the pre-exposure has an influence on the shape and size of the

Table 4.5: Overview of the loading conditions where a mixed H/He-flux exposure is applied to tungsten which was pre-loaded to ELM-like transients.

First Exposure	Label	Second Exposure	Label
$100 \times \mathrm{F}_{HF}$ 12 at RT	HRT-12	H/He-flux at 600 °C	S-H/He
$100 \times \mathrm{F}_{HF}$ 48 at RT	HRT-48	H/He-flux at 600 °C	S-H/He
$100 \times \mathrm{F}_{HF}$ 12 at 400 °C	H400-12	H/He-flux at 600 °C	S-H/He
$100 \times \mathrm{F}_{HF}$ 48 at 400 °C	H400-48	H/He-flux at 600 °C	S-H/He
$100 \times \mathrm{F}_{HF}$ 12 at RT	HRT-12	H/He-flux at 1000 °C	M-H/He
$100 \times \mathrm{F}_{HF}$ 48 at RT	HRT-48	H/He-flux at 1000 °C	M-H/He
$100 \times \mathrm{F}_{HF}$ 12 at 400 °C	H400-12	H/He-flux at 1000 °C	M-H/He
$100 \times \mathrm{F}_{HF}$ 48 at 400 °C	H400-48	H/He-flux at 1000 °C	M-H/He
$100 \times \mathrm{F}_{HF}$ 12 at RT	HRT-12	H/He-flux at 1500 °C	L-H/He
$100 \times \mathrm{F}_{HF}$ 48 at RT	HRT-48	H/He-flux at 1500 °C	L-H/He
$100 \times \mathrm{F}_{HF}$ 12 at 400 °C	H400-12	H/He-flux at 1500 °C	L-H/He
$100 \times \mathrm{F}_{HF}$ 48 at 400 °C	H400-48	H/He-flux at 1500 °C	L-H/He

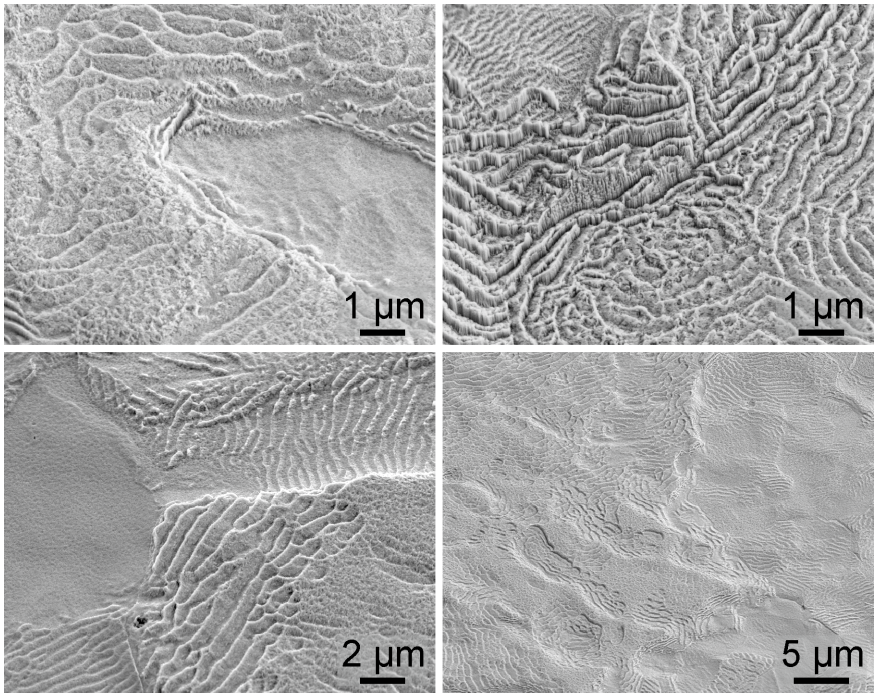

Figure 4.30: SEM pictures with different magnifications and tilt angles for tungsten which is first exposed in JUDITH 1 to HRT-48 (left, top), H400-48 (right, top), HRT-12 (left, bottom), H400-12 (right, bottom) and thereafter exposed in GLADIS to S-H/He.

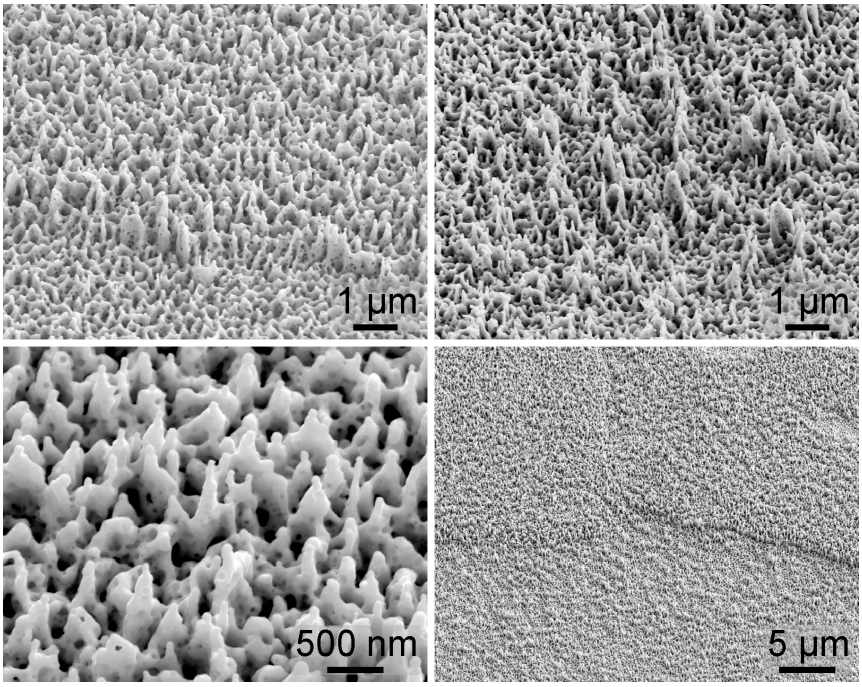

Figure 4.31: SEM pictures with different magnifications and tilt angles for tungsten which is first exposed in JUDITH 1 to HRT-48 (left, top), H400-48 (right, top), HRT-12 (left, bottom), H400-12 (right, bottom) and thereafter exposed in GLADIS to M-H/He.

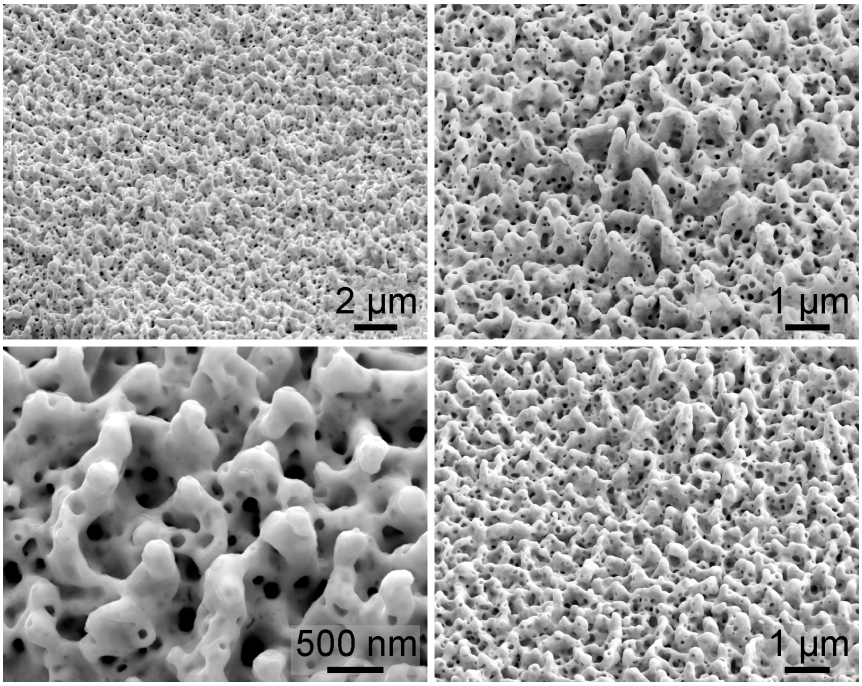

Figure 4.32: SEM pictures with different magnifications and tilt angles for tungsten which is first exposed in JUDITH 1 to HRT-48 (left, top), H400-48 (right, top), HRT-12 (left, bottom), H400-12 (right, bottom) and thereafter exposed in GLADIS to L-H/He. The picture with HRT-48 pre-exposure (left, top), is taken from an intermediate analysis of a sample that thereafter undergoes further testing, since the original sample from this test campaign was damaged during transport.

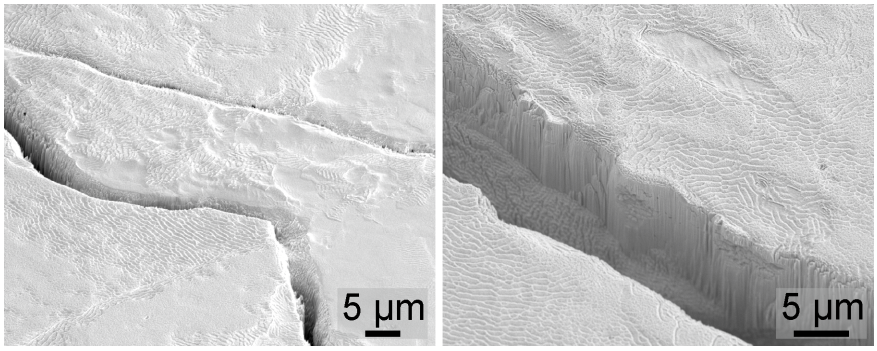

Figure 4.33: SEM pictures with different magnifications and tilt angles for the samples with ELM-like pre-exposure, i.e. HRT-12 (left) and HRT-48 (right), and afterwards S-H/He loading.

surface morphology and/or extrusions. Hence, in the case of the samples that have a crack network, these pictures are located in the area between two cracks. For the cracked samples additional SEM pictures are made that show the area around cracks and are used to study the interaction between the particle flux and the crack.

On these SEM pictures the cracks are still clearly visible. However, already on the S-H/He samples, as shown in figure 4.33, two ways on how the particle flux interact with the crack can be noticed. While the crack edge after ELM-like thermal shocks is sharp, this has changed and an enhanced erosion is observed at the crack edge. The crack edge is therefore less sharp and more rounded. Also within the crack features of erosion are observed. Furthermore, at a few locations the two sides of a crack are locally connected again. Such behaviour was never observed after ELM-like experiments and is solely allocated as an effect of the particle flux. The indications of local melting events, which are present after the HRT-400 pre-exposure, are no longer detected.

Similar SEM pictures for the two samples exposed to M-H/He after the ELM-like pre-exposure that resulted in the formation of a crack network are shown in figure 4.34. The surface extrusions that have grown during the mixed hydrogen/helium exposure cover the crack on several locations. This happened more often for the cracked samples with M-H/He exposure, than it was the case for the cracked samples with S-H/He exposure. Such 'crack bridging' occurs both on several small intervals of a crack, e.g. with a length of a few micrometer, and on longer stretches, e.g.with a length of 50 µm. For the sample with a HRT-48 pre-exposure, the tungsten droplets near cracks that are observed after the ELM-like loads, are no longer observed. Due to the limited height of the surface extrusions, it is concluded that the droplets are eroded away. Also inside the crack there are modifications like

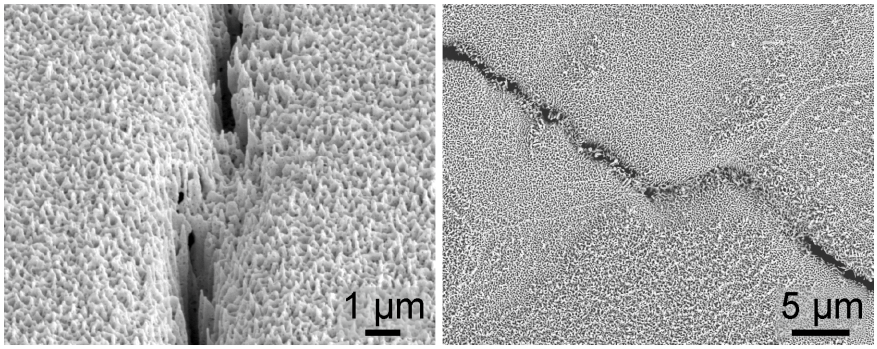

Figure 4.34: SEM pictures with different magnifications and tilt angles for the samples with ELM-like pre-exposure, i.e. HRT-12 (left) and HRT-48 (right), and afterwards M-H/He loading.

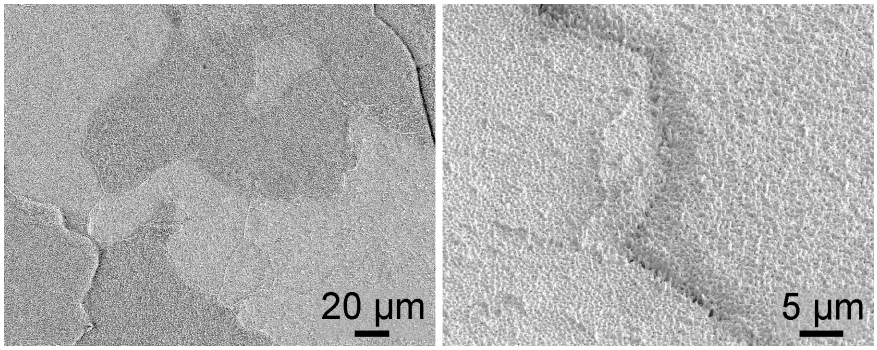

Figure 4.35: SEM pictures with different magnifications and tilt angles on two locations for a sample with HRT-12 pre-exposure and afterwards L-H/He loading.

enhanced erosion, and the presence of holes in the crack sides.

Interaction between the cracks and the particle flux is also observable for the samples exposed to L-H/He, as shown in figure 4.35. On several locations crack bridging is observed. By comparing overview pictures, it is concluded that the occurrence of crack bridging is the highest for L-H/He exposures. Additionally, the crack edge is blunt due to the combination of enhanced erosion and formation of surface extrusions. These extrusions are also detected inside the crack.

Besides the LM and SEM microscopy, the surface of each sample was also analysed with a 50 points/mm and a 250 points/mm laser profilometry scan. The corresponding R_a values from the 50 points/mm scan is shown in figure 4.36, together with the roughness of the 'GLADIS references' and 'ELM references'.

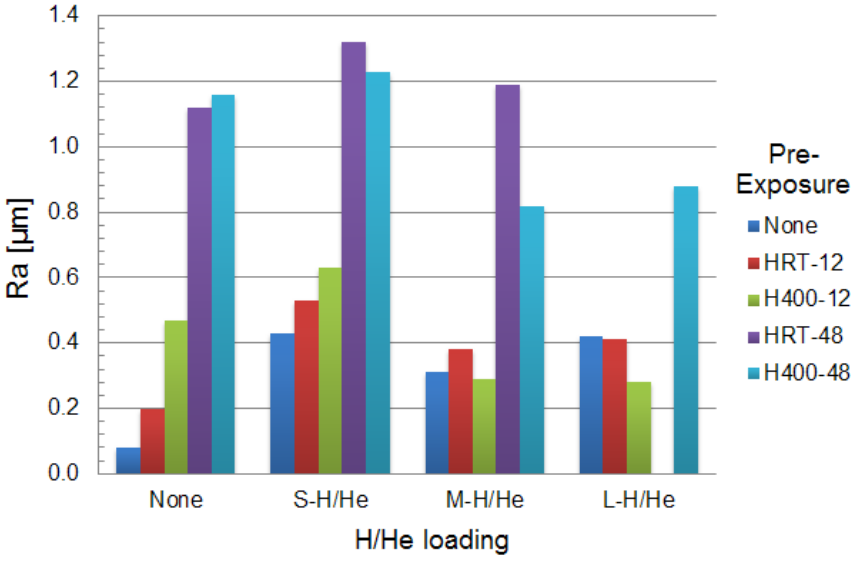

Figure 4.36: The R_a-value, derived from a 50 points/mm laser profilometry scan, after the experiments with a mixed hydrogen/helium beam in GLADIS on tungsten that has been pre-exposed to ELM-like thermal shocks in JUDITH 1. In addition, the respective 'GLADIS references' and 'ELM references' are also given for comparison.

A comparison between the samples which were not exposed to a particle flux and the samples that were loaded with S-H/He shows that the hydrogen/helium beam did not lead to a different behaviour. The H/He-induced erosion pattern causes an increase in the roughness, although that difference is less for pre-exposed samples than for the pristine tungsten. Furthermore, it is seen that for the cracked samples, i.e. the samples with the HRT-12 and HRT-48 pre-exposure, the difference in R_a is higher than for the roughened samples, i.e. the samples with the H400-12 and H400-48 pre-exposure. For the H400-48 pre-loading, this increase is smaller than the stipulated threshold value to be considered a distinct change. Since the R_a value for the cracked samples is mainly determined by the cracks [87], the difference in R_a increase for cracked and roughened samples is explained as follows.

During the particle flux, surface erosion occurs. While this can flatten the ELM-induced roughening, the erosion pattern introduces additional surface roughening. As a result, there is an increased roughening albeit that is less than a pure superposition of the ELM-induced R_a and the H/He-induced R_a. This effect takes place both for the cracked samples as well as the samples that only roughened. Because neither the crack nor the height differences introduced by cracking, where one side is elevated, disappears by the S-H/He flux, the roughness increase is not attenuated by the erosion. Hence, the total roughness can be approximated by a superposition of the roughening coming from the erosion pattern and the crack network.

After the M-H/He loading, the cracked samples have an increased roughness for HRT-12 pre-exposure, that is similar to the H/He-induced roughness increase on pristine tungsten, or an similar roughness for the HRT-48 pre-exposure, where the difference in R_a is below the stipulated threshold value. The erosion is higher for M-H/He than for S-H/He [88], but both the ELM-induced cracks and the height differences that are initiated during the crack formation are still present after the M-H/He loading and have not been removed. However, the samples that roughened during pre-exposure, i.e. H400-12 and H400-48, showed a decrease of the roughness after the M-H/He loading. This indicates either that the levelling caused by the erosion and the He-induced surface modifications is stronger than the ELM-induced roughening or that the surface temperature has an effect.

The R_a-values for the samples that are loaded with L-H/He after ELM-like pre-exposure follows the same pattern as for the samples with M-H/He loading. A decline of the roughness is seen after the particle flux for the samples that roughened during the pre-exposure. Whereas the sample with a crack network after the pre-exposure is additionally roughened after the H/He loading. Therefore, the same conclusion as for the M-H/He loaded samples is made.

Through cross sections, made by FIB, it is possible to further investigate the effect of the particle flux in and near the cracks. For the sample which was first exposed to HRT-12 and afterwards loaded with the S-H/He flux the overview of a single FIB-cut is shown in figure 4.37 alongside the close-

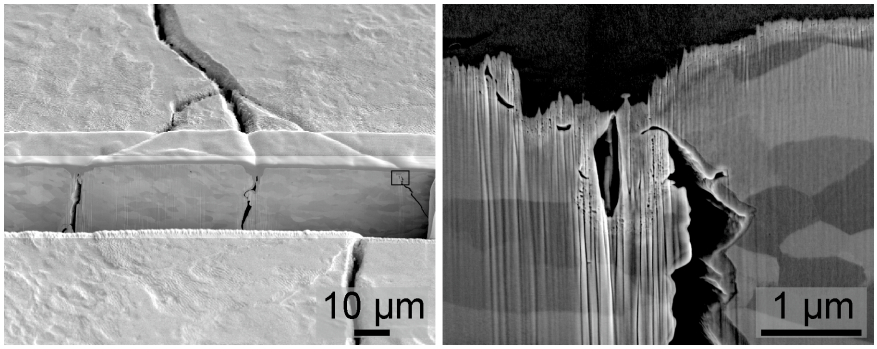

Figure 4.37: FIB performed on a HRT-12 pre-exposed sample which is loaded with S-H/He. The close-up picture features the third crack from the left on the overview picture. The sample was covered by a platinum protection layer before FIB, which is still visible at the top the image.

up of one crack. Due to the platinum protection layer that is deposited on the surface before the FIB cutting, the enhanced erosion at the crack edge is clearly visible in the overview picture.

Furthermore, the higher magnification picture in figure 4.37 indicates that while the crack edges are reconnected at the surface, this is not an in-depth crack repair mechanism. In the FIB and TEM analysis of the reference samples, as shown in figure 3.13, a layer of more than 200 nm deep is observed that exhibits cleavages and cavities. The higher magnification picture shows a similar layer. Additionally, there are also cavities formed alongside the crack as is shown in this picture. These are substantially larger than the ones from the H/He-affected sub-surface layer and can be found more than five times deeper.

FIB analysis performed after M-H/He exposure is shown in figure 4.38 for the sample with HRT-48 pre-exposure and in figure 4.39 for the sample with HRT-12 pre-exposure. The combination in figure 4.38 of the FIB cut with the surface where the FIB cut was taken, assures that the cracks can be fully covered by a shallow 'crack bridging'-layer of surface extrusions. Furthermore, the crack edges are blunted instead of sharp, the H/He-modified sub-surface layer stays unaltered and alongside the crack again cavities are found. Both for the HRT-12 as the HRT-48 pre-exposed sample a porous 'filling' structure is observed in the crack.

Since the different pictures in figure 4.39 are each time 50 nm further along the crack than the previous picture, the cavities within the filling structure can accurately be tracked. Thereby it is seen that most of the cavities can not be described as closed bubbles, but they rather form an interconnected network along the filling structure in the crack. A release of tungsten dust is normally observed during ELM-like transient heat loads

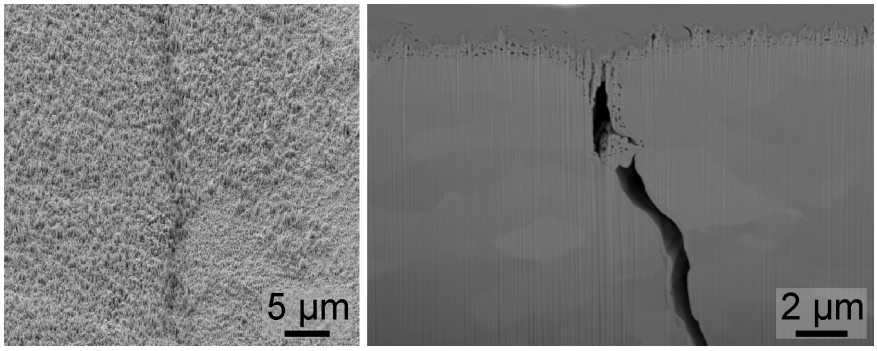

Figure 4.38: A combination of a SEM picture showing the surface of a HRT-48 pre-exposed sample which is loaded with M-H/He and a FIB section on this location. Comparing both images clearly shows that on the surface a shallow layer of surface extrusions cover the crack. The sample was covered by a platinum protection layer before FIB, which is still visible at the top of each image.

and not during the GLADIS exposure during which the filling structures are formed. Hence, the formation mechanism of this 'sponge-like' porous filling structure is considered to be related with the formation mechanism of the surface extrusions and it is considered less likely that it is related with tungsten dust attaching to the crack wall.

Inside the crack there would be a larger fraction of eroded tungsten atoms present that could redeposition or get adsorbed on the side of the cracks. This would result in a higher amount of adsorbed atoms that can get incorporated in the tungsten, similar to the mechanism of extrusion growth by adsorbed atoms [96]. While this should lead to the observance of a nano-structure extrusion phenomenon similar to the surface extrusion, this is not the case.

Another potential formation mechanism for surface extrusions, based on the viscoelastic properties of tungsten [98], is more plausibly related with these porous filling structures. Due to a particle flux that has a different angle distribution and lower fluence inside the crack than on the surface, the necessary conditions are not fulfilled to form new bubbles in the layer between the side of the crack and a previously formed bubble. However already existing bubbles that are located further away from the side of the crack, might still be able to grow and move due to a sufficiently low viscosity. Therefore, the H/He-induced bubbles can after a certain exposure time take up space inside the crack and become a sponge-like filling structure.

Two FIB cuts on a different location on the sample pre-exposed with HRT-12 and loaded with L-H/He are shown in figure 4.40. Similar observations can be made as for the M-H/He and L-H/He loaded samples with

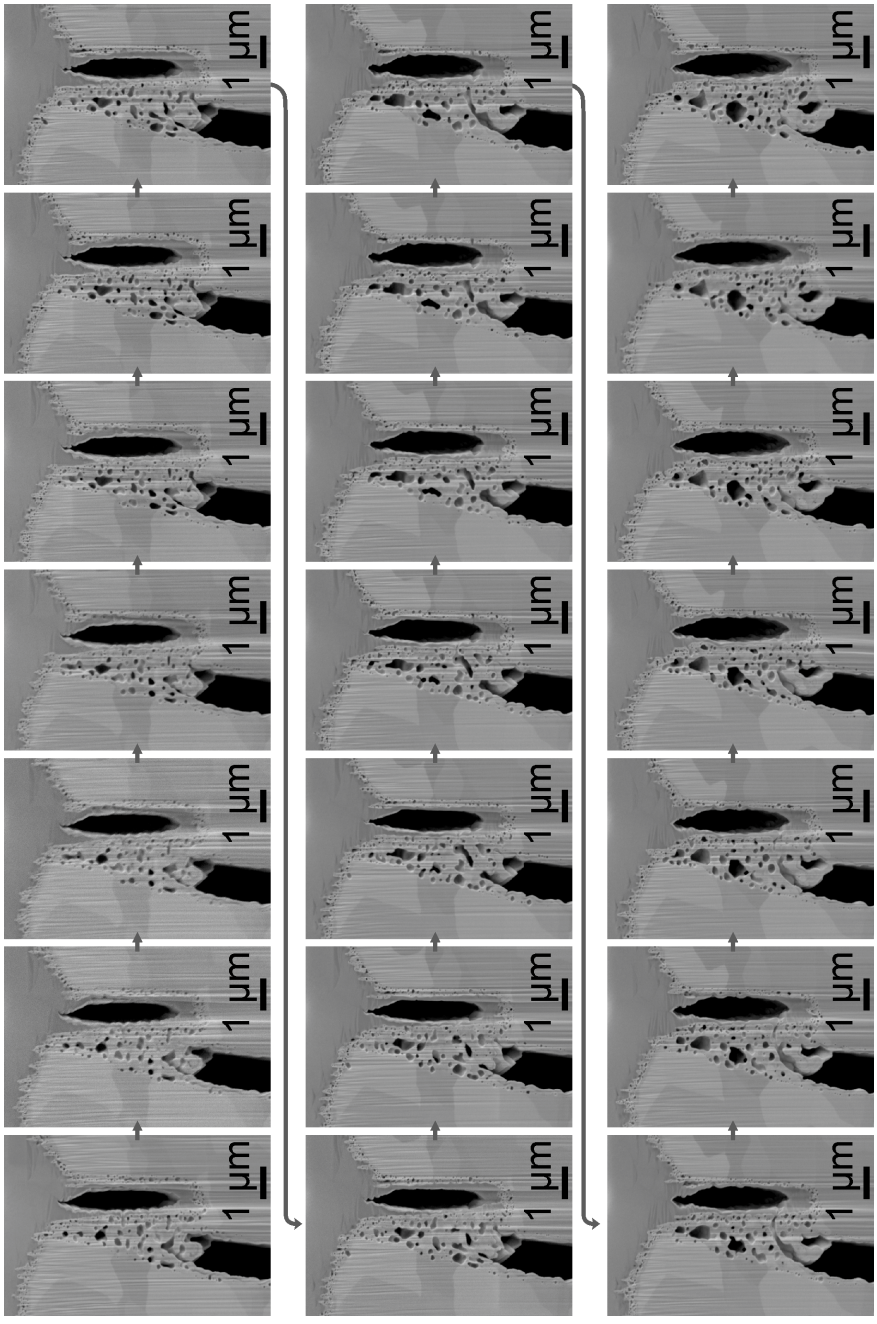

Figure 4.39: FIB-sections of a HRT-12 pre-exposed sample which is loaded with M-H/He. The pictures are taken 50 nm apart from each other.

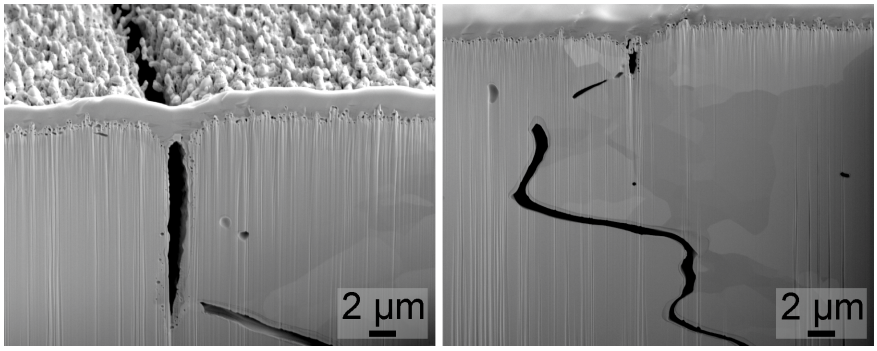

Figure 4.40: FIB performed on two locations of a HRT-12 pre-exposed sample which is loaded with L-H/He. The sample was covered by a platinum protection layer before FIB, which is still visible at the top of each image.

ELM-like pre-exposure. Once again the sub-surface bubble layer is unaltered and cavities are formed alongside the crack. However, it is now also visible that below the surface there is a local reconnection of the crack sides. Since this is only observed for L-H/He exposure, where the surface temperature is 1500 °C, this phenomenon is attributed to recrystallization and grain growth that occurred for this sample.

When the data from the various analysis methods is combined, it becomes clear that the damage from ELM-like pre-exposure under no circumstance in the range of the tested loading conditions leads to a modification of the H/He-induced surface extrusions. It was not possible in any of the analysis to observe a difference between the H/He-induced surface extrusions on a pristine sample or the H/He-induced surface extrusions on pre-damaged samples. This ELM-induced pre-damage includes not only the roughening, (local) melting, or cracking that is a focus point of the damage analysis. Also other damage for which the investigation is not part of this work, e.g. crystal defects [106], that will occur during the ELM-like pre-exposure did not cause an alteration of the surface extrusion.

However, this does not mean that no interaction is observed. The particle exposure showed in several ways an interaction with the cracks. This includes bubble formation along the sides of the crack, the bridging of the crack opening, the emergence of porous sponge-like filling structures inside cracks, and the formation of surface extrusions within the crack. Although it is currently not determined what the consequences are, they could potentially lead to an increase of the dust production, overheating and the occurrence of local melting events at lower power densities. In section 4.3, an initial investigation of the effects that the observed interactions of H/He exposure on pre-damaged tungsten has on the thermal shock behaviour is performed.

Additionally, for the R_a values it could be observed that the roughened samples, i.e. with H400-12 and H400-48 pre-exposure, had a lower R_a after M-H/He or L-H/He exposure. This is attributed towards the H/He-induced erosion that results in a levelling effect for the roughened samples and not for the cracked samples, whose R_a is dominated by the height differences originating from the crack networks. However, it needs to be noted that the erosion in a tokamak environment would occur at a longer time-scale than during the GLADIS exposure. Simultaneously ELMs shall occur, with a higher repetition rate than during the ELM-like loading in JUDITH 1. For that reason, the decrease in roughness might be less prevalent or not observed in a tokamak, since the ELM-induced damage would take place faster than the erosion can alter it [107].

4.3 ELM-Like Loading of H/He-Irradiated W Pre-Exposed to ELM-Like Loads

Phenomena such as crack bridging and the formation of a porous filling structure inside the cracks, as described in section 4.2, are considered to be a potential source of tungsten dust and enhanced erosion. To start investigating to which extent these or other interactions occur, a 'triple exposure' experimental campaign was performed. It might be the case that the cracks are a location to collect tungsten dust, but this can with the current experimental set-up not be verified. This comprised the exposure of pristine tungsten samples to ELM-like thermal loads in JUDITH 1, which were subsequently irradiated with a mixed H/He-beam in GLADIS, after which a final exposure was performed in JUDITH 1 with ELM-like thermal loads.

A summary of the loading conditions for the triple exposure experiments is given in table 4.6. There are four ELM-like loading conditions used in the initial exposure experiment, i.e. HRT-12, HRT-48, H400-12, and H400-48. Afterwards as second exposure, the sample surface was loaded with S-H/He, M-H/He, or L-H/He. The third and final exposure for each sample had the same ELM-like loading condition as used for the initial exposure. In total, this experimental campaign has 12 test specimens each exposed to different combined loading condition.

Only for three samples, i.e. HRT-12 combined with M-H/He, HRT-12 combined with L-H/He, and H400-12 combined with L-H/He, the ELM-loaded area is not detectable with a visual inspection. The nine other samples have an identifiable ELM-loaded area after the final exposure. In some cases also the ELM-loaded area of the initial exposure is still visible, making it clear that the initial and the final exposure did not always load exactly the same $4\,\mathrm{mm} \times 4\,\mathrm{mm}$ area on the sample surface, nevertheless a good overlap was achieved. The analysis is performed in the region where the two ELM-loaded areas intersect.

Table 4.6: Overview of the loading conditions for the triple test campaign where ELM-like thermal shocks are performed on tungsten that received a mixed H/He-flux exposure after an initial ELM-like transient exposure.

Initial & Final Exposure	Label	Intermediate Exposure	Label
$100 \times F_{HF}$ 12 at RT	HRT-12	H/He-flux at 600 °C	S-H/He
$100 \times F_{HF}$ 48 at RT	HRT-48	H/He-flux at 600 °C	S-H/He
$100 \times F_{HF}$ 12 at 400 °C	H400-12	H/He-flux at 600 °C	S-H/He
$100 \times F_{HF}$ 48 at 400 °C	H400-48	H/He-flux at 600 °C	S-H/He
$100 \times F_{HF}$ 12 at RT	HRT-12	H/He-flux at 1000 °C	M-H/He
$100 \times F_{HF}$ 48 at RT	HRT-48	H/He-flux at 1000 °C	M-H/He
$100 \times F_{HF}$ 12 at 400 °C	H400-12	H/He-flux at 1000 °C	M-H/He
$100 \times F_{HF}$ 48 at 400 °C	H400-48	H/He-flux at 1000 °C	M-H/He
$100 \times F_{HF}$ 12 at RT	HRT-12	H/He-flux at 1500 °C	L-H/He
$100 \times F_{HF}$ 48 at RT	HRT-48	H/He-flux at 1500 °C	L-H/He
$100 \times F_{HF}$ 12 at 400 °C	H400-12	H/He-flux at 1500 °C	L-H/He
$100 \times F_{HF}$ 48 at 400 °C	H400-48	H/He-flux at 1500 °C	L-H/He

Through LM, only the loaded area of the sample exposed to the combination of H400-12 with L-H/He could not be identified. Either cracking, for the samples with transient heat loading at RT, or only a clear deformation of the surface, for the samples with transient heat loading at 400 °C, is observed on the LM images for the other eleven samples.

Overview SEM images of the samples which have as second exposure a S-H/He loading, are visualized in figure 4.41. The observed surface damage is, as observed by LM, similar to the thermal shock behaviour of pristine samples that is described in subsection 3.2.1. A crack network is formed for the samples exposed to ELM-like loading at RT, while no cracks are observed for the samples which have an ELM-like loading at 400 °C. For the samples with as second exposure M-H/He, as shown in figure 4.42, and L-H/He, as shown in figure 4.43, the same observations are made. Despite the fact that these samples underwent 200 transient loads in total, in contrast to the 100 transient loads for the 'ELM reference' samples, no modifications with respect to the 'ELM reference' samples are observed in these overview figures.

Detailed SEM pictures of the triple-exposed tungsten can be used to examine the surface morphology as well as the cracks. The main focus will be on the inspection of the cracks as there are no ELM-reference experiments that were performed with 200 pulses with which to directly compare the surface morphology, although they could be very similar to the experiments with 100 pulses. Nevertheless, as shown in figure 4.44, the final ELM-like exposure has resulted in not earlier observed damage for the H400-48

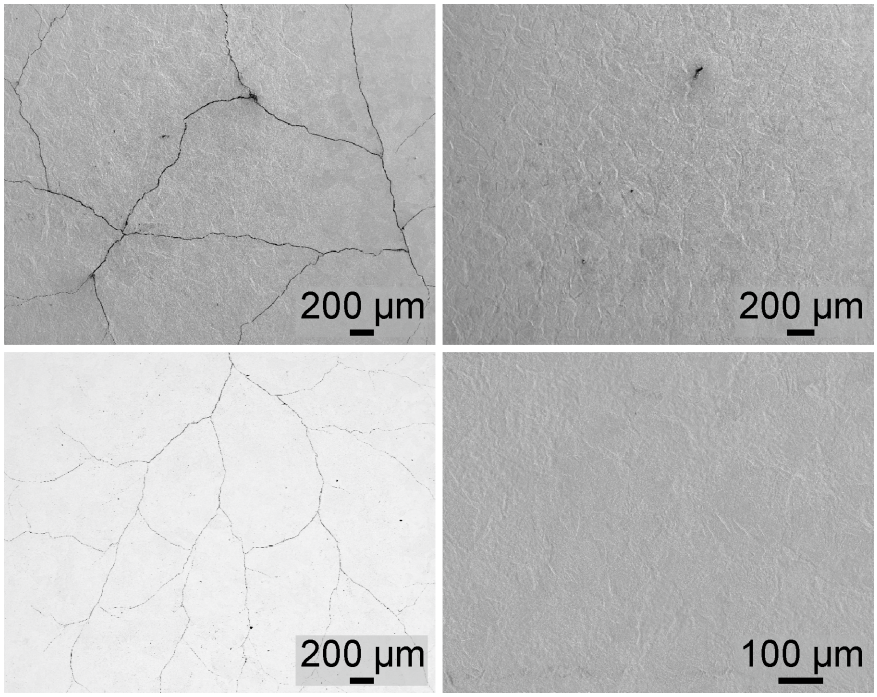

Figure 4.41: SEM overview pictures for tungsten which is first exposed in JUDITH 1 to HRT-48 (left, top), H400-48 (right, top), HRT-12 (left, bottom), H400-12 (right, bottom), thereafter exposed in GLADIS to S-H/He, and then again loaded to the same transient exposure.

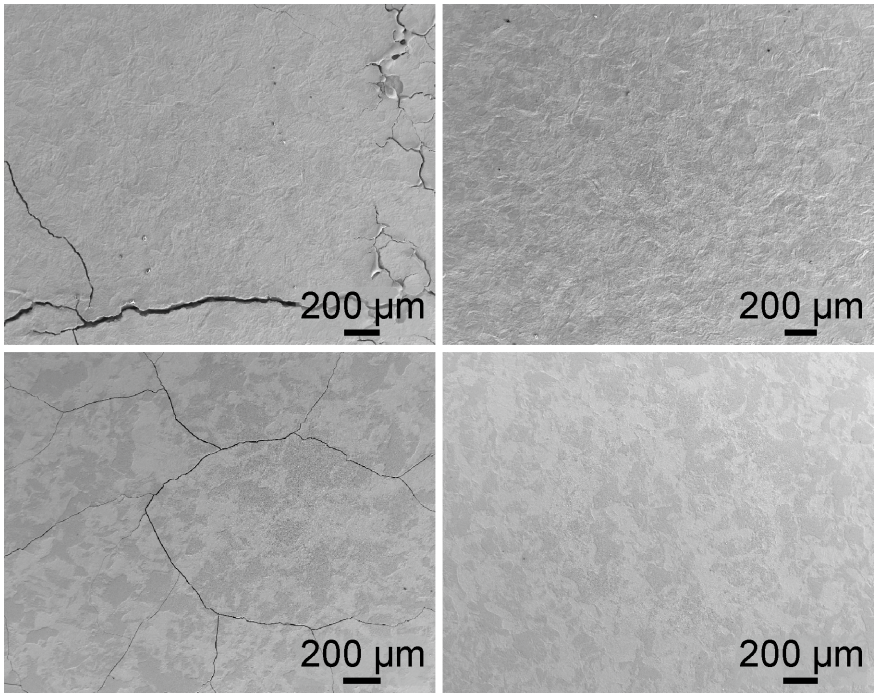

Figure 4.42: SEM overview pictures for tungsten which is first exposed in JUDITH 1 to HRT-48 (left, top), H400-48 (right, top), HRT-12 (left, bottom), or H400-12 (right, bottom), thereafter exposed in GLADIS to M-H/He, and then again loaded to the same transient exposure.

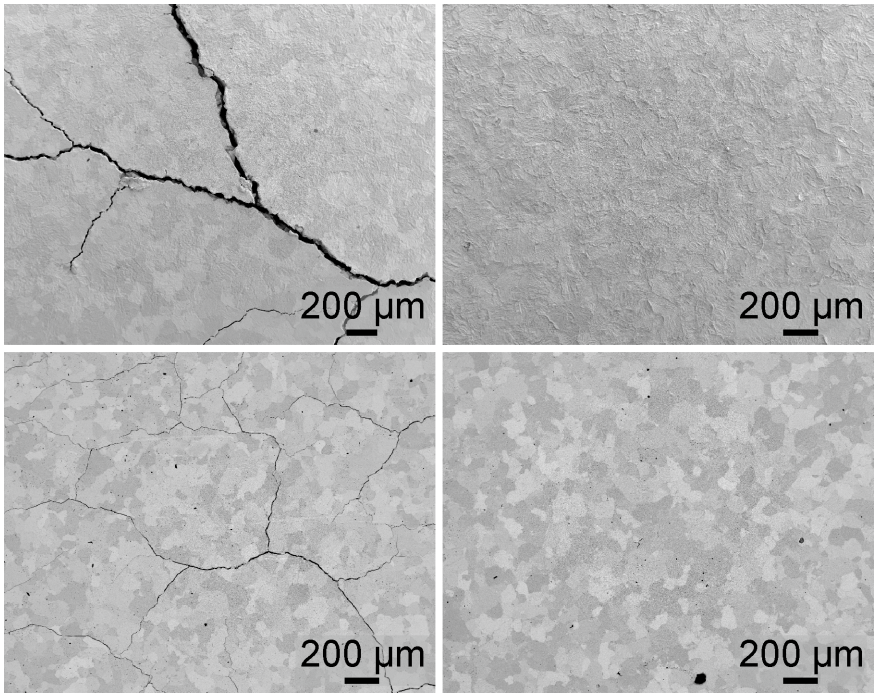

Figure 4.43: SEM overview pictures for tungsten which is first exposed in JUDITH 1 to HRT-48 (left, top), H400-48 (right, top), HRT-12 (left, bottom), or H400-12 (right, bottom), thereafter exposed in GLADIS to L-H/He, and then again loaded to the same transient exposure.

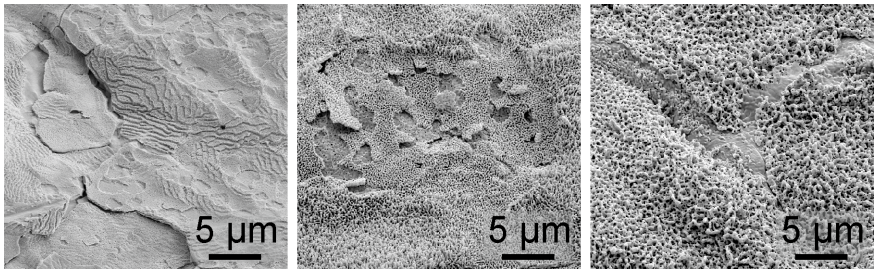

Figure 4.44: SEM detail pictures for tungsten which is first exposed in JUDITH 1 to H400-48, thereafter exposed in GLADIS to either S-H/He (left), M-H/He (middle), or L-H/He (right), and then again loaded to H400-48.

ELM-like loads. For the samples with S-H/He exposure this resulted in a modification of the H/He-induced surface pattern and the observance of height differences near some grain boundaries. The samples with M-H/He and L-H/He have on some locations a partial melting of the H/He-induced surface extrusions, and for M-H/He there is in addition the appearance of flaking on the surface, which were both not observable on lower magnification images. An local overheating, higher than the expected ELM-induced temperature rise as shown in table 3.7, is necessary for both phenomena to appear. Hence, the melting and appearance of flaking are in line with the earlier mentioned statements, e.g. in subsection 4.1.2, that the sub-surface cavities can alter the thermal conductivity and together with the surface extrusions might lead to overheating.

All six samples that were cracked after the triple exposure, i.e. HRT-12 or HRT-48 loading in combination with S-H/He, M-H/He, or L-H/He, are closely examined near their cracks with SEM. For none of these samples any indications are found for the 'crack bridging' described in section 4.2. Nevertheless, during an intermediate analysis on the samples after the middle exposure with a mixed H/He-flux in GLADIS, these 'crack bridges' were found on several locations. These 'crack bridges' are disappeared during the final ELM-like loading, most likely due to the same process as the crack formation described in section 3.2. A combination of plastic deformation during the transient heat load and tensile stresses between two transient heat loads removed the 'crack bridges, although it is not determined to which extent this resulted in additional erosion. An alternative mechanism for this removal could be melting, however a molten tungsten layer from the final ELM-like loading is not retrieved at the crack edges.

Most cracks have indications that they were formed during the first exposure. As shown in figure 4.45, this can be seen by the enhanced erosion at the crack edge, e.g. the sample with a triple exposure that combined HRT-12 with S-H/He. Furthermore, the occurrence of surface extrusions inside

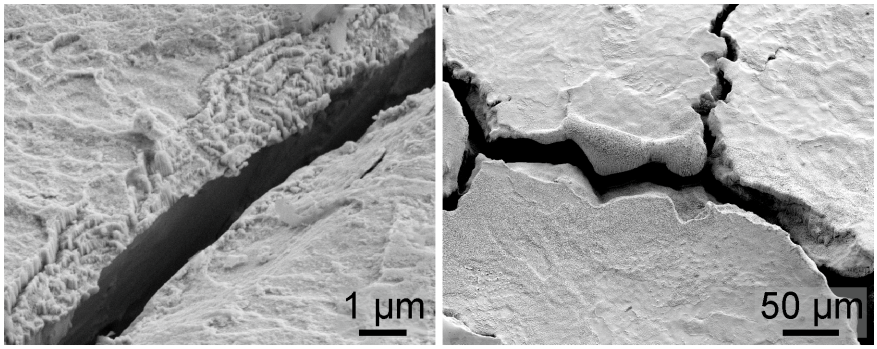

Figure 4.45: Detail SEM figures featuring cracks without an indication of crackbridging, as is observed after triple exposure experiments. This is shown for the exposure combining HRT-12 with S-H/He (left) and HRT-48 with M-H/He (right).

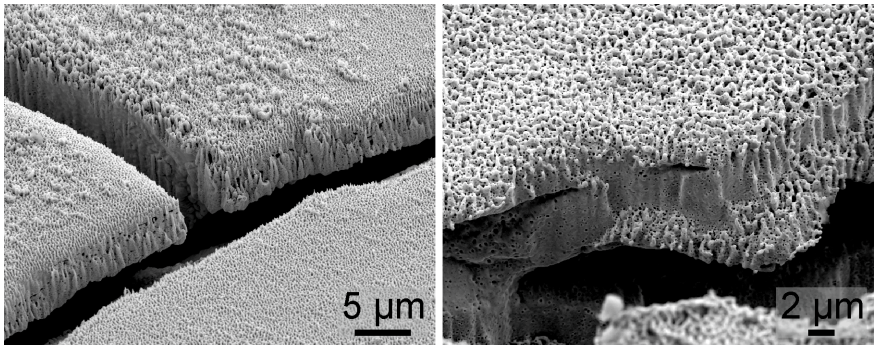

Figure 4.46: Detail SEM figures featuring cracks without an indication of crackbridging, as is observed after triple exposure experiments. This is shown for the exposure combining HRT-12 with M-H/He (left) and HRT-48 with L-H/He (right).

Table 4.7: The arithmetic mean roughness R_a of the samples from the triple exposure experiments, calculated with a 50 points/mm laser profilometry scan.

	S-H/He	M-H/He	L-H/He
HRT-12	0.49 µm	0.39 µm	0.42 µm
H400-12	0.57 µm	0.36 µm	0.50 µm
HRT-48	1.12 µm	2.17 µm	3.51 µm
H400-48	1.00 µm	1.22 µm	1.31 µm

the crack, e.g. the sample with a triple exposure that combined HRT-48 with M-H/He, also indicated that the crack has been formed during the first exposure. Although some minor cracks seem to have formed during the final exposure, they are only a minority when compared to the total amount of cracks.

Furthermore, the sample with a triple exposure that combined HRT-48 with M-H/He has at the crack edge, as shown in figure 4.45, a location where melting happened and a droplet was formed. Because this droplet is covered with surface extrusions, this was formed during the initial exposure. While local overheating and melting occurred during the first ELM-like loading, this can be excluded for the final ELM-like loading since these extrusions are not partially molten. In all likelihood this spot has suffered from overheating, but not to the extent that the droplet would undergo remelting.

Nevertheless, local overheating stays a potential cause for unwanted melting and enhanced erosion. On several locations, as shown in figure 4.46, cracks are observed that after an initial perpendicular propagation, continue to propagate in an unusual way. The non-perpendicular further crack propagation creates several locations where there is no direct contact between the surface and the bulk material, resulting in a hampering of the heat transport and potential overheating. In the range of used loading conditions, the consequences of these local instances of overheating are only rarely observed, e.g. as minor droplets, but they have the potential for serious material damage.

A laser profilometry scan is performed on the samples and used to calculate the arithmetic mean roughness, as shown in table 4.7. After the triple exposure experiments that combined HRT-48 with S-H/He, M-H/He, and L-H/He, the roughness values are higher than for the triple-exposed samples that combined H400-48 with S-H/He, M-H/He, and L-H/He respectively. This behaviour is also seen in figure 4.36 for the ELM-like pre-exposed samples that are loaded with a mixed hydrogen/helium beam.

Furthermore, for all four triple-exposed samples which had S-H/He loading the R_a is, with respect to the required minimal difference of 0.09 µm,

Table 4.8: An overview of the main results for the sequential exposure experiments.

Exposure	Main Results
H - ELM	∗ Thermal shock damage mapping is the same or improved with respect to the 'ELM reference'. ∗ ELM-induced roughness increase is equal or lower with respect to the 'ELM reference' or is not detected at all. ∗ Only L-H, which is recrystallized, has a higher crack depth and a lower crack distance.
H/He - ELM	∗ Thermal shock damage mapping is the same or improved with respect to the 'ELM reference'. ∗ No removal or modification of the H/He-induced surface extrusions after 100 pulses. ∗ ELM-induced roughness increase is lower with respect to the 'ELM reference' or is not detected at all for 100 pulses. ∗ For 1000 pulses, the ELM-induced roughness indicates both improved and degraded thermal shock behaviour, most likely due to the oxidation of the surface. ∗ Only L-H/He, which is recrystallized, has a higher crack depth. ∗ H/He-induced sub-surface cavities in the case of S-H/He grow after H1000-12 transients.
ELM - H/He	∗ Independent of the ELM-like pre-exposure, similar surface extrusions are formed. ∗ H/He-induced erosion can result in a decrease of the ELM-induced roughness. ∗ The H/He-flux interacts with cracks through crack bridging, porous filling structures, cavity formation along the crack edge, etc.
ELM - H/He - ELM	∗ Partial melting of the surface extrusions with H400-48 transients. ∗ Removal of crack bridges. ∗ HRT-48 transients after H/He exposure does not cause further remelting of the droplets located at crack edges.

either identical or lower in comparison to the R_a of the samples first exposed with the same transient heat load and thereafter loaded with the same mixed hydrogen/helium exposure. For samples HRT-12 combined with M-H/He, H400-12 combined with M-H/He, and HRT-12 combined with L-H/He, it is also observed that their roughness values is the same as for their equivalent samples described in section 4.2. The remaining samples have a higher R_a in comparison to their equivalent samples.

To allocate damage categories to each loading conditions, the SEM images make clear that all samples that had HRT-12 or HRT-48 exposure during the triple exposure experiments belong to *Crack Network*, independent of the fact that ELM-like loading was combined with S-H/He, M-H/H, or L-H/He. For the three samples which combined H400-12 with either S-H/He, M-H/He, or L-H/He, the SEM images showed that the occurrence of roughening. The samples are therefore allocated to *Additional Surface Damage*, just as the sample that combines H400-48 with S-H/He. The damage category *Melting* belongs to the two remaining samples, i.e. H400-48 combined with M-H/He and L-H/He.

4.4 Summary and Conclusions

Pure hydrogen and mixed hydrogen/helium exposures were applied on the samples at surface temperatures from 600 °C to 1500 °C and 100 or 1000 ELM-like transient heat loads were applied at base temperatures from RT to 1000 °C with an absorbed power density from 190 MW m^{-2} to 1514 MW m^{-2}. These loading conditions were combined by performing ELM-like loading after particle pre-exposure, particle exposure after ELM-like pre-loading, or triple exposure experiments with ELM-like loading after particle exposure on ELM-like pre-loaded tungsten. An overview of the main results is given in table 4.8.

In case of ELM-like loading on tungsten pre-exposed with a H beam, the thermal shock damage mapping is either similar or slightly improved with regard to the reference tungsten. This improvement is noticed for the 1000 °C experiments on L-H pre-exposed tungsten where the *Crack Initiations* were suppressed and only roughening occurred, which is a result of the increased ductility after recrystallization.

For the S-H and M-H samples shows the damage mapping that no damage is detected after 380 MW m^{-2} at 400 °C transients. The crack characteristics are similar or slightly improved with respect to the reference sample. Any ELM-induced damage is observed solely inside the loaded area and no crack propagation outside this area is observed, in contrast to what is once reported in literature under different disruption-like loading conditions [108]. An ELM-induced roughening increase is either not observable or remarkably lower for the pre-exposed samples than for the pristine samples. This can be an effect of the initial roughness after particle pre-loading

which conceals the ELM-induced damage in the measurements.

Only for the L-H pre-exposed tungsten are the cracks deeper and located closer to each other than for the pristine material. However, this change in the damage characteristics is not allocated to the hydrogen exposure, but to the recrystallization that takes place during the exposure in GLADIS. The conclusion that this solely is a temperature effect, is in line with earlier reported effects of the recrystallization of tungsten [103]. Also for the L-H tungsten, an ELM-induced increase in roughening is either not observable, or it is not higher than the increase in roughening for the reference sample.

The thermal shock behaviour of the hydrogen pre-exposed tungsten is overall very similar to the pristine tungsten without the observation of a thermal shock behaviour degradation. It is concluded that the hydrogen pre-exposure has no effect on the ELM-induced damage, or it causes a slight improvement which needs to be further investigated to be confirmed.

In case of the H/He pre-exposed samples, the thermal shock damage mapping is also either similar or has an apparent improvement with regard to the reference tungsten. This improvement is noticed for $380\,\mathrm{MW\,m^{-2}}$ transients, which at 400 °C on S-H/He and M-H/He tungsten and at RT on M-H/He tungsten are categorized as *No Damage* in contrast to their respective references that belong either to *Surface Modifications* or to *Crack Network*. Once again, the damage from the particle pre-loading can cause that the ELM-induced roughening is not detected, but for sure this result shows that there was no degradation. Furthermore, the fact that there was no formation of a crack network on M-H/He showed a clear improvement.

In case of crack formation, only the L-H/He sample has a deeper crack propagation than the reference sample, which is caused by the recrystallization and is a pure temperature effect. An ELM-induced roughening is only observed for $380\,\mathrm{MW\,m^{-2}}$ transients at 400 °C on L-H/He tungsten, but this increase is similar to the increase for the pristine sample and does not constitute a degradation of the damage behaviour. It is concluded that the recrystallization of L-H/He, which caused an increase of ductility, a reduced yield strength and a reduced ultimate tensile strength, is responsible that roughening is observed on L-H/He, but not on S-H/He or M-H/He.

In contrast to the tungsten pre-exposed to H, a clear improvement of the thermal shock performance after pre-exposure with H/He is found, i.e. the absence of a crack network for M-H/He. A possible explanation for this H/He-induced improvement can be the increase of the effective surface, as suggested in literature [104]. However, another reason is that the thin and porous layer of H/He-induced cavities can undergo thermal expansion and contraction without the same accumulation of stresses as is the case for bulk tungsten, which would inhibit crack formation. In addition is also a modification of the H/He-induced damage by the thermal shock exposure observed, i.e. an increase in size of the sub-surface H/He-induced cavities for the S-H/He sample after ELM-like exposure at 1000 °C, caused by a change in the Greenwood equilibrium.

Additional ELM-like loading is performed at a base temperature of 1000 °C for 1000 pulses on H/He pre-exposed tungsten, resulting in a similar thermal shock damage mapping for the S-H/He and M-H/He samples. The L-H/He samples were all oxidized, which is deemed responsible for the observed changes. Otherwise, the only change is for 380 MW m^{-2} transients on S-H/He where an higher ELM-induced roughening is observed than for the reference sample, which might partially be related to the growth in size of the sub-surface bubbles.

The damage of H/He exposure on tungsten pre-loaded with ELM-like transient loads, shows no modifications in either the H/He-induced erosion pattern itself nor in the surface extrusions. The roughness indicates that there is no influence of the ELM pre-exposure on the H/He-induced damage and shows that there is erosion in the ELM-induced roughened area by the H/He-beam, which makes the H/He-induced modifications prevalent in this experiment.

The main observed effect of ELM-like pre-loading are several features of interaction between the H/He-irradiation and the crack. On the surface, the erosion is increased at the crack edge and locations have a local reconnection of the crack sides by crack bridging. Inside the crack, FIB-sections and SEM show a sub-surface crack reconnection, cavity formation along the crack edge, the emergence of H/He-induced surface extrusions, and the formation of a porous 'sponge-like' filling structure. The consequences of these phenomena potentially include the production of tungsten dust and a local overheating that can lead to melting.

After the 'triple exposure' experimental campaign, the thermal shock damage mapping can not directly be compared with the other experiments, since the triple-exposed samples were subjected to double as much ELM-like heat loads. Nevertheless, for most loading conditions is no change in damage categories found, with respect to the 'ELM reference' samples. Only for 1514 MW m^{-2} transients at 400 °C combined with M-H/He and L-H/He resulted the ELM-like heat loads locally in a partial melting of the surface extrusions, which would be a noticeable effect of overheating due to the H/He-induced sub-surface cavities.

Although no other melting was observed, an unusual non-perpendicular crack propagation, that can lead to overheating, is found for the triple-exposed tungsten with ELM-like heat loads at RT. These are potential locations for overheating, melting, enhanced erosion and tungsten dust production. In addition, the 'crack bridging' has completely disappeared during the final ELM-like experiments.

The removal process is likely caused by the repeated thermal expansion during the transient heat loads and the thermal contraction between the transient heat loads. As a result, the crack can partially and/or completely close and reopen, inducing on the bridge layer compressive and tensile stresses with subsequent material failure as a consequence. It is unclear if this would mean that during simultaneous exposure the formation of a

'crack bridge' would not be initiated at all or if the formation would start, but never be completed due to a continuous removal process. The amount of tungsten dust that is produced or the extent of erosion that occurs during the 'crack bridge' removal is not yet quantified.

For a relevant damage assessment of tungsten, as became clear by performing sequential exposure experiments, the synergistic effects need to be taken into account. A particle pre-exposure in GLADIS does not deteriorate the thermal shock behaviour for low pulse numbers in JUDITH 1. Nevertheless, a growth of H/He-induced cavities is observed, the analysis after 1000 ELM-like pulses at high temperature shows that a degraded thermal shock behaviour for high pulse numbers can not be excluded at this point, and the recrystallized samples show a worse material performance from all pre-exposed samples.

Although the H/He-induced surface extrusions are not altered by an ELM-like pre-damaging, they can cover the cracks and are subsequently removed by additional thermal shocks. Together with porous 'filling structures' formed inside the cracks, these are potential sources for tungsten dust production that are not considered yet. In spite of the stable, or in some specific cases a possibly improved, thermal shock behaviour, potential negative side-effects that can not be neglected, are discovered and may lead to overheating and erosion.

Chapter 5

High Pulse Number Experiments

5.1 Overview

Although the thermal shock damage on tungsten can be observed already after 100 pulses [101], this does not exclude the occurrence of additional effects by long term fatigue after higher pulse numbers [68]. Hence, the interaction between the particle induced damage and the ELM-induced damage is not necessarily independent of the amount of transient events. Furthermore, the steady state heat flux is replaced by a constant base temperature during the ELM-like experiments in JUDITH 1. As a consequence, changing the experimental set-up of the sequential experiments to include higher pulse numbers and allowing for a steady state heat load during the ELM-like experiments, results in valuable supplementary information.

This is accomplished by performing a final test campaign in which tungsten is first pre-exposed to a mixed hydrogen/helium beam in GLADIS. Afterwards, the mock-up is loaded in the JUDITH 2 facility to a combination of simultaneous steady state heat load and ELM-like thermal loads. The high thermal shock repetition rate which can be used in JUDITH 2 enables an increase of the pulse number and results in a temperature gradient in the material, instead of a constant base temperature induced by an external heater. However, these tests could not be performed with the samples that are described in subsection 2.1.2 and used in the previous experiments.

Instead, a tungsten monoblock mock-up originating from the European Joint Undertaking for ITER and the Development of Fusion Energy (Fusion for Energy, or F4E), shown in figure 5.1, is used. This mock-up is labelled W-MMU-12-16, is produced by *Plansee SE*, and consists out of seven tungsten monoblocks that are joined through hot isostatic pressing to a CuCrZr cooling tube with a swirl tube. Each monoblock has a $23\,\mathrm{mm} \times 12\,\mathrm{mm}$ sur-

Figure 5.1: An as-received mock-up, produced by *Plansee SE*, that consists out of 7 tungsten monoblocks which are joined to a CuCrZr cooling tube. This mock-up is identical to the W-MMU-12-16 mock-up used in the experiments.

face. The total height of a monoblock is 28 mm and the distance in the monoblock between the cooling tube and the surface is 8 mm. The mock-up comes from a batch, whereof other mock-ups were used in earlier high heat flux experiments [109] in MAGNUM-PSI [110], GLADIS and JUDITH 2.

The tungsten of which the monoblocks are made, meets the ITER material specifications. Although the exact manufacturing method is not disclosed by the producer, it is known that the recrystallization temperature of these monoblocks is $\sim 1300\,^{\circ}\mathrm{C}$ [111]. Furthermore, the material has elongated grains which are oriented in a transversal grain orientation with respect to the loaded surface, as requested in the ITER specifications. This is in contrast with the samples that are used in the experiments described in chapter 3 and chapter 4, since these samples were longitudinally oriented.

The H/He pre-exposure in GLADIS uses different beam parameters from the experiments described in section 3.1. While the beam content stays 94 % hydrogen and 6 % helium, both the extraction voltage and the extraction current are increased to 34 kV and 10.4 A respectively. By assuming the same energy distribution for the hydrogen atoms as in the other GLADIS-experiments, i.e. 22 % at full energy, 43 % at half of the full energy, and 35 % at a third of the full energy, the mean hydrogen energy is 18 keV. The maximum heat flux at the beam centre is $13\,\mathrm{MW\,m^{-2}}$, which corresponds

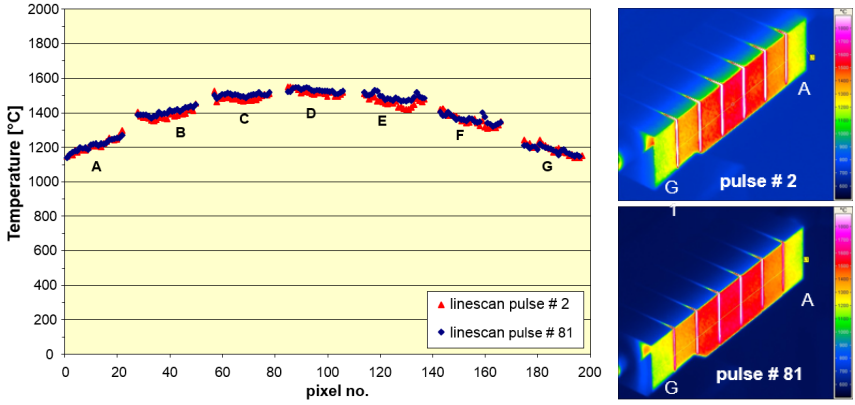

Figure 5.2: The emissivity corrected surface temperature for the W-MMU-12-16 mock-up during pulse #2 and pulse #81 of the GLADIS exposure (left) and two infra-red pictures during these respective pulses (right).

to a particle flux of $4.1 \times 10^{21}\,\mathrm{m^{-2}\,s^{-1}}$.

The pre-exposure is performed for 82 pulses, each of them having a duration of 30 s. In total the mock-up was exposed to a maximal fluence of $1 \times 10^{25}\,\mathrm{m^{-1}}$. During the experiments, as shown in figure 5.2, the surface temperature for monoblock A and monoblock G was $\sim 1200\,^{\circ}\mathrm{C}$, which is too low to result in recrystallization. The five central monoblocks, i.e. monoblock B to monoblock F, had a surface temperature of $\sim 1400\,^{\circ}\mathrm{C}$ to $\sim 1500\,^{\circ}\mathrm{C}$ and will have recrystallized layer. For monoblocks B and F, this layer would be less deep than for monoblocks C, D and E, but the exact depth can only be acquired by analysing cross sections.

After the GLADIS exposure, the samples are loaded in JUDITH 2, while using different surface temperatures, pulse numbers and transient heat loads. The loading conditions, shown in table 5.1, are chosen to enable a comparison with the experiments described in section 4.1 and to fit within earlier performed experiments on the same mock-ups [109] for future analysis. As a result, experiments are performed with 1000 pulses, 17 600 pulses, and 100 000 pulses, which are performed respectively in one exposure of 100 s, 89 exposures of 26.5 s, and 20 exposures of 500 s. During the experiment the surface temperature is kept at 1000 °C, 1200 °C, or 1500 °C, while the applied ELM-like heat loads are either F_{HF} 4.5 or F_{HF} 12.

The surface temperature during the experiments is obtained by a constant SSHF on the whole monoblock, by sweeping the electron beam over the monoblock surface. The steady state heat load used during the experiments is not measured directly, but is calculated based on the Gaussian shape of the electron beam. According to the calculations, they are $10.7\,\mathrm{MW\,m^{-2}}$, $11.4\,\mathrm{MW\,m^{-2}}$, and $13.5\,\mathrm{MW\,m^{-2}}$ for obtaining a surface temperature of

Table 5.1: Overview of the different exposure conditions in the JUDITH 2-facility for the high pulse number experiments. T_{Surf} is the equilibrium temperature of the surface between two ELM-like loads, while ΔT is the temperature rise during an ELM-like load.

Label	ELMs	$P_{abs,SSHF}$ [MW m^{-2}]	T_{Surf} [°C]	$P_{abs,ELM}$ [MW m^{-2}]	F_{HF}	ΔT [K]
A	17 600	11.4	1200	205	4.5	244
B	17 600	13.5	1500	548	12	651
C	17 600	13.5	1500	205	4.5	244
D	100 000	13.5	1500	205	4.5	244
E	100 000	13.5	1500	548	12	651
F	1000	10.7	1000	548	12	651
G	100 000	11.4	1200	205	4.5	244

1000 °C, 1200 °C, or 1500 °C respectively. Only monoblocks B, C, D, and E have a high enough surface temperature during JUDITH 2 exposure to undergo recrystallization. Simultaneously the ELM-like heat loads are applied with a frequency of 10 Hz near the centre of the monoblock surface through a circular beam pattern [112]. Since the duration of an ELM during the high pulse number experiments is shorter, i.e. 0.48 ms, than during experiments in JUDITH 1, the heat flux factor should be used as a basis of comparison, instead of the absorbed power density.

The temperature profile during the simultaneous steady state heat loads and ELM-like heat loads measured by a fast pyrometer, is shown in figure 5.3 for monoblock G. Because the measuring spot of the pyrometer does not necessarily perfectly coincide with the ELM-loaded area, the measured temperature spike can be smaller than the actual value. Due to the path of the electron beam, the tungsten surface also undergoes minor temperature spikes from the SSHF, resulting in a varying inter-ELM surface temperature. This is also captured by the fast pyrometer, as shown in figure 5.4 for a single ELM-like transient event on monoblock B.

Besides a final analysis that was performed after the completion of the whole campaign, a minor intermediate analysis between the GLADIS and JUDITH 2 exposures was executed. The intermediate analysis only comprised electron microscopy on selected monoblocks, to confirm the existence of surface extrusions. Since the monoblocks can not be analysed by a destructive method, the data is limited to light microscopy, electron microscopy and laser profilometry.

The size and weight of the mock-up, exceeds the limits of the sample table installed in the scanning electron microscope. As a consequence, the mock-up can not move during the electron microscopy performed in Forschungszentrum Jülich, which makes the SEM-analysis time-intensive.

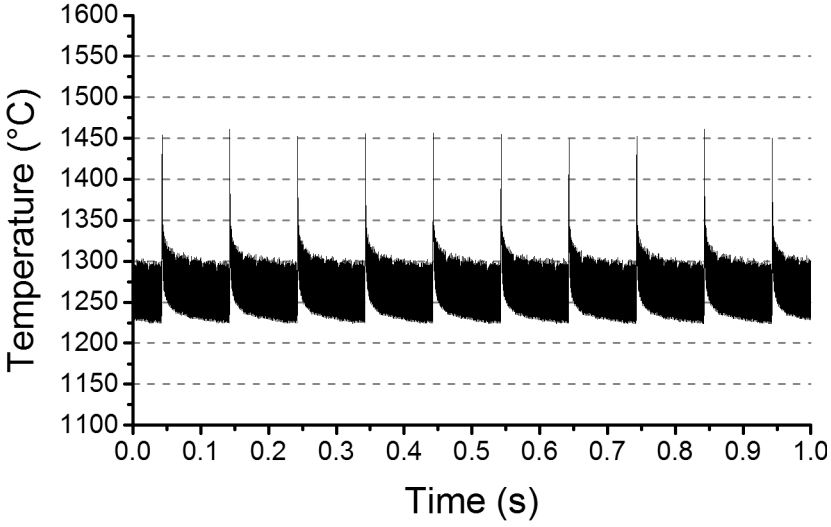

Figure 5.3: The surface temperature distribution measured by a fast pyrometer for measurement #17 of monoblock G during the JUDITH 2 exposure of simultaneous steady state heat loads and ELM-like transient heat loads.

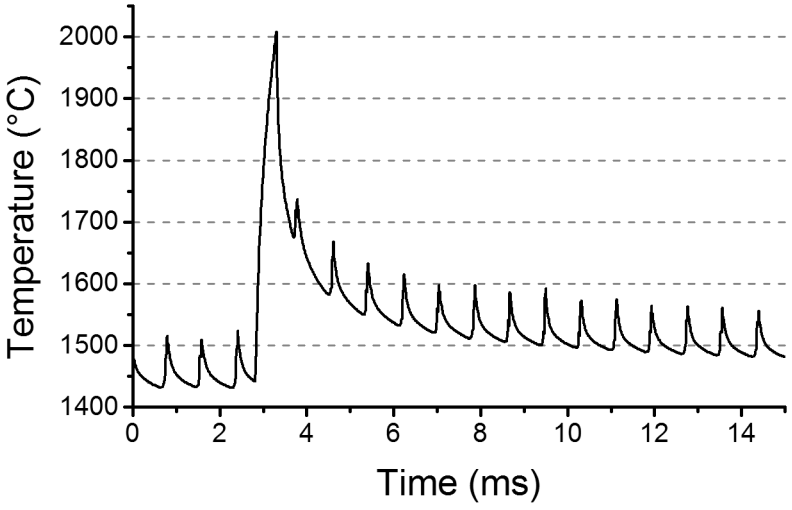

Figure 5.4: The temperature profile of a single ELM measured by a fast pyrometer in measurement #4 during JUDITH 2 exposure of monoblock B.

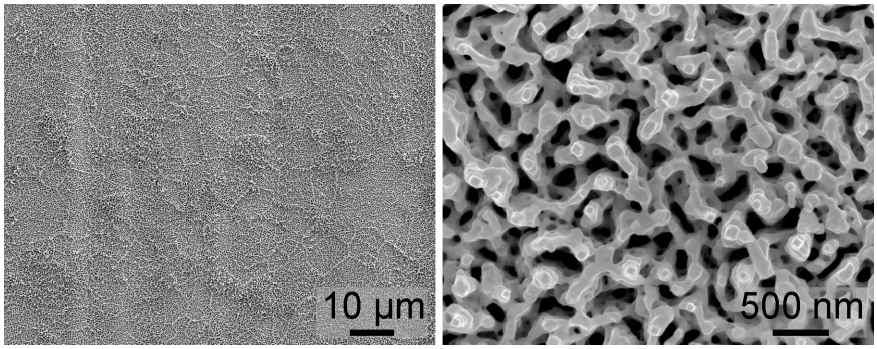

Figure 5.5: SEM pictures with different magnifications of monoblock D (left) and monoblock E (right) after H/He exposure in GLADIS.

Furthermore, not every monoblock is partially or completely within an area that can be visualized by the SEM. For that reason, the Large Chamber Scanning Electron Microscope LC-SEM from GFE, the central Facility for Electron Microsocopy of RWTH Aachen, is used. Instead of moving the sample under the detector, in LC-SEM the SEM detector can move over the sample surface [113]. However, the maximal magnification that can be obtained by LC-SEM is not always sufficient. Hence, after the completion of SEM analysis by LC-SEM an additional and time-intensive SEM analysis was performed in Forschungszentrum Jülich on designated locations of the monoblocks.

5.2 Experimental Results

During the intermediate analysis, performed after the mixed H/He pre-exposure but before the simultaneous steady state and transient heat loads, monoblock D and monoblock E were examined. No differences could be found between monoblock D and monoblock E. As shown in figure 5.5, in a SEM picture with a low magnification several parallel lines are visible. These are remnants of the machining grooves that originate from the production process. Also in earlier investigations, with a pure hydrogen exposure, these grooves were detected [109].

Furthermore, the SEM shows that the surfaces of both monoblocks were covered with H/He-induced extrusions. Although during these experiments the flux, the total exposure time, and the fluence are different from the GLADIS conditions described in section 3.1, the exposure temperature is similar to the L-H/He conditions. This is reflected in the observed surface extrusions, that look similar to the structures found on the L-H/He reference sample.

A visual inspection of all monoblocks, showed that a slight difference in

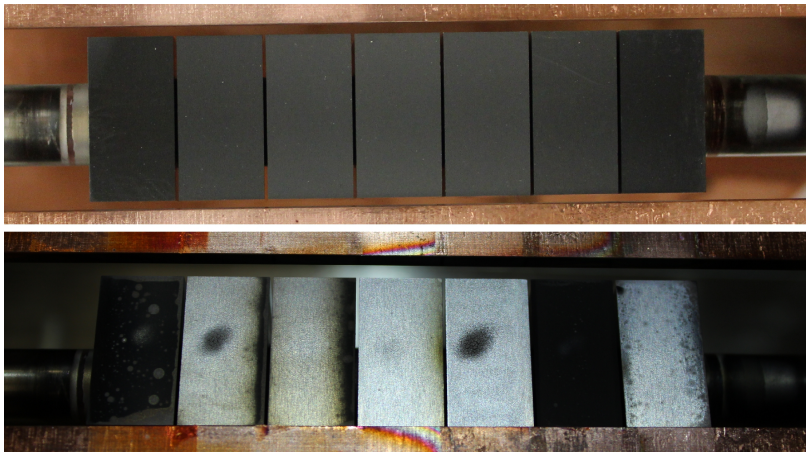

Figure 5.6: The W-MMU-12-16 mock-up, after the H/He exposure in GLADIS, installed in JUDITH 2 with monoblock A to monoblock G going from left to right. The pictures are taken before the simultaneous steady state and ELM-like heat loads (top) and after the exposure (bottom).

optical reflection, shown in figure 5.6, is observed between the two outer monoblocks and the five inner monoblocks. From the results in subsection 3.1.2, it can be expected that this is caused by a difference in the shape and size of the surface extrusions. This could not be verified during the intermediate analysis, since only SEM pictures perpendicular to the surface of mock-up D and E could then be obtained. However, on the SEM pictures of the final analysis, e.g. in figure 5.8, it is seen that the same surface extrusions are present on monoblock A, which is an indication that after the H/He exposure, the differences between the seven monoblocks in the shape and the size of the surface extrusions are minimal.

After the simultaneous steady state and ELM-like heat loading, the final analysis is performed. In a visual inspection the ELM-loaded regions are recognized on each monoblock, although not with the same ease for each. For some monoblocks, as shown in figure 5.6, the edge of the surface differs visually from the main part of the surface, which is explained by temperature differences. During the JUDITH 2 exposure of a monoblock copper beam dumps are used to protect the other monoblocks, the cooling tube, and the JUDITH 2 device itself. If the beam dump is not correctly positioned, the monoblock surface can be partially shielded from the electron beam. For example, the black area on the right side of monoblock B and monoblock C is an artefact from such shielding. It is also possible that the beam dumps are not placed close enough and the incident angle of the electron beam can partially expose the side of the monoblock in the slit between two monoblocks, resulting in a higher temperature near the edge. Because these

artefacts should not be taken into account for the analysis, the border of the monoblock surface is not a topic of further discussion.

With the exception of monoblock F, each monoblock shows a surface modification, caused by the steady state heat flux. In case of monoblocks B, C, D, and E, the color of the whole surface has changed from dark grey to a more reflective metallic, light grey. This indicates that the steady state heat load results in a removal or strong modification of the surface extrusions. The same phenomenon is observed for monoblock G, with the exception of a few small circular spots, where this process either has not been fully completed yet, or was already further advanced. For monoblock A circular spots can also be observed on the surface, although it can again not be determined at this stage if these spots are the least modified or the most modified areas.

With LM, shown in figure 5.7, similar observations are found for the effect of the steady state heat loading. An important difference is observed for monoblock F, where a few small circular spots are visible in LM. This indicates that there might be a modification or removal on at least a part of the surface for each monoblock. Furthermore, the machining grooves are also still detectable after the electron beam exposure.

A first assessment of the ELM-induced damage is performed with the LM pictures. On the surface of monoblock B and monoblock E an extensive crack network is visible. At high magnification, there are indications that also monoblock F has a crack network, although this can not be ascertained with LM. For the other monoblocks, which had a surface temperature of 1500 °C, the surface modifications that are visible in the LM pictures are limited to roughening.

The SEM pictures are divided into two categories, depending on whether they are taken within the region that is exposed to ELM-like heat loads or on a location that is remote from this region. In the SEM of the monoblock surface within the SSHF region, i.e. the area remote from the ELM-loaded region, the observed damage can partially be caused by the transient heat loads, as shown in figure 5.8. No damage is detected for monoblock A and F, this includes the lack of modifications of the surface extrusions. Even the circular spots found during the LM and visual inspection of monoblock A are not visible. The other monoblocks show minor or extensive cracking and in each case a distinctive morphology change for the extrusions.

The extrusions on monoblock C are strongly modified on the whole surface, reduced in height and having a morphology similar to a spherical dome. A similar removal of the surface extrusions is observed for monoblock B. On some locations of monoblock D, although not as frequent as for monoblock B and C, are these remnants also present. However, most parts from the surface of monoblock D are characterized by a strong deformation of the surface, without any remains of the surface extrusions. This deformation has lead to the erosion of whole tungsten grains. Although monoblock E had no detectable erosion, this deformation was more prominently present

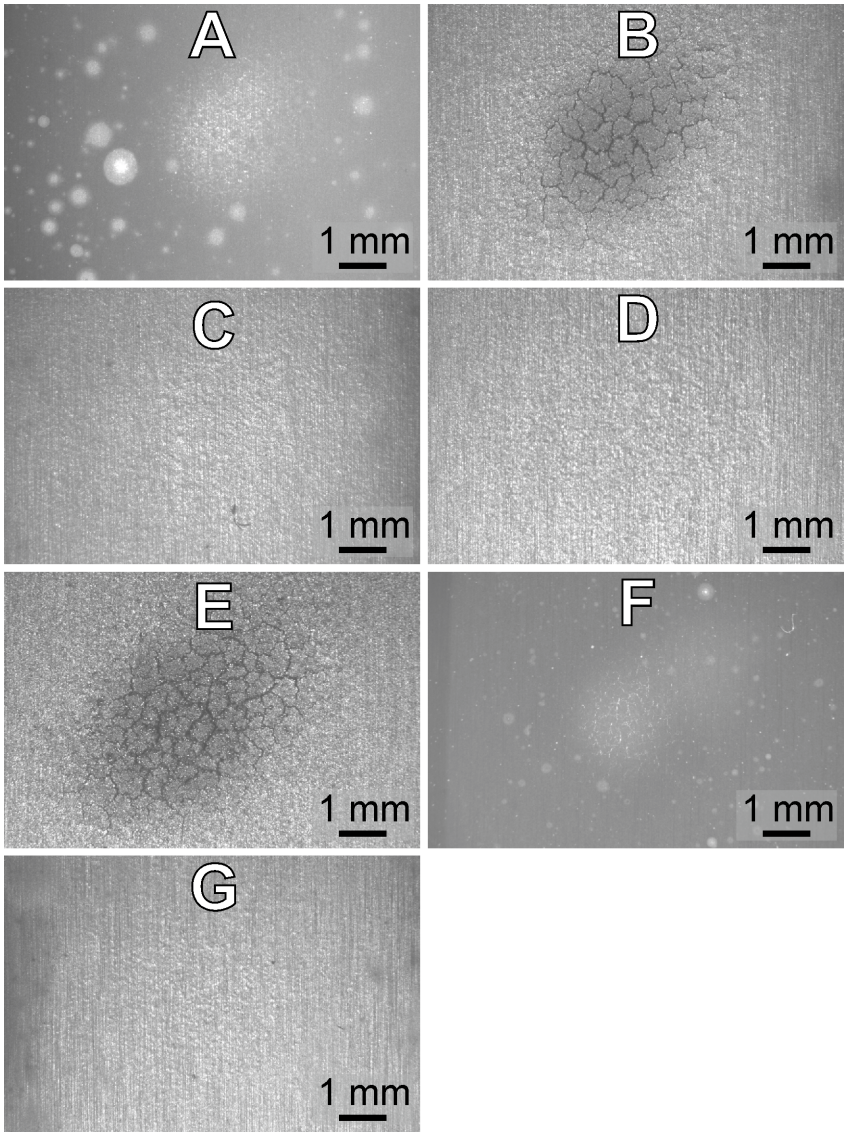

Figure 5.7: LM for each monoblock with H/He pre-exposure, after the combined ELM-like and steady state heat loading in JUDITH 2.

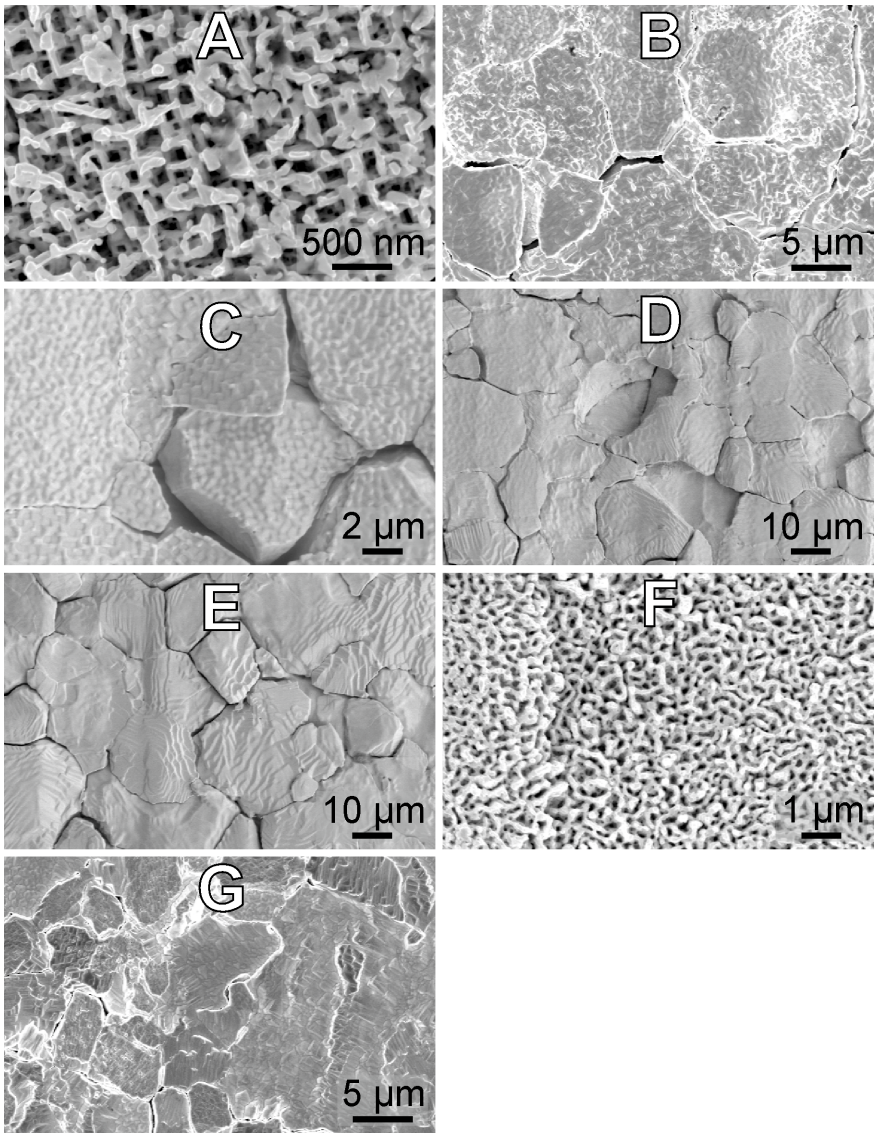

Figure 5.8: SEM pictures for each monoblock exposed to the combined ELM-like and steady state heat loading in JUDITH 2 after a H/He pre-exposure. All pictures are taken in the SSHF region.

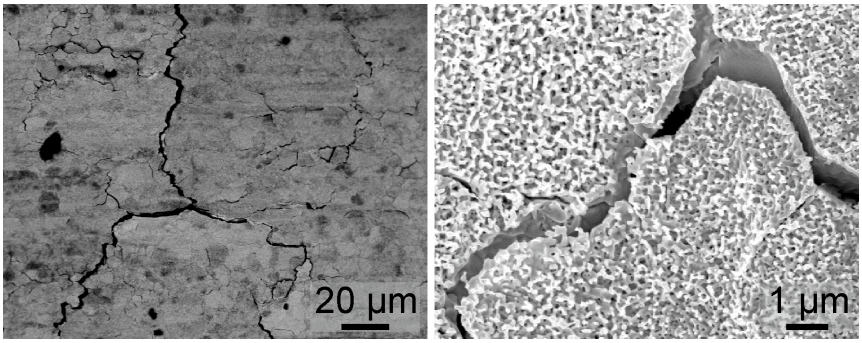

Figure 5.9: SEM pictures for the ELM-loaded region of monoblock A, which is exposed to the combined ELM-like and steady state heat loading in JUDITH 2 after a H/He pre-exposure.

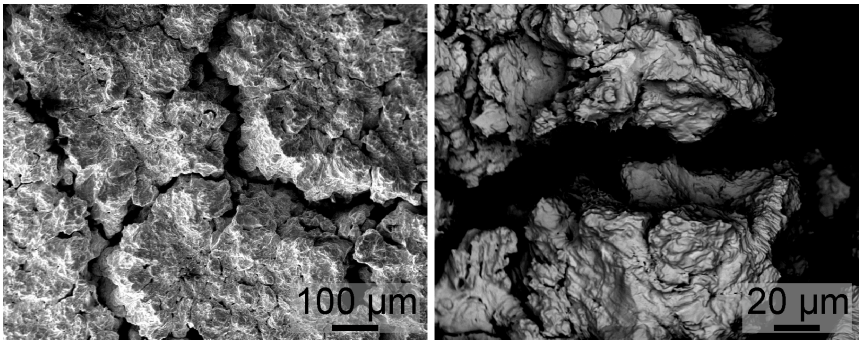

Figure 5.10: SEM pictures for the ELM-loaded region of monoblock B, which is exposed to the combined ELM-like and steady state heat loading in JUDITH 2 after a H/He pre-exposure.

on the surface and all remnants of the surface extrusions have completely disappeared. For monoblock G the surface extrusions have completely disappeared, but in contrast to monoblock D and E, there are no deformation lines.

A further assessment of the damage is performed with SEM in the region loaded with the ELM-like transients. On monoblock A, shown in figure 5.9, a crack network has formed in the ELM-loaded area, which was not detected in the LM. Furthermore, the extrusions are unaltered by the transient loading, even near the ELM-induced cracks. This is identical to what is observed in subsection 4.1.2 for the transient exposure in JUDITH 1 after a mixed H/He pre-exposure, e.g. in figure 4.8.

Monoblock B has, as shown in figure 5.10, an extensive crack network in combination with a strong deformation of the surface. None of the surface

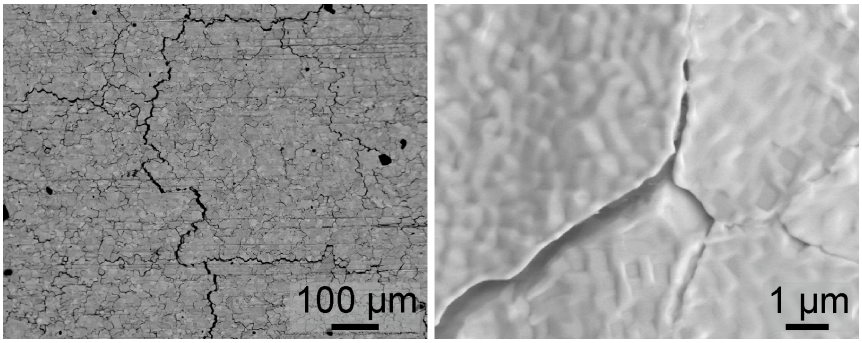

Figure 5.11: SEM pictures for the ELM-loaded region of monoblock C, which is exposed to the combined ELM-like and steady state heat loading in JUDITH 2 after a H/He pre-exposure.

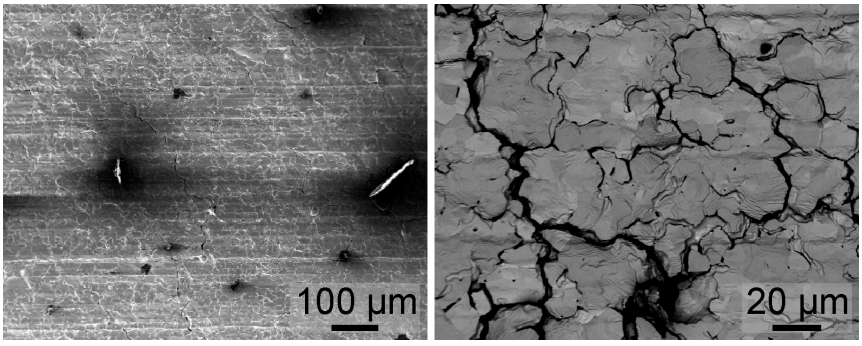

Figure 5.12: SEM pictures for the ELM-loaded region of monoblock D, which is exposed to the combined ELM-like and steady state heat loading in JUDITH 2 after a H/He pre-exposure.

extrusions, nor the specific surface pattern that is detected elsewhere on this monoblock surface, remain. Tungsten droplets or other indications of melting are not retrieved on the surface.

Although it could not be detected by LM, a crack network is formed on the ELM-loaded areas of monoblock C and monoblock D, shown in figure 5.11 and figure 5.12 respectively. On monoblock C remnants from the surface extrusions are still observed, while this is not the case for monoblock D. Besides the formation of a crack network a deformation can be found for monoblock D, which occurred to a lesser extent than the deformation that is observed for the ELM-loaded region of monoblock B. Furthermore, a singular isolated tungsten droplet is found on monoblock D.

The cracking that is observed during LM of monoblock E, is also seen on the SEM, as shown in figure 5.13. On the surface a strong deformation has

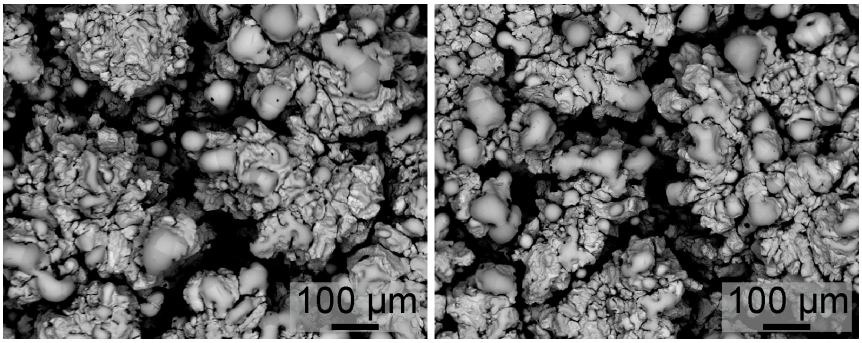

Figure 5.13: SEM pictures for the ELM-loaded region of monoblock E, which is exposed to the combined ELM-like and steady state heat loading in JUDITH 2 after a H/He pre-exposure.

taken place, similar to the deformation found on monoblock B. Additionally, an abundance of tungsten droplets are found on the surface, indicating that the combination of strong deformation and cracking has reduced the heat transport capabilities to such extent that on several locations the melting temperature is exceeded.

In the ELM-loaded region of monoblock F, shown in figure 5.14, plastic deformed locations are found which do not contain any surface extrusions. No cracks are observed at all on the monoblock surface. The indications for cracking that were observed during LM coincide with the extrusion-free deformed areas and are not related with surface cracking. On an extrusion-free deformed area the reflection is different from the reflection on the rest of the surface, resulting in the wrongly perceived crack indications. Besides in these extrusion-free areas, the H/He-induced extrusions are still prevalent on the surface without any observed modification to their shape and height.

Also for monoblock G a crack network is formed, as shown in figure 5.15, despite the observations with LM. The surface extrusions are no longer present, nor are any extrusion remnants, as could be expected from the images taken outside the ELM-loaded area. Furthermore, the surface morphology that is observed for the SSHF region of this monoblock and monoblock B, has also appeared here on the ELM-loaded region.

Laser profilometry scanning of the monoblock surface is performed with a 100 points/mm resolution. The corresponding R_a values, both for the ELM-loaded region and the SSHF region, are shown in table 5.2. A comparison of R_a values with the R_a values from the experiments described in chapter 3 and chapter 4 is not reasonable, since the monoblocks are not polished before the execution of the experiments and are also made from another tungsten grade. For a pristine monoblock, without any polishing or processing, the laser profilometry scan results in a reference R_a of 0.50 µm.

In the SSHF region, the R_a values are the highest for monoblock D

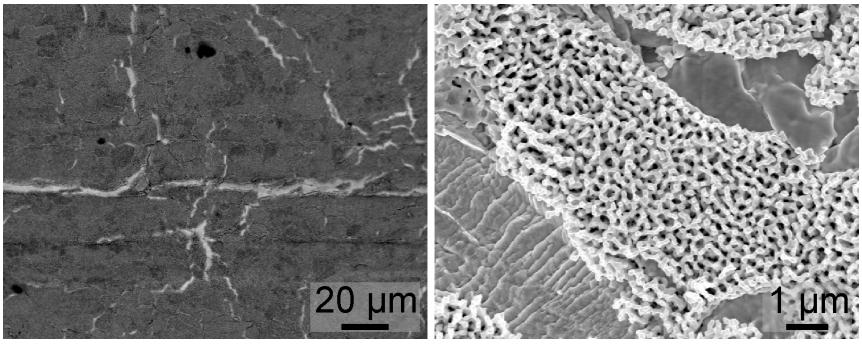

Figure 5.14: SEM pictures for the ELM-loaded region of monoblock F, which is exposed to the combined ELM-like and steady state heat loading in JUDITH 2 after a H/He pre-exposure.

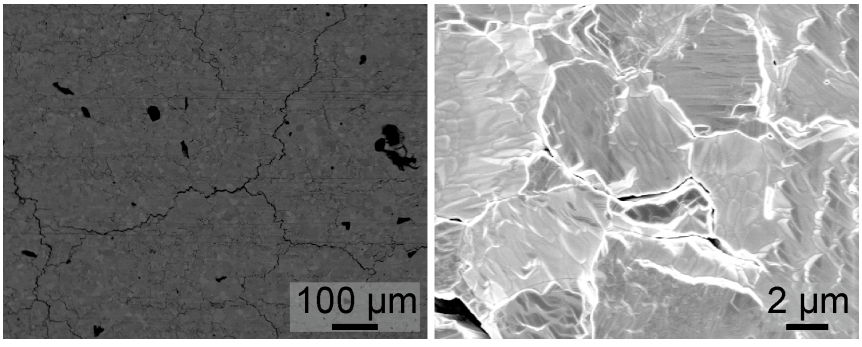

Figure 5.15: SEM pictures for the ELM-loaded region of monoblock G, which is exposed to the combined ELM-like and steady state heat loading in JUDITH 2 after a H/He pre-exposure.

Table 5.2: The arithmetic mean roughness R_a in the ELM-loaded region and in the SSHF region for combined ELM-like and steady state loading after H/He pre-exposure. The R_a is calculated based on a 100 points/mm laser profilometry scan.

Monoblock	R_a [µm]	
	SSHF region	ELM-loaded region
A	0.50	0.73
B	0.71	18.2
C	0.65	1.28
D	0.90	1.40
E	1.06	37.3
F	0.58	1.11
G	0.61	0.92

and E, which have both the same GLADIS exposure and SSHF exposure in JUDITH 2, that lead for both monoblocks to recrystallization. Their ELM-like heat loading has the same pulse number, but they differ in F_{HF}. The monoblock with the highest F_{HF}, i.e. monoblock E, also had a higher roughening, although the difference in R_a, 0.16 µm, is relatively small in comparison to the reference R_a of 0.50 µm. It does suggest that the ELM-like thermal loads might have an influence on the SSHF region.

If the JUDITH 2 loading conditions from monoblock D and E are reduced to 17 600 pulses, i.e. into the loading conditions of monoblock C and B respectively, also the roughening is lower by 0.25 µm and 0.35 µm respectively. This shows that the pulse number, which is directly connected to the SSHF exposure time, is a relevant parameter that has an influence on the roughening in the SSHF region. Since the difference in R_a between monoblock B and C is only 0.06 µm, it can be said that if the ELM-loading has an effect on the SSHF region, that effect does not play a role at this exposure time.

For the roughness in the SSHF region of the monoblocks that did not undergo recrystallization during JUDITH 2 exposure, i.e. monoblocks A, F, and G, the data is too close to the reference R_a value to draw conclusions. Furthermore, these three monoblocks differ from the other four monoblocks in at least two loading parameters, inhibiting the allocation of any perceived behaviour to a specific loading parameter.

The R_a for each monoblock is higher in the ELM-loaded region than in the SSHF region, showing that each loading condition results in ELM-induced damage. Although this is in contrast with the visual inspection and the LM, where no ELM-induced damage was identified for some monoblocks, the same observation is made based on SEM images. The thermal shock damage threshold is therefore located below F_{HF} 4.5 for ELM-like thermal

loads at a surface temperature of 1000 °C and a pulse number of 1000 for these pre-exposed monoblocks. While this is substantially lower than the damage threshold determined in subsection 3.2.1, it needs to be taken into account that they can not be directly compared since that was a different material grade, i.e. double forged tungsten with longitudinal grain orientation.

Monoblocks B and E have a vastly higher R_a in the ELM-loaded region than the other five monoblocks. Both of them have been exposed to F_{HF} 12 transients at 1500 °C, which has caused the extensive deformation and cracking that is reflected in the R_a value. The increased roughening for monoblock E when compared to monoblock B is caused by the higher pulse number for monoblock E.

Two factors are responsible for the fact that the roughening in the ELM-loaded region is lower for monoblock F, i.e. the other monoblock with F_{HF} 12 ELM-like loading. Firstly, the dominant factor is the pulse number, i.e. 1000 ELM-like loads, which is too low to have enough damage accumulated to reach this level of roughening. A second factor, although one that plays a minor role in the roughening for the ELM-loaded region of monoblock F, is the lower surface temperature, i.e. 1000 °C.

The damage categorization of the monoblocks based on these analyses is straightforward. Due to the clear plastic deformation and the lack of any other damage, monoblock F belongs to the category *Additional Surface Damage*. Two damage categories are assigned for the loading conditions of monoblok E, i.e. *Cracking* and *Melting*. For all other cases, i.e. monoblocks A, B, C, D, and G, the damage category is *Cracking*, as is made clear by the SEM.

The monoblocks differ from the double forged tungsten samples not only in material grade and loading conditions, but also in testing method. In the JUDITH 2 experiments, the electron beam follows a programmed beam path to have a combined SSHF and ELM-loading in JUDITH 2, while in the JUDITH 1 experiments the electron beam performs a triangular scanning of the ELM-loaded area on a pre-heated surface. Due to the differences, a meaningful direct comparison of the thermal shock behaviour can not be done. Nevertheless, the samples described in subsection 4.1.4 that are first exposed to M-H/He or L-H/He and thereafter loaded in JUDITH 1 to T1000-12 have strong resemblance with the exposure for monoblock F. It is interesting to note that, as shown in figure 4.22 and figure 4.24, these samples have surface cracks in contrast to monoblock F, where the damage is limited to a plastic deformation.

If the monoblocks are compared with high pulse number experiments performed earlier in JUDITH 2 at a surface temperature of 700 °C [100], similarities are found, despite the differences in surface temperature. After 100 000 ELM-like heat loads with F_{HF} 12 in both cases, i.e. for monoblock E and the earlier performed research, a crack network is observed on a strongly deformed surface with local melting. Monoblock B, exposed to 17 600 ELM-

like loads with F_{HF} 12, has a similar strongly deformed surface with crack network as the sample exposed to 10 000 ELM-like loads with F_{HF} 12, although the R_a is higher for monoblock B [68]. The comparison with these less severely exposed samples, gives the indication that there is no deterioration of the thermal shock behaviour due to a mixed hydrogen/helium pre-exposure.

Additionally, an identical monoblock mock-up, i.e. W-MMU-12-18, has earlier been investigated with exposure conditions similar to monoblocks A, C, D, and E [111]. Either solely the simultaneous SSHF and ELM-like transient heat loading in JUDITH 2 was applied on W-MMU-12-18, or the SSHF from the mixed hydrogen/helium exposure was first simulated by the electron beam as a pre-loading and then the simultaneous SSHF and ELM-like transient heat loading was applied on W-MMU-12-18. For monoblocks A and C a comparison is possible both with and without the pre-loading, while for monoblocks D and E only a comparison exists without the pre-loading. In each case, the monoblock with hydrogen/helium pre-exposure has lower R_a values and either a similar surface morphology or a less severely damaged surface morphology than for mock-up W-MMU-12-18 as reported in literature. W-MMU-12-18 shows for example several tungsten melt droplets after both loading conditions with pre-loading and both loading conditions with 100 000 pulses, while only monoblock E contained melt droplets.

A comparison of each loading condition that takes into account the differences between the ELM-loaded region and the SSHF region demonstrates that the surface extrusions remain unmodified on the ELM-loaded region if they are also present on the SSHF region. The transient heat loading has no observable effect on the removal of the surface extrusions under the tested range of loading conditions. It is not excluded that the process of extrusion removal is facilitated by ELM-like exposure, but under these loading conditions the transient loading is not a dominant factor. Under more intense exposures, such as the extreme case of transient heat loads that result in surface melting which is observed in subsection 4.1.4, this conclusion is no longer valid.

Two parameters that do have an effect on the removal of the H/He-induced surface extrusions are identified. Since the extrusions are no longer present in the SSHF region of monoblocks B, C, D and E, i.e. all the monoblocks with a surface temperature of 1500 °C, independently of the exposure time, the surface temperature is a factor. This corresponds with the reported removal of nano-tendril on tungsten by annealing for 3600 s in a vacuum furnace at 1400 °C [114]. By comparing the two monoblocks exposed in JUDITH 2 at 1200 °C, i.e. monoblocks A and G, which only differ in exposure time, a surface temperature of 1200 °C can be sufficient to have extrusion removal. However, the removal process only occurs if the exposure time is sufficiently long.

The surface damage, such as the occurrence of cracks and even grain loss, in the SSHF region for some monoblocks indicated that the ELM-

like exposure influences the damage in an area that is broader than the ELM-loaded region. However, this does not lead to the conclusion that the observed damage is only allocated to transient heat load effects. It is important to find out to which extent this damage comes from the steady state exposure and the transient exposure and the influence on the H/He pre-exposure. However, the limited amount of loading conditions in this experimental campaign prevents drawing further conclusions.

5.3 Summary and Conclusions

A mock-up consisting of seven tungsten monoblocks was exposed in the electron beam facility JUDITH 2 to a simultaneous SSHF and ELM-like loading with high pulse numbers after a H/He pre-exposure. The pre-exposure was performed in the neutral beam facility GLADIS with surface temperatures ranging from 1200 °C to 1500 °C. The H/He-flux, although different in exposure time, particle energy, absorbed power density, particle flux, and total fluence, resulted in surface modifications similar to the M-H/He and L-H/He reference samples, including the H/He-induced surface extrusions. For each monoblock, the H/He-induced modifications were uniformly spread over the whole surface. After the final exposure, the surface of the monoblock is divided into two regions, i.e. the SSHF region and the ELM-loaded region.

Due to the SSHF only, the surface extrusions of five monoblocks have been removed. Only monoblocks A and F, which are loaded in the SSHF region at 1200 °C for the duration of 17 600 pulses and at 1000 °C for the duration of 1000 pulses, respectively, are still covered with surface extrusions. For the other monoblocks, besides a removal of the surface extrusions in the SSHF region also cracks were found. Because the surface structure removal is identical for the SSHF region and the ELM-loaded region, the ELM-loading is here not a dominant factor in the removal of surface structures. Two factors are identified that influence the extrusion removal, i.e. the surface temperature and the exposure time.

The ELM-loaded region of monoblock F, which was loaded with 1000 pulses of F_{HF} 12 at 1000 °C, has extrusion-free locations due to plastic deformation. Similar behaviour was not observed for the double forged tungsten, which showed crack formation under equivalent loading conditions. The other six monoblocks have a cracked ELM-loaded region. For monoblock B i.e. loaded with 17 600 pulses of F_{HF} 12 at 1500 °C, this occurred in combination with a strong surface deformation, while a further increase of the pulse number to 100 000 pulses, i.e. monoblock E, additionally resulted in the formation of tungsten melt droplets.

The monoblocks showed in several ways, e.g. the roughening or the damage category, an increase of damage for higher surface temperatures, higher pulse number, and higher F_{HF}. Besides the temperature dependant yield strength that can cause stronger deformation at higher temperatures [102],

also the recrystallization that occurred at the highest temperature results in increased damage [103]. However, previous research on a different material without a particle pre-exposure at less severe loading conditions in JUDITH 2 [100] showed similar damage, thereby giving an indication that the thermal shock behaviour is not deteriorated due to hydrogen/helium pre-exposure despite the recrystallization for mock-ups B, C, D, E and F. The comparison with the experiments on W-MMU-12-18 [111] shows that with respect to the roughness and the occurrence of melt droplets, an actual improvement for the H/He pre-exposed mock-up at the high pulse numbers.

The same kind of damage that is seen here on the H/He pre-exposed W-MMU-12-16 is also observed on other tungsten grades and on W-MMU-12-18, although the damage is often less severe for H/He pre-exposed samples. It is not clear if either the H/He-induced sub-surface cavities or the surface extrusions, which were removed under some of the loading conditions, play a dominant role. The analysis of the monoblocks demonstrates that at high pulse numbers, there is no degradation of the thermal shock performance due to the H/He pre-exposure, but other interactions, e.g. enhanced erosion due to the extrusion removal, can not be excluded.

Chapter 6

Overall Conclusions and Outlook

During the operation of a fusion reactor, the plasma facing material (PFM) will be exposed to intense particle fluxes, steady state heat loads and transient heat loads. Each loading condition on its own can result in damage of the PFM, but the interactions between several loading conditions can modify the damage mechanism. For tungsten, one of the most promising choices of PFMs, these interactions were investigated by performing a combination of sequential exposures in the neutral beam facility GLADIS and the electron beam facilities JUDITH 1 and JUDITH 2 and comparing them to single exposure experiments. During the single exposure experiments, tungsten was exposed either solely to a particle flux or to the transient heat loads from edge localised modes (ELMs).

Tungsten that was pre-loaded with a hydrogen or hydrogen/helium particle flux was modified in several ways, e.g. retention of hydrogen and helium, erosion, surface morphology, surface extrusions, sub-surface cavities, etc. Despite the particle-induced modifications, the damage resistance against ELM-like transient heat loads did not deteriorate for either the low pulse number experiments nor for the high pulse number experiments. Instead, under some loading conditions a quantifiable, e.g. roughness, or qualitative, e.g. damage category, decrease in damage was observed in comparison to thermal shock experiments on polished pristine tungsten.

Both for the single exposure experiments, and the sequential exposure experiments, including the high pulse number experiments, a high base temperature during the heat load exposure resulted in a reduced material performance, e.g. 'crack initiations'. Additionally, the pre-exposure resulted in a recrystallization for some samples, which were subsequently more prone to damage. This behaviour is also reported in the literature and the recrystallized particle pre-exposed tungsten is not observed to be more severely

damaged than recrystallized polished tungsten.

The consequences that arise from the particle induced modifications are nevertheless a potential matter of concern. High heat fluxes can either remove or partially melt the H/He-induced surface extrusions at high pulse numbers, temperatures, or power densities, resulting in a possible increase of erosion and tungsten dust. Additionally, the sub-surface cavities were shown to grow if the temperature during ELM-like loading was higher than during the particle flux. Due to the particle induced modifications, it can be necessary to impose a limitation on both the base temperature and the temporal temperature increase by transients, so that recrystallization of tungsten and the partial melting of the surface extrusions are avoided.

An essential interaction between the H/He particle induced damage and the damage induced by the ELM-like heat loads occurs inside the cracks and near the cracks. At the crack edge, the particle flux resulted in an enhanced erosion, although this would not happen as extensively for a fusion reactor because there the energy of the impinging particle flux is smaller than during the experiments in GLADIS. The H/He-induced surface extrusions can also cover the crack, i.e. 'crack bridging', or form a porous 'filling' structure inside the crack.

However, further ELM-like heat loading will cause a repeated (partial) closing of the crack, due to the thermal expansion during ELM-like heat loads and the thermal contraction between ELM-like heat loads. The resulting compressive and tensile stresses will break the 'crack bridge', while frictional forces can destroy the porous structure. This might result in the release of tungsten dust and erosion.

For further research, an extensive increase of the loading parameters, especially for high pulse numbers, will make it possible to determine the maximum values for both the surface temperature and the power density, or heat flux factor, of the transient heat loads that still lead to an acceptable amount of tungsten degradation with respect to reactor performance and operation. These values can be different for pristine tungsten, pre-exposed tungsten, and tungsten that is simultaneously loaded with combined loading conditions, although the current experiments did not point towards a clear decrease of acceptable loading conditions. The high pulse number experiments already show the difference in damage that can occur between $205\,\mathrm{MW\,m^{-2}}$ and $548\,\mathrm{MW\,m^{-2}}$ ELM-like loads with a 0.48 s pulse length, which shows that an earlier reported maximum damage threshold in the range of $0.14\,\mathrm{GW\,m^{-2}}$ to $0.27\,\mathrm{GW\,m^{-2}}$ for pristine tungsten [68], might also be applicable for tungsten that has been pre-exposed to a H/He-flux.

The mechanism behind the removal of the surface extrusions needs to be determined, together with the consequent impact on tungsten erosion. This also needs to be done for the porous 'filling' structures and the 'crack bridging' phenomena, which might be either altered or not formed during a simultaneous exposure. Hence, an extension of this investigation to a simultaneous ELM-like heat loading and a H/He-particle loading would be vital.

Within Forschungszentrum Jülich, this would be possible with the linear plasma device PSI-2 [115], although under adjusted loading conditions.

Furthermore, no experiments were performed to investigate the influence of the angle of the impinging particle flux, which should be part of future work. The effects of neutron irradiation are not within the scope of this work, but are an essential part for ITER and future devices. Including neutron irradiation among the set of loading conditions in future research will provide crucial information on the performance of PFMs and would be recommended, despite the enhanced complexity of testing activated material.

Appendix A

Overview of Applied Loading Conditions

Table A.1: An overview and the nomenclature of the labels for the steady state hydrogen exposures in GLADIS.

Label	Beam	T_{Surf} [°C]	Heat Flux [MW m^{-2}]	Fluence [m^{-2}]
S-H	100 % H	600	9.4	1.8×10^{25}
M-H	100 % H	1000	10.2	1.9×10^{25}
L-H	100 % H	1500	10.5	2.0×10^{25}

Table A.2: An overview and the nomenclature of the labels for the steady state hydrogen/helium exposures in GLADIS

Label	Beam	T_{Surf} [°C]	Heat Flux [MW m^{-2}]	Fluence [m^{-2}]
S-H/He	6 % He, 94 % H	600	9.4	1.8×10^{25}
M-H/He	6 % He, 94 % H	1000	10.2	1.9×10^{25}
L-H/He	6 % He, 94 % H	1500	10.5	2.0×10^{25}

Table A.3: An overview and the nomenclature of the labels for the ELM-like transient heat loads in JUDITH 1 with 100 pulses

Label	T [°C]	F_{HF}	P [MW m^{-2}]	Pulse number
HRT-6	RT	6	190	100
HRT-12	RT	12	380	100
HRT-48	RT	48	1514	100
H400-6	400	6	190	100
H400-12	400	12	380	100
H400-48	400	48	1514	100
H1000-6	1000	6	190	100
H1000-12	1000	12	380	100
H1000-48	1000	48	1514	100

Table A.4: An overview and the nomenclature of the labels for the ELM-like transient heat loads in JUDITH 1 with 1000 pulses

Label	T [°C]	F_{HF}	P [MW m^{-2}]	Pulse number
T1000-6	1000	6	190	1000
T1000-12	1000	12	380	1000
T1000-48	1000	48	1514	1000

Bibliography

[1] S. Atzeni and J. Meyer-ter Vehn, *The Physics of Inertial Fusion: Beam-Plasma Interaction, Hydrodynamics, Hot Dense Matter*, International Series of Monographs on Physics, Oxford Science Publications, 2004, ISBN 9780198562641

[2] E. G. Adelberger, A. García, R. G. H. Robertson *et al.*, "Solar fusion cross sections. II. the *pp* chain and CNO cycles", *Reviews of Modern Physics* 83 (2011) pp. 195–245, doi:10.1103/RevModPhys.83.195

[3] J. Wesson, *Tokamaks*, International Series of Monographs on Physics, Oxford University Press, 3rd edition, 2004, ISBN 9780198509226

[4] G. Audi, A. Wapstra, and C. Thibault, "The AME2003 atomic mass evaluation: (II). Tables, graphs and references", *Nuclear Physics A* 729 (2003) 1 pp. 337 – 676, doi:10.1016/j.nuclphysa.2003.11.003

[5] J. D. Lawson, "Some criteria for a power producing thermonuclear reactor", *Proceedings of the Physical Society. Section B* 70 (1957) 1 p. 6, doi:10.1088/0370-1301/70/1/303

[6] U. Stroth, *Einführung in die Plasmaphysik*, Institut für Plasmaforschung, Universität Stuttgart, 2007

[7] J. Jacquinot, "Fifty years in fusion and the way forward", *Nuclear Fusion* 50 (2010) 1 p. 014001, doi:10.1088/0029-5515/50/1/014001

[8] T. C. Simonen, "Tandem mirror experiments at the Lawrence Livermore National Laboratory", *Nuclear Fusion* 25 (1985) 9 p. 1205, doi:10.1088/0029-5515/25/9/036

[9] V. Smirnov, "Tokamak foundation in USSR/Russia 1950–1990", *Nuclear Fusion* 50 (2010) 1 p. 014003, doi:10.1088/0029-5515/50/1/014003

[10] L. Spitzer, "The stellarator concept", *Physics of Fluids* 1 (1958) 4 p. 253, doi:10.1063/1.1705883

[11] Max-Planck-Institut für Plasmaphysik, "Max-Planck-Institut für Plasmaphysik | Research | Projects | Wendelstein 7-X | Introduction | Concept planning", `https://www.ipp.mpg.de/2815232/konzeptentwicklung`

[12] D. Hartmann, "Stellarators", *Fusion Science and Technology* 49 (2006) 2T pp. 43–55

[13] EUROfusion, "The electromagnetic coil set-up of JET", `https://www.euro-fusion.org/fusion/jet-tech/magnets/`

[14] E. Teller, *Fusion Part B: Magnetic confinement*, Elsevier Science, 2012, ISBN 9780323146616

[15] J. Jacquinot, "JET relevance to ITER, new trends and initial results", *Fusion Engineering and Design* 30 (1995) pp. 67–84, doi:10.1016/0920-3796(94)00402-S

[16] EUROfusion, "EUROfusion website", `https://www.euro-fusion.org/`

[17] G. Federici, C. Skinner, J. Brooks *et al.*, "Plasma-material interactions in current tokamaks and their implications for next step fusion reactors", *Nuclear Fusion* 41 (2001) 12 pp. 1967–2137, doi:10.1088/0029-5515/41/12/218

[18] R. Aymar, P. Barabaschi, and Y. Shimomura, "The ITER design", *Plasma Physics and Controlled Fusion* 44 (2002) 5 p. 519, doi:10.1088/0741-3335/44/5/304

[19] G. Janeschitz and ITER JCT, "Plasma-wall interaction issues in ITER", *Journal of Nuclear Materials* 290-293 (2001) pp. 1–11, doi:10.1016/S0022-3115(00)00623-1

[20] ITER Organization, "ITER website", `http://www.iter.org`

[21] F. Romanelli, *Fusion Electricity - A roadmap to the realisation of fusion energy*, European Fusion Development Agreement, 2012

[22] D. Maisonnier, I. Cook, S. Pierre *et al.*, "DEMO and fusion power plant conceptual studies in Europe", *Fusion Engineering and Design* 81 (2006) 8–14 pp. 1123–1130, doi:10.1016/j.fusengdes.2005.08.055

[23] K. Kim, H. C. Kim, S. Oh *et al.*, "A preliminary conceptual design study for Korean fusion DEMO reactor", *Fusion Engineering and Design* 88 (2013) 6–8 pp. 488–491, doi:10.1016/j.fusengdes.2013.02.123

[24] K. Tobita, S. Nishio, M. Enoeda *et al.*, "Design study of fusion DEMO plant at JAERI", *Fusion Engineering and Design* 81 (2006) 8–14 pp. 1151–1158, doi:10.1016/j.fusengdes.2005.08.058

[25] PPPL, "PPPL teams with South Korea on the forerunner of a commercial fusion power station", `http://www.pppl.gov/news/2012`

[26] W. O. Hofer and J. Roth, *Physical processes of the interaction of fusion plasmas with solids*, Plasma-materials interactions, Academic Press, 1996, ISBN 9780123515308

[27] A. Kirschner, "Erosion and deposition mechanisms in fusion plasmas", *Fusion Science and Technology* 53 (2008) 2T pp. 259–277

[28] M. Ye, H. Kanehara, S. Fukuta *et al.*, "Blister formation on tungsten surface under low energy and high flux hydrogen plasma irradiation in NAGDIS-I", *Journal of Nuclear Materials* 313–316 (2003) pp. 72–76, doi:10.1016/S0022-3115(02)01349-1

[29] S. Gilliam, S. Gidcumb, N. Parikh *et al.*, "Retention and surface blistering of helium irradiated tungsten as a first wall material", *Journal of Nuclear Materials* 347 (2005) 3 pp. 289–297, doi:10.1016/j.jnucmat.2005.08.017

[30] N. Lemahieu, H. Greuner, J. Linke *et al.*, "Synergistic effects of ELMs and steady state H and H/He irradiation on tungsten", *Fusion Engineering and Design* 98–99 (2015) pp. 2020–2024, doi:10.1016/j.fusengdes.2015.06.051

[31] S. Kajita, W. Sakaguchi, N. Ohno *et al.*, "Formation process of tungsten nanostructure by the exposure to helium plasma under fusion relevant plasma conditions", *Nuclear Fusion* 49 (2009) 9 p. 095005, doi:10.1088/0029-5515/49/9/095005

[32] H. Greuner, H. Maier, M. Balden *et al.*, "Investigation of W components exposed to high thermal and high H/He fluxes", *Journal of Nuclear Materials* 417 (2011) 1 pp. 495–498, doi:10.1016/j.jnucmat.2010.12.215

[33] R. Pitts, S. Carpentier, F. Escourbiac *et al.*, "A full tungsten divertor for ITER: physics issues and design status", *Journal of Nuclear Materials* 438 (2013) pp. S48–S56, doi:10.1016/j.jnucmat.2013.01.008

[34] J. Linke, "High heat flux performance of plasma facing materials and components under service conditions in future fusion reactors", *Fusion Science and Technology* 49 (2006) pp. 455–464

[35] A. Loarte, G. Saibene, R. Sartori *et al.*, "Characteristics of type I ELM energy and particle losses in existing devices and their extrapolation to ITER", *Plasma Physics and Controlled Fusion* 45 (2003) 9 pp. 1549–1569

[36] M. Merola, D. Loesser, A. Martin *et al.*, "ITER plasma-facing components", *Fusion Engineering and Design* 85 (2010) 10 pp. 2312–2322, doi:10.1016/j.fusengdes.2010.09.013

[37] R. E. H. Clark and D. Reiter, *Nuclear Fusion Research: Understanding Plasma-Surface Interactions*, *Springer Series in Chemical Physics*, volume 78, Springer Berlin Heidelberg, 2006, ISBN 9783540273622

[38] D. N. Hill, "A review of ELMs in divertor tokamaks", *Journal of Nuclear Materials* 241 (1997) pp. 182–198, doi:10.1016/S0022-3115(97)80039-6

[39] W. Fundamenski, V. Naulin, T. Neukirch *et al.*, "On the relationship between ELM filaments and solar flares", *Plasma Physics and Controlled Fusion* 49 (2007) 5 p. R43, doi:10.1088/0741-3335/49/5/R01

[40] S. C. Cowley, H. Wilson, O. Hurricane, and B. Fong, "Explosive instabilities: from solar flares to edge localized modes in tokamaks", *Plasma Physics and Controlled Fusion* 45 (2003) 12A p. A31, doi:10.1088/0741-3335/45/12A/003

[41] NASA, "Solar dynamics observatory's picture of the week", `http://sdo.gsfc.nasa.gov/gallery/potw/item/577`

[42] W. Suttrop, "The physics of large and small edge localized modes", *Plasma Physics and Controlled Fusion* 42 (2000) 5A pp. A1–A14, doi:10.1088/0741-3335/42/5A/301

[43] G. Federici, "Plasma wall interactions in ITER", *Physica Scripta* 2006 (2006) T124 pp. 1–8, doi:10.1088/0031-8949/2006/T124/001

[44] T. E. Evans, "ELM mitigation techniques", *Journal of Nuclear Materials* 438 (2013) pp. S11–S18, doi:10.1016/j.jnucmat.2013.01.283

[45] A. Loarte, G. Saibene, R. Sartori *et al.*, "Transient heat loads in current fusion experiments, extrapolation to ITER and consequences for its operation", *Physica Scripta* 2007 (2007) T128 pp. 222–228, doi:10.1088/0031-8949/2007/T128/043

[46] G. Federici, P. Andrew, P. Barabaschi *et al.*, "Key ITER plasma edge and plasma–material interaction issues", *Journal of Nuclear Materials* 313-316 (2003) pp. 11–22, doi:0.1016/S0022-3115(02)01327-2

[47] A. Hassanein, T. Sizyuk, and M. Ulrickson, "Vertical displacement events: A serious concern in future ITER operation", *Fusion Engineering and Design* 83 (2008) 7-9 pp. 1020–1024, doi:10.1016/j.fusengdes.2008.05.032

[48] V. Barabash, M. Akiba, I. Mazul *et al.*, "Selection, development and characterisation of plasma facing materials for ITER", *Journal of Nuclear Materials* 233 (1996) pp. 718–723, doi:10.1016/S0022-3115(96)00323-6

[49] H. Bolt, V. Barabash, G. Federici *et al.*, "Plasma facing and high heat flux materials - needs for ITER and beyond", *Journal of Nuclear Materials* 307 (2002) pp. 42–52, doi:10.1016/S0022-3115(02)01175-3

[50] A. Kirschner, K. Ohya, D. Borodin *et al.*, "Prediction of long-term tritium retention in the divertor of ITER: influence of modelling assumptions on retention rates", *Physica Scripta* 2009 (2009) T138 p. 014011, doi:10.1088/0031-8949/2009/T138/014011

[51] UCB, "Periodieke tabel der elementen", Brochure distributed by Ghent University, 2005

[52] L. Singheiser, T. Hirai, J. Linke *et al.*, "Plasma-facing materials for thermo-nuclear fusion devices", *Transactions of the Indian Institute of Metals* 62 (2009) 2 pp. 123–128, doi:10.1007/s12666-009-0016-y

[53] V. Barabash, M. Akiba, J. Bonal *et al.*, "Carbon fiber composites application in ITER plasma facing components", *Journal of Nuclear Materials* 258 (1998) pp. 149–159, doi:10.1016/S0022-3115(98)00267-0

[54] R. W. Conn, R. P. Doerner, and J. Won, "Beryllium as the plasma-facing material in fusion energy systems - experiments, evaluation, and comparison with alternative materials", *Fusion Engineering and Design* 37 (1997) 4 pp. 481–513, doi:10.1016/S0920-3796(97)00092-6

[55] P. F. Wambach and J. Laul, "Beryllium health effects, exposure limits and regulatory requirements", *Journal of Chemical Health and Safety* 15 (2008) 4 pp. 5–12, doi:10.1016/j.jchas.2008.01.012

[56] K. Wittlich, T. Hirai, J. Compan *et al.*, "Damage structure in divertor armor materials exposed to multiple ITER relevant ELM loads", *Fusion Engineering and Design* 84 (2009) 7 pp. 1982–1986, doi:10.1016/j.fusengdes.2008.11.049

[57] J. Coenen, G. Arnoux, B. Bazylev *et al.*, "ELM-induced transient tungsten melting in the JET divertor", *Nuclear Fusion* 55 (2015) 2 p. 023010, doi:10.1088/0029-5515/55/2/023010

[58] S. Kaufman and W. F. Libby, "The natural distribution of tritium", *Physical Review* 93 (1954) pp. 1337–1344, doi:10.1103/PhysRev.93.1337

[59] F4E - European Joint Undertaking for ITER and the Development of Fusion Energy, "Fusion for Energy website", `http://fusionforenergy.europa.eu/`

[60] I. Cristescu, I. Cristescu, L. Doerr *et al.*, "Tritium inventories and tritium safety design principles for the fuel cycle of ITER", *Nuclear Fusion* 47 (2007) 7 p. S458, doi:10.1088/0029-5515/47/7/S08

[61] M. E. Sawan and M. A. Abdou, "Physics and technology conditions for attaining tritium self-sufficiency for the DT fuel cycle", *Fusion Engineering and Design* 81 (2006) 8 pp. 1131–1144, doi:10.1016/j.fusengdes.2005.07.035

[62] J. Linke, "Plasma facing materials and components for future fusion devices—development, characterization and performance under fusion specific loading conditions", *Physica Scripta* 2006 (2006) T123 p. 45, doi:10.1088/0031-8949/2006/T123/006

[63] M. Taniguchi, K. Sato, K. Ezato *et al.*, "Disruption tests on repaired tungsten by CVD coating", *Journal of Nuclear Materials* 307–311 (2002) pp. 719–722, doi:10.1016/S0022-3115(02)01041-3

[64] J. Davis, V. Barabash, A. Makhankov *et al.*, "Assessment of tungsten for use in the ITER plasma facing components", *Journal of Nuclear Materials* 258 (1998) pp. 308–312, doi:10.1016/S0022-3115(98)00285-2

[65] N. Lemahieu, J. Linke, G. Pintsuk *et al.*, "Performance of yttrium doped tungsten under 'edge localized mode'-like loading conditions", *Physica Scripta* 2014 (2014) T159 p. 014035, doi:10.1088/0031-8949/2014/T159/014035

[66] A. Prokhodtseva, *Characterization of tungsten based material under fusion specific thermal loads*, Universiteit Gent, 2009, MSc thesis

[67] G. Pintsuk, A. Prokhodtseva, and I. Uytdenhouwen, "Thermal shock characterization of tungsten deformed in two orthogonal directions", *Journal of Nuclear Materials* 417 (2011) 1-3 pp. 481–486, doi:10.1016/j.jnucmat.2010.12.109

[68] T. Loewenhoff, *Combined Steady State and High Cycle Transient Heat Load Simulation with the Electron Beam Facility JUDITH 2*, PhD thesis, RWTH Aachen University, 2012, ISBN 9783893368693, `http://publications.rwth-aachen.de/record/197556/files/4313.pdf`

[69] N. Rust, J. Baldzuhn, M. Kick *et al.*, "Recent results from W7-AS with the new radial NBI injector", *29th EPS Conference on Plasma Physics and Controlled Fusion, ECA* 26B (2002) P-4.045

[70] H. Greuner, H. Bolt, B. Böswirth *et al.*, "Design, performance and construction of a 2MW ion beam test facility for plasma facing components", *Fusion Engineering and Design* 75 (2005) pp. 345–350, doi:10.1016/j.fusengdes.2005.06.021

[71] H. Greuner, B. Boeswirth, J. Boscary, and P. McNeely, "High heat flux facility GLADIS: Operational characteristics and results of W7-X pre-series target tests", *Journal of Nuclear Materials* 367 (2007) pp. 1444–1448, doi:10.1016/j.jnucmat.2007.04.004

[72] O. Vollmer, R. Bilau-Faust, J. Feist *et al.*, "Initial operation and performance of the ASDEX long-pulse injection system", *Fusion Technology* (1989) pp. 625–630

[73] H. Greuner, Private Correspondence, 2015

[74] H. Maier, H. Greuner, M. Balden *et al.*, "Tungsten erosion under combined hydrogen/helium high heat flux loading", *Physica Scripta* (2014) T159 p. 014019, doi:10.1088/0031-8949/2014/T159/014019

[75] H. Falter, M. Proschek, S. Menhart *et al.*, "Helium doped hydrogen or deuterium beam as cost effective and simple tool for plasma spectroscopy", *Review of Scientific Instruments* 71 (2000) 10 pp. 3723–3727, doi:10.1063/1.1289678

[76] B. Schweer, F. Irrek, G. Sergienko *et al.*, "In situ diagnostic for monitoring of deuterium and tritium in re-deposited carbon layers by laser induced desorption", *Journal of Nuclear Materials* 363–365 (2007) pp. 1375–1379, doi:10.1016/j.jnucmat.2007.01.247

[77] B. Schweer, G. Beyene, S. Brezinsek *et al.*, "Laser techniques implementation for wall surface characterization and conditioning", *Physica Scripta* 2009 (2009) T138 p. 014008, doi:10.1088/0031-8949/2009/T138/014008

[78] M. Wirtz, J. Linke, G. Pintsuk *et al.*, "Comparison of thermal shock damages induced by different simulation methods on tungsten", *Journal of Nuclear Materials* 438 (2013) pp. S833–S836, doi:10.1016/j.jnucmat.2013.01.180

[79] K.-J. Bathe, *Finite Element Procedures*, Prentice Hall, 2nd edition, 1996, ISBN 9780133014587

[80] M. Merola, V. Barabash, R. Jakeman, and I. Smid, "ITER plasma facing component materials database in ANSYS format", ITER Doc. G 17 MD 71 96-11-19 W 0.1, 2000, version 1.3

[81] E. Lassner and W.-D. Schubert, *Tungsten: properties, chemistry, technology of the element, alloys, and chemical compounds*, Kluwer Academic / Plenum Publishers, 1999, ISBN 9780306450532

[82] J. Huba, "NRL plasma formulary", NRL/PU/6790–13-589, 2013, supported by The Office of Naval Research

[83] J. R. Welty, C. E. Wicks, R. E. Wilson, and G. L. Rorrer, *Fundamentals of Momentum, Heat and Mass Transfer*, John Wiley & Sons, 5th edition, 2008, ISBN 9780470128688

[84] R. Winterton, "Where did the Dittus and Boelter equation come from?", *International Journal of Heat and Mass Transfer* 41 (1998) 4–5 pp. 809–810, doi:10.1016/S0017-9310(97)00177-4

[85] T. Hirai and G. Pintsuk, "Thermo-mechanical calculations on operation temperature limits of tungsten as plasma facing material", *Fusion Engineering and Design* 82 (2007) 4 pp. 389–393, doi:10.1016/j.fusengdes.2007.03.032

[86] T. Koppitz, Private Correspondence, 2015

[87] N. Lemahieu, H. Greuner, J. Linke *et al.*, "Thermal shock behaviour of H and H/He-exposed tungsten at high temperature", *Physica Scripta* 2015 (2016) T167 p. 014008, doi:10.1088/0031-8949/T167/1/014008

[88] H. Maier, H. Greuner, M. Balden *et al.*, "Erosion behavior of actively cooled tungsten under H/He high heat flux load", *Journal of Nuclear Materials* 438 (2013) pp. S921–S924, doi:10.1016/j.jnucmat.2013.01.200

[89] M. Balden, Private Correspondence, 2014

[90] G. De Temmerman, K. Bystrov, J. J. Zielinski *et al.*, "Nanostructuring of molybdenum and tungsten surfaces by low-energy helium ions", *Journal of Vacuum Science and Technology A* 30 (2012) 4 p. 041306, doi:10.1116/1.4731196

[91] Y. Ueda, J. Coenen, G. De Temmerman *et al.*, "Research status and issues of tungsten plasma facing materials for ITER and beyond", *Fusion Engineering and Design* 89 (2014) 7 pp. 901–906, doi:10.1016/j.fusengdes.2014.02.078

[92] L. M. Garrison and G. L. Kulcinski, "Irradiation resistance of grains near {0 0 1} on polycrystalline tungsten under 30 keV He^+ bombardment at 1173 K", *Physica Scripta* 2014 (2014) T159 p. 014020, doi:10.1088/0031-8949/2014/T159/014020

[93] G. Greenwood, A. Foreman, and D. Rimmer, "The role of vacancies and dislocations in the nucleation and growth of gas bubbles in irradiated fissile material", *Journal of Nuclear Materials* 1 (1959) 4 pp. 305–324, doi:10.1016/0022-3115(59)90030-3

[94] C. Sang, J. Sun, X. Bonnin *et al.*, "Numerical simulation of the bubble growth due to hydrogen isotopes inventory processes in plasma-irradiated tungsten", *Journal of Nuclear Materials* 443 (2013) 1 pp. 403–408, doi:10.1016/j.jnucmat.2013.07.052

[95] G. Wright, D. Brunner, M. Baldwin *et al.*, "Tungsten nano-tendril growth in the Alcator C-Mod divertor", *Nuclear Fusion* 52 (2012) 4 p. 042003, doi:10.1088/0029-5515/52/4/042003

[96] Y. V. Martynenko and M. Y. Nagel, "Model of fuzz formation on a tungsten surface", *Plasma Physics Reports* 38 (2012) 12 pp. 996–999, doi:10.1134/S1063780X12110074

[97] A. Lasa, S. K. Tähtinen, and K. Nordlund, "Loop punching and bubble rupture causing surface roughening —a model for w fuzz growth", *Europhysics Letters* 105 (2014) 2 p. 25002, doi:10.1209/0295-5075/105/25002

[98] S. I. Krasheninnikov, "Viscoelastic model of tungsten 'fuzz' growth", *Physica Scripta* 2011 (2011) T145 p. 014040, doi:10.1088/0031-8949/2011/T145/014040

[99] J. Linke, T. Loewenhoff, V. Massaut *et al.*, "Performance of different tungsten grades under transient thermal loads", *Nuclear Fusion* 51 (2011) p. 6p, doi:10.1088/0029-5515/51/7/073017

[100] T. Loewenhoff, J. Linke, G. Pintsuk, and C. Thomser, "Tungsten and CFC degradation under combined high cycle transient and steady state heat loads", *Fusion Engineering and Design* 87 (2012) 7–8 pp. 1201–1205, doi:10.1016/j.fusengdes.2012.02.106

[101] M. Wirtz, *Thermal Shock Behaviour of Different Tungsten Grades under Varying Conditions*, PhD thesis, RWTH Aachen University, 2012, ISBN 9783893368426, `http://publications.rwth-aachen.de/record/62897/files/4314.pdf`

[102] T. Loewenhoff, A. Bürger, J. Linke *et al.*, "Evolution of tungsten degradation under combined high cycle edge-localized mode and steady-state heat loads", *Physica Scripta* (2011) T145 p. 014057, doi:10.1088/0031-8949/2011/T145/014057

[103] M. Wirtz, G. Cempura, J. Linke *et al.*, "Thermal shock response of deformed and recrystallised tungsten", *Fusion Engineering and Design* 88 (2013) 9–10 pp. 1768–1772, doi:10.1016/j.fusengdes.2013.05.077

[104] D. Nishijima, Y. Kikuchi, M. Nakatsuka *et al.*, "Effects of steady-state plasma exposure on tungsten surface cracking due to elm-like pulsed plasma bombardment", *Fusion Science and Technology* 60 (2011) 4 pp. 1447–1450

[105] W. W. Webb, J. T. Norton, and C. Wagner, "Oxidation of tungsten", *Journal of the Electrochemical Society* 103 (1956) 2 pp. 107–111, doi:10.1149/1.2430238

[106] W. Van Renterghem, I. Uytdenhouwen, T. Loewenhoff, and M. Wirtz, "TEM analysis of recrystallized double forged tungsten after exposure in JUDITH 1 and JUDITH 2", *Journal of Nuclear Materials and Energy* In press (2016), doi:10.1016/j.nme.2016.04.003

[107] N. Lemahieu, M. Balden, S. Elgeti *et al.*, "H/He irradiation on tungsten exposed to ELM-like thermal shocks", *Fusion Engineering and Design* 109-111 (2016) pp. 169–174, doi:10.1016/j.fusengdes.2016.03.035

[108] M. Wirtz, J. Linke, G. Pintsuk *et al.*, "Thermal shock behaviour of tungsten after high flux h-plasma loading", *Journal of Nuclear Materials* 443 (2013) pp. 497–501, doi:10.1016/j.jnucmat.2013.08.002

[109] T. Loewenhoff, S. Bardin, H. Greuner *et al.*, "Impact of combined transient plasma/heat loads on tungsten performance below and above recrystallization temperature", *Nuclear Fusion* 55 (2015) 12 p. 123004, doi:10.1088/0029-5515/55/12/123004

[110] G. De Temmerman, M. A. van den Berg, J. Scholten *et al.*, "High heat flux capabilities of the Magnum-PSI linear plasma device", *Fusion Engineering and Design* 88 (2015) pp. 483–487, doi:10.1016/j.fusengdes.2013.05.047

[111] T. Loewenhoff, J. Linke, G. Pintsuk *et al.*, "ITER-W monoblocks under high pulse number transient heat loads at high temperature", *Journal of Nuclear Materials* 463 (2015) pp. 202–205, doi:10.1016/j.jnucmat.2014.11.002

[112] T. Loewenhoff, T. Hirai, S. Keusemann *et al.*, "Experimental simulation of Edge Localised Modes using focused electron beams – features of a circular load pattern", *Journal of Nuclear Materials* 415 (2011) pp. S51–S54, doi:10.1016/j.jnucmat.2010.08.065

[113] J. Mayer, J. Kallinna, P. Watermeyer *et al.*, "Non-destructive analysis of engineering components in the large-chamber scanning electron microscope", *Microscopy and Microanalysis* 13 (2007) pp. 1010–1011, doi:10.1017/S1431927607074314

[114] G. Wright, G. van Eden, L. Kesler *et al.*, "Characterizing the recovery of a solid surface after tungsten nano-tendril formation", *Journal of Nuclear Materials* 463 (2015) pp. 294–298, doi:10.1016/j.jnucmat.2014.11.083

[115] B. Unterberg, R. Jaspers, R. Koch *et al.*, "New linear plasma devices in the trilateral euregio cluster for an integrated approach to plasma surface interactions in fusion reactors", *Fusion Engineering and Design* 86 (2011) 9-11 pp. 1797–1800, doi:10.1016/j.fusengdes.2011.03.082

List of Publications and Presentations

Publications

N. Lemahieu, H. Greuner, J. Linke, H. Maier, G. Pintsuk, M. Wirtz, G. Van Oost and J.-M. Noterdaeme
H/He irradiation on tungsten exposed to ELM-like thermal shocks
Fusion Engineering and Design 109-111 (2016) 169-174
doi:10.1016/j.fusengdes.2016.03.035

N. Lemahieu, H. Greuner, J. Linke, H. Maier, G. Pintsuk, M. Wirtz, G. Van Oost and J.-M. Noterdaeme
Thermal shock behaviour of H and H/He-exposed tungsten at high temperature
Physica Scripta T167 (2016) 014008
doi:10.1088/0031-8949/2016/T167/014008

N. Lemahieu, H. Greuner, J. Linke, H. Maier, G. Pintsuk, G. Van Oost and M. Wirtz
Synergistic effects of ELMs and steady state H and H/He irradiation on tungsten
Fusion Engineering and Design 98-99 (2015) 2020-2024
doi:10.1016/j.fusengdes.2015.06.051

N. Lemahieu, J. Linke, G. Pintsuk, G. Van Oost, M. Wirtz and Z. Zhou
Performance of yttrium doped tungsten under 'edge localized mode'-like loading conditions
Physica Scripta T159 (2014) 014035
doi:10.1088/0031-8949/2014/T159/014035

N. Lemahieu, J. Linke, G. Pintsuk, G. Van Oost, M. Wirtz and Z. Zhou
Resistance of tungsten with yttrium doping to ELM-like thermal shocks
Proceedings of the 45th Annual Meeting on Nuclear Technology (2014) 9081:1-9081:6

Oral Presentations

Sino-German workshop on Plasma-Surface-Interaction, Successive e-beam and particle loads on tungsten, May 2015, Jülich (Germany)

15th International Conference on Plasma-Facing Materials and Components for Fusion Applications, Thermal shock behavior of H and H/He-exposed tungsten at high temperature, May 2015, Aix-en-Provence (France)

4th FUSENET PhD Event, Combining H/He particle fluxes and ELM-like loading conditions on tungsten, November 2014, Lisbon (Portugal)

Tungsten IEA Implementing Agreement Meeting for Fusion Materials Development, Transient thermal shocks on tungsten pre-exposed to a pure H or a mixed H/He neutral beam, September 2014, San Sebastian (Spain)

45th Annual Meeting on Nuclear Technology / Jahrestagung Kerntechnik, Resistance of tungsten with yttrium doping to ELM-like thermal shocks, May 2014, Frankfurt (Germany)

IInd European workshop on Renewable Energy Systems, Plasma Facing Materials in fusion: thermal loads on tungsten, September 2013, Antalya (Turkey)

Poster Presentations

15th International Symposium on Fusion Nuclear Technology, H/He irradiation on tungsten exposed to ELM-like thermal shocks, September 2015, Jeju (Korea)

28th Symposium on Fusion Technology, Synergistic effects of ELMs and steady state H and H/He irradiation on tungsten in plasma facing components, October 2014, San Sebastian (Spain)

11th Carolus Magnus Summer School, Synergetic effects of transient heat loads and H/He particle exposure, August 2013, Bad Honnef (Germany)

3rd FUSENET PhD Event, Synergetic effects of H/He particle fluxes and transient thermal loads on tungsten, June 2013, York (United Kingdom)

14th International Conference on Plasma-Facing Materials and Components for Fusion Applications, Performance of yttrium doped tungsten under ELM-like loading conditions, May 2013, Jülich (Germany)

2nd FUSENET PhD Event, Investigation of tungsten exposed to fusion relevant H/He particle fluxes and thermal loads, October 2012, Pont-a-Mousson (France)

Acknowledgements

It is only with the advice and support from numerous colleagues, my family, and my friends that I have been able to complete this PhD adventure. They have provided me with motivation, guidance, and especially with quite a few pleasant distractions during the course of my research, all of which were essential in their own way. I am very grateful for this and appreciate that I could count on them, especially during the moments when doing a PhD is harder than I could have imagined beforehand.

First of all, I would like to thank my promoters. Much credit goes to prof. Guido Van Oost, who encouraged my enrolment in the Erasmus Mundus master FUSION-EP, brought me in contact with Forschungszentrum Jülich for my master thesis, supported my PhD application, and is always available to give me suggestions, feedback, and advice. When a second promoter was required at Ghent University, I am glad that prof. Jean-Marie Noterdaeme agreed to take up this role and make time free to properly follow up my work. I would like to thank also prof. Thomas Hirth, who initially took me as his PhD student and formed the link between my research and the University of Stuttgart. When I needed a new promoter at the University of Stuttgart, prof. Günter Tovar accepted this role, for which I am grateful.

In Forschungszentrum Jülich, I had the pleasure of being welcomed into an excellent environment to perform my research. Many thanks go to Dr. Jochen Linke who accepted me in his group, provided a continuous source of useful advice and contributions, and always made himself available for me and my questions. Luckily, I could rely on a superb supervisor who tirelessly listened to me, answered my questions with a 'yes, yes, maybe, yes, no' seconds before I actually could ask them, and never ceased to tell me to stop worrying. Therefore, I deeply thank Dr. Marius Wirtz. Because of the eagerness and precision with which he has shared his knowledge and given his constructive feedback, my work has clearly been improved and I was able to learn a lot, for which I am grateful to Dr. Gerald Pintsuk.

During my research and writing, I could always count on Dr. Thorsten Loewenhoff, Dr. Juan Du, and Dr. Thomas Weber for new ideas, comments on my work, and entertaining conversation, for which I am grateful. I had the pleasure of sharing an office with Isa, Ben, and Matthias, who have provided an enjoyable atmosphere, several smiles, an excellent soundboard

for my questions, and more than one discussion about how strong the coffee should be. For the assistance with technical questions and support, such as the manufacturing of my cooling structures or the cutting of my samples, my gratitude goes to Gaby and Gerd. Siau and Aurélie, a stop in your office has become an essential part of my coffee routine and was a source of friendship, laughter, and support, which I cherish deeply. I could not have thought of any better intermezzo between polishing, data analysis, and writing, than our conversations.

The work performed in the partner institutes has been crucial for the completion of this research. Particularly the support, advice, and assistance from Dr. Hans Maier and Henri Greuner in the Max-Planck-Institut für Plasmaphysik was indispensable for planning, performing, and improving my research and my thesis, for which they have my gratitude and appreciation.

The requirements of an Erasmus Mundus Joint Doctoral Program and the collaboration between two universities and two research institutes have provided some administrative hurdles that had to be faced, the navigation of which would not have been possible without help from Kathleen Van Oost and Frank Janssens at Ghent University and Dr. Carsten Lechte at the University of Stuttgart, for which I deeply thank them. I am happy that Aqsa, Patrick, and Xiaolong were willing to open their office at Ghent University and offer me a stimulating working environment, where there was always room for a pleasant conversation.

My friends have provided me with unwavering support and motivation for which I am grateful. I would to thank everyone who visited me in Aachen during these years. Two groups have exceeded my expectations and have become 'regulars' in my flat. Thomas, Wouter, Nico, Astrid, Lisa, Ruth, Sara, and Nele, a.k.a. 'De bende van Aachen', it was an honour to be able to host you and have our numerous trips together. Matthias, Toon, Piro, Astrid, and Anke, each time you came to Aachen, I could start the next week completely relaxed. I am confident we will find a way to keep our little tradition going on, even after I left Aachen.

Many improvements to the grammar and language have occurred between the first drafts of my thesis and this final version. For this, I am extremely grateful to Bailey and Rupert who have spent much time in answering my language-related questions, found many of my original mistakes, and given me very useful feedback on how to improve the language of my thesis.

Of course, a crucial factor in succeeding was the unyielding support from my girlfriend and my family. I thank them for visiting me and the interest they have shown for my choices. Naturally, I would like to especially thank Astrid for being so patient, understanding, and supportive with me, my father for listening to my stories and proofreading my thesis, my mother for her support and many maternal concerns, and my siblings Ellen and Rupert whose visits and interest in my work I deeply appreciate.